UNIVERSITÄT OSNABRÜCK

Department of Physics

Advancement of growth and characteristics of ultrathin ferrite films

Jari Rodewald, M.Sc.

Dissertation (kumulativ)

zur Erlangung des Doktorgrades (Dr. rer. nat.)

vorgelegt am Fachbereich Physik der Universität Osnabrück

Osnabrück, November 2020

Examiners:

Prof. Dr. Joachim Wollschläger

Prof. Dr. Thomas Schröder

Contents

1 Introduction

Within the last decades, the requirements for computational processes have grown continuously, demanding a progressive development of more and more powerful devices. Nowadays, logic operations are still merely performed by using conventional semiconducting electronics, which are based on the manipulation of electron charge currents. However, the continuous improvement of respective applications pushes the device size limits to smaller dimensions. This ongoing process in turn results in a higher density of electronic circuits and, consequently, in an increasing energy consumption. In this regard, the generation of waste heat further represents a difficulty to be minimized. As a consequence, the steadily increasing number and variety of electronic devices results in an enhanced energy demand. For instance, while the global energy consumption in the sector of information and communication technology was determined to 710 TWh in 2007 [1], it increased by ∼13% to 805 TWh in 2015 [2]. This development motivates the search for more efficient methods of data storage and processing.

This challenge can be addressed by implementing devices based on spintronics [3]. In contrast to conventional charge-based electronics, spintronic applications use the electron spin as an additional carrier of information. Thus, spintronic effects are based on the generation, manipulation, and detection of spin-polarized currents, which in turn enable information transfer at significantly lower charge current densities. In particular, due to the absence of mobile charge carriers in insulating materials the spin is not transported by free electrons but can be transported via magnonic spin waves and, thus, without charge transport.

The initial breakthrough of spintronics can be traced back to the discovery of the giant magnetoresistance (GMR) effect by P. Grünberg and A. Fert in the late 1980s [4,5]. The GMR effect describes the crucial dependence of electrical resistivity on the relative angle between the magnetizations of two ferro-/ferrimagnetic (FM) materials, which are separated by a conductive non-magnetic layer. Therefore, the GMR can serve as a highly-sensitive detector of magnetic fields, which forms the basis of readback heads incorporated nowadays in commercially available hard-disk drives, allowing for size reduction of the device while enhancing its storage capacity.

The discovery and significant impact of the GMR urged the advancement of further spintronic devices such as magnetic tunnel junctions (MTJs) [6,7]. Instead of a conductive layer in a GMR, an MTJ consists of an ultrathin insulating barrier separating the two FM electrodes to enable electron tunneling through the barrier. If the electrodes are spin-polarized, meaning a different density of states of spin-up and spin-down electrons at the Fermi level, the tunneling probability for parallel magnetization directions in both electrodes significantly differs from the one for antiparallel alignment. This behavior is known as the tunneling magnetoresistance (TMR) effect and can be understood by taking into account the spin polarization in both electrodes and the fact that the spin is preserved during the tunneling process [8].

In this regard, functional oxides moved into the focus for spintronic applications due to their broad variety of significant magnetic and electronic properties. As the quality of spintronic devices based on TMR or GMR effects depend on the degree of polarization in the generated spin-polarized currents, half-metallic materials exhibiting complete spin polarization at the Fermi-level serve as promising electrode materials in MTJs. For instance, the transition metal (TM) oxide Fe_3O_4 represents a suitable candidate for MTJ electrodes, as it is ferrimagnetic with half-metallic character and a predicted 100% spin polarization at the Fermi level [9] and therefore would be suitable for

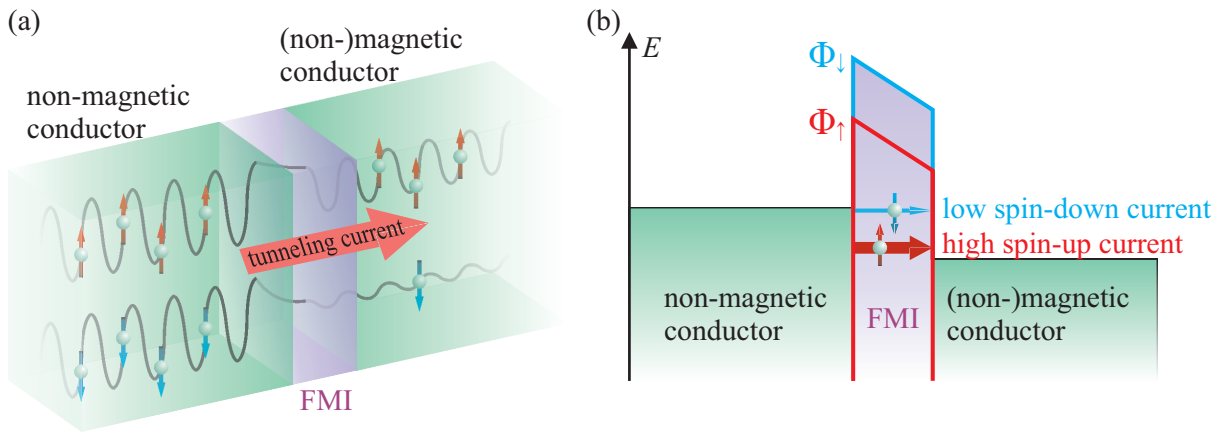

Fig. 1.1: (a) Schematic drawing of a spin filter, consisting of a thin ferro-/ferrimagnetic insulating (FMI) layer between a non-magnetic and a non-magnetic or FM electrode. (b) Principle energy diagram of a spin filter. The different tunneling barrier heights $\Phi_\uparrow$ and $\Phi_\downarrow$ of the FMI for spin-up and spin-down electrons, respectively, result in different tunneling probabilities through the barrier for both spin directions and therefore in highly spin-polarized tunneling currents.

the generation and detection of highly spin-polarized currents. However, due to effects occurring at the interface between electrode and tunneling barrier (including interface states and possible spin-flips) [8, 10] experimentally obtained TMR effects are still significantly smaller than theoretically predicted [11–13], which hinders the implementation in functional spintronic devices.
As an alternative, magnetic insulators can be used as tunneling barrier material as the exchange splitting of the spin-dependent conduction bands provides different tunneling barrier heights $\Phi_\uparrow$ and $\Phi_\downarrow$ for spin-up and spin-down electrons, respectively [cf. Fig. 1.1(b)]. Thus, the tunneling probabilities for both spin directions differ, which results in highly spin-polarized tunneling currents, making magnetic insulators extremely applicable as spin valves or spin filters [cf. Fig. 1.1(a)]. Here, the TM ferrites $CoFe_2O_4$ (CFO) and $NiFe_2O_4$ (NFO) are promising candidates for application, since both materials are ferrimagnetic with high Curie temperatures T_C ($T_C^{CFO} = 790\,K$, $T_C^{NFO} = 865\,K$ [14]) and exhibit insulating character. However, due to the rather complex inverse spinel-type structure, the growth of crystalline TM ferrites as CFO and NFO is usually accompanied by the incorporation of structural imperfections [15, 16], which in turn have an impact on the magnetic and electronic structure and, hence, on the spin-filter efficiencies. Several studies showed that significant spin-filter efficiencies of CFO and NFO tunneling barriers are merely obtained in the low-temperature regime [17–21]. Room temperature spin filtering has only been obtained for CFO films with a spin-filter efficiency of up to -8% [17]. Thus, to enable larger spin polarizations in spin-filter applications, epitaxial growth of well-ordered TM ferrite thin films with low defect densities is still a challenging task to conquer and the main motivation of this work.
Hence, within this cumulative thesis, (ultra)thin NFO and CFO films are prepared via reactive molecular beam epitaxy (RMBE) on MgO(001) and $SrTiO_3$(001) substrates and are characterized in terms of their structural, electronic, and magnetic properties. First, the relevant theoretical background is given in Chap. 2 to provide the fundamentals of crystalline thin film growth and magnetism, as well as the theoretical basis of the used measurement techniques. Further, the investigated materials with focus on their structural, electronic, and magnetic properties are presented in Chap. 3. A description of the experimental setups used to perform the respective measurements is given in Chap. 4, followed by the main parts of this work, which present the experimental results. First, the initial growth of four exemplary off-stoichiometric $Ni_xFe_{3-x}O_4$ thin films with $0 \leq x \leq 1.5$ on MgO(001) is structurally characterized *in situ* by synchrotron radiation-based x-ray diffraction (XRD) measurements during the growth process. Here, the influence of the rather small strain

induced by the substrate on the structural quality of the NFO films and at the interface between film and substrate is investigated in dependence of the film thickness and the cationic Ni content x. In addition to the vertical structural components obtained by XRD, high energy surface x-ray diffraction (HESXRD) measurements are conducted after film growth merely to determine the complementary lateral film lattice parameters. Further, hard x-ray photoelectron spectroscopy (HAXPES) measurements are performed to obtain information on the chemical and electronic structure of the prepared NFO films. The results of these investigations are published in *Applied Physics Letters* **117**, 011601 (2020) [22] and can be found in the reprinted version in Chap. 5.
Although varying cationic stoichiometries have been investigated in several studies for $Co_xFe_{3-x}O_4$ thin films [23–31], the reports of cationic variations in $Ni_xFe_{3-x}O_4$ thin films are still rare [32] and therefore in need of further systematic investigation. Hence, in the second major step of this work, a more extensive study on the dependence of the cationic ratio in $Ni_xFe_{3-x}O_4$ thin films ($0 \leq x \leq 2.07$) grown on MgO(001) is conducted with regard to the structural, electronic, and magnetic properties. The film surface structure and chemical composition is characterized *in situ* by low energy electron diffraction (LEED) and laboratory-based soft x-ray photoelectron spectroscopy (XPS), respectively. Film thicknesses are determined via analysis of x-ray reflectivity (XRR) data, while the film structure is analyzed by XRD measurements. Further, chemical properties and the electronic structure of the NFO films with focus on the cationic valencies of Ni and Fe cations with varying x is investigated by means of HAXPES. A depth-dependent chemical analysis via angle-resolved (AR-)HAXPES measurements further provides information on the vertical cationic distribution within the films. Complementary x-ray absorption spectroscopy (XAS) and x-ray magnetic circular dichroism (XMCD) investigations are conducted to obtain information on the cationic site occupancies and on the element-specific magnetic moments. The latter are compared to magnetic properties characterized via superconducting quantum interference device (SQUID) magnetometry. Thus, these complementary results presented in Chap. 6 give a comprehensive picture of structural, electronic, and magnetic properties of thin off-stoichiometric $Ni_xFe_{3-x}O_4$ films on MgO(001).
In a third step, the type of substrate is changed to $SrTiO_3$(001) to investigate the influence of a larger strain applied by the substrate to the film. Several studies reported an unusual strain, namely vertical compression, in ultrathin ferrite films on $SrTiO_3$(001), although, assuming an adaption of the film to the substrate lattice, lateral compression and consequently vertical expansion would be expected. In particular, Hoppe *et al.* ascribed the vertical compression of ultrathin NFO films grown on $SrTiO_3$(001) to an auxetic behavior, but without showing the experimental evidence of simultaneous lateral compression [33]. One further remarkable property of NFO films deposited on $SrTiO_3$(001) is the reported enhanced magnetization for ultrathin films below 3 nm thickness [33, 34]. However, a doubtless explanation for this behavior is still lacking. Hence, both intriguing phenomena, the unusual type of strain as well as the enhanced magnetization in ultrathin NFO films grown on $SrTiO_3$(001), therefore remain unclarified up to now and are investigated within this thesis. Therefore, several stoichiometric $NiFe_2O_4$ films with thicknesses between 3.7 and 55.5 nm are deposited via RMBE on $SrTiO_3$(001). The structure and chemical composition in the near-surface region of the films are characterized *in situ* by LEED and XPS measurements, respectively. In addition, the chemical composition and cationic valence states in deeper layers are characterized by HAXPES, whereas the structure of the NFO films and at the interfaces is analyzed by means of synchrotron radiation-based XRD and grazing incidence XRD (GIXRD). Moreover, GIXRD measurements of site-sensitive diffraction peaks are used to obtain information on the relative occupancies of tetrahedral and octahedral film lattice sites. Finally, magnetic properties of the prepared films are characterized by SQUID magnetometry. The results are published in *Physical Review Materials* **4**, 064404 (2020) [35] and reprinted in Chap. 7.
In a fourth step, an alternative pathway for the formation of ferrite thin films is demonstrated exemplarily for $CoFe_2O_4$ films on $SrTiO_3$(001). Here, in contrast to the simultaneous co-evaporation

of the respective transition metals as used in Chaps. 5 - 7, Fe_3O_4/CoO bilayers are deposited on $SrTiO_3$(001) and, subsequently, are annealed to induce thermal interdiffusion of the bilayer system and consequently form $CoFe_2O_4$ thin films. This method was first applied and successfully demonstrated by Kuschel *et al.* for the formation of thin $NiFe_2O_4$ films by interdiffusion of Fe_3O_4/NiO bilayers [36]. However, the application of this technique for the formation of CFO thin films is still lacking and therefore presented within this work. In total, three samples with different initial Fe_3O_4/CoO film thickness ratios have been prepared via RMBE on $SrTiO_3$(001). Subsequently, the interdiffusion process was monitored via XRR, soft XPS and AR-HAXPES to determine the bilayer/film structure, stoichiometry, and chemical properties. Analysis of complementary XAS measurements provides additional information on the occupancies of Fe and Co cations during interdiffusion. Final SQUID magnetometry measurements are performed to gain information on the magnetic properties before and after complete interdiffusion. The results are published in *Physical Review B* **100**, 155418 (2019) [37] and presented in the reprinted version in Chap. 8.
Finally, a concluding summary of all obtained results is given in Chap. 9.

2 Theoretical background

In this chapter the theoretical basis relevant for this work is established. First, a principal description of crystal structures of single crystals and thin films is introduced. Furthermore, the theory of the used x-ray diffraction experiments is presented. In addition, the basis of the spectroscopic techniques as well as the concepts of magnetism of thin films are described.

2.1 Periodic structures - single crystals and thin films

2.1.1 Single crystals

An ideal crystal is defined by a three-dimensional periodic arrangement of atoms or atom groups. Based on this periodicity, a repetitive structural element, the so-called unit cell, can be defined to describe the complete symmetry of the crystal. It is spanned by three linearly independent vectors $\boldsymbol{a}$, $\boldsymbol{b}$ and $\boldsymbol{c}$. Its translation

$$\boldsymbol{R}_n = n_a\,\boldsymbol{a} + n_b\,\boldsymbol{b} + n_c\,\boldsymbol{c} \quad \text{with} \quad n_a, n_b, n_c \in \mathbb{Z} \tag{2.1}$$

then defines the crystal lattice. Note that several possibilities are given to choose a unit cell describing the same crystal lattice, since only translational symmetry has to be fulfilled. The unit cell with the smallest possible volume is called primitive unit cell.
If the unit cell consists of not only one, but two or even more atoms, an atomic basis with its origin at each lattice point has to be defined. The atom positions within the unit cell can be obtained by

$$\boldsymbol{r}_j = u_j\,\boldsymbol{a} + v_j\,\boldsymbol{b} + w_j\,\boldsymbol{c} \quad \text{with} \quad 0 \leq u_j, v_j, w_j \leq 1, \tag{2.2}$$

pointing from the origin of the unit cell to the j-th atom of the basis with its respective coordinates u_j, v_j and w_j within the unit cell. With this, each atom position in the crystal is given by the

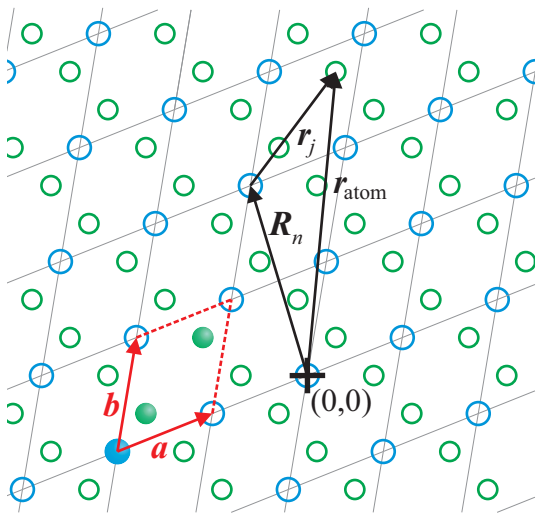

Fig. 2.1: Schematical representation of a two dimensional crystal with the primitive crystallographic lattice vectors $\boldsymbol{a}$ and $\boldsymbol{b}$, which span the primitive unit cell (red) consisting of a three atomic basis (filled blue and green circles). Proceeding from the origin of a unit cell at the position of a blue circle/atom, each atom position $\boldsymbol{r}_{\text{atom}}$ of the crystal is given by a vectorial superposition of the lattice point $\boldsymbol{R}_n$ and the atom position $\boldsymbol{r}_j$ within the unit cell.

vectorial superposition

$$\boldsymbol{r}_{\text{atom}} = \boldsymbol{R}_n + \boldsymbol{r}_j \,, \tag{2.3}$$

if the origin of the coordinate system is defined at a crystal lattice point. Thus, the complete crystal structure is given by a combination of the crystal lattice and its atomic basis. Due to reasons of clarity, an exemplary two-dimensional crystal lattice is schematically shown in Fig. 2.1. In this example, the (primitive) unit cell (red) is spanned by the (primitive) unit cell vectors $\boldsymbol{a}$ and $\boldsymbol{b}$ and consists of a three atomic basis (one blue, two green circles). One exemplary atom position $\boldsymbol{r}_{\text{atom}}$, given by superposition of the lattice point $\boldsymbol{R}_n$ and the position $\boldsymbol{r}_j$ within the unit cell, is shown additionally.
As an alternative to the description of the unit cell by its unit cell vectors $\boldsymbol{a}$, $\boldsymbol{b}$ and $\boldsymbol{c}$ it can also be characterized by the angles α, β and γ between the vectors in addition to their absolute values a, b and c - also called lattice constants.

2.1.2 Bravais lattices

In general, crystals are classified by their degree and type of symmetry. Here, symmetry operations as, i.e., rotation, reflection and inversion lead to a classification into seven different crystal systems (cubic, tetragonal, orthorhombic, hexagonal, trigonal, monoclinic, triclinic). Considering also translational operations, seven centered unit cells (face-centered, body-centered, base-centered) are added to the primitive types. Thus, in total 14 possible so-called *Bravais lattices* can be defined (cf. Fig. 2.2), which suffice the description of all existing crystal lattices.

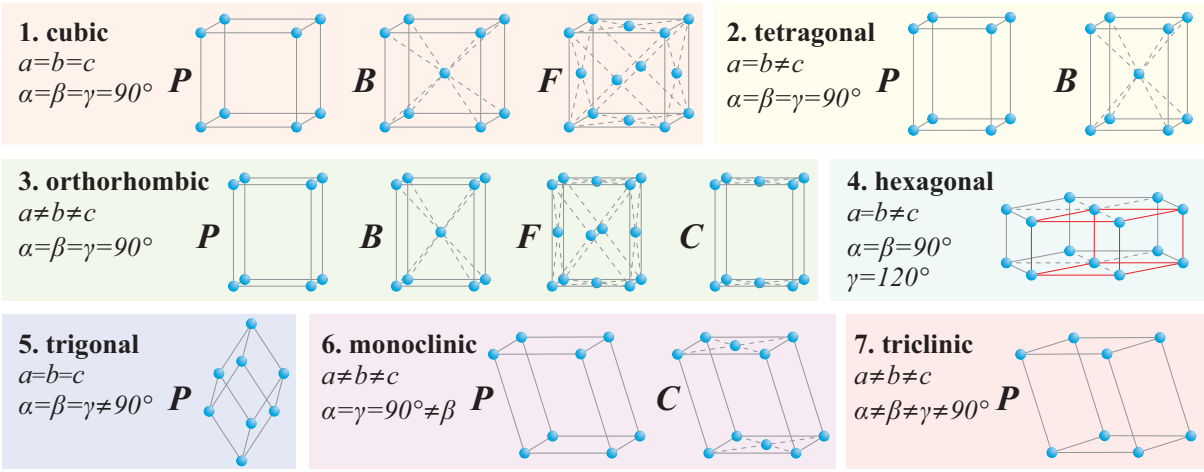

Fig. 2.2: The 14 Bravais lattices categorized in their seven crystal systems. The primitive unit cell is denoted by P, while B, F and C denote body-, face- and base-centered unit cells, respectively. The unit cell of the hexagonal system is primitive and only comprises the red framed regular prism. The trigonal system is described by a rhombohedral unit cell.

2.1.3 Lattice planes

To identify certain crystallographic planes in a crystal, three integer values h, k and l are established, denoting the (hkl) lattice plane. These *Miller indices hkl* are obtained by, first, determining the intersection points with the crystallographic axes and, second, inverting and reducing them to the (usually smallest) integer triplet (hkl) with the same ratios. For instance, the intercepts $3a$, $1b$ and

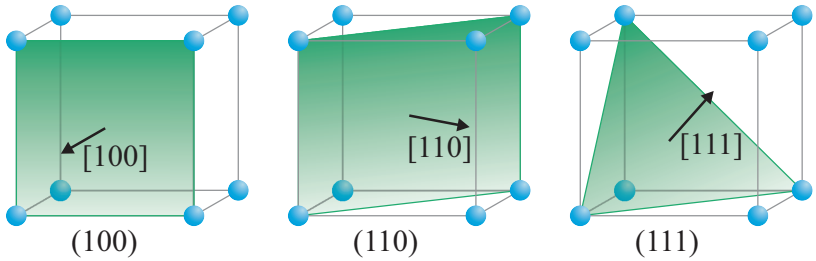

Fig. 2.3: Exemplary Miller notations of some common crystallographic planes (green) and directions in a simple cubic crystal system. Crystal planes are denoted by round brackets, crystal directions by square brackets. Here, only directions perpendicular to the depicted lattice planes are shown.

$2c$ of a lattice plane with the crystallographic axes, giving the inverted values of $\frac{1}{3}$, 1 and $\frac{1}{2}$, result in the smallest integer triplet and, thus, the Miller indices (263). If the plane does not intersect with a crystallographic axis, the corresponding index is zero, while negative Miller indices are denoted by a bar, e.g., -3 is denoted as $\bar{3}$. In order to designate equivalent lattice planes the notation $\{hkl\}$ is used.
Analogously to lattice planes, directions within a crystal are denoted by a triplet $[\tilde{h}\tilde{k}\tilde{l}]$ (note the square instead of round brackets for lattice planes). Here, $[\tilde{h}\tilde{k}\tilde{l}]$ are given by the smallest integer numbers with the same ratio as the single components (along the crystal axes) of a vector in this direction. For instance, a direction, which is characterized by the vectorial components $6a$, $2b$ and $4c$, is denoted as the [312] direction. Note that for cubic lattices the direction $[\tilde{h}\tilde{k}\tilde{l}]$ represents a vector which is perpendicular to the (hkl) plane with the same indices $\tilde{h}$=h, $\tilde{k}$=k and $\tilde{l}$=l. However, this relation is not generally valid for other crystal systems. Similar to the notation of parallel lattice planes, equivalent crystal directions are denoted by $\langle\tilde{h}\tilde{k}\tilde{l}\rangle$. Some common crystallographic planes and directions are exemplarily depicted in Fig. 2.3 for a simple cubic crystal system.

2.1.4 Epitaxial film growth

The growth of single crystalline films with a well-defined crystallographic orientation on a single crystalline substrate is known as *epitaxy* [38]. Furthermore, it can be subdivided into *homoepitaxy* (when the material of substrate and film are the same) and *heteroepitaxy* (when the film and substrate material are different). The growth behavior is strongly influenced by thermodynamic and kinetic processes. However, three major growth modes can be distinguished (cf. Fig. 2.4):

- **Layer-by-layer (or Frank-van der Merwe) growth**
  This growth mode is obtained, if film atoms are more strongly bound to the substrate than to each other. Consequently, each layer is completely filled before the next layer starts to grow.
- **Island (or Volmer-Weber) growth**
  In contrast to layer-by-layer growth, this growth mode refers to the case when film atoms are more strongly bound to each other than to the substrate. As a result, three-dimensional islands emerge directly on the substrate.
- **Layer-plus-island (or Stranski-Krastanov) growth**
  This growth mode is a combination of the latter two. After forming a closed two-dimensional layer on the substrate, film growth proceeds by forming three-dimensional islands.

The division into these three growth modes can be understood qualitatively by taking into account the surface or interface tensions γ of/between film and substrate. Interpreting γ as a force per unit length of boundary, force equilibrium at the contact point of film and substrate results in

$$\gamma_{\mathrm{s}} = \gamma_{\mathrm{f/s}} + \gamma_{\mathrm{f}} \cos(\vartheta) \tag{2.4}$$

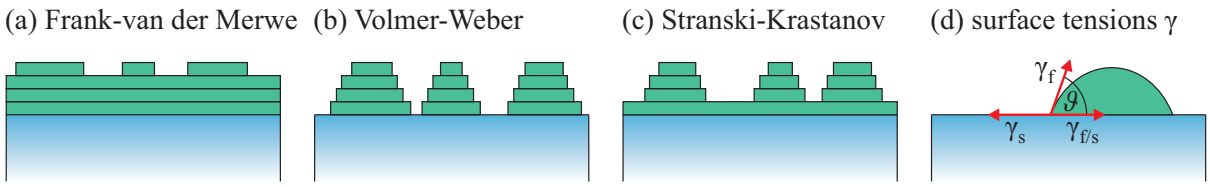

Fig. 2.4: Schematical representation of the three different growth modes of a film (green) on a substrate (blue): (a) layer-by-layer (Frank-van der Merwe), (b) island (Volmer-Weber) and (c) layer-plus-island (Stranski-Krastanov) growth. (d) Sketch of the respective surface and interface tensions γ and the resulting wetting angle ϑ between film island and substrate.

with γ_s as the surface tension of the substrate, $\gamma_\mathrm{f/s}$ as the interface tension between film and substrate, γ_f as the surface tension of the film and ϑ as the contact angle between film island and substrate, also called wetting angle [cf. Fig. 2.4(d)]. Considering Eq. (2.4), the case $\gamma_\mathrm{s} \geq \gamma_\mathrm{f/s} + \gamma_\mathrm{f}$ results in a wetting angle of $\vartheta = 0$ and, thus, completely two-dimensional growth corresponding to layer-by-layer growth. In contrast, if the condition $\gamma_\mathrm{s} < \gamma_\mathrm{f/s} + \gamma_\mathrm{f}$ is fulfilled, islands with a wetting angle $\vartheta > 0$ are formed, resulting in three-dimensional island growth. For layer-plus-island growth, the first relation as in layer-by-layer growth is fulfilled for the initial growth steps, but the formation of this intermediate layer enhances the film tension resulting in the formation of three-dimensional islands during further growth.

2.1.5 Strain effects

In heteroepitaxy, perfect lattice matching between film and substrate is extremely rare. In most cases the lattice constants of the film differ from the ones of the substrate [cf. Fig. 2.5(a)]. This deviation can be quantified by the lattice mismatch

$$f = \frac{a_\mathrm{f} - a_\mathrm{s}}{a_\mathrm{s}} \tag{2.5}$$

with a_f and a_s as the relaxed lateral lattice constants of film and substrate, respectively. Due to the lattice mismatch lateral (or in-plane) strain

$$\epsilon_\parallel = \frac{a_\mathrm{f,str} - a_\mathrm{f}}{a_\mathrm{f}} = \frac{\Delta a_\mathrm{f}}{a_\mathrm{f}} \tag{2.6}$$

can be induced in the film. Here, $a_\mathrm{f,str}$ and a_f denote the strained and relaxed in-plane film lattice constants, respectively. Similarly, the vertical (out-of-plane) strain can be defined as

$$\epsilon_\perp = \frac{c_\mathrm{f,str} - c_\mathrm{f}}{c_\mathrm{f}} = \frac{\Delta c_\mathrm{f}}{c_\mathrm{f}} \tag{2.7}$$

with $c_\mathrm{f,str}$ and c_f as the respective strained and relaxed out-of-plane film lattice constants. Assuming a tetragonally distorted film with homogeneous biaxial in-plane strain, the relation between lateral ($\epsilon_\parallel = \Delta a_\mathrm{f}/a_\mathrm{f}$) and vertical strain ($\epsilon_\perp = \Delta c_\mathrm{f}/c_\mathrm{f}$) can be expressed by

$$\frac{\Delta c_\mathrm{f}}{c_\mathrm{f}} = \frac{2\nu}{\nu - 1}\frac{\Delta a_\mathrm{f}}{a_\mathrm{f}} \tag{2.8}$$

with ν as the Poisson ratio of the film material [39]. A detailed derivation and definition of ν is given in standard textbooks [40].
The induced strain can either result in pseudomorphic film growth or in the formation of so-called

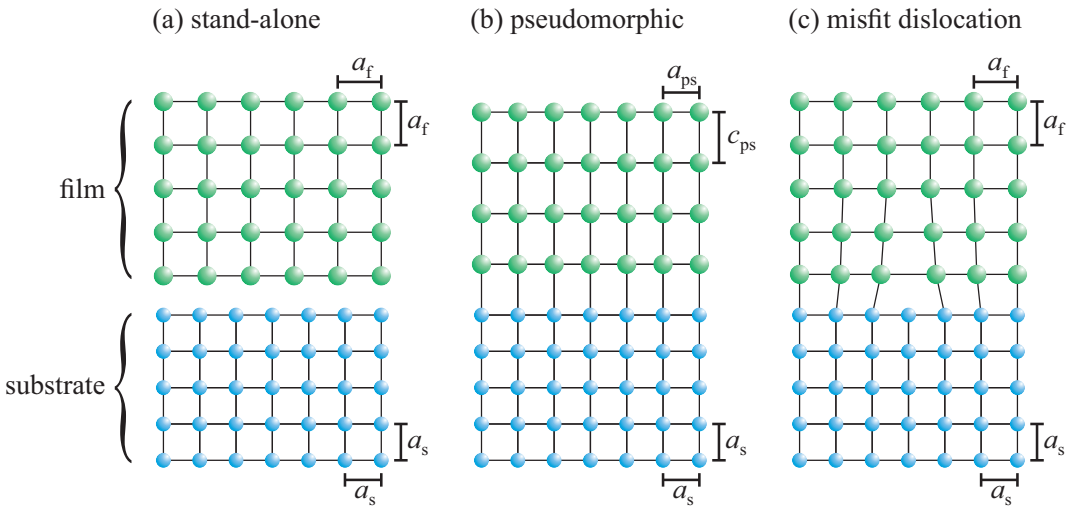

Fig. 2.5: Sketch of the two main processes in heteroepitaxy exemplarily shown for cubic crystal systems (if completely relaxed) of film and substrate. (a) Stand-alone configuration of the film without any influence of the substrate: the relaxed film lattice constant a_f is larger than the one of the substrate (a_s), resulting in mismatch between both lattices. (b) Pseudomorphic growth with lateral adaption of the film to the substrate ($a_{ps} = a_s$). Lateral compression results in vertical tension ($c_{ps} > a_f$). (c) Formation of a misfit dislocation at the substrate/film interface, leading to relaxed subsequent film growth.

misfit dislocations, depending on the relation of free energy densities for each mechanism [38]. Both processes are schematically depicted in Figs. 2.5(b) and 2.5(c), respectively. In the case of pseudomorphic growth, the film adopts the periodicity of the substrate in lateral direction [cf. Fig. 2.5(b)]. As a consequence, the film exhibits in-plane strain with a lateral lattice constant coinciding with the lateral lattice constant of the substrate. Due to energy minimization this lateral strain results in homogeneous compression or tension of the lattice constant in vertical direction.

For higher lattice mismatches, strain is more likely released by the formation of misfit dislocations directly at the substrate/film interface [cf. Fig. 2.5(c)]. The distance between dislocations can be estimated via

$$d_{\mathrm{dis}} = \frac{a_{\mathrm{f}}\, a_{\mathrm{s}}}{|a_{\mathrm{s}} - a_{\mathrm{f}}|} \ . \tag{2.9}$$

For completely relaxed films, however, misfit dislocations can also be incorporated in the film far beyond the interface between film and substrate, since for pseudomorphic growth the strain energy increases linearly with increasing film thickness, while the energy of dislocations only increases logarithmically [38]. Thus, misfit dislocations are energetically favored and more likely incorporated for increasing film thicknesses, resulting in a transition from pseudomorphic growth to dislocation formation. The film thickness upon which misfit dislocations begin to be favorably incorporated in the film is called critical film thickness $\mathrm{D_c}$. Several models can be applied to obtain an estimation of $\mathrm{D_c}$ for the case of heteroepitaxial film growth. Following the most widely used model from Matthews and Blakeslee [41], the critical thickness can be estimated via

$$\frac{\mathrm{D_c}}{b} = \frac{\left(1 - \nu\, \cos^2\alpha\right)\, \left(\ln\left(\frac{\mathrm{D_c}}{b}\right) + 1\right)}{2\,\pi\, f\, (1+\nu)\, \cos(\lambda)} \ . \tag{2.10}$$

Here, b is the magnitude of the Burgers vector, f is the lattice mismatch, ν is the Poisson ratio, α is the angle between the Burgers vector and the dislocation line ($\alpha = 90°$ for edge dislocations), and

λ is the angle between the slip direction and that line in the interface plane which is perpendicular to the line of intersection between the slip plane and the interface ($\lambda = 45°$ for rock salt structures).

2.2 X-ray diffraction

The phenomenon of x-ray diffraction can be used to determine the structure of long range ordered periodic, i.e., (poly-)crystalline systems. Its principle is based on the mechanism of x-ray scattering, where electromagnetic waves are scattered when encountering an object or inhomogeneity. Since the cross-sections of x-rays for the interaction with electrons are orders of magnitude larger than for scattering at atomic nuclei, mainly the electrons surrounding the atom act as scattering centers. Assuming only elastical scattering (which is not exact but a sufficient approximation for x-rays interacting with condensed matter), this mechanism can be described following classical electromagnetic theory as a periodic deflection of the electrons by the incoming wave. As a consequence, these oscillating electrons act as a Hertzian dipole and are the source of the outgoing/scattered electromagnetic wave exhibiting the same frequency as the incoming wave. In general, x-ray scattering at long range ordered periodic structures is called x-ray diffraction. Here, due to the periodic nature of the material, constructive and destructive interference of the scattered waves can occur, resulting in spots of high intensity at certain scattering angles, also known as Bragg peaks, for constructive interference.

2.2.1 The Bragg condition

William Henry Bragg and William Lawrence Bragg described the diffraction of x-rays at crystals by a superposition of waves reflected at parallel crystal lattice planes [42], as depicted in Fig. 2.6. Here, the phase differences between the reflected waves cause an interference pattern, which is determined by the lattice plane distance d_{hkl}, also known as layer distance of (hkl) planes, and the used x-ray wavelength λ. If the path difference of the reflected beams is an integer multiple of their wavelength, constructive interference occurs. This condition is described by Bragg's law

$$n\lambda = 2d_{hkl} \sin\theta \tag{2.11}$$

with $n \in \mathbb{N}$ as the order of the Bragg peak and θ as the angle between incident/reflected wave and respective lattice planes.

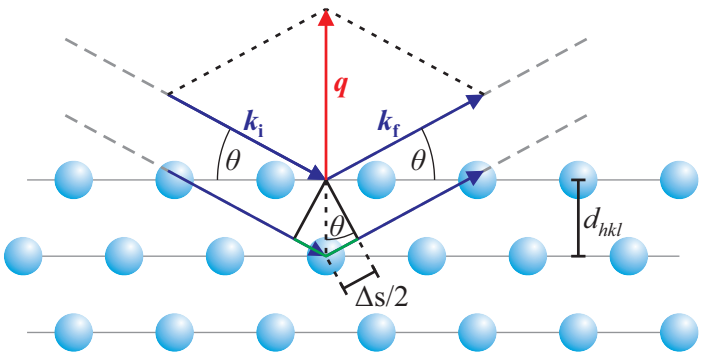

Fig. 2.6: Sketch for the derivation of Bragg's law. The incident waves $\boldsymbol{k_i}$ are reflected under angle θ at lattice planes (solid lines) with a layer distance d_{hkl}. The reflected waves $\boldsymbol{k_f}$ are phase-shifted towards the incident waves $\boldsymbol{k_i}$ due to a path difference Δs. If the condition $\Delta s = n\lambda$ is fulfilled, constructive interference occurs. The scattering vector $\boldsymbol{q} = \boldsymbol{k_f} - \boldsymbol{k_i}$ is oriented perpendicular to the lattice planes.

Following Bragg's law, a condition for observing interference phenomena for scattering at crystals is given: the used wavelength has to be in the order of the distance of scattering centers. If $\lambda \leq 2d_{hkl}$ is not fulfilled, no Bragg reflection and, thus, no diffraction pattern can be observed. As the layer distances of single crystals are typically in the range of a few Ångstroms, the used wavelength

should also be of the same order or even less. This condition is fulfilled for x-rays, which are most commonly used in the energy range of 5 - 100 keV for x-ray diffraction experiments to gain information about the crystalline structure of solids.

2.2.2 Laue equations and reciprocal lattice

An equivalent formulation of the Bragg condition for constructive interference is given by the Laue equations[1] [43]

$$\boldsymbol{q} \cdot \boldsymbol{a} = 2\pi h \ , \quad \boldsymbol{q} \cdot \boldsymbol{b} = 2\pi k \ , \quad \boldsymbol{q} \cdot \boldsymbol{c} = 2\pi l \ , \tag{2.12}$$

with the basis vectors $\boldsymbol{a}$, $\boldsymbol{b}$ and $\boldsymbol{c}$ of the crystal lattice (see Sec. 2.1.1) and the integer numbers h, k and l, which correspond to the Miller indices used to denote lattice planes (see Sec. 2.1.3). The scattering vector $\boldsymbol{q} = \boldsymbol{k_f} - \boldsymbol{k_i}$ is given by the difference between final and initial wave vectors $\boldsymbol{k_f}$ and $\boldsymbol{k_i}$, respectively (cf. Fig. 2.6).
At this point, the concept of the reciprocal lattice is introduced, since it is very useful to describe diffraction phenomena and is closely related to the Laue equations. The reciprocal lattice, complementary to the crystal lattice in real space, consists of three reciprocal lattice vectors, which are related to the real space lattice vectors $\boldsymbol{a}$, $\boldsymbol{b}$ and $\boldsymbol{c}$ via

$$\boldsymbol{a^*} = 2\pi \frac{\boldsymbol{b} \times \boldsymbol{c}}{\boldsymbol{a} \cdot (\boldsymbol{b} \times \boldsymbol{c})} \ , \quad \boldsymbol{b^*} = 2\pi \frac{\boldsymbol{c} \times \boldsymbol{a}}{\boldsymbol{a} \cdot (\boldsymbol{b} \times \boldsymbol{c})} \ , \quad \boldsymbol{c^*} = 2\pi \frac{\boldsymbol{a} \times \boldsymbol{b}}{\boldsymbol{a} \cdot (\boldsymbol{b} \times \boldsymbol{c})} \ , \tag{2.13}$$

where $\boldsymbol{a} \cdot (\boldsymbol{b} \times \boldsymbol{c})$ is the volume of the unit cell. In analogy to the crystal lattice in real space, which describes the positions of atoms in the crystal, the reciprocal lattice points

$$\boldsymbol{G} = h\boldsymbol{a^*} + k\boldsymbol{b^*} + l\boldsymbol{c^*} \quad \text{with} \quad h, k, l \in \mathbb{Z} \tag{2.14}$$

give the positions of possible Bragg peaks. For orthogonal crystal lattices ($\alpha = \beta = \gamma = 90°$), the reciprocal lattice vectors are also orthogonal and their length is given by

$$a^* = \frac{2\pi}{a} \ , \quad b^* = \frac{2\pi}{b} \ , \quad c^* = \frac{2\pi}{c} \ . \tag{2.15}$$

Taking into account the reciprocal lattice, the Laue equations can be rearranged to

$$\boldsymbol{q} = \boldsymbol{k_f} - \boldsymbol{k_i} = \boldsymbol{G} \ . \tag{2.16}$$

Meaning, constructive interference occurs, if the scattering vector $\boldsymbol{q}$ coincides with a lattice vector $\boldsymbol{G}$ of the reciprocal lattice.

2.2.3 Kinematic diffraction theory

Both, Laue and Bragg conditions, only describe the positions of constructive interference and can be used to determine the periodicity of the crystal lattice. However, the atomic structure within the unit cell is still completely disregarded. By also taking the inner atomic structure of the unit cells into account, intensity modulations of the Bragg peaks can occur. Even completely vanishing intensities at Bragg positions can be obtained due to destructive interference of x-rays scattered at different atoms within the unit cell (so-called structurally forbidden Bragg peaks).

[1] The equivalence to the Bragg condition can be followed for interference of reflected beams from, e.g., {100} planes with distance a, considering parallel alignment of lattice vector $\boldsymbol{a}$ and scattering vector $\boldsymbol{q}$ with $q = \frac{4\pi}{\lambda} \sin\theta$, giving $\boldsymbol{q} \cdot \boldsymbol{a} = q \cdot a$. Thus, Eq. (2.12) results in $\frac{4\pi}{\lambda} a \sin\theta = 2\pi h$, which is equivalent to the Bragg condition in Eq. (2.11).

Hence, a description of diffracted intensities is derived in the following. Within this derivation, the diffraction phenomena are described by the concept of classical kinematic diffraction theory. Here, due to the weak interactions of x-rays with matter, some approximations can be applied. For instance, multiple scattering as well as refraction and absorption processes are neglected within this theoretical model. Furthermore, x-ray scattering from atomic nuclei is not considered due to the small cross section compared to x-ray scattering at electrons. Considering these simplifications, a quantitative derivation of diffracted intensities from crystalline semi-infinite and thin film structures is presented here, based on theoretical work found in Refs. [44, 45].

Scattering at a single electron

If the distances between radiation source and scattering center as well as between scattering center and detection point are large compared to the used wavelength, the Fraunhofer (or far field) approximation becomes valid and the incoming and scattered waves can be considered as plane waves. Neglecting inelastic scattering processes, the amplitude $A(\boldsymbol{q})$ of a wave scattered at a single electron at position $\boldsymbol{r}_e$ can be described by the Thomson equation

$$A(\boldsymbol{q}) = A_0\, C\, e^{i\boldsymbol{q}\cdot\boldsymbol{r}_e} \quad \text{with} \quad C = \frac{e^2}{m_e\, c^2\, R_0} \quad . \tag{2.17}$$

Here, A_0 is the amplitude of the incident wave, R_0 the distance between electron and detection point, c the speed of light and e and m_e the charge and mass of the electron, respectively. Due to the strong dependence on the specific scattering geometry, the polarization of the incident wave is not considered here. It will be taken into account as a correction factor in Sec. 4.3.4.

Scattering at a single atom

X-ray scattering at a single atom can be described by the superposition of waves scattered at all electrons surrounding this atom, considering the path and, thus, phase differences between the different scattered waves. Here, it should be noted that the electrons are not discretely localized at the atom position $\boldsymbol{r}_{\text{atom}}$, but are distributed around the atom, more appropriately described by an electron distribution function $\rho(\boldsymbol{r})$. Moreover, the distance R_0 between scattering center and detector [cf. Eq. (2.17)] can be assumed to be the same for all electrons, as it is much larger than the nucleus-electron distance $|\boldsymbol{r}|$ within the atom. The amplitude of a wave scattered at a single atom is then given by

$$A(\boldsymbol{q}) = A_0\, C \int d^3r\, \rho(\boldsymbol{r})\, e^{i\,\boldsymbol{q}\cdot(\boldsymbol{r}_{\text{atom}}+\boldsymbol{r})} \tag{2.18}$$

$$= A_0\, C\, f(\boldsymbol{q})\, e^{i\,\boldsymbol{q}\cdot\boldsymbol{r}_{\text{atom}}} \quad . \tag{2.19}$$

Here, the atomic form factor is defined by

$$f(\boldsymbol{q}) = \int d^3r\, \rho(\boldsymbol{r})\, e^{i\,\boldsymbol{q}\cdot\boldsymbol{r}} \quad , \tag{2.20}$$

which thereby represents the Fourier transform of the electron density of the atom. In this work, solely spherical electron distributions are assumed. Thus, the atomic form factor only depends on the absolute value of $\boldsymbol{q}$ and not on its direction and can be approximated by four Gaussian

functions

$$f(q) = \sum_{i=1}^{4} a_i \; e^{-b_i \left(\frac{q}{4\pi}\right)^2} + c \; . \tag{2.21}$$

Parameters a_i, b_i and c determined for different atoms and ions can be found in Ref. [46].

Scattering at a single unit cell

Equivalent to the scattering process of an atom as a summation of the scattered waves at all electrons, the scattered amplitude of a unit cell results from a superposition of waves scattered at each atom within the unit cell. Thus, it is given by

$$A(\boldsymbol{q}) = A_0 \, C \sum_j f_j(q) \, e^{i\boldsymbol{q} \cdot (\boldsymbol{R}_n + \boldsymbol{r}_j)} \tag{2.22}$$

$$= A_0 \, C \, F(\boldsymbol{q}) \; e^{i\boldsymbol{q} \cdot \boldsymbol{R}_n} \tag{2.23}$$

with $\boldsymbol{R}_n$ as the position of the unit cell and $\boldsymbol{r}_j$ as the position of the j-th atom within the unit cell (cf. Sec. 2.1.1). In analogy to the definition of the atomic form factor, the structure factor

$$F(\boldsymbol{q}) = \sum_j f_j(q) \, e^{i\boldsymbol{q} \cdot \boldsymbol{r}_j} \tag{2.24}$$

is defined as the summation of all atomic form factors within the unit cell. Thus, it represents the Fourier transform of the electron distribution within the unit cell. In contrast to the electron distribution of each atom, the structure factor is not isotropic and thereby significantly depends on the direction of the scattering vector $\boldsymbol{q}$.

Debye-Waller factor

In the description of the structure factor given above [cf. Eq. (2.24)] the atoms within the unit cell are treated as located at their fixed positions. However, in real crystals these are only average positions about which the atoms oscillate due to, i.e., thermal vibrations. This displacement of electrons results in a (time-dependent) change of the electron density function and, thus, in a change of the atomic form factor and, in turn, in a change of the scattered intensity. This effect can be considered by a modified atomic form factor

$$f^m(\boldsymbol{q}) = f(\boldsymbol{q}) \; e^{-M(\boldsymbol{q}, T)} \; , \tag{2.25}$$

where the additional exponential term is called the Debye-Waller factor. Assuming an isotropic Gaussian displacement distribution around the mean position $\boldsymbol{r}_j$ of the j-th atom, the corresponding factor $M_j(\boldsymbol{q}, T)$ results in the simplified expression

$$M_j(q, T) = \frac{1}{2} \, U_j(T) \, |\boldsymbol{q}|^2 \; , \tag{2.26}$$

where the factor $U_j(T)$ describes the temperature dependency. With this, the structure factor is adapted to

$$F(\boldsymbol{q}) = \sum_j f_j^m(q)\, e^{i\boldsymbol{q}\cdot\boldsymbol{r}_j} \tag{2.27}$$

$$= \sum_j f_j(q)\, e^{i\boldsymbol{q}\cdot\boldsymbol{r}_j}\, e^{-\frac{1}{2}U_j(T)\,|\boldsymbol{q}|^2} \ . \tag{2.28}$$

In general, the vibrations of an atom in a crystal and, thus, the Debye-Waller factor are anisotropic (although the Gaussian distribution gives a good approximation in first order). Then, the factor $U_j(T)$ is a symmetric second order tensor, also called "vibrational ellipsoid", which may result in different Debye-Waller factors for different $[hkl]$ directions. The derivation of the Debye-Waller factor made here, as well as further detailed descriptions of the effect of thermal vibrations on x-ray diffraction can be found in Refs. [47, 48].

Diffraction at a single crystal

A single crystal is a periodic arrangement of the unit cells in all three spatial directions (cf. Sec. 2.1.1). The amplitude of a wave diffracted at these periodic structures can therefore be described by a summation of the amplitudes scattered at all unit cells taking into account the phase shifts between the scattered waves. Thus, the diffracted amplitude is given by

$$A(\boldsymbol{q}) = A_0\, C \sum_n F_n(\boldsymbol{q})\, e^{i\boldsymbol{q}\cdot\boldsymbol{R}_n} \ . \tag{2.29}$$

Considering that the crystal consists of equal unit cells, the structure factors $F_n(\boldsymbol{q})$ of all unit cells are identical. Also assuming finite numbers N_a, N_b and N_c of unit cells in the respective crystallographic directions and replacing $\boldsymbol{R}_n$ by the definition given in Eq. (2.1), the diffracted amplitude can be rewritten as

$$A(\boldsymbol{q}) = A_0\, C\, F(\boldsymbol{q}) \sum_{n_a=0}^{N_a-1}\sum_{n_b=0}^{N_b-1}\sum_{n_c=0}^{N_c-1} e^{i\boldsymbol{q}\cdot(n_a\boldsymbol{a}+n_b\boldsymbol{b}+n_c\boldsymbol{c})} \tag{2.30}$$

$$= A_0\, C\, F(\boldsymbol{q}) \sum_{n_a=0}^{N_a-1} e^{in_a\,\boldsymbol{q}\cdot\boldsymbol{a}} \sum_{n_b=0}^{N_b-1} e^{in_b\,\boldsymbol{q}\cdot\boldsymbol{b}} \sum_{n_c=0}^{N_c-1} e^{in_c\,\boldsymbol{q}\cdot\boldsymbol{c}} \ . \tag{2.31}$$

Each of the sums can be identified as a geometric series, allowing the rearrangement for each single direction (here, the sum along the crystallographic c axis with N_c scattering centers is selected exemplarily) to the form

$$B_{N_c}(\boldsymbol{q}) = \sum_{n_c=0}^{N_c-1} e^{in_c\,\boldsymbol{q}\cdot\boldsymbol{c}} = \frac{1-e^{iN_c\,\boldsymbol{q}\cdot\boldsymbol{c}}}{1-e^{i\,\boldsymbol{q}\cdot\boldsymbol{c}}} \ . \tag{2.32}$$

The diffracted intensity is obtained by the square of Eq. (2.31) and, thus, proportional to the square of Eq. (2.32). Substituting $x = \boldsymbol{q}\cdot\boldsymbol{c}$ results in

$$S_{N_c}(x) = |B_{N_c}|^2(x) = \frac{\sin^2(N_c\,x/2)}{\sin^2(x/2)} \ , \tag{2.33}$$

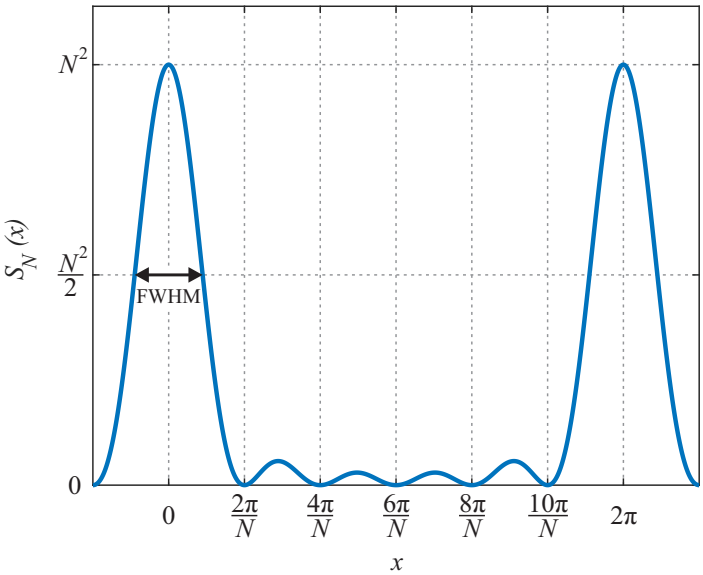

Fig. 2.7: N-slit function depicted exemplarily for $N = 6$, exhibiting main maxima with an amplitude of N^2 at x values of integer multiples of 2π. In between two main maxima, $N - 2$ side maxima - also called fringes - are visible. The spacing between neighboring minima of these fringes is given by $2\pi/N$. The full width at half maximum (FWHM) of the main maxima is proportional to the inverse of N (FWHM $\propto 1/N$).

which is also known as N-slit function and depicted in Fig. 2.7 exemplarily for $N_c = N = 6$. This function exhibits main maxima with the maximum intensity of N^2 separated by integer multiples of 2π. In addition, $N - 2$ smaller side maxima - also called fringes - appear between these main maxima. The spacing between the minima of neighboring fringes equals $2\pi/N$. The full width at half maximum (FWHM) of the main maxima is proportional to the inverse of the number of unit cells N in the respective crystal direction, following the Scherrer formula

$$\text{FWHM} = K_\text{S} \frac{2\pi}{N} \tag{2.34}$$

with $K_\text{S} = 0.89$ [49]. Thus, if the number of unit cells (along one particular crystallographic direction) is increased, the FWHM of the main maxima and fringes decreases and the number of fringes between the main maxima increases.
Assuming an infinite number N_a, N_b and N_c of unit cells in each crystallographic direction, which is the case for an ideal single crystal, all of the diffracted intensity is redistributed to the main maxima. The resulting diffracted amplitude is then given by

$$A(\boldsymbol{q}) \propto A_0\, C\, F(\boldsymbol{q}) \sum_h \sum_k \sum_l \delta(\boldsymbol{q}\cdot\boldsymbol{a} - 2\pi\, h)\, \delta(\boldsymbol{q}\cdot\boldsymbol{b} - 2\pi\, k)\, \delta(\boldsymbol{q}\cdot\boldsymbol{c} - 2\pi\, l) \tag{2.35}$$

as a representation of δ-distributions, which are in accordance with the Laue equations introduced earlier [cf. Eq. (2.12)], resulting in distinct points of high intensity, known as Bragg peaks.

Diffraction at a semi-infinite crystal

The concept of diffraction at single (ideal) crystals spanned infinitely far in all spatial directions as presented above is not realistic, since all real crystals exhibit surfaces and, thus, boundaries of their periodic atomic arrangement. An x-ray beam, which irradiates a real crystal, penetrates the crystal surface. This surface in turn exhibits a finite roughness, which has to be taken into account for the description of the diffracted intensity. Moreover, due to the relatively weak interaction of x-rays with matter, the x-ray beam penetrates deeper into the crystal (typically in the μm range) and passes through a large number of crystal layers, which all contribute to the diffracted intensity. However, during their way through the crystal the x-rays undergo absorption processes, which weaken the contribution to the diffracted intensity from atoms in deeper layers. Thus, if the

diffraction pattern of real crystals should be described, also the decreasing x-ray intensity due to absorption (and reflection) during the pass-through has to be considered, which therefore extends the models of classical kinematic diffraction theory.

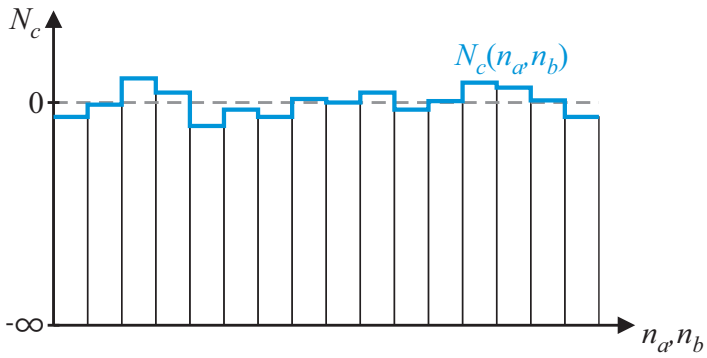

Fig. 2.8: Schematical display of a semi-infinite crystal with a height distribution $N_c(n_a, n_b)$ of the crystal surface. The profile's average is at zero level.

If the real crystal is significantly thicker than the penetration depth of the x-rays, it can be assumed to be semi-infinite along the direction perpendicular to the surface. As this condition is fulfilled for the substrates used in this work, the semi-infinite crystal model is adequate for the description of the diffracted intensity caused by the substrate. Considering an absorption ϵ per layer, the amplitude resulting from diffraction at a semi-infinite crystal limited in vertical direction (corresponding to the direction perpendicular to the plane spanned by the crystallographic vectors $\boldsymbol{a}$ and $\boldsymbol{b}$) is then given by

$$A_{substrate}(\boldsymbol{q}) = A_0\, C\, F(\boldsymbol{q}) \sum_{n_a=0}^{N_a-1} e^{i n_a \boldsymbol{q}\cdot\boldsymbol{a}} \sum_{n_b=0}^{N_b-1} e^{i n_b \boldsymbol{q}\cdot\boldsymbol{b}} \sum_{n_c=-\infty}^{N_c(n_a,n_b)} e^{i\, n_c\, \boldsymbol{q}\cdot\boldsymbol{c}}\; e^{n_c \epsilon} \;. \tag{2.36}$$

Here, absorption is taken into account by the exponential term $e^{n_c\epsilon}$, whereas $N_c(n_a, n_b)$ gives the height variation in dependence of the lateral positions n_a and n_b, which corresponds to the surface roughness (cf. Fig. 2.8). Considering exactly fulfilled Laue conditions in lateral directions [cf. Eq. (2.12)], the amplitude in vertical direction is then given by

$$A_{substrate}(\boldsymbol{q}) = A_0\, C\, F(\boldsymbol{q}) \sum_{n_a=0}^{N_a-1} 1 \sum_{n_b=0}^{N_b-1} 1 \sum_{n_c=-\infty}^{N_c(n_a,n_b)} e^{i\, n_c\, \boldsymbol{q}\cdot\boldsymbol{c} + n_c\epsilon} \tag{2.37}$$

$$= A_0\, C\, F(\boldsymbol{q}) \sum_{n_a=0}^{N_a-1} \sum_{n_b=0}^{N_b-1} \frac{e^{(i\,\boldsymbol{q}\cdot\boldsymbol{c}+\epsilon)\, N_c(n_a,n_b)}}{1 - e^{-(i\,\boldsymbol{q}\cdot\boldsymbol{c}+\epsilon)}} \;. \tag{2.38}$$

As the summations over n_a and n_b represent an averaging of the height function $N_c(n_a, n_b)$, Eq. (2.38) can be rewritten as

$$A_{substrate}(\boldsymbol{q}) = A_0\, C\, F(\boldsymbol{q})\, N_a N_b \frac{\left\langle e^{(i\,\boldsymbol{q}\cdot\boldsymbol{c}+\epsilon)\, N_c(n_a,n_b)} \right\rangle}{1 - e^{-(i\,\boldsymbol{q}\cdot\boldsymbol{c}+\epsilon)}} \;. \tag{2.39}$$

Moreover, assuming a Gaussian shaped height distribution $N_c(n_a, n_b)$ around a mean level set to zero (cf. Fig. 2.8), the diffraction amplitude for a semi-infinite crystal is given by

$$A_{substrate}(\boldsymbol{q}) = A_0\, C\, F(\boldsymbol{q})\, N_a N_b \frac{e^{-\sigma^2 (1-\cos \boldsymbol{q}\cdot\boldsymbol{c})}}{1 - e^{-(i\,\boldsymbol{q}\cdot\boldsymbol{c}+\epsilon)}} \tag{2.40}$$

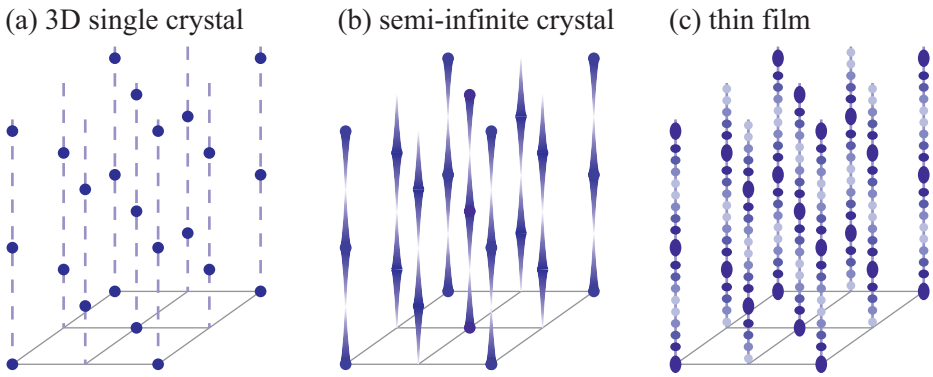

Fig. 2.9: Schematical display of intensity distributions in the reciprocal space for diffraction at different crystalline structures. (a) Ideal three-dimensional single crystals infinitely spanned in all spatial directions produce sharp diffraction spots knwon as Bragg peaks. The dashed lines are direction indications only. (b) Diffraction at semi-infinite crystals (exhibiting a surface) results in a vertically smeared out intensity distribution (known as crystal truncation rods) with maxima at the nominal Bragg peak positions and minima in between these positions. (c) Thin films cause a diffracted intensity pattern with diffraction spots and oscillations (fringes) in vertical direction. Adapted from Ref. [50].

with σ as the standard deviation, corresponding to the root mean square (RMS) roughness of the surface.
Evaluating Eq. (2.40) shows that if the lateral Laue conditions are fulfilled, intensity is obtained (with absolute variations) everywhere in the direction perpendicular to the surface. In contrast to distinct Bragg peaks [cf. Fig. 2.9(a)] obtained for ideal infinite crystals and without considering absorption effects, the concept of semi-infinite (real) crystals results in smeared out reflexes in the direction perpendicular to the surface, forming so-called crystal truncation rods (CTRs), as shown in Fig. 2.9(b). These CTRs exhibit maximum intensity at the nominal Bragg peak positions, whereas the intensity contribution around a Bragg peak can be described by a Lorentzian function with a FWHM, which depends inversely on the penetration depth of the x-rays. Further, the CTRs exhibit minimum intensity in the middle between two nominal Bragg peak positions, also known as anti-Bragg positions.

Diffraction at a crystalline thin film

A similar formalism as for the semi-infinite crystal presented above can be used to describe the diffracted intensity from a crystalline thin film. However, for thin films consisting of only a few crystalline layers (which results in a small thickness value compared to the penetration depth of x-rays), absorption processes can be neglected. In addition, the roughnesses of two surfaces have

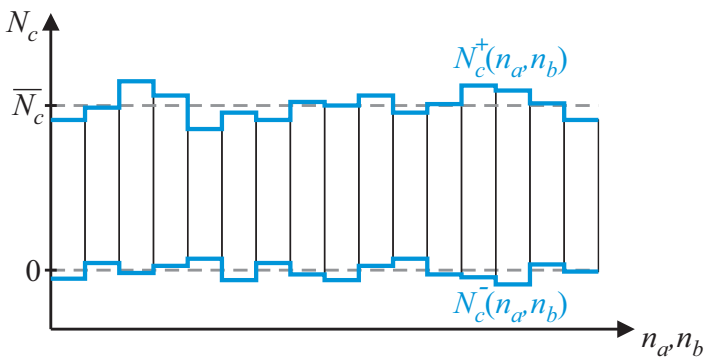

Fig. 2.10: Schematical drawing of height distributions for the two surfaces of a crystalline thin film. The height distribution of the bottom surface of the film is given by $N_c^-(n_a, n_b)$, while its mean value is set to zero. The average value of the top surface height distribution $N_c^+(n_a, n_b)$ is given by the average number of unit cells $\overline{N_c}$ in vertical direction.

to be considered, which will be described by the height distributions $N_c^+(n_a, n_b)$ and $N_c^-(n_a, n_b)$ for the top and bottom surface of the film, respectively (cf. Fig. 2.10).
Hence, the amplitude of a wave diffracted at a thin film infinitely spanned in lateral, but limited in vertical direction can be expressed by

$$A_{film}(\boldsymbol{q}) = A_0\, C\, F(\boldsymbol{q}) \sum_{n_a=0}^{N_a-1} 1 \sum_{n_b=0}^{N_b-1} 1 \sum_{n_c=N_c^-(n_a,n_b)}^{N_c^+(n_a,n_b)} e^{i\, n_c\, \boldsymbol{q}\cdot\boldsymbol{c}} \tag{2.41}$$

$$= A_0\, C\, F(\boldsymbol{q}) \sum_{n_a=0}^{N_a-1} \sum_{n_b=0}^{N_b-1} \frac{e^{i\,\boldsymbol{q}\cdot\boldsymbol{c}\, N_c^-(n_a,n_b)} - e^{i\,\boldsymbol{q}\cdot\boldsymbol{c}\, N_c^+(n_a,n_b)+1}}{1 - e^{i\,\boldsymbol{q}\cdot\boldsymbol{c}}} \,. \tag{2.42}$$

The mean value of the bottom height distribution is (w.l.o.g.) set to zero and the average of the top height distribution is described as $\overline{N_c}$, which equals the intermediate number of unit cells in the vertical direction of the film. With this, the amplitude results [equivalent to the averging in Eq. (2.39)] in

$$A_{film}(\boldsymbol{q}) = A_0\, C\, F(\boldsymbol{q})\, N_a N_b \frac{\left\langle e^{i\boldsymbol{q}\cdot\boldsymbol{c}\, u_c^-} \right\rangle - e^{i\,\boldsymbol{q}\cdot\boldsymbol{c}\,\overline{N_c}} \left\langle e^{i\boldsymbol{q}\cdot\boldsymbol{c}\, u_c^+} \right\rangle}{1 - e^{i\,\boldsymbol{q}\cdot\boldsymbol{c}}} \,, \tag{2.43}$$

where u_c^+ and u_c^- are the deviations from $\overline{N_c}$ at the top and the bottom of the film, respectively. Assuming a Gaussian shape of these deviations, the amplitude can be written as

$$A_{film}(\boldsymbol{q}) = A_0\, C\, F(\boldsymbol{q})\, N_a N_b \frac{e^{-\sigma_-^2 (1-\cos \boldsymbol{q}\cdot\boldsymbol{c})} - e^{i\,\boldsymbol{q}\cdot\boldsymbol{c}\overline{N_c}}\, e^{-\sigma_+^2 (1-\cos \boldsymbol{q}\cdot\boldsymbol{c})}}{1 - e^{i\,\boldsymbol{q}\cdot\boldsymbol{c}}} \,. \tag{2.44}$$

Note that for vanishing top (σ_+) and bottom RMS roughnesses (σ_-) this expression reduces to the form of the N-slit function [cf. Eq. (2.33)]. Hence, the diffracted intensity from thin films can be described as diffraction peaks (main maxima) and oscillations (side maxima or fringes) between these peaks, resulting in an intensity modulation schematically depicted in Fig. 2.9(c).

Diffraction at a thin film system

A thin film system typically consists of one or more thin films on top of a substrate. For complete pseudomorphic growth of these films, the lateral lattice constants and, thus, the lateral positions of the CTRs coincide. In this case, the amplitude of the diffracted wave along the CTRs is given by the sum of the amplitudes from substrate and films via

$$A_{\text{system}}(\boldsymbol{q}) = A_{\text{substrate}}(\boldsymbol{q}) + \sum_i \Theta_i\, e^{i\,\boldsymbol{q}\cdot\boldsymbol{p}_i}\, A_{\text{film},i}(\boldsymbol{q}) \,, \tag{2.45}$$

where Θ_i is the occupation factor, which takes into account impurities and vacancies in the i-th film ($\Theta = 1$ for a perfectly structured film without inhomogeneities). Furthermore, the phase difference between the films is considered by the additional exponential term, including $\boldsymbol{q}\cdot\boldsymbol{p}_i$ in the exponent.

Here, $\boldsymbol{p}_i$ is defined as

$$\boldsymbol{p}_i = \sum_{j=0}^{i-1} \boldsymbol{g}_j + \overline{N_{cj}} \boldsymbol{c}_j \tag{2.46}$$

with the interface vector $\boldsymbol{g}_j$ between adjacent films j and $j+1$, which considers the distance and lateral shift between the films. In addition, $\overline{N_{cj}} \boldsymbol{c}_j$ gives the phase shift due to the film thickness of the j-th film.

2.3 X-ray reflectivity

X-ray reflectivity (XRR) is an interface sensitive technique to study the layer structure of thin films, as it is based on the interference of electromagnetic waves reflected at different interfaces. In XRR measurements, the sample is irradiated by x-rays at small angles α_i between sample surface and x-ray beam, typically below 5°. The reflected intensity at the reflection angle $\alpha_\mathrm{f} = \alpha_\mathrm{i}$ is then measured in dependence of the incident angle α_i. From the recorded intensity contribution, information on film thicknesses, the stacking order of multilayer structures, refractive indices of the different films and interface and surface roughnesses can be obtained. First, the principle of x-ray reflection at a single interface is given, followed by the description of reflection at a multilayer system and the reflectivity of rough interfaces. More detailed descriptions on the theory of XRR can be found in, e.g., Refs. [48, 51].

2.3.1 Reflection at a single interface

If an electromagnetic wave with wave vector $\boldsymbol{k_\mathrm{i}}$ encounters an interface between two optically different media with refraction indices n_1 and n_2, it is partly reflected with wave vector $\boldsymbol{k_\mathrm{f}}$ and partly refracted and transmitted into the adjacent medium (for incident angles above the critical angle, see below) with a wave vector $\boldsymbol{k_\mathrm{t}}$. This process is schematically depicted in Fig. 2.11(a), whereas the corresponding theoretically calculated reflectivity curve for reflection at a single interface is shown in Fig. 2.11(b).
Regarding an interface between vacuum and a solid state medium, energy conservation results in the wavenumber $|\boldsymbol{k_\mathrm{i}}| = |\boldsymbol{k_\mathrm{f}}| = k$ in vacuum, whereas $|\boldsymbol{k_\mathrm{t}}| = nk$ applies for the wavenumber in the solid. Thus, for the case of reflection at $\alpha_\mathrm{f} = \alpha_\mathrm{i}$ the magnitude of the scattering vector $\boldsymbol{q} = \boldsymbol{k_\mathrm{f}} - \boldsymbol{k_\mathrm{i}}$ is given by

$$q = 2k \sin \alpha_\mathrm{i} = \frac{4\pi}{\lambda} \sin \alpha_\mathrm{i} \ . \tag{2.47}$$

The crucial parameter, which determines the reflectivity and transmittivity of a material, is the material and wavelength dependent refractive index n. For x-rays with energies far away from the material's absorption edges, the refractive index of a homogeneous medium can be expressed by

$$n = 1 - \delta + i\beta \quad \text{with dispersion} \quad \delta = \frac{\lambda^2}{2\pi} r_e \rho \quad \text{and absorption} \quad \beta = \frac{\lambda}{4\pi} \mu \ , \tag{2.48}$$

where λ denotes the x-ray wavelength, r_e the classical electron radius, ρ the electron density and μ the absorption coefficient [51]. In the case of x-rays, the dispersion δ is typically in the range of 10^{-6} to 10^{-5}, whereas the absorption β is usually even one or two orders of magnitude lower, leading to real parts of refractive indices slightly below one. Only in vacuum both contributions

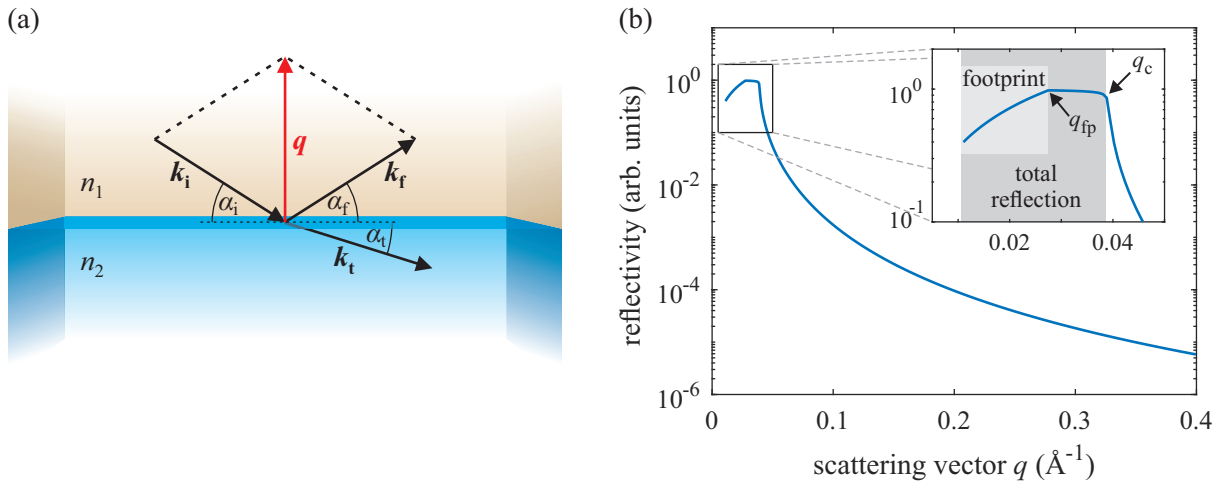

Fig. 2.11: (a) Principle of XRR at an interface between two optically different media with refractive indices n_1 and n_2, respectively. For incident angles α_i bigger than the critical angle α_c, the x-ray beam with incident wave vector $\boldsymbol{k}_\mathbf{i}$ in the first medium is partly transmitted into the second medium ($\boldsymbol{k}_\mathbf{t}$) and partly reflected at the interface ($\boldsymbol{k}_\mathbf{f}$). The transmitted wave is refracted upon entering the second medium exhibiting an angle α_t between wave vector $\boldsymbol{k}_\mathbf{t}$ and interface. (b) Corresponding reflectivity curve for reflection at a single interface. It is obtained by measuring the intensity contribution at the reflection angle $\alpha_\mathrm{f} = \alpha_\mathrm{i}$ as a function of the scattering vector $\boldsymbol{q} = \boldsymbol{k}_\mathbf{f} - \boldsymbol{k}_\mathbf{i}$, which is varied during the measurement by changing α_i. The XRR curve is scaled to the incident intensity. Up to the critical angle α_c and the corresponding scattering vector q_c total reflection is obtained. Increasing intensity for very small angles below the footprint angle α_fp and the corresponding q_fp (shown in the inset) originates from only partial illumination of the sample. The reflectivity significantly drops above the critical scattering vector q_c due to partial transmission into the second medium.

δ and β evidently vanish, resulting in $n_{vac} = 1$. As a consequence, if an electromagnetic wave encounters an interface between vacuum and a solid state medium, it can be totally reflected, if the incident angle is small enough. This total reflection occurs below a critical angle α_c, which can be calculated using Snell's law[2] and is approximately given by

$$\alpha_\mathrm{c} \approx \sqrt{2\delta} \tag{2.49}$$

for the use of x-rays. Above the critical angle α_c or the corresponding scattering vector q_c, x-rays can penetrate into the material with wave vector $\boldsymbol{k}_\mathbf{t}$, resulting in a sudden decrease of the reflected intensity [cf. Fig. 2.11(b)].

However, for angles even smaller than α_c, the sample surface is irradiated by only parts of the x-ray beam, resulting in an initial linear increase of the reflected intensity with increasing q [shown in the inset of Fig. 2.11(b)]. This effect is due to the spatially extended beam and finite sample size in the reflection plane and is called footprint. If the incident angle is increased in this glancing region, more and more parts of the x-ray beam hit the sample surface, resulting in an increase of the reflected intensity. If the footprint angle α_fp is reached, the sample surface of length l in beam direction is completely illuminated by the x-ray beam. Hence, all beam intensity is reflected (for $\alpha_\mathrm{fp} < \alpha_\mathrm{c}$). Assuming an approximately rectangular beam profile with vertical expansion b, the footprint angle is given by $\alpha_\mathrm{fp} = \arcsin(b/l)$.

The reflected intensity can be normalized to the incident x-ray intensity, as depicted in Fig. 2.11(b), to obtain the so-called reflectivity $R = I_\mathrm{r}/I_\mathrm{i}$ as the ratio of reflected and incident intensity. It is related to the complex reflection coefficient r via $R = |r|^2$, whereas the transmission can be

[2]Snell's law describes the relation between incident angle α_i and angle of refraction α_t when an electromagnetic wave encounters an interface between two media with refractive indices n_1 and n_2: $n_1 \cos\alpha_\mathrm{i} = n_2 \cos\alpha_\mathrm{t}$.

described analogously by $T = I_\mathrm{t}/I_\mathrm{i} = |t|^2$. Note that as for x-rays $n \approx 1$, the reflection and transmission coefficients can be described independent of the polarization (s- or p-polarization) [51], giving the Fresnel formulas

$$r = \frac{k_{\mathrm{i},z} - k_{\mathrm{t},z}}{k_{\mathrm{i},z} + k_{\mathrm{t},z}} \quad \text{and} \quad t = \frac{2k_{\mathrm{t},z}}{k_{\mathrm{i},z} + k_{\mathrm{t},z}} \tag{2.50}$$

with $k_{\mathrm{i},z} = k \sin \alpha_\mathrm{i}$ and $k_{\mathrm{t},z} = nk \sin \alpha_\mathrm{t} = k\sqrt{n^2 - \cos^2 \alpha_\mathrm{i}}$ as the components normal to the interface (denoted as the z-direction) of the wave vectors $\boldsymbol{k_\mathrm{i}}$ and $\boldsymbol{k_\mathrm{t}}$, respectively.

2.3.2 Reflection at multiple interfaces

The reflection of x-rays at a single interface as described above is only applicable for the reflectivity of the single substrates used in this work. However, since thin films are deposited on these substrates, reflection at multiple interfaces has to be taken into account. The most simple case of multiple interfaces consists of one single thin film on a substrate and, thus, exhibits two interfaces. The principle of an XRR experiment at such a system is exemplarily depicted in Fig. 2.12.

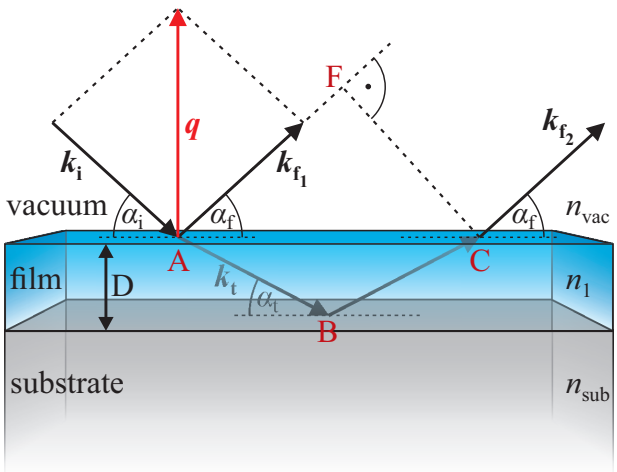

Fig. 2.12: Principle of XRR at a thin film of thickness D and refractive index n_1 on a substrate with a different refractive index n_sub. For incident angles α_i bigger than the critical angle α_c, the x-ray beam in vacuum ($n_\mathrm{vac} = 1$) with initial wave vector $\boldsymbol{k_\mathrm{i}}$ is partly transmitted into the thin film ($\boldsymbol{k_\mathrm{t}}$) and partly reflected at the vacuum/film interface ($\boldsymbol{k_{\mathrm{f}_1}}$). The transmitted wave is in turn partly reflected at the film/substrate interface under an angle α_t and leaves the sample surface with wave vector $\boldsymbol{k_{\mathrm{f}_2}}$. The interference of $\boldsymbol{k_{\mathrm{f}_1}}$ and $\boldsymbol{k_{\mathrm{f}_2}}$ determines the reflected intensity contribution.

If the x-ray beam with wave vector $\boldsymbol{k_\mathrm{i}}$ in vacuum encounters the vacuum/film interface, it is partly reflected (wave vector $\boldsymbol{k_{\mathrm{f}_1}}$) and partly refracted and transmitted into the material for $\alpha_\mathrm{i} > \alpha_\mathrm{c}$, as already described above. The transmitted wave with wave vector $\boldsymbol{k_\mathrm{t}}$ is in turn partly reflected and transmitted at the film/substrate interface, whereas this second reflected wave can escape the film surface with a wave vector $\boldsymbol{k_{\mathrm{f}_2}}$, which is parallel to $\boldsymbol{k_{\mathrm{f}_1}}$. By changing the incident angle α_i and, thus, the magnitude of the scattering vector q [cf. Eq. (2.47)], the path difference between the waves reflected at the vacuum/film and the film/substrate interface is varied and interference occurs between both waves (denoted with wave vectors $\boldsymbol{k_{\mathrm{f}_1}}$ and $\boldsymbol{k_{\mathrm{f}_2}}$ in Fig. 2.12).
The total reflected intensity of a multilayer system can be calculated by the recursive approach introduced by Parratt [52]. Within this algorithm the total reflectivity is expressed by a recursive formulation considering the reflectivity of the interface between layer j and layer $j-1$ in a system consisting of N layers in total. The corresponding reflected amplitude is denoted as $R_{j-1,j}$ and can be expressed by

$$R_{j-1,j} = \frac{r_{j-1,j} + R_{j,j+1} \exp\left(i\,\mathrm{D}_j q_j\right)}{1 + r_{j-1,j}\, R_{j,j+1} \exp\left(i\,\mathrm{D}_j q_j\right)} \quad \text{for } j \in \{1, ..., N\} \tag{2.51}$$

with

$$r_{j-1,j} = \frac{q_{j-1} - q_j}{q_{j-1} + q_j} \tag{2.52}$$

as the Fresnel coefficient at the interface between layer j and layer $j-1$. Furthermore, D_j denotes the thickness of the j-th layer and $q_j = n_j 2k \sin(\alpha_{\mathrm{t},j}) = 2k\sqrt{n_j^2 - n_{j-1}^2 \cos^2(\alpha_{\mathrm{t},j-1})}$ the scattering vector in layer j. The starting point of the recursion is $R_{N,N+1} = r_{N,N+1}$ as the reflectivity of the interface between substrate (denoted as 'layer $N+1$') and the adjacent layer N. The total reflected intensity is obtained by successively inserting $R_{j,j+1}$ in Eq. (2.51) for N iterations. The last iteration comprises the reflectivity of the interface between the uppermost layer and the medium vacuum/air, which is denoted as 'layer 0', and gives the total reflectivity $R = I_\mathrm{r}/I_\mathrm{i} = |R_{0,1}|$.

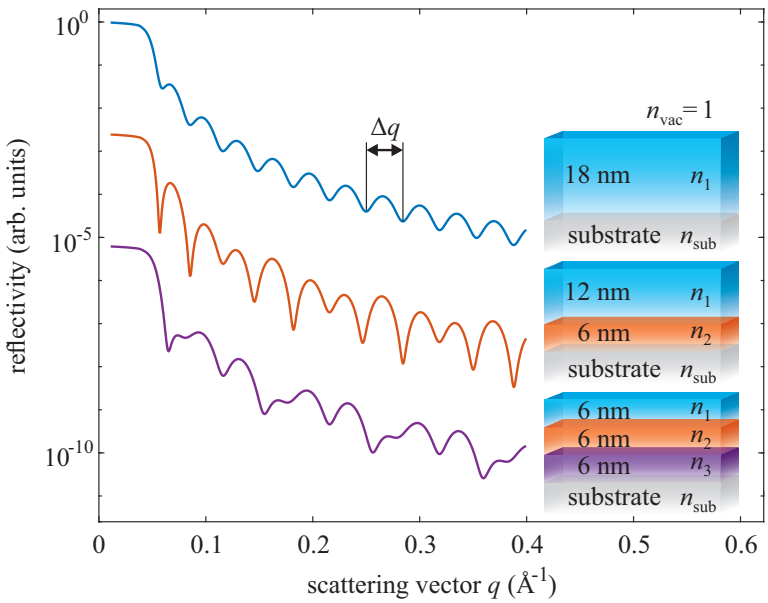

Fig. 2.13: Theoretically calculated XRR curves for the models of one (top), two (middle), and three (bottom) thin films with different refractive indices n_1, n_2, and n_3 on the same substrate (n_{sub}). The topmost layer is adjacent to vacuum (n_{vac}=1). The total thickness of the multilayer stack is held constant at 18 nm for better comparison. Clear Kiessig-fringes with distance $\Delta q \approx 2\pi/\mathrm{D}$ are obtained for the single film of thickness D due to interference of waves reflected at both interfaces. For the case of two or more stacked films (and interfaces), the reflectivity is more complex. The footprint is not considered here and the XRR curves are vertically shifted for clarity.

In Fig. 2.13, calculated reflectivity curves are depicted exemplarily for one, two, and three optically different thin films, each exhibiting a different refractive index n_1, n_2, and n_3, respectively. All curves are modeled as deposited on the same (infinitely thick) substrate with refractive index n_{sub} and the topmost interface is between the top layer and vacuum ($n_{\mathrm{vac}} = 1$). For better comparison, the overall thickness of the multilayer stack was kept at a constant thickness of 18 nm. For the rather simple case of only one film on the substrate, which consequently exhibits two interfaces, clear oscillations - so-called *Kiessig-fringes* - are obtained, resulting from constructive and destructive interference of the waves reflected at both interfaces, as described above. Here, the fringe distance Δq can serve as an estimation for the film thickness D via

$$\mathrm{D} \approx \frac{2\pi}{\Delta q}\ , \tag{2.53}$$

considering that $n \approx 1$ for the use of x-rays. For the case of two or more stacked films and, thus, at least three interfaces, which contribute to the reflected intensity, the reflectivity is more complex. Then, the oscillations stemming from reflection at different interfaces superimpose, causing a beating effect of the total reflectivity. In order to gain insight into these layer structures, an in-house developed fitting tool [53], which was applied for the analysis of reflectivity curves, is used in this work. By fitting the calculated reflectivity to the experimental data parameters like film

thicknesses, film stacking order, refractive indices (dispersion and absorption) of each film, as well as interface roughnesses are determined. As the latter has substantial impact on the reflectivity, it is briefly discussed in the following.

2.3.3 Reflection at rough interfaces

Up to now, reflectivity of only completely sharp interfaces has been regarded. However, real interfaces usually consist of structural defects, resulting in a finite interface roughness. Thus, the transition from one medium to the adjacent medium can no longer be described as a sudden jump from one refractive index to another, as it has been assumed before. More accurately, the refractive index is described as a continuous variation $n_j(x, y, z)$ in all spatial directions. Since for reflectivity experiments the scattering vector q only consists of a z component, one-dimensional refractive index profiles

$$n_j(z) = \int\int n_j(x, y, z)\, dx\, dy \tag{2.54}$$

as a lateral average over x and y are considered. A rough interface can now be regarded as an ensemble of sharp interfaces with different vertical coordinates $z_j + z$, which are weighted by a probability density $P_j(z)$ [cf. Fig. 2.14(a)]. Here, z_j denotes the mean vertical coordinate of the interface and z the fluctuations around this value. A continuous refractive-index profile of type

$$n_j(z) = \frac{n_j + n_{j+1}}{2} - \frac{n_j - n_{j+1}}{2} \operatorname{erf}\left(\frac{z - z_j}{\sqrt{2}\,\sigma_j}\right) \tag{2.55}$$

between layers j and $j + 1$ can now be assumed, where σ_j denotes the standard deviation of the height distribution[3]. Here, the error function is defined by

$$\operatorname{erf}(z) = \frac{2}{\sqrt{\pi}} \int_0^z \exp(-t^2)\, dt\ , \tag{2.56}$$

exemplarily depicted in Fig. 2.14(b) for a transition from $\delta = 1.15 \cdot 10^{-5}$ to $\delta = 1.57 \cdot 10^{-5}$ in the cases of a sharp and a rough interface with standard deviation $\sigma_j = 5\,\text{Å}$[4]. This yields a Gaussian probability density

$$P_j(z) = \frac{1}{\sqrt{2\,\pi}\,\sigma_j} \exp\left(-\frac{z^2}{2\,\sigma_j^2}\right) \tag{2.57}$$

of the interface height fluctuations z. These considerations result in a modified Fresnel coefficient

$$\tilde{r}_{j-1,j} = r_{j-1,j} \exp\left(-2\,k_{z,j-1}\,k_{z,j}\,\sigma_j^2\right) \tag{2.58}$$

for reflection at rough interfaces, which has to be considered in the recursive formula of Eq. (2.51). The exponential term is called the Névot-Croce factor [54]. The standard deviation σ_j is also called the root mean square (RMS) roughness of interface j and is an important fitting parameter in the analysis of XRR data. Depending on the location of the corresponding interface (either the

[3] Note that for the case $\sigma_j \to 0$ one has $\operatorname{erf}\left[(z - z_j)/(\sqrt{2}\,\sigma_j)\right] \to \pm 1$ for $z > z_j$ and $z < z_j$, respectively, thus obtaining the case of a sharp interface.

[4] Dispersion values correspond to the interface between MgO and $NiFe_2O_4$ for the use of Cu Kα radiation with an x-ray energy of 8048.0 eV.

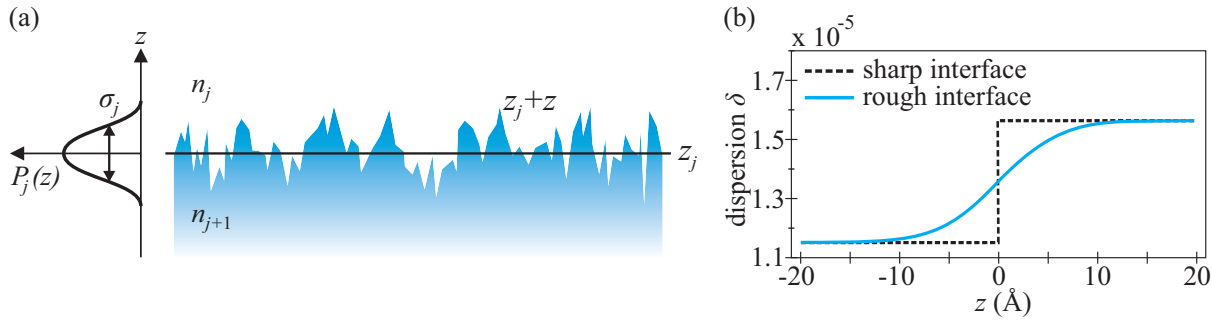

Fig. 2.14: (a) Sketch of a rough interface with fluctuations z around the mean height z_j described as an ensemble of sharp interfaces at coordinates $z_j + z$ with probability density $P_j(z)$ and standard deviation σ_j. (b) Density profile of a sharp and a rough interface represented by an error function for a transition from $\delta = 1.15 \cdot 10^{-5}$ to $\delta = 1.57 \cdot 10^{-5}$ with an RMS roughness of 5 Å. Adapted from Refs. [51, 53].

surface or buried interfaces), increasing RMS roughnesses mainly result in a stronger decay of the reflectivity curve or in a damping of the Kiessig-fringes with larger scattering vectors q. It should be noted that the presented Névot-Croce roughness model is only valid for interface roughnesses, which are small compared to the film thickness. If this is not the case, other approaches as, e.g., layer segmentation have to be applied.

2.4 Low-energy electron diffraction

Low-energy electron diffraction (LEED) is an experimental technique to determine the structure and morphology of surfaces. Here, low-energy electrons (10 – 500 eV) are backscattered from the topmost surface atoms of the investigated sample. As the de-Broglie wavelength of such electrons is in the range of atomic distances in crystals, the backscattered electron waves interfere with each other, forming a diffraction pattern dependent on the crystal surface structure and morphology. In contrast to x-rays, electrons exhibit a much larger cross-section for the interaction with matter. In particular, electrons of such low energy exhibit a rather small inelastic mean free path in solids, as illustrated in the so-called universal curve in Fig. 2.15, leading to high surface sensitivity (typically ∼10 Å) of this technique.

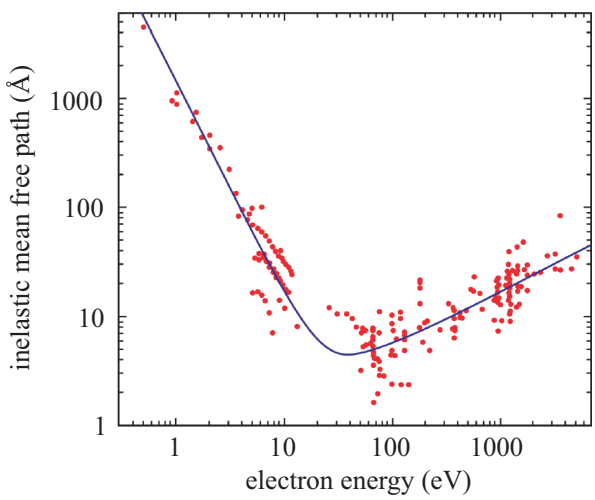

Fig. 2.15: Experimental data of inelastic mean free paths of electrons in solids in dependence of their kinetic energy. Note the double-logarithmic scale. The solid line represents the so-called universal curve for inelastic mean free paths of electrons. For kinetic energies in the LEED regime below ∼500 eV the curve exhibits a minimum with IMFP values of ∼10 Å. Taken and adapted from [55].

Thus, the surface structure that contributes to the elastically backscattered electrons has two-dimensional character and consequently exhibits a loss of periodicity in vertical direction. So, in

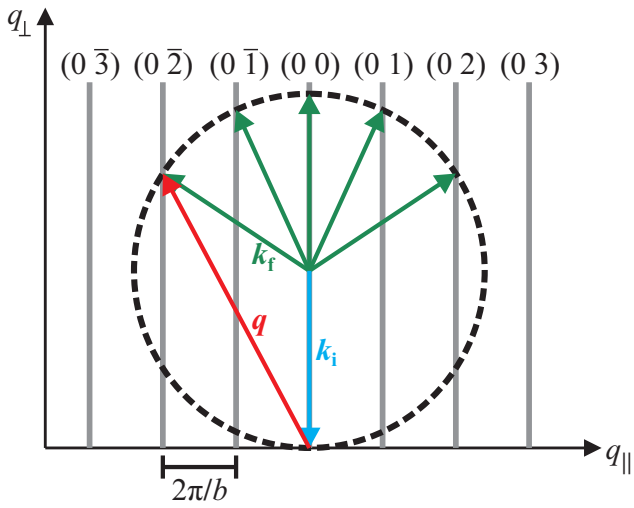

Fig. 2.16: Construction of the Ewald sphere (dashed circle) for diffraction at a two-dimensional lattice with normal incidence of the incoming wave vector $\boldsymbol{k}_\mathbf{i}$, as usually used for LEED experiments. The Ewald sphere is defined by all possible final wave vectors $\boldsymbol{k}_\mathbf{f}$. Here, only the relevant backscattered wave vectors $\boldsymbol{k}_\mathbf{f}$ are depicted. Diffraction spots occur, where the Ewald sphere and, thus, the scattering vector $\boldsymbol{q}$ intercepts with a reciprocal lattice rod (grey lines) and the lateral component $q_\parallel$ is an integer multiple of the lattice rod distance $2\pi/b$. For clarity, only the plane with $h=0$ is shown.

real space the vertical lattice distance can be regarded as infinitely large, resulting in reciprocal lattice points located infinitely close together in vertical direction. As a consequence, in contrast to the formation of Bragg peaks or CTRs for diffraction at three-dimensional (semi-infinite) bulk structures (cf. Fig. 2.9), so-called Bragg rods (or lattice rods) are obtained for diffraction at a two-dimensional lattice, exhibiting only lateral periodicity of the reciprocal lattice. Compared to the Laue equations for diffraction at three-dimensional structures [cf. Eq. (2.16], the Laue equation for diffraction at a two-dimensional lattice can be written as

$$\boldsymbol{q}_\parallel = (\boldsymbol{k}_\mathbf{f} - \boldsymbol{k}_\mathbf{i})_\parallel = \boldsymbol{G}_\parallel = h\boldsymbol{a}^* + k\boldsymbol{b}^* \ , \tag{2.59}$$

as the Laue condition for diffraction direction perpendicular to the surface lapses. Hence, the momentum perpendicular to the surface $\boldsymbol{q}_\perp$ (here, along $\boldsymbol{c}^*$ direction) can attain any value without affecting the Laue condition. However, to fulfill the Laue condition, the part of the momentum parallel to the surface $\boldsymbol{q}_\parallel$ has to coincide with a lateral reciprocal lattice vector $\boldsymbol{G}_\parallel$. The respective Bragg rods are consequently denoted by (hk).

Fig. 2.16 shows the Ewald construction for the described LEED experiment with an incoming electron beam with wave vector $\boldsymbol{k}_\mathbf{i}$ normal to the surface [along (00) direction]. For clarity, only the plane with $h=0$ is shown. The Ewald sphere (indicated by a dashed circle) is constructed by considering all scattered electron waves $\boldsymbol{k}_\mathbf{f}$ with $|\boldsymbol{k}_\mathbf{f}| = |\boldsymbol{k}_\mathbf{i}|$ for solely elastic scattering. Diffraction spots occur, where the Ewald sphere and, thus, the scattering vector $\boldsymbol{q}$ intercepts with the reciprocal lattice rods.

As the incident angle of the electron beam is held constant (usually vertical to the sample surface) during LEED experiments, the scattering condition can only be modified by changing the kinetic energy of the electrons and with this varying the wave vector magnitude $|\boldsymbol{k}_\mathbf{i}|$. For instance, increasing the electron energy also increases the radius $|\boldsymbol{k}_\mathbf{f}| = |\boldsymbol{k}_\mathbf{i}|$ of the Ewald sphere. Consequently, more reciprocal lattice rods intersect with the Ewald sphere and a larger segment of the reciprocal space can be probed, which in turn brings the diffraction spots closer together on a detector in real space.

The obtained LEED pattern directly reflects the symmetry and size of the reciprocal surface unit cell. From this, also the symmetry of the surface lattice in real space is determined. However, a crystal surface lattice can exhibit a modified periodic structure and symmetry compared to the bulk. This superstructure may occur upon reconstruction of the surface due to, e.g., dangling bonds or adsorbed atoms on the surface. Hence, additional lattice rods may appear in LEED compared to the lateral periodicity of the reciprocal bulk lattice. Further, as LEED contains statistic

information on large parts of the sample surface, locally disordered structures as, e.g., point defects without any periodical order, result in a diffuse background intensity in the LEED pattern but do not have an impact on the diffraction spots themselves. In contrast, ordered defective structures as, e.g., mosaics, dislocation networks, or domain boundaries modify the diffracted intensity distribution [56]. Thus, by analyzing spot widths and intensities quantitative information of line defects can be obtained. Further, the intensity of diffraction spots may differ for varying electron energies (thus, along the diffraction rods) due to terraces/atomic steps at the surface or small bulk contributions to the diffracted intensity.

2.5 X-ray photoelectron spectroscopy

X-ray photoelectron spectroscopy (XPS)[5] is a powerful core-level spectroscopic technique to determine the chemical composition and electronic structure of the investigated material. Other core-level spectroscopic techniques used in this work are x-ray absorption spectroscopy (XAS) and x-ray magnetic circular dichroism (XMCD), described in more detail in Secs. 2.6 and 2.7. However, all three techniques are based on the photoexcitation process, which describes the excitation of an electron in the investigated material by an incoming photon. Thus, a closer look on this process with respect to its principle description for XPS, XAS, and XMCD is given first, followed by a more detailed explanation of XPS.

2.5.1 The photoexcitation process

All three spectroscopic techniques, XPS, XAS, and XMCD, are based on the excitation of bound core-electrons by photons[6]. In the case of XPS, a core-electron is excited into a high-energy continuum state, if the energy of the absorbed photon is large enough to overcome the material's ionization threshold. This process is known as the (external) photoelectric effect and the emitted photoelectron can be detected in dependence of the kinetic energy. Thus, by using XPS the occupied core-levels of a solid are probed. In contrast, in XAS and XMCD the amount of absorbed light is measured (with opposite circular polarizations for XMCD), while tuning the incident x-ray energy. Here, the core-electron can also be excited into an empty state in the valence or conduction band below the ionization threshold, therefore probing the unoccupied states of the band structure.
Besides these differences, all techniques are classified as first-order optical processes, where only one photon and one electron is included in an excitation process. Moreover, to excite electrons from deeply-bound core-levels into either continuum (XPS) or unoccupied band states (XAS, XMCD) photon energies of the same order or larger than the binding energies in a solid are necessary, which is why x-rays are used for these techniques. In contrast to XPS, XAS, and XMCD, e.g., x-ray fluorescence spectroscopy (XRF) or Auger electron spectroscopy (AES) are second-order processes, where core-electrons are excited by incident x-ray photons and the excited state of the system decays either radiatively by emitting x-rays (XRF) or by emitting so-called Auger electrons (AES).
To understand the details of the used spectroscopic techniques, the underlying photoexcitation process has to be considered first. Before excitation, the electrons of the probed atom, molecule, or solid are in their most favorable energetic constitution, giving the initial ground state described by the wave function Ψ_i. However, after excitation, a core-hole is created by exciting an electron into an unoccupied state above the Fermi level, resulting in an excited final state of the corresponding

[5] In some literature XPS is called x-ray photoemission spectroscopy.
[6] In fact, also less bound electrons, i.e., from the valence band are excited, but those are probed more efficiently by, e.g., ultraviolet photoelectron spectroscopy (UPS) and are not explicitly investigated in this work.

system represented by the wave function Ψ_f. To describe this process theoretically, the incoming electromagnetic wave is considered as a perturbation to the many electron system [57, 58], which results in *Fermi's golden rule* describing the transition probability

$$w \sim |\langle \Psi_\mathrm{f} \,|\, \mathcal{T} \,|\, \Psi_\mathrm{i} \rangle|^2 \; \delta(E_\mathrm{f} - E_\mathrm{i} - h\nu) \tag{2.60}$$

from the initial ground state Ψ_i to the final state Ψ_f with $\mathcal{T}$ as the transition operator between the two states. Here, E_f and E_i denote the energies of the final and initial state, respectively, and $h\nu$ is the incident photon energy. Thus, the δ-distribution ensures the energy conservation law and transition only occurs if the energy of the final state equals the energy of the initial state plus the x-ray photon energy. The transition rate is then given by the squared matrix element, which is determined by the transition operator $\mathcal{T}$ and the possible initial and final states. Theoretical approaches for the description of $\mathcal{T}$, in particular for the respective excitation processes in XPS and XAS/XMCD, can be found in literature [57].

2.5.2 Principle of XPS

XPS is a powerful and widely used spectroscopic technique to investigate the electronic structure and chemical composition of a material. It is based on the photoelectric effect, which was discovered first in 1887 by H. Hertz [59], who found out that an electrostatically charged metal plate discharges faster if it is irradiated by UV light. In the following year, W. Hallwachs discovered that the discharging can be ascribed to the emission of electrons if the material is exposed to radiation above a threshold frequency [60]. The theoretical explanation for this behavior was found by A. Einstein in 1905, when he published his Nobel Prize awarded hypothesis about the quantification of electromagnetic radiation [61].
The spectroscopic process of photoelectron emission is schematically depicted in Fig. 2.17. If the incident photon energy $h\nu$ is large enough to eject an electron originating from a core-level with binding energy E_b (relative to the Fermi level E_F) the kinetic energy of the emitted photoelectron can be estimated via energy conservation in a one-electron picture by

$$E_\mathrm{kin} = h\nu - E_\mathrm{b} - \Phi \; . \tag{2.61}$$

Here, Φ is the so-called work function of the material, defined as the difference between vacuum and Fermi energy ($\Phi = E_\mathrm{vac} - E_\mathrm{F}$), which has to be overcome by an electron originating from the Fermi level to escape the solid. Most commonly, both the detector and the sample are electrically grounded to the same potential, resulting in equal Fermi levels. Thus, the kinetic energy E'_kin measured in the detector depends on the work function of the spectrometer $\Phi = \Phi_\mathrm{spec}$ and not on the one of the sample (cf. Fig. 2.17). Following Eq. (2.61) and using monochromatic light with a photon energy $h\nu$ and an energy-dependent detection of the photoelectrons, it is possible to determine the binding energy E_b of the photoelectrons in the investigated solid. However, although this picture is intuitive, Eq. (2.61) neglects the many body interaction of the remaining electrons in the system. More accurately, due to energy conservation the binding energy measured by XPS is given as the energy difference between the initial state consisting of N electrons and the final state consisting of the emergent core-hole and, thus, $N-1$ electrons:

$$E_\mathrm{b} = E_\mathrm{f}^{N-1} - E_\mathrm{i}^{N} \; . \tag{2.62}$$

Though, the determination of absolute energy values is not very easy and approximations are made to obtain them. Following Koopmanns' theorem, the binding energy E_b measured after ionization is equal to the negative orbital energy ε_HF, determined by Hartree-Fock calculations, from which

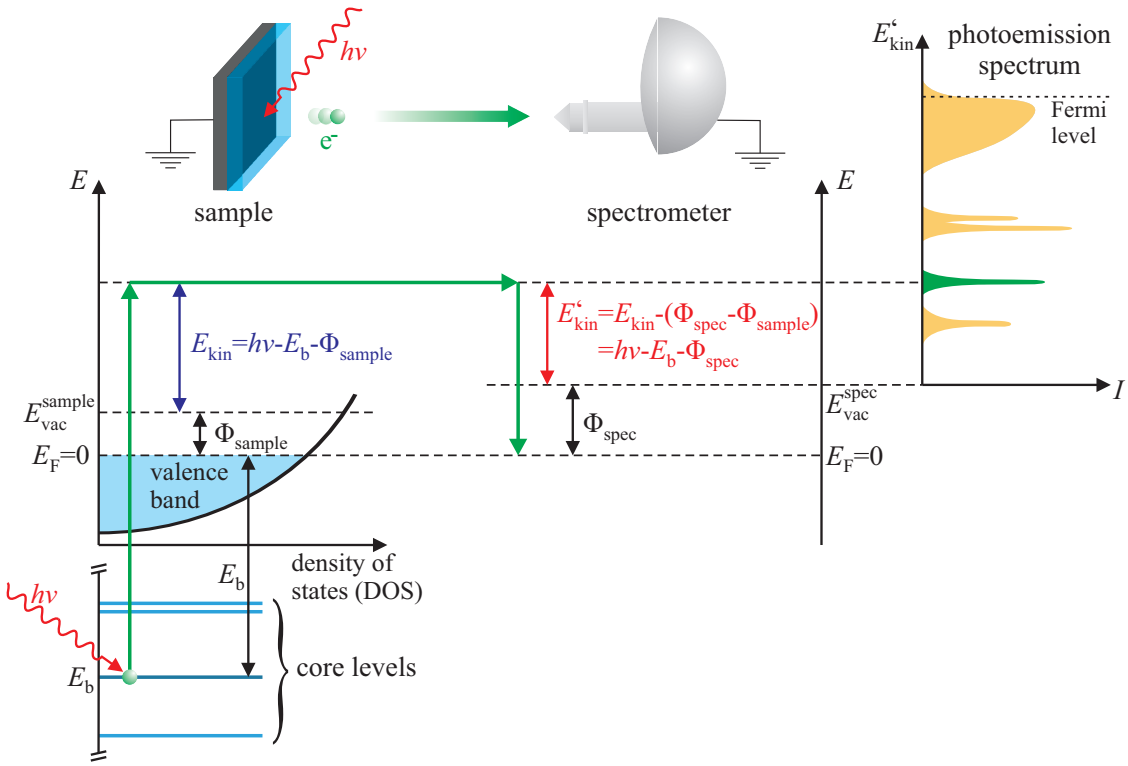

Fig. 2.17: Schematic drawing of a photoelectron emission process in an energy diagram. An x-ray photon with energy $h\nu$ excites a deeply-bound core-electron into continuum to the expense of the binding energy E_b and the work function $\Phi_\mathrm{sample} = E_\mathrm{vac}^\mathrm{sample} - E_\mathrm{F}$. As the spectrometer is set to the same potential as the sample, both Fermi levels E_F equalize and the photoelectron is detected with the kinetic energy $E'_\mathrm{kin} = h\nu - E_\mathrm{b} - \Phi_\mathrm{spec}$. The right part depicts the measured phtoelectron spectrum. Adapted from Refs. [62, 63].

the photoelectron is emitted. However, this approximation is only valid for the one-electron (or frozen-orbital) picture, as the other orbitals are treated as unchanged during the photoelectron emission process and relaxation processes in consequence of the core-hole formation are neglected. In order to relate Koopmanns' approximation to the binding energies effectively measured, one has to consider the relaxation energy contributions due to potentials created by other orbitals of the atom containing the core-hole (intra-atomic relaxation) and by its surrounding atoms (extra-atomic relaxation).

However, photoelectrons which do not suffer from any energy loss in the photoemission process are directly related to the electronic structure of the material. These electrons are only subject to elastic scattering on their way through the sample towards the surface and their kinetic energies correspond to the specific binding energies of the atom's core-levels. This makes XPS an element-specific technique as the atomic binding energies are characteristic for an element. Nevertheless, excited electrons are not only subject to elastic scattering but also undergo energy loss on their path through the solid due to inelastic scattering events. If the remaining kinetic energy of inelastically scattered electrons is high enough to leave the sample these photoelectrons contribute to a continuous background signal in the photoemission spectrum.

The characteristic parameter, which is related to the average path length under which electrons do not undergo inelastic scattering is the ineleastic mean free path (IMFP), which was already introduced in Sec. 2.4. It depends on the material the electron is travelling through and even more significantly on the kinetic energy of the electron (cf. Fig. 2.15). In laboratory-based XPS systems usually soft x-rays ($h\nu \lesssim 3\,\mathrm{keV}$) are used (soft XPS), which makes the technique very surface sensi-

tive, as the IMFP of electrons excited by this energy is in the range of a few nanometers (typically below 10 nm). To achieve a more bulk-like sensitivity x-ray sources with higher photon energies can be used to increase the kinetic energy and, thus, the IMFP of the excited electrons to obtain a larger information depth. This technique is consequently known as hard x-ray photoelectron spectroscopy (HAXPES) and is used as a complementary technique to soft XPS in this work to obtain not only information about chemical composition and electronic structure at the surface, but also in deeper layers of the prepared films.

2.5.3 Spectral features

Apart from the inelastic background mentioned above, different effects can influence the shape and position of photoemission peaks in XPS. A detailed description of the photoemission process and the spectral characteristics can be found in Refs. [57, 58, 62]. Here, the most important effects also contributing to the photoelectron spectra recorded in this work are briefly described in the following.

Chemical shift

The binding energies of photoemission peaks measured by XPS may significantly deviate from the values expected for the corresponding free atom. This deviation is known as the chemical shift and is a consequence of the bonding between the respective element and surrounding atoms in a solid. For instance, in ionic crystals the bonding is formed via valence electrons of the cations that are transferred to neighboring anions, which is in turn quantified by the valence state of the respective atoms. Thus, the missing or extra electrons (compared to the respective uncharged free atom) changes the electrostatic interaction between nucleus and electron shell due to the decreased or increased screening. For instance, in a cation, where one or more electrons are missing, the remaining electrons are bound stronger to the nucleus, which therefore enhances the respective binding energies. Consequently, this chemical shift in the photoemission spectrum can be used as a fingerprint for the valence state of the corresponding ion. An example of a chemical shift is depicted in Fig. 2.18, where the iron oxide FeO clearly exhibits a shift to higher binding energy positions of the Fe $2p$ peaks compared to the pure Fe metal.
The chemical shift can be described theoretically by applying the charge potential model, which correlates the shift with the potentials created by the valence electrons of the same atom and by the electrons of the surrounding atoms. Within this model, the effective binding energy is obtained as

$$E_{\mathrm{b,eff}} = E_{\mathrm{b}}^{0} + K\Delta q_i + \sum_{j\neq i} \frac{q_j}{r_{ij}} \tag{2.63}$$

with E_{b}^{0} as the binding energy in the ground state of the free atom. This reference state is modified by the term $K\Delta q_i$ with K as an empirical parameter, which is correlated to the interaction of valence electrons and core-hole within the atom, and Δq_i as the charge shift compared to the neutral atom. Thus, this term corresponds to the potential change within the atom containing the core-hole. Further, q_j with $j \neq i$ represents the charge of the surrounding atom j in a distance r_{ij} from the atom in question. Hence, this last term of Eq. (2.63), also known as the Madelung term, describes the summed up potential change due to the interaction with the surrounding atoms.

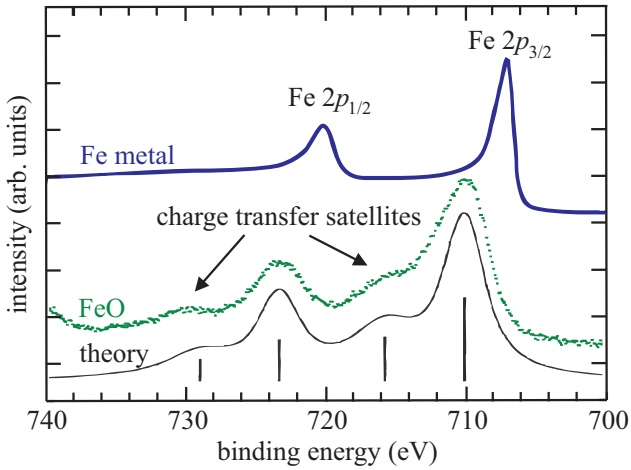

Fig. 2.18: Fe $2p$ core-level spectra for a pure Fe metal and for the iron oxide FeO. The binding energies of the spin-orbit split Fe $2p_{3/2}$ and $2p_{1/2}$ peaks in FeO clearly deviate to higher values compared to the positions in Fe due to the chemical shift. Additionally, FeO shows clear charge-transfer satellites at slightly higher binding energies than the main Fe $2p$ lines. FeO spectrum and theoretical calculation are adapted from Ref. [64].

Spin-orbit coupling

The photoemission of a core-level electron creates a core-hole with spin $s = 1/2$ and angular momentum $l = 0, 1, 2, ...$ etc., which are often denoted as the familiar $s, p, d, ...$ orbitals. Coupling of spin and orbital momentum results in an energetic splitting into two non-degenerate states with total angular momentum $j_\pm = l \pm s$. In a semi-classical picture these states can be attributed to a magnetic coupling of the angular/orbital momentum and the spin with either parallel or antiparallel alignment. As a consequence, all core-levels with angular momentum $l > 0$ (all levels except the s-shells) are each split into two distinct energy levels. In the case of Fe and FeO, as depicted in Fig. 2.18, the resulting spin-orbit split photoelectron peaks of the Fe $2p$ spectra denoted as Fe $2p_{1/2}$ and Fe $2p_{3/2}$, respectively, can be distinguished clearly. The relative intensity ratio of both photoelectron peaks can be derived by the degree of degeneracy $2j_\pm + 1$ of each state:

$$\frac{I_-}{I_+} = \frac{2j_- + 1}{2j_+ + 1} = \frac{2(l - \frac{1}{2}) + 1}{2(l + \frac{1}{2}) + 1} = \frac{l}{l + 1} \ . \tag{2.64}$$

This results in an intensity ratio of $1 : 2$ for p-, $2 : 3$ for d-, $3 : 4$ for f-shells.

Satellites

The final state of an atom in the photoemission process is not necessarily present in the energetically lowest ground state, which contributes to the main photoemission line. Instead, there is a finite probability of being in an energetically slightly higher excited state. As a consequence, the kinetic energy of the emitted photoelectron is reduced by the corresponding energy difference. Hence, an increased binding energy is measured due to the larger difference between initial and final state [cf. Eq. (2.62)]. These resulting additional lines in the photoemission spectrum are so-called satellites, which in turn can be divided into *extrinsic* satellites, which are due to inter-atomic excitations, and into *intrinsic* satellites, which originate from intra-atomic relaxations.
In the latter case, the emitted photoelectron is subject to energy loss due to excitation of a second electron. If this secondary electron is excited into a higher unoccupied state, the emergent peak is called 'shake-up' satellite. As this transition is distinctly quantized (for the case of insulators and semiconductors), shake-up satellites exhibit discrete energy shifts to higher binding energies compared to the main photoemission line. If the secondary excited electron is emitted into continuum, the corresponding photoemission signal is called 'shake-off' satellite. Though, in contrast to

shake-up satellites, these transitions are not discrete, which therefore results in a broad feature in the photoelectron spectrum typically hidden in the background signal. For the case of metals, the secondary electron in a shake-up process can be excited into the energetically continuous conduction band. As the transition probability into these continuous final states decreases gradually with increasing energy, metals most commonly exhibit an asymmetric tail at the high binding energy side of the main line in the photoemission spectrum (cf. Fe spectrum in Fig. 2.18). Moreover, due to the excitation into the conduction band in metals, plasmons with discrete energies can be created and the respective energy-loss is also seen in the photoemission spectrum by so-called plasmonic excitation lines at significantly higher binding energies.
One possibility of extrinsic satellites is the consequence of so-called charge-transfer processes, which are commonly apparent in most transition metal oxides. In FeO, for instance, an electron is transferred from the O $2p$ orbital to the Fe $3d$ orbital. The energy required for this charge-transfer process is given by

$$\Delta = E(3d^{\mathrm{n}+1}L^{-1}) - E(3d^{\mathrm{n}}L) \ , \tag{2.65}$$

where L denotes the ligand (oxygen) from which an electron is transferred into the (Fe) $3d$ orbital that consists of n electrons before the charge-transfer process. The ligand hole is therefore described by L^{-1}. As the kinetic energy of the photoelectron is reduced by Δ, an additional so-called charge-transfer satellite appears in the spectrum with an energy difference Δ shifted to higher binding energies compared to the main photoemission line (cf. Fig. 2.18 for the example of FeO).

Multiplet splitting

Multiplet splitting arises from spin coupling of unpaired electrons (or holes) in the atom's core-levels after photoemission with unpaired electrons in the valence band. This coupling results in a lot of final state constitutions as also, e.g., spin-orbit splitting and charge-transfer has to be considered, which in consequence are the origin of an enhanced number of photoemission lines, so-called multiplets. Though, for electrons emitted from shells with an angular momentum of $l > 0$ mostly these lines are located closely together and form the total photoemission lines by overlap.

2.5.4 Quantitative analysis and depth profiling

One major advantage of XPS is the quantitative determination of the chemical composition of near-surface regions or (ultra)thin films. Here, the area below photoemission spectra corresponding to an element of the sample are directly related to the amount of the corresponding element. However, several factors, such as instrumental parameters of x-ray source and spectrometer as well as the photoelectric cross-sections for the specific element and atomic subshell and the IMFP of the excited photoelectrons have to be considered in the determination of elemental quantities. Further, a background has to be subtracted from the photoemission lines before determining the areas enclosed by the (elastic) photoemission peaks. In this work, solely the well-known Shirley background has been subtracted from the analyzed spectra [65].
Within the so-called straight-line-approximation, which assumes a straight trajectory of photoelectrons emitted from the sample, the photoemission intensity from orbital j of element i in a thin film with thickness $\mathrm{D_f}$ is given by [66, 67]

$$I_{ij} = S_i^j \int_0^{\mathrm{D_f}} e^{-z/\lambda_i'} dz = S_i^j \lambda_i' \left(1 - e^{-\mathrm{D_f}/\lambda_i'}\right) \ . \tag{2.66}$$

Here, z is the depth with regard to the film surface from which the photoelectrons are emitted and $\lambda_i' = \lambda_i \cos(\phi)$ is the effective IMFP at emission angle ϕ between detector and surface normal. λ_i denotes the IMFP for electrons ejected from element i at a given kinetic energy within the film material (cf. Fig. 2.15). Within this work, the IMFP of photoelectrons is estimated by the TPP-2M formula, develpoed by Tanuma, Powell, and Penn [68]. The factor S_i^j for electrons from orbital j of element i is given by

$$S_i^j = F(h\nu) \cdot T(E_{\text{kin}}) \cdot N_i \cdot A \cdot \sigma_i^j(h\nu) \ . \tag{2.67}$$

Here, $F(h\nu)$ denotes the flux density of x-rays with photon energy $h\nu$, $T(E_{\text{kin}})$ is the efficiency of the spectrometer, N_i gives the number of atoms i per unit volume, A denotes the analyzed sample area, and $\sigma_i^j(h\nu)$ is the subshell photoelectric cross-section, which can be defined by

$$\sigma_i^j(h\nu) = \int \frac{d\sigma_i^j(h\nu)}{d\Omega} d\Omega \tag{2.68}$$

as the integration of the differential photoelectric cross-section $d\sigma_i^j/d\Omega$ over the spherical angle section $d\Omega$.
Since within most measurements the experimental conditions are held constant, parameters like the photon flux $F(h\nu)$ and the analyzed sample area A can be assumed to be constant as well. Thus, by determining intensity ratios of different elements, these parameters will cancel out and can therefore be neglected. Further, most instruments are operated in the so-called fixed analyzer transmission (FAT) mode to obtain an energy-independent resolution (cf. Sec. 4.2.2), which means that the photoelectrons entering the spectrometer are retarded by a lens system to a specific pass energy E_{p} before entering the analyzer. Thus, by determining photoemission intensity ratios only the transmission of the lens system has to be considered within the factor $T(E_{\text{kin}})$. The corresponding transmission function of a spectrometer is often provided by the manufacturer but can also be measured experimentally. In addition, this factor depends on the photoelectron energy but can be neglected if intensities of photoemission lines are compared, which do not differ significantly in their kinetic energy (e.g., the $3p$ photoemission lines of Fe, Co, and Ni).
The anisotropic angular distribution of photoelectrons originating from orbital j of atom i is taken into account by the differential photoelectric cross-section $d\sigma_i^j/d\Omega$. In most cases, especially for relatively low photon energies, as in soft XPS, the photoexcitation process is dominated by dipole transitions [69] and the photoelectric differential cross-section is given within the dipole approximation by

$$\frac{d\sigma_i^j(h\nu)}{d\Omega} = \frac{\widetilde{\sigma}_i^j(h\nu)}{4\pi} \left[1 - \frac{\beta_i^j(h\nu)}{2} P_2(\cos \underline{\vartheta})\right] \tag{2.69}$$

for circularly polarized or unpolarized x-rays [70] and by

$$\frac{d\sigma_i^j(h\nu)}{d\Omega} = \frac{\widetilde{\sigma}_i^j(h\nu)}{4\pi} \left[1 + \beta_i^j(h\nu) P_2(\cos \vartheta)\right] \tag{2.70}$$

for linearly polarized x-rays [71]. Here, $\widetilde{\sigma}_i^j(h\nu)$ is the total photoelectric cross-section and $\beta_i^j(h\nu)$ is the angular asymmetry parameter for electrons excited from orbital j of atom i, which both depend on the incident photon energy $h\nu$. The terms $P_2(\cos \underline{\vartheta})$ and $P_2(\cos \vartheta)$ are each the second-order Legendre polynomials with $\underline{\vartheta}$ as the angle between the incident x-ray beam and the propagation direction of the photoelectrons and ϑ as the angle between x-ray polarization and photoelectron propagation direction (cf. Fig. 2.19). In most common laboratory XPS systems unpolarized x-rays

are used and the angle $\underline{\vartheta}$ is fixed at the so-called magic angle of 54.7° between x-ray source and spectrometer. In this case, the polynomial term $P_2(\cos\underline{\vartheta})$ vanishes and for the use of Al Kα and Mg Kα radiation, as typical lab-based x-ray sources, values for σ_i^j can be extracted from, e.g., the work of Scofield [72].
For higher photon energies, as used for HAXPES measurements in this work, additional non-dipole parameters have to be taken into account due to their increasing impact on the differential photoelectric cross-sections [69]. Thus, one obtains

$$\frac{d\sigma_i^j(h\nu)}{d\Omega} = \frac{\widetilde{\sigma}_i^j(h\nu)}{4\pi}\left[1 - \frac{\beta_i^j(h\nu)}{2}P_2(\cos\underline{\vartheta}) + \left(\frac{\gamma_i^j(h\nu)}{2}\sin^2\underline{\vartheta} + \delta_i^j(h\nu)\right)\cos\underline{\vartheta}\right] \tag{2.71}$$

for circularly polarized or unpolarized x-rays and

$$\frac{d\sigma_i^j(h\nu)}{d\Omega} = \frac{\widetilde{\sigma}_i^j(h\nu)}{4\pi}\left[1 + \beta_i^j(h\nu)\,P_2(\cos\vartheta) + (\gamma_i^j\cos^2\vartheta + \delta_i^j)\sin\vartheta\cos\varphi\right] \tag{2.72}$$

for linearly polarized x-rays [73] with the additional non-dipole parameters γ_i^j and δ_i^j, both also depending on the incident photon energy $h\nu$. For linear polarization, the additional angle φ is considered, which is the angle between direction of the x-ray beam and the component of the photoelectron propagation direction projected to the plane normal to the x-ray polarization (cf. Fig. 2.19). Tabulated values for the parameters $\widetilde{\sigma}_i^j$, β_i^j, γ_i^j, and δ_i^j in the photon energy range of 0.1-10 keV can be found in the works of Trzhaskovskaya *et al.* [74,75].
For the case of a multiple thin film stack, the intensity from an element in a buried film is attenuated exponentially (following Lambert-Beer's law) by each layer above the film in question. Regarding bulk material covered by n homogeneous thin films, its intensity I_b^m in a multilayer system can be determined by

$$I_\mathrm{b}^\mathrm{m} = S_\mathrm{b}^j\lambda_\mathrm{b}'\prod_{i=1}^{n} e^{-\mathrm{D}_i/\lambda_i'}\ , \tag{2.73}$$

where $S_\mathrm{b}^j\lambda_\mathrm{b}'$ is the non-attenuated intensity from the bulk material obtained for $\mathrm{D_f} \to \infty$ in Eq. (2.66). Thus, the intensity of photoelectrons originating from a buried layer f with film thickness D_f covered by $(n-f)$ layers in a multilayer system is given by

$$I_f^\mathrm{m} = S_f^j\lambda_f'\left(1 - e^{-\mathrm{D}_f/\lambda_f'}\right)\prod_{i=f+1}^{n} e^{-\mathrm{D}_i/\lambda_i'}\ . \tag{2.74}$$

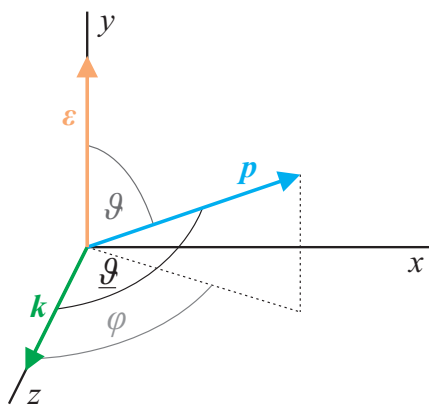

Fig. 2.19: Definition of angles and directions for the description of the differential photoelectric cross-sections of photoelectrons. The direction of the x-ray beam is denoted by $\boldsymbol{k}$, the polarization by $\boldsymbol{\varepsilon}$ and the photoelectron direction by $\boldsymbol{p}$. The angle $\underline{\vartheta}$ is enclosed by $\boldsymbol{p}$ and $\boldsymbol{k}$, ϑ is the angle between photoelectron and polarization and φ gives the angle between $\boldsymbol{k}$ and the projection of $\boldsymbol{p}$ to the plane normal to $\boldsymbol{\varepsilon}$.

Due to the angular dependence of the effective IMFP λ_i', so-called depth-profile measurements can be performed by varying the photoelectron detection angle in relation to the sample surface. For large angles ϕ between surface normal and detector the effective IMFP λ_i' is decreased and, thus, the contribution of the near-surface region to the total photoemission signal is increased, enhancing the surface sensitivity compared to detection normal to the surface. Hence, by varying ϕ the information depth is varied and depth-dependent measurements can be performed, providing information about the composition as a function of depth and also about film thicknesses in a multilayer system. A variation of the emission angle ϕ can be realized by either tilting the sample with respect to the analyzer between the single measurements or by using a wide-angle detector allowing for parallel data acquisition in a wide angular range. The latter method for angle resolved XPS/HAXPES measurements is used in this work (cf. Sec. 4.3.2).

2.6 X-ray absorption spectroscopy

Analogous to XPS, x-ray absorption spectroscopy leads to valuable information like the chemical composition and the electronic structure of the investigated material. Further, the local symmetry of the respective elements in a solid, as, for instance, the crystal field symmetry around a transition metal in TM oxides or TM ferrites, can be probed by analysis of XAS data. In this chapter, the principle of XAS is described first, followed by a phenomenological description of effects, which determine the XAS signals and are considered within the calculations of respective spectra.

2.6.1 Principle of XAS

Like XPS, XAS is a core-level spectroscopic technique, where core-electrons of the investigated material are excited due to absorption of incident x-rays (internal photoelectric effect). In contrast to XPS, the excited electron is not emitted into continuum, but rather excited into unoccupied states in the band structure of the material [cf. Fig. 2.21(a)]. Thus, this technique merely probes the unoccupied states of the material in question.

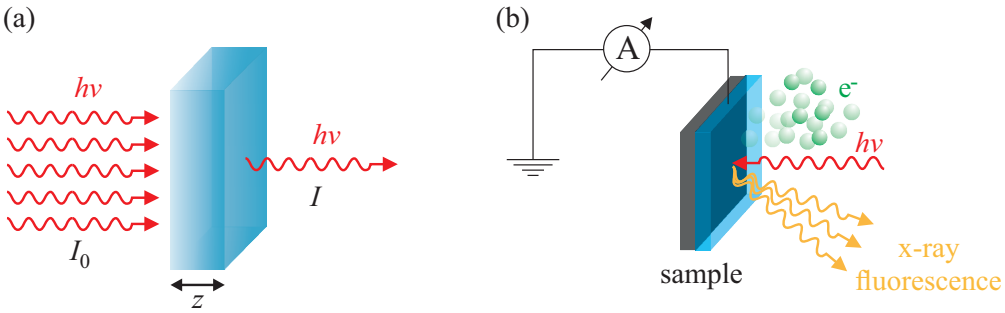

Fig. 2.20: Principle sketch of different absorption spectroscopy measurements. (a) For very thin (or liquid) samples, absorption can be measured in transmission geometry, recording the transmitted light intensity I in relation to the initial intensity I_0. (b) Secondary excitation processes such as fluorescence or Auger electron emission can be measured to gain information about the absorbed intensity of thicker (solid) samples. Fluorescent light can be measured by a photon detector (fluorescence yield) and stems from several μm within the sample. Auger electrons produce an electron cascade by exciting further electrons. The total electron yield is very surface sensitive (nm range) and can be recorded by measuring a drain current from ground to the sample to compensate for the charge loss.

The absorption process is quantified by the energy-dependent absorption coefficient μ of a material, which is defined by the amount of absorbed intensity when light passes through the material in

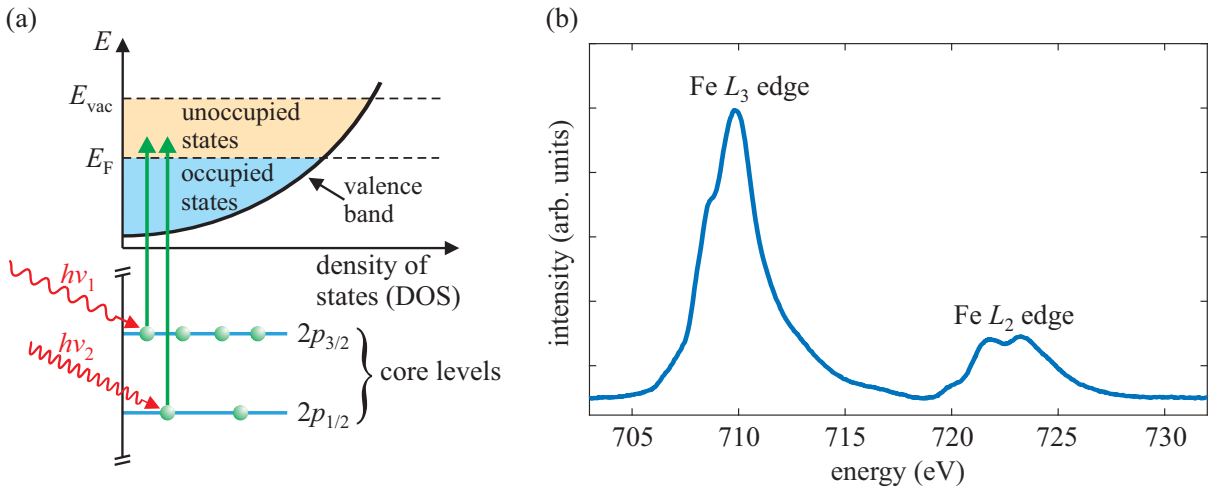

Fig. 2.21: (a) Schematic drawing of the photoexcitation process in XAS, where core-electrons are excited into unoccupied states of the valence band. Here, excitation from the two spin-orbit split $2p$ orbitals are depicted exemplarily. An x-ray photon energy $h\nu_1$ is large enough to excite a core-electron from the $2p_{3/2}$ level into an unoccupied state above the Fermi level E_F, resulting in increased absorption. If the photon energy is further increased ($h\nu_2 > h\nu_1$) also the stronger bound $2p_{1/2}$ electrons are excited, giving a second absorption line. (b) Exemplary x-ray absorption spectrum for the excitation from $2p$ levels for the case of Fe in Fe_3O_4. Excitation of the spin-split $2p_{3/2}$ and $2p_{1/2}$ electrons results in increased absorbed intensity, denoted as the Fe L_3 and Fe L_2 absorption edges, respectively.

question. Following Lambert-Beer's law, the transmitted intensity I of light passing through a sample of thickness z is given by

$$I(h\nu) = I_0(h\nu)\, e^{-\mu(h\nu)\, z} \tag{2.75}$$

with I_0 as the initial intensity. Thus, $\mu(h\nu)$ could be determined straightforwardly by recording the transmitted intensity $I(h\nu)$ in relation to the incident intensity $I_0(h\nu)$ [cf. Fig. 2.20(a)] by varying the photon energy $h\nu$ and applying Eq. (2.75). However, as the x-ray attenuation length $\lambda_{\mathrm{EAL}}(h\nu) = 1/\mu(h\nu)$ (EAL: effective attenuation length) in solids is in the μm range (far beyond absorption edges), only very thin samples could be measured, since otherwise the x-ray beam is completely damped by the material.

As an alternative, the photon absorption can be measured by detecting the decay processes of the emergent core-hole. Within the absorption process the final excited state decays by refilling the core-hole by an electron from an energetically higher state. The resulting gain in energy can be released by either emitting (i) fluorescent x-rays or (ii) secondary excited Auger electrons [cf. Fig. 2.20(b)]. In case (i), the emitted fluorescent x-rays can be easily detected by a photon detector and are directly related to the absorption coefficient. An advantage of this *fluorescent yield* (FY) detection is that the attenuation length λ_{EAL} of the x-ray fluorescence light is of the same order as the one of the initial x-rays, yielding high probing depths in the μm range. However, x-ray absorption spectra recorded by the FY method often suffer from saturation effects due to self-absorption [76–79].

The secondary excitation of Auger electrons in case (ii) is dominating for initial x-ray energies in the soft x-ray regime ($h\nu \leq 3$ keV) [57]. In this case, the Auger electrons travel through the material to leave it at the sample surface. On their way through the material, the Auger electrons can excite further electrons producing an electron cascade which is emitted from the sample. The sum of all electrons escaping the sample is called *total electron yield* (TEY) and can be detected by measuring a drain current from ground to the sample that compensates for the resulting charge due to electron

emission. An advantage of the TEY method is the amplification of the absorption signal due to the evolving electron cascade. Hence, even small deviations of the absorption coefficient $\mu(h\nu)$ can be detected. However, as the information depth of the TEY mode is limited to the IMFP of the excited electrons, only near-surface regions in the topmost few nanometers of the investigated sample can be probed. In this work, only the TEY mode is used for detection of x-ray absorption spectra.
An exemplary x-ray absorption spectrum for absorption of electrons from the Fe $2p$ levels into the unoccupied $3d$ states in Fe_3O_4 is depicted in Fig. 2.21(b). The main absorption peaks are denoted as L_3 and L_2 absorption edges, corresponding to absorption from the spin-orbit split Fe $2p_{3/2}$ and Fe $2p_{1/2}$ orbitals, respectively.

2.6.2 Multiplet calculations for XAS

After photoabsorption in XAS the excited electron still occupies a state within the material. Thus, the dipole selection rules have to be fulfilled for this transition, i.e., the total angular momentum has to change by $\Delta j = \pm 1$, the spin momentum has to be conserved ($\Delta s = 0$), and m_j as the z-component of the total orbital momentum has to change by $\Delta m_j = 0, \pm 1$. The probability for these transitions can still be described by Fermi's golden rule [cf. Eq. (2.60)], where the dipole transition matrix elements, consisting of the initial and final state wave functions, as well as the transition operator $\mathcal{T}$, are only non-vanishing for allowed transitions. However, for a system consisting of multiple electrons, there are numerous further transitions from initial to final states that occur compared to the single-electron-picture, which all contribute as multiplets to the absorption spectra. To describe x-ray absorption spectra, i.e., of transition metal oxides or ferrites as used in this work, theoretically by calculations of the multiplet structure, further effects essentially resulting from the bonding of the TM cation to oxygen ligands have to be considered. Here, the influence of the local symmetry of the respective cation surrounded by oxygen anions in different geometries leads to so-called ligand field splitting of the energetic states. Further, charge-transfer processes (cf. Sec. 2.5.3) between transition metal cation and oxygen anion have to be taken into account as well. Both effects are described qualitatively in the following. A detailed theoretical derivation of the respective dipole matrix elements in Eq. (2.60) for XAS can be found in Ref. [57].

Ligand field splitting

The ligand field theory is completely based on an electrostatical approach, but serves well for the description of properties of, e.g., transition metal complexes. Here, the ligand field splitting is described in terms of a transition metal cation, which is bound by its d orbitals to the surrounding oxygen ligands in different geometries (cf. Fig. 2.22). If the (TM) cation is assumed to be isotropically surrounded by the charges of the (oxygen) ligands, it can be regarded as located in the center of a spherical electrostatic field. Due to the Coulomb repulsion of electrons from cation and ligand, this state is energetically enhanced compared to the free cation. Though, as the isotropic field shifts all energy-levels to the same extent, no further splitting of energy levels occurs so far.
However, if the ligand charges occupy positions corresponding to the real ligand positions of the complex in a crystal, e.g., the corners of octa- or tetrahedra around the cation, the resulting electrostatic field is anisotropic. In this case, the mean energy of d states remains unchanged as in the isotropic case, but the energy of orbitals that are directed towards the ligands is enhanced, while the energy levels of orbitals located between the bonding directions are decreased. This energy splitting due to the (electrostatic) ligand fields is known as ligand field splitting.
The transition metal cations in the investigated spinel-type ferrites (i.e., $NiFe_2O_4$ and $CoFe_2O_4$, cf. Chap. 3) are either octahedrally or tetrahedrally coordinated by O^{2-} anions. In the case of

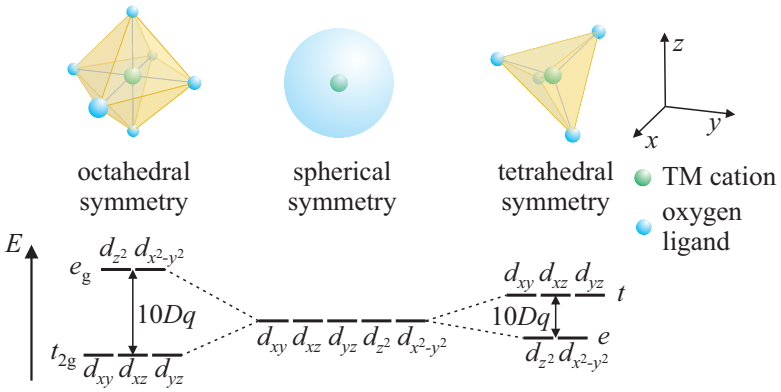

Fig. 2.22: Principle of ligand field splitting of d states of a transition metal cation surrounded by oxygen ligands in different geometries. For an isotropic/spherical charge distribution, no splitting occurs. For octahedral symmetry, the d states split into two energetically higher e_g and three lower lying t_{2g} levels. For tetrahedral coordination of the TM cation, the d states split into three higher t levels and two lower e states. The separation between t_{2g} (t) and e_g (e) states is denoted as $10Dq$.

octahedral coordination, the ligand (or crystal) field splitting of the $3d$ electrons results in three lower energy levels (for the coordinate system in Fig. 2.22: d_{xy}, d_{xz}, d_{yz}), denoted as the t_{2g} states, and two energetically higher states (d_{z^2}, $d_{x^2-y^2}$), denoted as e_g levels. For tetrahedral coordination of the respective cation, the energy levels split into three degenerate higher t states and two degenerate lower e levels. The energy difference between t_{2g} (or t) and e_g (or e) states, denoted as $10Dq$, is lower for tetrahedral symmetry compared to octahedral coordination and is a crucial parameter in the ligand field multiplet (LFM) calculations as it contributes significantly to the shape of the x-ray absorption spectra.

Charge-transfer

In the case of transition metal oxides or ferrites, charge-transfer occurs between the oxygen ligand and the TM cation. Here, a $2p$ electron of the oxygen atom is transferred to an unoccupied $3d$ orbital of the respective TM cation. However, the transferred electron still has a finite probability of being located in the $2p$ orbital of its originating oxygen atom, which can be taken into account by assuming only partial charge-transfer processes. In the case of L edge absorption within the cation, this can be realized by mixing the transitions from the initial $3d^nL$ to the final $2p^53d^{n+1}L$ states for neglecting charge-transfer processes with the transitions considering complete charge-transfer from the $3d^{n+1}L^{-1}$ ground to the $2p^53d^{n+2}L^{-1}$ final states (cf. Fig. 2.23).

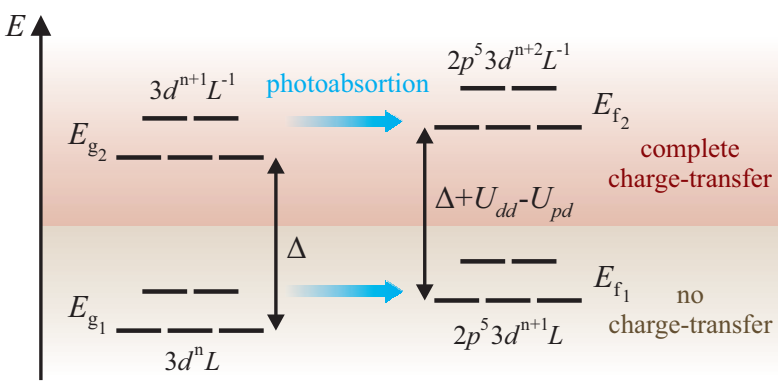

Fig. 2.23: Comparison of the energies of ground (E_{g_1}, E_{g_2}) and final states (E_{f_1}, E_{f_2}) for photoabsorption from $2p$ to $3d$ states assuming complete charge-transfer between ligand L and TM cation (upper part) and neglecting charge-transfer (lower part). For clarity, only the ligand field split $3d$ levels are shown. Δ is the charge-transfer energy and U_{dd} and U_{pd} are the potentials resulting from Coulomb interactions between d electrons and between core-hole (in the p orbital) and d electrons, respectively.

As known from Eq. (2.65), the ground state energy $E_{g_2} = E(3d^{n+1}L^{-1})$ is given by the charge-transfer energy Δ if the ground state energy $E_{g_1} = E(3d^{n}L)$ without charge-transfer is (w.l.o.g.) set to zero (in fact, Δ describes only the difference between the lowest states of each constitution, but the difference between the total energies is well approximated by $E_{g_2} - E_{g_1} \approx \Delta$). If transitions in both cases are mixed, also the two final state energies E_{f_1} and $E_{f_2} = E_{f_1} + \Delta + U_{dd} - U_{pd}$ for the cases without and with charge-transfer, have to be taken into account, respectively [57]. Here, U_{dd} describes the Coulomb repulsion between d electrons and U_{pd} the interaction between the emergent core-hole (in the p orbital) and the d valence electrons. All three parameters, Δ, U_{dd}, and U_{pd} are considered within the so-called charge-transfer multiplet (CTM) theory for the calculation of absorption spectra. In this work, the CTM theory is used under consideration of the ligand field splitting (see above) for XAS calculations of the respective TM cations.

2.7 X-ray magnetic circular dichroism

X-ray magnetic circular dichroism describes the difference between x-ray absorption of a magnetized sample obtained with oppositely circularly polarized light. Thus, on the one hand, XMCD provides the same chemical, electronic, and local symmetry information as XAS. Though, on the other hand, element specific information about the magnetically involved atoms in ferro- or ferrimagnetic material (cf. Sec. 2.8) can also be obtained by analysis of XMCD data. In the following, the principle of XMCD is briefly described first, followed by a presentation of the sum rule analysis applied for XMCD spectra of transition metal cations.

2.7.1 Principle of XMCD

XMCD is based on the differences for absorption of circularly polarized x-rays with opposite polarization directions. If XAS spectra of a ferri- or ferromagnetic material are measured with left circularly polarized (LCP) and right circularly polarized (RCP) x-rays (and polarization[7] and magnetization directions are not perpendicular), both recorded absorption spectra differ. This effect is known as x-ray magnetic circular dichroism, which was first theoretically described by Erskine and Stern in 1975 [80] and first experimentally verified by Schütz *et al.* in 1987 [81]. Following the theoretical description of Erskine and Stern, the XMCD effect can be basically explained by a simple two-step process. First, the polarized x-rays excite electrons with merely one spin direction, which, in a second step, are detected by the exchange split valence shell [cf. Fig. 2.25(a)]. In the following, this two-step model is described in more detail.
In the first step, the well-defined angular momentum of the circularly polarized photon is transferred to the excited electron. In the absence of spin-orbit splitting, the angular momentum of the photon is completely transferred to the orbital momentum of the electron [82]. This is the case, e.g., for the excitation from atomic s core levels. In contrast, if the core state from which the electron is excited is split by spin-orbit interaction, e.g., regarding the excitation from $2p_{3/2}$ and $2p_{1/2}$ substates, the photon angular momentum can also be transferred in part to the spin, which results in a preferential excitation of one spin direction. This is known as the Fano effect, which describes the spin polarization of electrons originating fom spin-orbit coupled orbitals [83]. This effect can be understood by considering the transition probabilities and the respective transition matrix elements in Fermis golden rule [cf. Eq. (2.60)] for circularly polarized photon absorption of spin-orbit split states and in the simplification of regarding the absorption process in a one-electron picture [80, 82]. Though, due to reasons of complexity, the derivation of the transition matrix elements is not explicitly shown here but can be followed in more detail in the initial determination

[7] the quantization axis of the circular polarization is considered as being parallel to the beam direction

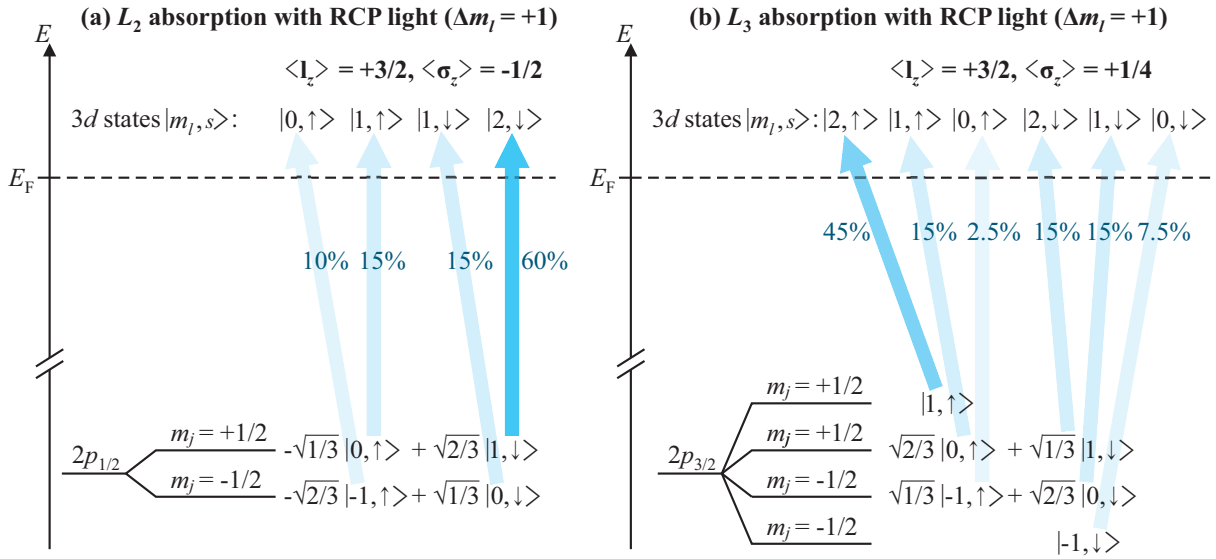

Fig. 2.24: Allowed transitions for (a) L_2 absorption and (b) L_3 absorption of right circularly polarized (RCP) light in the one-electron picture, assuming spin-orbit coupling in the $2p$ core levels but no spin-orbit coupling in the $3d$ states. The contributing substates are expressed as $|m_l, s\rangle$ eigenstates to follow the allowed transitions considering the dipole selection rule $\Delta m_l = +1$ for RCP light. The m_j states in the $2p$ orbitals are each formed by superposition of two $|m_l, s\rangle$ eigenstates, each weighted by the respective Clebsch-Gordan coefficients. The respective transition probabilities result from the determination of the transition matrix elements in Fermis golden rule and are denoted additionally. As a result, the expectation value of the spin in photon beam direction z is $\langle \sigma_z \rangle = -0.5$ after L_2 and $\langle \sigma_z \rangle = +0.25$ after L_3 absorption, expressing the respective spin polarization at each absorption edge. The corresponding value of the orbital moment $\langle l_z \rangle = +1.5$ is constant for both edges.

of Bethe and Salpeter [84] and in further subsequent publications as, e.g., in Refs. [80, 85, 86]. As a main result of these considerations, one obtains different absorption cross sections for the excitation of electrons with different spin directions from the spin-orbit split states by the incoming photons of the same helicity [80, 85]. This behavior for the example of allowed $2p_{1/2} \rightarrow 3d$ (L_2 edge) and $2p_{3/2} \rightarrow 3d$ transitions (L_3 edge), as typically investigated in $3d$ transition metals, for absorption of RCP light is schematically visualized in Fig. 2.24, based on an atomic picture in the one-electron model. For simplicity, spin-orbit coupling in the $3d$ states is neglected here. Further, the m_j states in the $2p_{1/2}$ and $2p_{3/2}$ orbitals are expressed by a superposition of the contributing eigenstates $|m_l, s\rangle$, which are weighted by the Clebsch-Gordan coefficients (spin-up and spin-down states are denoted by ↑ and ↓, respectively). For an allowed transition, the dipole selection rules $\Delta l = \pm 1$, $\Delta m_l = \pm 1$, $\Delta s = 0$ (and $\Delta m_j = \pm 1$) for absorption of RCP (+) or LCP (-) light have to be considered. The probabilities for the allowed transitions, which result from the determination of the transition matrix elements in Fermis golden rule [cf. Eq. (2.60)], are denoted additionally. By separately summing up the transition probabilities for spin-up and spin-down states, one can straight-forwardly determine the spin polarization of the excited electrons: if RCP (LCP) light is used, 62.5% of the excited electrons from the $2p_{3/2}$ level (L_3 edge) are spin-up (spin-down) and 37.5% are spin-down (spin-up) electrons [cf. Fig. 2.24(b)]. In contrast, the electrons excited from $2p_{1/2}$ levels (L_2 edge) are 75% spin-down (spin-up) and 25% spin-up (spin-down) when using RCP (LCP) light [cf. Fig. 2.24(a)]. As a consequence of this, the expectation value of the spin in photon beam direction z is $\langle \sigma_z \rangle = -0.5$ after L_2 and $\langle \sigma_z \rangle = +0.25$ after L_3 absorption, while the corresponding value of the orbital moment $\langle l_z \rangle = +1.5$ is constant for both edges. Thus, due to the opposite spin-orbit coupling at $2p_{3/2}$ ($j_+ = l + s$) and $2p_{1/2}$ levels ($j_- = l - s$), the spin-polarization is opposite at the two edges L_3 and L_2. Though, the determined spin-polarization values are only

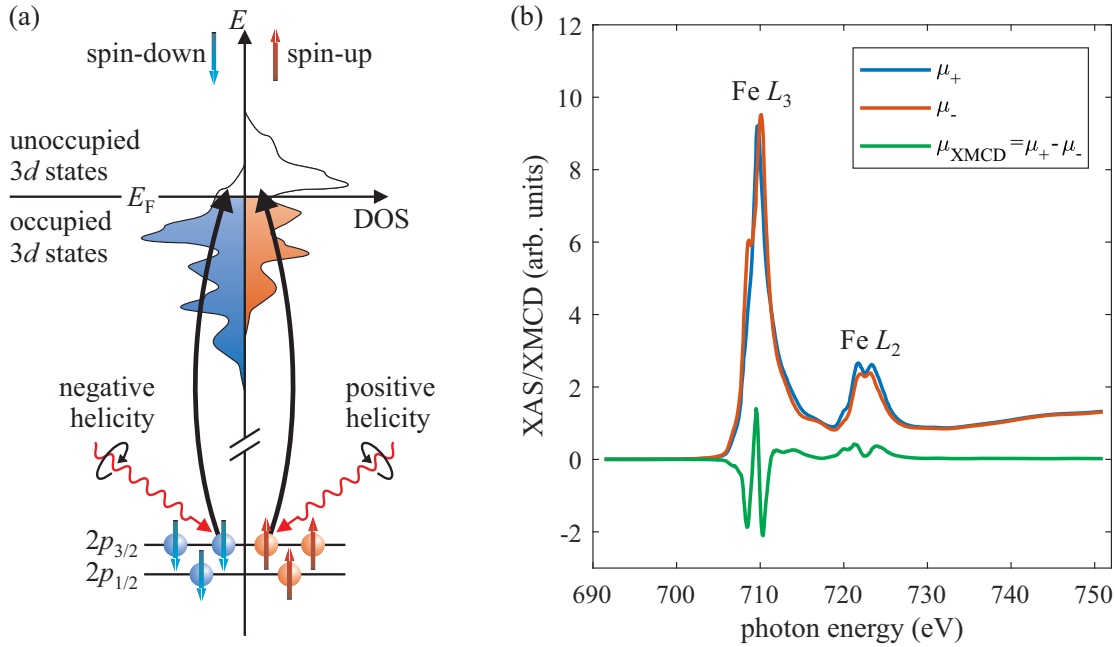

Fig. 2.25: (a) Schematic drawing of the XMCD process in a magnetized ferri-/ferromagnetic $3d$ transition metal. The density of states (DOS) is split into spin-up and spin-down states. The absorption of left or right circularly polarized x-rays (negative or positive helicity) results in a spin polarization of the excited electrons. Here, solely the preferential absorption of spin-up electrons by positive helicity and spin-down electrons by negative helicity at the L_3 edge are indicated. The exchange split conduction bands exhibit differently unoccupied states, which act as a spin detector. (b) Exemplary Fe $L_{2,3}$ XAS spectra of a thin Fe_3O_4 film recorded with parallel alignment of circular x-ray polarization and magnetization (μ_+) and antiparallel alignment (μ_-). The difference of both spectra forms the XMCD signal μ_{XMCD}.

valid in the simple one-electron model. In a more realistic case of multiple electrons in the initial and final states, Coulomb and exchange interactions should be considered as well (as it is done in multiplet calculations of x-ray absorption, cf. Sec. 2.6.2), resulting in significant modifications of the polarization values determined here. Note that within this first step of the two-step absorption process the discussed effects are independent of the magnetic properties of the sample.

The magnetic properties enter in the second step, where the electron is excited into an empty state in the conduction band. As the spins of a ferri-/ferromagnetic material are aligned, e.g., by applying an external magnetic field, the conduction band exhibits differently unoccupied spin split states [cf. Fig. 2.25(a)]. Thus, there are more empty states for one spin direction than for the opposite one and the excited and already polarized electrons (see above) are in turn weighted by the unoccupied states above the Fermi level. The conduction band therefore acts as a spin-detector accepting more electrons of one spin orientation.

In practice, the XMCD spectrum is obtained by recording two XAS spectra with either reversed helicity of the incoming photon and a constant magnetization or with reversed magnetization direction of the sample and a constant polarization. The difference

$$\mu_{\mathrm{XMCD}}(h\nu) = \mu_+(h\nu) - \mu_-(h\nu) \tag{2.76}$$

between both XAS signals (μ_+ and μ_- for, e.g., right and left circular polarization with constant magnetization) then represents the XMCD signal, as exemplarily depicted in Fig. 2.25(b) for the case of the Fe $L_{2,3}$ edges of a thin Fe_3O_4 film. Experimentally, usually both configurations, i.e., reversal of the magnetization direction with constant polarization and reversing polarization direc-

tion with constant magnetization, are measured. With this, spectra with similar relative alignment of polarization and magnetization directions can be averaged to discriminate artifacts from the dichroic signal and eliminate influences of the experimental components, which differ for, e.g., both polarization orientations.

2.7.2 Sum rules

XMCD data not only provides information about the chemical and electronic structure of the investigated material, but also contains element specific information about the separate spin and orbital magnetic contributions. Due to the spin polarization, XMCD measurements of, e.g., $2p \rightarrow 3d$ transitions of $3d$ transition metals, can be directly correlated with the spin magnetic contributions of the respective element. As the spin polarization is reversed between $2p_{1/2} \rightarrow 3d$ and $2p_{3/2} \rightarrow 3d$ transitions, the XMCD signals at L_2 and L_3 edges is also reversed in sign, if the spin magnetic contribution to the overall magnetic moment of the element is predominant. Further, since the orbital momentum is directly connected to the absorption of a circularly polarized photon by $\Delta m_l = \pm 1$, the XMCD signal also contains information about the orbital magnetic contribution of the respective element. In contrast to the solely spin polarized XMCD signal, both L_2 and L_3 edges exhibit the same sign of orbital polarization. As a consequence, the total XMCD signal at the $L_{2,3}$ absorption edges is generally a superposition of both spin and orbital contributions.
By applying the so-called *sum rules* derived by Thole *et al.* and Carra *et al.* [87, 88] and first successfully confirmed by Chen *et al.* [89], the separate orbital and spin magnetic moments m_{orb} and m_{spin} (in units of μ_B/atom) of $3d$ transition metals can be determined from TM $L_{2,3}$ XMCD data via

$$m_{\text{orb}} = -\frac{4\int_{L_3+L_2}(\mu_+ - \mu_-)dE}{3\int_{L_3+L_2}(\mu_+ + \mu_-)dE}(10 - n_{3d}) \tag{2.77}$$

and

$$m_{\text{spin}} = -\frac{6\int_{L_3}(\mu_+ - \mu_-)dE - 4\int_{L_3+L_2}(\mu_+ - \mu_-)dE}{\int_{L_3+L_2}(\mu_+ + \mu_-)dE}(10 - n_{3d})\left(1 + \frac{7\langle T_z\rangle}{2\langle S_z\rangle}\right)^{-1} . \tag{2.78}$$

Here, $\int_{L_3} dE$ and $\int_{L_3+L_2} dE$ denote the integrals over the sole L_3 edge and the complete $L_{2,3}$ edges, respectively, and $(\mu_+ - \mu_-)$ represent the XMCD and $(\mu_+ + \mu_-)$ the summed XAS spectra. The number of occupied $3d$ states in the respective TM cation is given by n_{3d}. $\langle T_z\rangle$ and $\langle S_z\rangle$ denote the expectation values of the magnetic dipole operator and of the total spin in z-direction. In the bulk of cubic crystals, the last term $7\langle T_z\rangle/2\langle S_z\rangle \ll 1$ and can therefore usually be neglected. Fig. 2.26 illustrates the sum rule analysis exemplarily at the Fe $L_{2,3}$ absorption edges of a thin Fe_3O_4 film. The parameters p and q denote the integrated intensities

$$p = \int_{L_3}(\mu_+ - \mu_-)dE , \tag{2.79}$$

$$q = \int_{L_3+L_2}(\mu_+ - \mu_-)dE \tag{2.80}$$

of the sole L_3 edge and the complete $L_{2,3}$ edge in the XMCD spectrum, respectively, whereas

$$r = \int_{L_3+L_2}(\mu_+ + \mu_-)dE \tag{2.81}$$

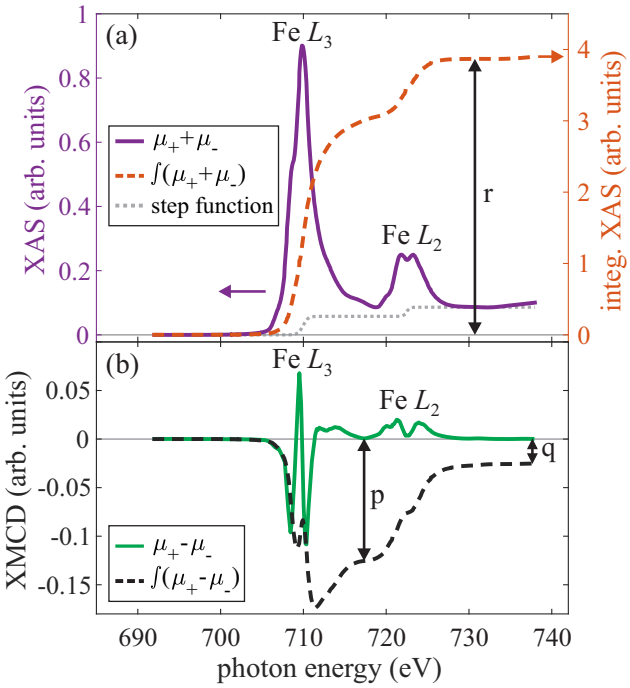

Fig. 2.26: Schematic illustration of the parameters p, q, and r for the sum rule analysis of XMCD data for the example of Fe $L_{2,3}$ edge spectra of a thin Fe_3O_4 film. (a) The parameter $r = \int_{L_3+L_2}(\mu_+ + \mu_-)dE$ denotes the integration over the complete $L_{2,3}$ absorption edges (dashed line) of the summed XAS spectra $(\mu_+ + \mu_-)$ after subtracting a step function (dotted line). (b) $p = \int_{L_3}(\mu_+ - \mu_-)dE$ and $q = \int_{L_3+L_2}(\mu_+ - \mu_-)dE$ are the respective integrated values over the sole L_3 and the complete $L_{2,3}$ edges in the XMCD spectrum, which is given as the difference between both XAS spectra measured with parallel and antiparallel alignment of the polarization and magnetization directions $(\mu_+ - \mu_-)$.

is the integrated $L_{2,3}$ intensity of the summed XAS spectra. Although this determination illustrates the powerful character of XMCD, since orbital and spin magnetic moments can be determined element specifically in a rather simple way, it should be noted that the sum rule analysis for Fe, Co, and Ni cations is subject to an uncertainty of up to ±30% [90].

2.8 Matter in magnetic fields

To describe the magnetic properties of a material the magnetization

$$\boldsymbol{M} = \frac{1}{V}\sum_j \boldsymbol{m}_j \tag{2.82}$$

as a summation over all atomic moments $\boldsymbol{m}_j$ normalized to the material's volume V can be introduced. If the material is placed in an external field $\boldsymbol{H}$, its response is given by

$$\boldsymbol{M} = \hat{\chi}\,\boldsymbol{H} \tag{2.83}$$

with the second-order tensor $\hat{\chi}$ as the material's magnetic susceptibility, which indicates how strong and in which way the material reacts to the external field $\boldsymbol{H}$. As a result, the total magnetic flux density (or magnetic induction) $\boldsymbol{B}$ induced by a material in a magnetic field $\boldsymbol{H}$ is given by

$$\boldsymbol{B} = \mu_0\,(\boldsymbol{M} + \boldsymbol{H}) \tag{2.84}$$

$$= \mu_0\,(\mathbb{1} + \hat{\chi})\,\boldsymbol{H} \tag{2.85}$$

$$= \mu_0\,\hat{\mu}_r\,\boldsymbol{H}\ , \tag{2.86}$$

where μ_0 denotes the vacuum permeability (or magnetic field constant) and the second-order tensor $\hat{\mu}_r = \mathbb{1} + \hat{\chi}$ denotes the relative permeability, which indicates (as its denotation suggests) how permeable the material is to the magnetic field (material, which concentrates a large amount of flux density in its interior, exhibits high magnetic permeability). Various kinds of substances can be

divided into different classes of magnetic behavior based on their response to an external magnetic field (and can therefore be indicated by their magnetic susceptibility value χ):

- **Diamagnetism**
  Diamagnetic substances exhibit no (atomic) magnetic moments in the absence of a magnetic field. However, by applying an external magnetic field to a diamagnetic material, magnetic moments with antiparallel alignment to the applied magnetic field are induced (Lenz's law). This behavior results in negative (and small) values for χ and relative permeability values μ_r slightly lower than one. Consequently, diamagnetic materials tend to exclude the magnetic field out of their interior, leading to a smaller magnetic flux density inside the material compared to the outside.
- **Paramagnetism**
  Paramagnetic materials, in contrast to diamagnetic substances, already exhibit magnetic moments without an external magnetic field. However, these magnetic moments (which in general result from orbital and spin magnetic moments of the electrons) are randomly oriented, resulting in a vanishing overall magnetization. An external magnetic field causes a (rather weak) alignment of these magnetic moments, resulting in an increased magnetic flux within the material compared to the magnetic flux outside of it. Thus, paramagnets are characterized by a small and positive susceptibility χ and a slightly bigger value than one for the relative permeability μ_r.
- **Ferro-, ferri- and antiferromagnetism**
  In ferro-, ferri- and antiferromagnetic materials, spontaneous magnetic ordering occurs without an applied external field (below a critical material dependent temperature). The origin of this behavior is the (quantum mechanical) exchange interaction between permanent magnetic dipole moments, causing a collective alignment of these moments. In ferromagnets, all existing moments tend to line up in the same direction [cf. Fig. 2.27(a)]. If the temperature of the ferromagnetic material is increased above its so-called Curie temperature T_C, the ferromagnetic ordering vanishes and the material becomes paramagnetic. In contrast to ferromagnets, antiferromagnets exhibit (at least) two magnetic sublattices with the exact same magnetizations, but with antiparallel alignment, resulting in a vanishing overall magnetic moment [cf. Fig. 2.27(b)]. This ordering is maintained for temperatures below the material's Néel-temperature T_N, upon which the antiferromagnetic ordering transforms into a paramagnetic state. Ferrimagnets also consist of antiparallel magnetic sublattices as in antiferromagnets, but with different absolute magnetization values, resulting in only partial compensation of magnetic moments and a finite net magnetization [cf. Fig. 2.27(c)]. Below the critical temperature, ferri- and ferromagnets exhibit susceptibilities and permeabilities and, thus, inner magnetic flux densities, which are several orders of magnitude larger than for paramagnets or antiferromagnets. Both, χ and μ_r, are non-linear functions of the applied magnetic field.

As this work focuses on the characterization of ferrimagnetic thin ferrite films (cf. Chap. 3), the principles of collective magnetic ordering (ferro-, ferri- and antiferromagnetism) are described in the following in more detail, based on formulations in Refs. [40, 91–94].

2.8.1 Collective magnetism

Collective magnetism is a phenomenon of, i.e., solids, which is based on the exchange interaction between atomic magnetic moments, resulting in spontaneous magnetic ordering within the material without applying an external magnetic field. As the classical dipole-dipole interactions between magnetic atoms of a crystal are too small (~ 0.1 meV [40]) to explain the phenomenon of collective magnetic ordering, the origin of the underlying exchange interactions is only accessible via a

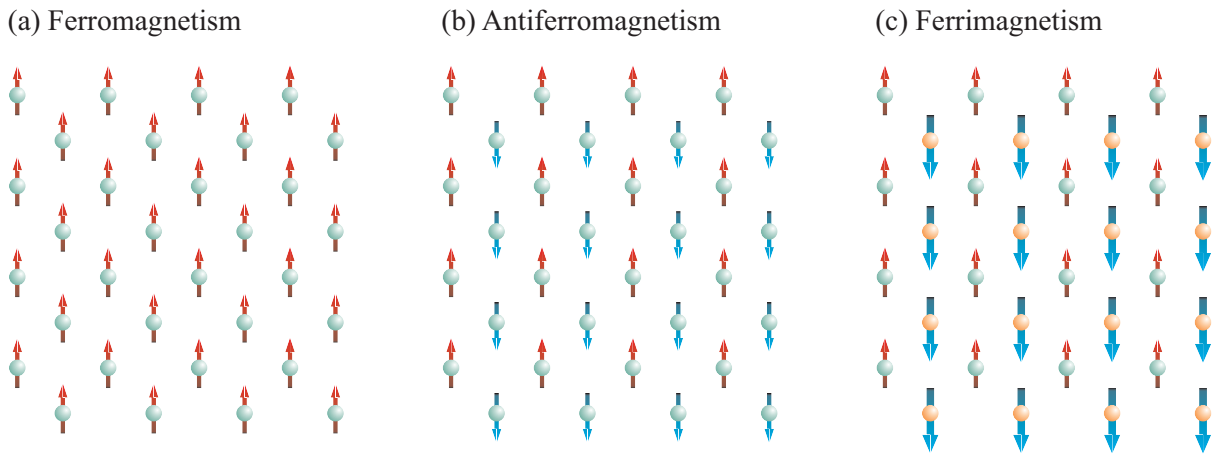

Fig. 2.27: Alignment of atomic magnetic moments in the three types of collective magnetic ordering. (a) Ferromagnets exhibit parallel alignment of magnetic moments (red arrows). (b) Antiferromagnetic materials exhibit atomic sublattices with antiparallel magnetic alignment (red and blue arrows), resulting in a vanishing overall magnetization. (c) As in antiferromagnets, ferrimagnetic materials exhibit antiferromagnetically coupled sublattices, but with each exhibiting different magnetization values due to different absolute atomic moments (red and blue arrows of different size). This results in a non-vanishing overall magnetization.

quantum mechanical approach.
In solid states the atomic energy levels overlap and form energy bands, resulting in a continuous density of states (DOS) within these bands. In contrast to metals, where the conduction band is occupied by quasi-free conduction electrons, insulators (and semiconductors) exhibit an energy band gap E_g between valence and conduction band, resulting in an unoccupied conduction band if the band gap is large enough. Hence, no electric conducting behavior is obtained and the crystal electrons of insulators can be described as quasi-localized at the positions of the corresponding lattice atoms. The investigated ferrite films in this work (i.e., $NiFe_2O_4$ and $CoFe_2O_4$; cf. Chap. 3) have essentially insulating character. Thus, the electrons, which are responsible for the magnetic behavior of these materials (i.e., electrons of the partially filled $3d$ bands of the transition metals), can be treated as quasi-localized at their atomic lattice positions.
To understand the collective magnetic ordering in insulators, the simple picture of two electrons on adjacent lattice sites is considered. Regarding the Pauli principle, the overall wave function of both electrons, which consists of a spin and a spatial part, has to be antisymmetric. Thus, either the spin wave function has to be antisymmetric (meaning antiparallel spin alignement) and the spatial wave function symmetric (meaning the electrons are localized closely together) or vice versa.
For antiparallel spin alignment, the spatial wave function is symmetric and both electrons are localized closely together. This in turn increases the potential energy due to the Coulomb interaction between both electrons. In contrast, for parallel spin alignment and therefore antisymmetric spatial parts, the potential energy is decreased. However, due to the Pauli principle, electrons with parallel spin alignment have to occupy different energetic states, resulting in an increase of their kinetic energy. As a consequence, potential and kinetic energies are competing with each other in terms of minimizing the total energy.
Werner Heisenberg found that both arrangements can be described only by the interaction between the spins, which can be understood considering that the symmetry of the spatial wave function is dependent on the spin part. Hence, the energetic description of interacting electrons can be described by the Heisenberg model [95], which generalizes the interaction to many-electron atomic spins $\boldsymbol{S}_i$ of the i-th atom. Hereby, the Hamiltonian for the spin-spin interaction between pairs of

atoms on sites i and j of a lattice is given by

$$\mathcal{H} = -2 \sum_{i>j} J_{ij} \boldsymbol{\mathcal{S}}_i \cdot \boldsymbol{\mathcal{S}}_j \tag{2.87}$$

with $\boldsymbol{\mathcal{S}}_i$ and $\boldsymbol{\mathcal{S}}_j$ as dimensionless spin operators, describing the many-electron atomic spins of the respective atoms. J_{ij} is the so-called exchange integral (or simplified: exchange constant) and describes the type and strength of exchange interaction between atom i and j. If only adjacent atoms and identical atom pairs are considered, the exchange constant simplifies to J. For positive values of J, Eq. (2.87) is minimized by parallel spin alignment, meaning ferromagnetic ordering. In contrast, antiparallel alignment is preferred for negative exchange constants J, resulting in antiferromagnetic ordering.

2.8.2 Exchange interactions

The exchange interaction described by the exchange constant J depends on the overlap of the electron wave functions of the contributing lattice atoms. Here, one option is the direct overlap of the electron wave functions of adjacent magnetic atoms (as described above), resulting in *direct exchange interaction*, depicted in more detail in the following. However, the exchange interaction can also be mediated by atoms lying in between the magnetic atoms, which thereby leads to indirect exchange mostly determining the magnetic properties of several oxides. In particular, transition metal ferrites, as used in this work, exhibit two most common indirect exchange interactions, namely *superexchange* and *double-exchange*, which are also described in the following. As all presented exchange interactions can be understood by virtual electron hopping from one atom to another, the theoretical model to describe these processes (*Mott-Hubbard model*) is explained first.

Mott-Hubbard model

To describe the principle of direct and indirect exchange interactions in energetical terms, virtual electron hopping between adjacent atoms is considered. Here, the virtual hopping process can be regarded as a temporal hopping of one electron to the adjacent site and back again. Following the tight-binding model, the atoms are treated in a single atom picture and the overlap of the electron functions of adjacent atoms is handled as a perturbation to this.
With regard to the minimization of the total energy, both competing energy contributions, the Coulomb and the kinetic energy, have to be considered. A reduction of the kinetic energy results in a delocalization of the electrons[8] and therefore increased electron hopping, which is characterized by the hopping energy (or interatomic transfer integral) t. In contrast, the Coulomb energy U, which accounts for repulsion of the electrons, is reduced by preferably large electron distances, leading to a localization at the atomic lattice sites. Both competing mechanisms as well as the Pauli principle are considered within the Mott-Hubbard model for the description of the hopping process between adjacent lattice sites [96, 97]. Here, only the case for one orbital consisting of one electron per lattice atom is depicted for simplicity. The resulting Hamiltonian within this model is then given by

$$\mathcal{H} = -t \sum_{\langle i,j \rangle, \sigma} \left(c^\dagger_{i,\sigma} c_{j,\sigma} + c^\dagger_{j,\sigma} c_{i,\sigma} \right) + U \sum_{i=1}^{N} n_{i,\uparrow} n_{i,\downarrow} \tag{2.88}$$

[8] The delocalization of the electrons due to a decreased kinetic electron energy is a consequence of the Heisenberg uncertainty principle of momentum p and position x: $\Delta p \Delta x \geq \hbar/2$. With this, the kinetic energy can be expressed as $p^2/2m_e \approx \Delta p^2/2m_e \propto \hbar^2/(2m_e(\Delta x)^2)$. A reduction of kinetic energy therefore leads to larger uncertainty Δx and, thus, delocalization.

with the first sum running over all adjacent lattice sites $\langle i, j \rangle$ and spins σ ($\uparrow$ or $\downarrow$). Here, $c^{\dagger}_{i,\sigma}$ is the creation and $c_{i,\sigma}$ the annihilation operator for an electron with spin σ on lattice site i. The product $c^{\dagger}_{i,\sigma} c_{j,\sigma}$ therefore transfers an electron from site j to site i with the hopping energy t. For increasing t, the kinetic energy of the electrons is reduced, resulting in a delocalization and the formation of bands with a width $W \propto t$ [91]. The counting operator $n_{i,\sigma} = c^{\dagger}_{i,\sigma} c_{i,\sigma}$ equals one if an electron with spin σ is located on site i and vanishes otherwise. Hence, the second term of Eq. (2.88) accounts for the Coulomb repulsion U between two electrons located on the same lattice site.
For small values of U ($U \ll W$), the second term of the model Hamiltonian given in Eq. (2.88) becomes negligible and the model transforms into the description of a metallic state. In contrast, if the on-site repulsion U becomes reasonably larger than the band width W, the electrons tend to avoid multiple occupancies of a lattice site. The remaining finite hopping amplitude results in antiferromagnetic spin alignment of the quasi-localized electrons [40]. Moreover, splitting into two seperate bands occurs with a lower filled band and a higher empty band, exhibiting an energy gap in between. Thus, with increasing U/W ratios the band structure migrates from a metallic to an insulating state, which is also known as the Mott-Hubbard (metal-insulator) transition.

Direct exchange

The direct exchange interaction results from a direct overlap of the neighboring electron wave functions of the atoms with a magnetic dipole moment. Fig. 2.28 schematically shows the virtual electron hopping processes and, thus, the direct exchange between magnetic atoms with half-full, almost empty or almost full d shells. For the case of half-filled shells, there is no ferromagnetic exchange, since hopping from one shell to another with the same spin direction, as depicted in Fig. 2.28(a), would contravene the Pauli exclusion principle. Hence, direct exchange of half-filled shells is necessarily antiferromagnetic, since the energy gain associated with overlapping wave functions of neighboring atoms is only achieved for antiparallel spin alignment [cf. Fig. 2.28(b)]. In contrast, nearly empty or nearly filled shells tend to be ferromagnetic [91], since in both cases electrons can hop into empty states while preserving their spin [cf. Figs. 2.28(c)-(d)].

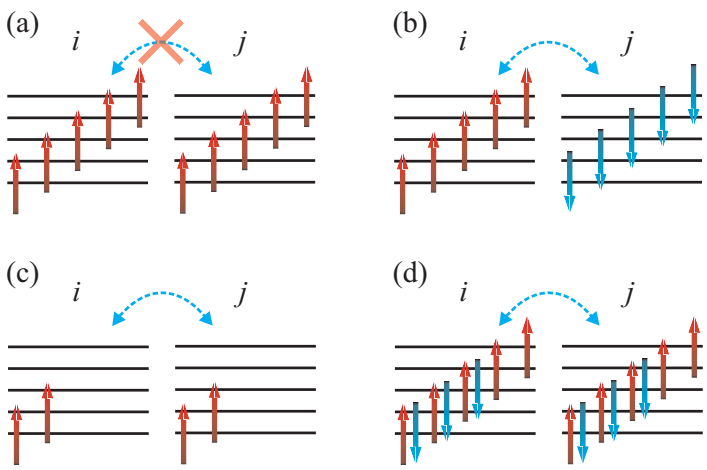

Fig. 2.28: Schematical drawing of direct exchange by virtual electron hopping between d shells of two neighboring atoms i and j. (a) Direct electron hopping between half-filled d shells with parallel spin alignment is forbidden due to the Pauli exclusion principle. (b) Direct exchange of half-filled shells therefore results in antiferromagnetic ordering. (c) Almost empty or (d) almost filled shells merely lead to ferromagnetic ordering, since electrons can hop into empty states of the neighboring shell while preserving the spin direction.

Superexchange

As mentioned above, the orbitals of the atoms with magnetic moments have to overlap for a direct exchange. Instead, if the distance between the magnetic atoms is large, the overlap of the electron wave functions vanishes and direct electron hopping becomes rather unlikely. However, the exchange interaction between atoms with magnetic dipole moments can still be mediated by atoms or ions

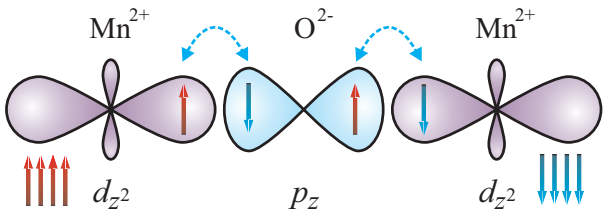

Fig. 2.29: Schematical drawing of the O^{2-} mediated superexchange interaction between two Mn^{2+} cations in MnO. The spin in the $3d_{z^2}$ orbital of the Mn^{2+} cation couples with the spins in the filled O $2p_z$ orbital, resulting in antiparallel spin alignment at each bond and, thus, antiferromagnetic superexchange between the Mn^{2+} ions. For clarity, only the coupling orbitals (Mn $3d_{z^2}$ and O $2p_z$) are depicted. The four remaining $3d$ spins of the Mn^{2+} ions are also shown.

localized in between. One common indirect interaction is called superexchange, which occurs in several oxides and, in particular, in transition metal ferrites such as $NiFe_2O_4$ and $CoFe_2O_4$.
Here, the principle of superexchange interaction is described for the example of MnO, where the spin interaction of two Mn^{2+} ions (with half-filled $3d$ shells) is coupled by a diamagnetic O^{2-} ion, which is located in between and exhibits a completely filled $2p$ shell. Due to the overlap of the Mn $3d$ and O $2p$ orbitals, spin coupling between the electrons of the Mn^{2+} and O^{2-} ions occurs, resulting in an indirect exchange of the moments of both Mn^{2+} cations (cf. Fig. 2.29). The spin coupling can be described by a virtual hopping process of an electron from the O $2p$ orbital (here, p_z orbital) into the overlapped $3d$ orbital (d_{z^2} orbital) of the Mn^{2+} ion and back again. This hopping process can now occur between both electrons in the O $2p_z$ orbital (which have antiparallel alignment) and the coupled (singly-filled) $3d_{z^2}$ orbital of each adjacent Mn^{2+} cation. Due to the Pauli exclusion principle, the spin of the virtually hopping electron must have antiparallel alignment to the spin of the electron which already occupies the orbital where the electron is hopping in. Thus, the superexchange interaction between the Mn^{2+} ions in the case of MnO is antiferromagnetic.
The corresponding effective exchange constant J_{se} for such a superexchange interaction can be estimated by

$$J_{\mathrm{se}} = -2\,t^2/U \ , \tag{2.89}$$

where U is the on-site Coulomb repulsion and t the hopping energy, indicating the hopping probability between O $2p$ and Mn $3d$ orbitals, both introduced in Eq. (2.88). However, J_{se} crucially depends on the interatomic separation and the bonding angles between oxygen and involved magnetic ions. Moreover, the simplified model with one electron in only one orbital, as introduced above in the Mott-Hubbard model, is not sufficient to describe the interactions in most oxide crystals, where the details of the orbital structure (occupancy, orbital degeneracy, overlap with O $2p$ levels, etc.) have to be considered. Thus, determining the strength and sign of superexchange interactions can be very complex. However, Goodenough, Kanamori and Anderson have formulated empirical rules [98–100], which are able to predict the exchange interactions in most transition metal oxides:

- The superexchange interaction between partially filled d orbitals of two magnetic cations under a cation-ligand-cation angle of 180° is strongly antiferromagnetic.
- The superexchange interaction between partially filled d orbitals of two magnetic cations under a cation-ligand-cation angle of 90° is relatively weak and ferromagnetic.
- The superexchange interaction between a partially filled d orbital of one magnetic cation and an empty or full d orbital of the same type of the second magnetic cation under a cation-ligand-cation angle of 180° is relatively weak and ferromagnetic.

These Goodenough-Kanamori-Anderson-rules can also be applied for the transition metal ferrites $NiFe_2O_4$ and $CoFe_2O_4$ investigated in this work, which results in their ferrimagnetic ordering, discussed in more detail in Sec. 3.2.6.

Double-exchange

Similar to superexchange, double-exchange interactions are mediated by diamagnetic O^{2-} ions between two magnetic cations, but in this case both cations exhibit different valence states, e.g., Mn^{3+} and Mn^{4+}, as depicted in Fig. 2.30. Then, an electron can hop from the oxygen ion to a free orbital in Mn^{4+}, if simultaneously an electron from the Mn^{3+} cation hops into the free O $2p$ orbital to fill the emerging hole. Following Hund's first rule[9], the spin alignment of the hopping electron from O $2p$ to the Mn $3d$ band has to be parallel to the other d electrons of the initial Mn^{4+} ion. Thus, also the hopping electron from Mn^{3+} to the O^{2-} anion has to exhibit the same spin direction. If the spins of the Mn^{3+} and Mn^{4+} ions were aligned antiparallel, the emerging hole in the O $2p$ orbital could not be refilled by an electron of the Mn^{3+} $3d$ shell, as it would have the same spin as the remaining electron in the O $2p$ orbital. As a consequence, the described double-exchange interaction is necessarily ferromagnetic. Moreover, the final Mn^{4+}–O^{2-}–Mn^{3+} state of the described hopping process [cf. Fig. 2.30(b)] is energetically degenerate to the initial Mn^{3+}–O^{2-}–Mn^{4+} state [cf. Fig. 2.30(a)] and, thus, not forbidden. In contrast to the virtual hopping processes in, e.g., superexchange, the hopping processes in double-exchange interactions can actually occur and are therefore closely related to increased electric conductivity [91].

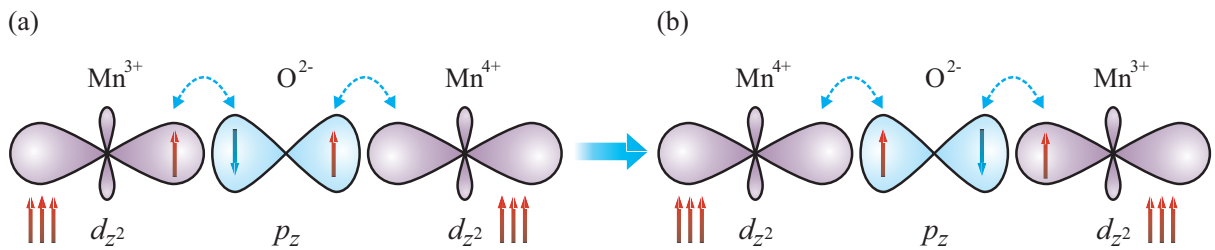

Fig. 2.30: Schematical drawing of the O^{2-} mediated double-exchange interaction between a Mn^{3+} and a Mn^{4+} cation. An electron fom the filled O $2p_z$ orbital can hop into the free d_{z^2} orbital of the Mn^{4+} ion if its spin is aligned parallel to the spins of the other Mn^{4+} $3d$ electrons. The emerging hole in the O $2p_z$ orbital can be refilled by an electron from the Mn^{3+} ion, resulting in ferromagnetic double-exchange between the Mn cations. The initial configuration in (a) is energetically degenerate to the final state in (b), enabling real instead of virtual electron hopping. For clarity, only the coupling orbitals (Mn $3d_{z^2}$ and O $2p_z$) are depicted. The remaining $3d$ spins of the Mn cations are also shown.

2.8.3 Magnetic domains and magnetization curves

Due to the exchange interactions described above, ideal ferromagnets should exhibit solely parallel alignment of all (resulting) magnetic moments. Though, also ferro(i)magnetic materials can exhibit smaller or even vanishing spontaneous magnetizations than expected by only regarding the exchange interactions in the material. This behavior can be explained by the formation of magnetic domains (so-called Weiss domains) within the material. Here, each domain exhibits the expected ideal magnetization by parallel alignment of the magnetic moments, but the magnetizations of different domains point in different directions, resulting in a total magnetization averaged to zero (or at least smaller values than the magnetization of each single domain). The origin of these magnetic domains is found in the minimization of the total free energy

$$E_{\text{tot}} = -\boldsymbol{H} \cdot \boldsymbol{M} + \sum_i E_i \ , \tag{2.90}$$

[9] Hund's first rule states that the overall atomic spin of an atom in its ground state should be maximized, resulting in first parallel spin alignment with different quantum numbers m_l in order not to break Pauli's exclusion principle and to minimize the Coulomb repulsion.

where the first term is the Zeeman energy $E_{\mathrm{Z}} = -\boldsymbol{H} \cdot \boldsymbol{M}$, which accounts for the interaction of a magnetic body with magnetization $\boldsymbol{M}$ (here: a single magnetic domain) with an external magnetic field $\boldsymbol{H}$. The summation includes additional energy contributions E_i as, i.e., domain wall energy E_{dw}, anisotropy energy E_{ani}, strain energy E_{str} and magnetostriction energy E_{ms}. Here, as a reasonable approximation, the two latter contributions E_{str} and E_{ms} due to applied stress and magnetostriction, respectively, are neglected, since their energies are relatively small [91]. The domain wall energy E_{dw} is the energy necessary to form a domain wall between adjacent domains. As the anisotropy energy E_{ani}, in addition to E_{dw} and E_{Z}, has substantial impact on the formation of magnetic domains, its origin is briefly discussed in the following in more detail. It can be subdivided into its main contributions of magnetocrystalline (E_{mc}) and shape anisotropy (E_{sh}). Other contributions to the magnetic anisotropy as, e.g., interface or magnetoelastic anisotropies, are not considered here.

Magnetic anisotropies

The *magnetocrystalline anisotropy* is a dominant contribution to the magnetic anisotropy of ferro- and ferrimagnetic crystals. It mainly results from the spin-orbit interaction in magnetic crystals, which is influenced by a coupling between the crystal structure and the orbital alignment. As the alignment of the orbitals in a crystal is fixed, the spin orientation also exhibits a preferred direction (magnetic easy direction) due to finite spin-orbit-coupling. Hence, energy is needed to rotate the spins off the magnetic easy directions. Consequently, the crystal structure crucially influences preferred spin orientations and therefore determines the magnetocrystalline ansiotropy.
In contrast, the *shape anisotropy* of a ferro- or ferrimagnet depends on the macroscopic shape of the magnetic material. This, i.e., commonly results in a preferred magnetization orientation along spatially more extended than spatially shorter directions of the magnetic sample. This behavior can be understood by the concept of a demagnetizing field

$$\boldsymbol{H}_N = -\hat{N}\boldsymbol{M} \ , \tag{2.91}$$

which is created by uncompensated magnetic moments at the material's surfaces and directed in opposite direction to $\boldsymbol{M}$ inside the material and therefore partially demagnetizes the sample. $\hat{N}$ is the demagnetization tensor, which depends on the shape of the sample. The magnetostatic self-energy, which is necessary to rotate the magnetization from a preferred to an unfavorable direction, is given by

$$E_{\mathrm{sh}} = -\frac{1}{2}\mu_0 \int_V \boldsymbol{H}_N \cdot \boldsymbol{M}\, dV \ = \ \frac{1}{2}\mu_0 \int_V (\hat{N} \cdot \boldsymbol{M}) \cdot \boldsymbol{M}\, dV \ . \tag{2.92}$$

Outside the magnetic sample, the demagnetizing field is called stray field $\boldsymbol{H}_{\mathrm{S}}$, which has an important influence on not only the shape anisotropy of macroscopic samples, but also on the domain structure within a crystal, as described in the following.

Magnetic domain formation

The principle of magnetic domain formation can be understood by regarding the energy contributions of the total free energy in Eq. (2.90) for different magnetic domain structures in a single-crystalline solid, as schematically depicted in Fig. 2.31. Here, the domain structure of a ferro- or ferrimagnet is considered in the absence of an external magnetic field, hence, the Zeeman term vanishes. If the magnetic sample only consists of one single domain [cf. Fig. 2.31(a)], also called monodomain state, the direction of magnetization is determined by the energetic minimum

of magnetic anisotropy contributions, as described above. This state is characterized by a large demagnetization/stray field, leading to an enhancement of the magnetostatic self-energy E_{sh} [cf. Eq. (2.92)] and an increased total free energy E_{tot}. The magnetostatic self-energy can be reduced by the formation of magnetic domains with antiparallel alignment within the sample [cf. Figs. 2.31(b)-(c)]. Hereby, the stray fields of the single domains overlap with each other, lowering the total stray field of the macroscopic sample, which in turn decreases the magnetostatic self-energy and its contribution to the total free energy. However, the formation of walls between adjacent domains with antiparallel alignment increases the exchange energy, since parallel alignment should be preferred. Thus, the domain wall energy E_{dw} necessary to build these walls increases the total free energy and counteracts the reduction of the magnetostatic self-energy.
A reduction of the exchange energy, which rises due to the formation of a domain wall, can be achieved by a gradual spin rotation over several atoms forming these domain walls. The domain wall is called a Bloch-wall, if the rotations of magnetic moments are parallel to the domain wall. In contrast, domain walls exhibiting rotations of spins that lie in a single plane (in-plane) and are therefore not parallel to the domain wall are called Néel-walls. These spin rotations in turn could increase the energy that is given by the anisotropy contributions, since several spins of the domain wall could be aligned off the easy direction. Thus, the domain walls themselves are subject to a competition between the different energy contributions.
Considering the minimization of the magnetostatic energy, it becomes favorable, if antiparallel domains are confined by so-called *domains of closure* [cf. Fig. 2.31(d)]. The resulting domain arrangement leaves no (uncompensated) magnetic poles at the sample surfaces and thereby minimizes the stray field. Though, in this case the magnetization direction in the domains of closure are not necessarily aligned in a magnetic easy direction, which in turn increases the anisotropy energy contribution. Note that most magnetic crystals with cubic crystal structure exhibit perpendicular easy axes and perpendicular domains of closure may then readily be formed.

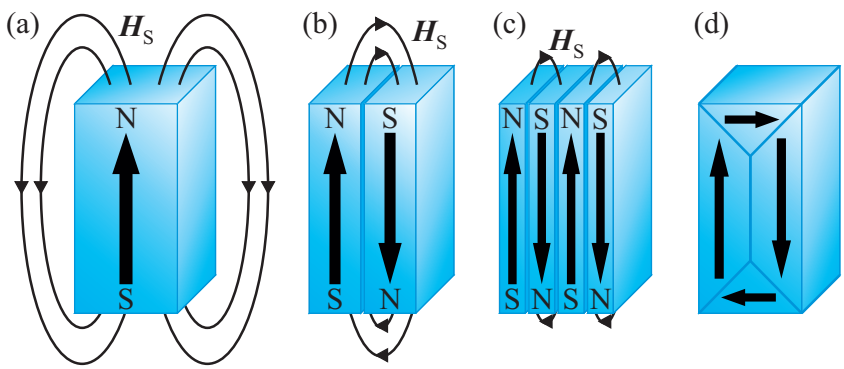

Fig. 2.31: Principle of domain formation in a ferro(i)magnetic material with corresponding total magnetic stray field $\boldsymbol{H}_{\mathrm{S}}$ outside the sample. From (a) to (d): the magnetostatic self-energy decreases, whereas the domain wall and anisotropy energies increase. Adapted from Ref. [40].

In general, the domain structure of real ferro- or ferrimagnetic crystals can be very complex [101]. However, its origin is always based on a minimization of the total free energy with a competition between its main contributions, the Zeeman energy, the (magnetocrystalline) anisotropy energy, the magnetostatic self-energy and the domain wall energy.

Magnetization curves

If a ferro- or ferrimagnetic material is brought into an external magnetic field, also the Zeeman term [cf. Eq. (2.90)], which tries to align the magnetization parallel to the applied field, contributes to the total free energy. Hence, by applying a magnetic field, the domain structure within a sample can be modified due to the contribution of the Zeeman energy, which depends on the strength and direction of the external magnetic field. The magnetization process of ferro- and ferrimagnets

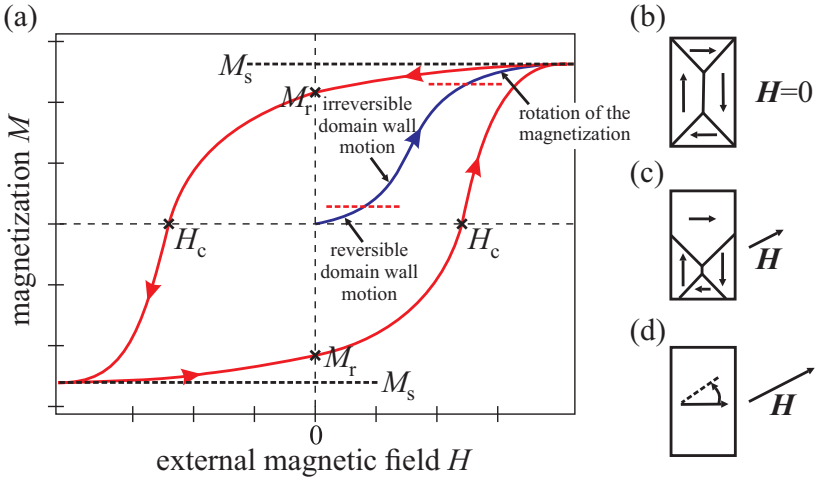

Fig. 2.32: (a) Typical magnetization curve of a ferro(i)magnet. The initial magnetization curve is plotted in blue and the subsequent magnetization curve in red. (b)-(d) Schematical depiction of the changes in the domain structure depending on the external magnetic field $\boldsymbol{H}$. Adapted from Ref. [40].

can therefore be related to the changing domain structure during magnetization, which can be characterized by the so-called magnetization or M vs H curve, as depicted in Fig. 2.32.

Applying an external magnetic field to the ferro- or ferrimagnetic material, in particular in the initial magnetization process [indicated by a blue line in Fig. 2.32(a)], results in a motion of the domain walls, whereas the magnetizations of the domains are aligned along the magnetic easy axes. The domain wall motion is reversible for very low fields, but becomes irreversible, if the magnetic field is further increased and therefore results in a growth of domains with magnetization directions favored for the direction of the external magnetic field and in a shrinking of domains with unfavored magnetization orientations [cf. Figs. 2.32(b)-(c)]. This in turn reduces the number of domains, until the magnetic field is high enough to create completely parallel spin alignment within the material. By applying even higher fields, the magnetization of this monodomain state can still be rotated towards the external field [cf. Fig. 2.32(d)], resulting in a completely saturated alignment of magnetic moments parallel to the applied magnetic field, indicated by reaching the saturation magnetization M_s in the magnetization curve.

If the magnetic field is removed after reaching M_s, ferro- and ferrimagnetic materials still exhibit a non-vanishing overall magnetization projected to the direction of the earlier applied magnetic field. This remanent magnetization is indicated by M_r in the magnetization curve and can be removed by applying a magnetic field in the opposite direction until the coercive field H_c is reached. If the external field is further increased in the reversed direction, a monodomain state with parallel alignment to the applied field is created again and the opposed magnetic saturation is reached. The second part of the magnetization curve is the same process as from one saturation magnetization to the opposed one, but only in reversed direction.

The resulting hysteresis curve is characteristic for ferro- and ferrimagnetic material. If this material exhibits large coercive fields, its magnetization direction can only be reversed by large magnetic fields, which justifies its denotation as a hard magnetic substance. In contrast, the magnetization of a soft magnetic material is reversed quite easily, as it exhibits comparably small coercive fields. The anisotropy of the investigated sample and, thus, its orientation to the applied magnetic field also influences the shape of the magnetization curve due to favored magnetization in easy direction and harder processes of magnetization in magnetic unfavored directions. Furthermore, the domain wall motion can be significantly influenced by the existence of imhomogeneities in the crystal, such as structural defects, impurities or vacancies. These defects can act as pinning centers for domain walls and therefore hinder their motion during the magnetization process [93]. As a consequence, the shape of the magnetization curve also strongly depends on the type and density of inhomogeneities within the investigated material.

3 Investigated materials

Within this work, $NiFe_2O_4$ thin films were prepared on single crystalline MgO(001) and $SrTiO_3$(001) substrates via reactive molecular beam epitaxy by co-evaporation of the transition metals Ni and Fe in a molecular oxygen atmosphere. Further, $CoFe_2O_4$ thin films were prepared via thermally induced interdiffusion of initial Fe_3O_4/CoO bilayers on $SrTiO_3$(001). Hence, the properties of both substrate (MgO, $SrTiO_3$) and film materials (CoO, Fe_3O_4, $NiFe_2O_4$, $CoFe_2O_4$) are presented in the following.

3.1 Substrate material

3.1.1 Magnesium oxide - MgO

Magnesium oxide (MgO) crystallizes in the so-called rock salt structure with a bulk lattice constant of $a_{\mathrm{MgO}} = 4.2117$ Å at room temperature [102]. The crystal structure is given by two face-centered cubic (fcc) sublattices each containing solely either Mg^{2+} or O^{2-} ions, respectively. Both sublattices are shifted by half a lattice constant along one cubic lattice vector with respect to another (cf. Fig. 3.1). Hence, the Mg^{2+} cations are located at the octahedral sites of the fcc sublattice formed by the O^{2-} anions and vice versa. Within this work, single crystalline MgO substrates with a (001) surface orientation are used. For the respective MgO(001) surface, a primitive surface unit cell can be defined, which exhibits its lateral lattice vectors along the [110] and [$\bar{1}$10] bulk directions with a surface lattice constant given by $a^{\mathrm{s}}_{\mathrm{MgO}} = a_{\mathrm{MgO}}/\sqrt{2}$. The resulting square surface unit cell is rotated laterally by 45° with respect to the bulk unit cell. Further, MgO is diamagnetic at room temperature and insulating with a band gap of ∼7.8 eV [103, 104].

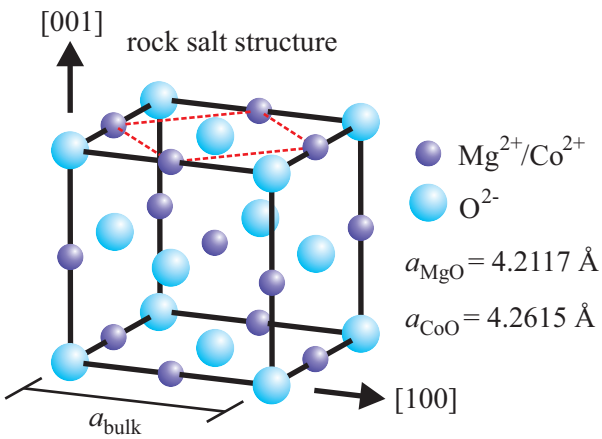

Fig. 3.1: Sketch of a rock salt type unit cell consisting of two face-centered cubic sublattices shifted by half a lattice constant a_{bulk} in one cubic lattice direction with respect to each other. One sublattice is occupied by O^{2-} anions, whereas the second fcc sublattice is occupied by Mg^{2+} or Co^{2+} for MgO or CoO, respectively. The bulk lattice constants a_{bulk} of MgO and CoO are denoted as a_{MgO} and a_{CoO}, respectively. The primitive surface unit cell, marked by the red dashed line, is laterally rotated by 45° with respect to the bulk unit cell.

3.1.2 Strontium titanate - $SrTiO_3$

At room temperature, $SrTiO_3$ (STO) crystallizes in the cubic perovskite structure (cf. Fig. 3.2) with a bulk lattice constant of $a_{\mathrm{STO}} = 3.905$ Å [105]. The crystal structure consists of Ti^{4+} cations octahedrally coordinated by six O^{2-} anions and of Sr^{2+} cations each surrounded by twelve O^{2-}

anions as nearest neighboring atoms. Thus, one Sr^{2+} cation is surrounded by eight TiO_6 octahedra. In this work, single crystalline STO substrates with solely (001) surface orientation are used. As in [001] direction the lattice exhibits alternating TiO_2 and SrO monolayers both separated by half a lattice constant, the (001) surface can either be TiO_2- or SrO-terminated. However, the surface unit cell with lattice vectors pointing in [100] and [010] directions exhibits the same size and orientation as the lateral components of the bulk unit cell independent of the surface termination.
Stoichiometric $SrTiO_3$ is a diamagnetic and insulating material with a band gap of ~3.2 eV [106]. However, the magnetic and electronic properties can be tuned either by varying the stoichiometry, i.e., via oxygen vacancies, or by doping the crystal, whereas the latter allows for a more controlled variation of the electronic structure. Thus, in this work, the used $SrTiO_3$ crystals are doped with 0.05wt% Nb (n-type doping) to obtain a still diamagnetic but more conductive substrate material without crucially affecting the crystal structure and composition. With this, charge effects as obtained for insulating support materials in the applied measurement techniques, i.e., in LEED, XPS/HAXPES, and XAS, are prevented.

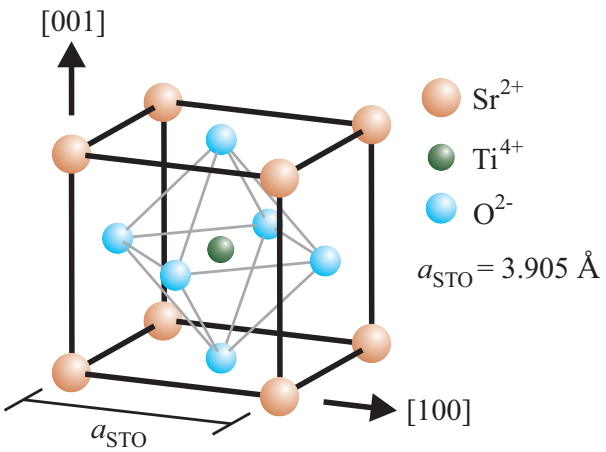

Fig. 3.2: Sketch of the $SrTiO_3$ unit cell crystallizing in the cubic perovskite structure. Each Ti^{4+} cation is octahedrally coordinated (gray lines) by six O^{2-} anions, whereas each Sr^{2+} cation is surrounded by twelve nearest neighboring O^{2-} anions. The bulk lattice constant is denoted as a_{STO}. For (001) surface orientation, the terminating layer can either be a TiO_2 or a SrO monolayer, both separated by half a lattice constant in [001] direction.

3.2 Film material

3.2.1 Cobalt(II) oxide - CoO

Cobalt(II) oxide (CoO) is a transition metal oxide crystallizing, similar to MgO, in the rock salt structure (cf. Fig. 3.1) with a lattice constant of $a_{CoO} = 4.2615$ Å at room temperature [107]. Hence, CoO consists of two fcc sublattices each containing either solely O^{2-} anions or solely Co^{2+} cations, respectively, which are both shifted by half a lattice constant in one cubic lattice direction with respect to each other. Further, for a (001) surface orientation a surface unit cell can be defined, which is rotated by 45° with respect to the bulk unit cell and exhibits a lateral lattice constant of $a^{s}_{CoO} = a_{CoO}/\sqrt{2}$ (cf. Fig. 3.1). CoO is electrically insulating with a band gap of ~2.7 eV [108] and paramagnetic at room temperature. However, below a Néel temperature of around $T_N \simeq 293$ K [109, 110] collective magnetic ordering occurs and CoO becomes antiferromagnetic.

3.2.2 Magnetite - Fe_3O_4

Magnetite (Fe_3O_4) crystallizes in the so-called cubic inverse spinel structure (cf. Fig. 3.3) with a bulk lattice constant of $a_{Fe_3O_4} = 8.396$ Å [111]. The bulk unit cell consists of eight formula units (f.u.) and therefore exhibits 32 O^{2-} anions and 24 Fe cations, which can further be subdivided into eight Fe^{2+} and 16 Fe^{3+} cations. While the O^{2-} anions form an fcc lattice, the Fe cations occupy

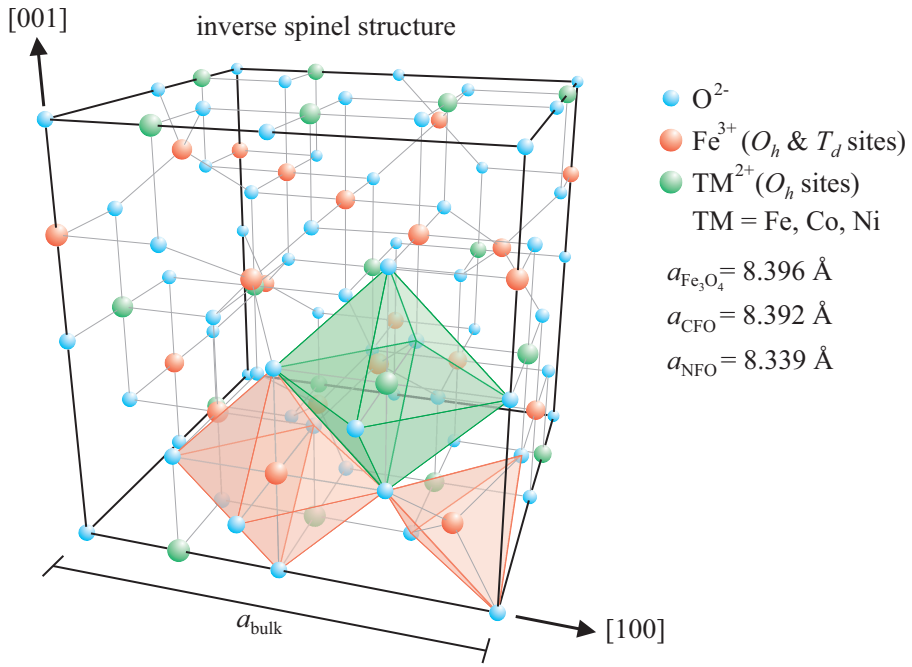

Fig. 3.3: Sketch of the inverse spinel structure as it can be found for several transition metal ferrites with, such as, e.g., Fe_3O_4, $CoFe_2O_4$, and $NiFe_2O_4$. In magnetite, the Fe^{3+} cations are distributed equally across tetrahedral (T_d) and octahedral sites (O_h), while Fe^{2+} cations occupy only O_h sites. For cobalt ferrite (CFO) and nickel ferrite (NFO) the Fe^{2+} cations are replaced by Co^{2+} or Ni^{2+}, respectively. The lattice constants $a_{Fe_3O_4}$, a_{CFO}, and a_{NFO} are the bulk lattice constants of the respective material marked by a_{bulk}.

one eighth of tetrahedral (T_d) and one half of octahedral interstitial lattice sites (O_h) within this oxygen fcc sublattice. For the case of the inverse spinel structure in Fe_3O_4, the Fe^{2+} cations are solely octahedrally coordinated by O^{2-} anions, whereas the Fe^{3+} cations occupy O_h and T_d sites to the same extent. Further, considering an $Fe_3O_4(001)$ surface orientation, a surface unit cell with a lattice constant of $a^{s}_{Fe_3O_4} = a_{Fe_3O_4}/\sqrt{2}$ can be defined, which is laterally rotated by 45° with respect to the bulk unit cell, as the axes of the surface unit cell are aligned in [110] and [$\bar{1}$10] bulk directions, respectively.
Moreover, Fe_3O_4 is half-metallic and ferrimagnetic with a Curie temperature of $T_C = 850\,K$ [111]. The half-metallicity of Fe_3O_4 results from a predicted total negative spin polarization at the Fermi level [9, 112], which leads to only small electric conductivity at room temperature. More details about the electronic structure and the magnetic interactions in magnetite are described in Secs. 3.2.5 and 3.2.6, respectively.
In contrast to the inverse spinel structure as introduced above for the case of Fe_3O_4, in a normal spinel structure, only the divalent cations occupy tetrahedral sites, whereas the trivalent cations are solely distributed among the octahedral lattice sites. In fact, although the investigated ferrites in this work (Fe_3O_4, $CoFe_2O_4$, $NiFe_2O_4$, see below) should all crystallize in the inverse spinel structure, also intermediate configurations between a normal and an inverse spinel structure can occur. A quantitative parameter to characterize the respective cationic configuration is given by the degree of inversion γ, which can be defined as the fraction of divalent cations occupying octahedral lattice sites. The cationic order of transition metal ferrites is then given by

$$[TM^{2+}_{1-\gamma}Fe^{3+}_{\gamma}]_{T_d}[TM^{2+}_{\gamma}Fe^{3+}_{2-\gamma}]_{O_h}O_4 \ , \tag{3.1}$$

where TM denotes the respective transition metal (Fe, Co, Ni, etc.), while the first brackets account for tetrahedral and the second brackets for octahedral site occupancy. Hence, γ can attain values between $\gamma = 0$ for a normal spinel and $\gamma = 1$ for a completely inverse spinel structure and can serve as a quantitative estimation of the cationic order in transition metal ferrites.

3.2.3 Cobalt ferrite - $CoFe_2O_4$

Similar to magnetite, cobalt ferrite (CFO) also crystallizes in the cubic inverse spinel structure (cf. Fig. 3.3) with a bulk lattice constant of $a_{\mathrm{CFO}} = 8.392\,\text{Å}$ at room temperature [113]. The bulk unit cell also contains 32 O^{2-} anions forming an fcc sublattice, 16 Fe^{3+} cations equally distributed at O_h and T_d sites, and eight Co^{2+} cations solely occupying octahedral sites. Thus, compared to Fe_3O_4, the Fe^{2+} cations that are octahedrally coordinated by O^{2-} anions of the fcc oxygen sublattice are completely replaced Co^{2+} cations in ideal and stoichiometric $CoFe_2O_4$. Similar to Fe_3O_4, a smaller surface unit cell with a lattice parameter of $a^{\mathrm{s}}_{\mathrm{CFO}} = a_{\mathrm{CFO}}/\sqrt{2}$ can be defined, which is laterally rotated by 45° with respect to the bulk unit cell. In addition, CFO is ferrimagnetic with a Curie temperature of $\mathrm{T_C} = 790\,\mathrm{K}$ [14] and exhibits insulating character with a theoretically predicted band gap of ∼0.8 eV [112]. A detailed description of the electronic structure and magnetic interactions in CFO is given in Secs. 3.2.5 and 3.2.6, respectively.

3.2.4 Nickel ferrite - $NiFe_2O_4$

Analogous to Fe_3O_4 and $CoFe_2O_4$, nickel ferrite (NFO) also crystallizes in the cubic inverse spinel structure as depicted in Fig. 3.3 and exhibits a bulk lattice constant of $a_{\mathrm{NFO}} = 8.339\,\text{Å}$ at room temperature [114]. Hence, the $NiFe_2O_4$ bulk unit cell consists of 16 Fe^{3+} cations, which are equally distributed among O_h and T_d sites and of eight Ni^{2+} cations, which occupy solely O_h lattice sites within the fcc oxygen sublattice, which is formed by 32 O^{2-} anions. Still, the surface unit cell with a surface lattice constant of $a^{\mathrm{s}}_{\mathrm{NFO}} = a_{\mathrm{NFO}}/\sqrt{2}$ can be defined as rotated laterally by 45° towards the bulk unit cell with its lateral surface unit cell axes pointing in [110] and [$\bar{1}$10] bulk directions, respectively. Further, NFO is ferrimagnetic with a Curie temperature of around $\mathrm{T_C} = 865\,\mathrm{K}$ [14] and has insulating character with a theoretically predicted band gap of ∼1.0 eV [112, 115]. In the following Secs. 3.2.5 and 3.2.6 a more detailed description of the electronic structure and magnetic interactions is given.

3.2.5 Electronic structure of ferrites

Extensive theroetical calculations of the electronic structure of ferrites based on density functional theory (DFT) can be found in literature [9, 112, 115–121]. A promising approach for, i.e., Fe_3O_4, CFO, and NFO is the self-interaction corrected local spin density (SIC-LSD) approximation, as applied by Szotek *et al.* [112, 118]. The respective predicted electronic structures for Fe_3O_4, CFO, and NFO are depicted in Fig. 3.4. Here, the total density of states (DOS) is calculated for both spin-up (majority) and spin-down (minority) orientations in the energy region close to the Fermi level E_{F}. The oxygen contribution to the DOS is depicted additionally.
The ground state of each investigated ferrite was found to be the inverse spinel structure. However, the ground state of Fe_3O_4 was achieved by additionally assuming a delocalization of the sixth d electron of the original Fe^{2+} cations within the inverse spinel structure, which therefore can be regarded as randomly populating the O_h sites occupied by only Fe^{3+} cations [112]. As a consequence, a finite DOS at the Fermi level solely in the minority spin channel is observed [cf. Fig. 3.4(a)], constituting the half-metallic character of Fe_3O_4.
In contrast to Fe_3O_4, a band gap is observed between the valence and conduction bands of NFO

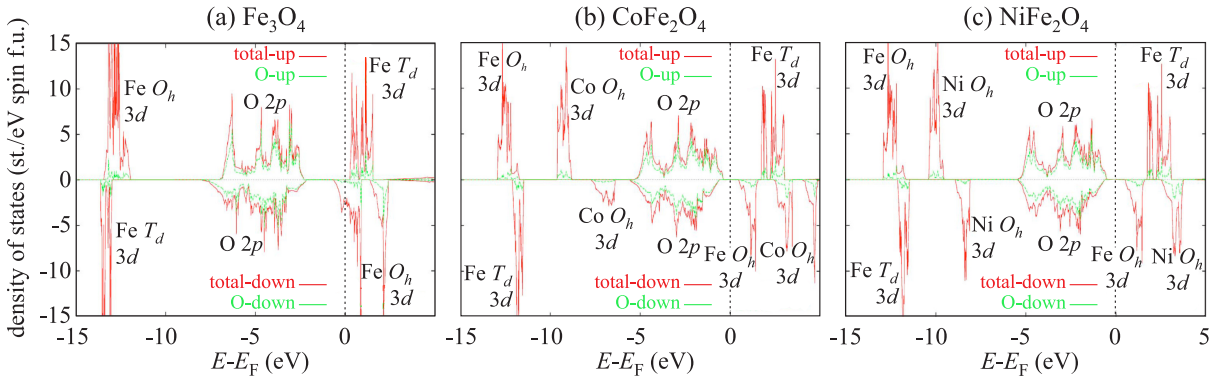

Fig. 3.4: Calculated spin-dependent density of states (DOS) of the cubic inverse spinels (a) Fe_3O_4, (b) $CoFe_2O_4$, and (c) $NiFe_2O_4$. The majority DOS (spin-up) is shown in the upper part, whereas the minority DOS (spin-down) is depicted in the lower half. The different bands are denoted by their main contributing atomic species and site occupancies (T_d or O_h lattice sites). The total and the oxygen DOS are given by the red and green lines, respectively. The Fermi level is marked by a dashed line. Adapted from Ref. [112].

and CFO, respectively [cf. Figs. 3.4(b) and 3.4(c)]. Further, it becomes evident that the valence bands of CFO and NFO mostly consist of O 2p states. This property results from a strong Coulomb repulsion U [cf. Eq. (2.88)] between TM 3d electrons, which in turn gives rise to a large separation of the occupied and unoccupied 3d states, shifting the occupied TM 3d states below the O 2p levels. Thus, mainly O 2p levels represent the highest occupied states forming the valence band, whereas the lowest unoccupied states in the majority (minority) spin channel slightly above the Fermi level are Fe 3d levels in tetrahedral (octahedral) symmetry. This behavior characterizes the investigated cobalt and nickel ferrites as so-called charge-transfer (CT) insulators, as the minimal energy needed for a transition between occupied and unoccupied states is correlated to the energy difference between filled O 2p and empty TM 3d states.
Moreover, the conduction bands of CFO and NFO both exhibit a significant exchange splitting between the two spin channels, which is characterized by the energy differences between the minority (spin-down) and majority (spin-up) states. For CFO, an exchange splitting in the conduction band [comparing the energy minima of spin-up and spin-down states for $E - E_F > 0$, cf. Fig. 3.4(b)] of 1.28 eV is obtained, whereas NFO exhibits an exchange splitting of 1.21 eV [cf. Fig. 3.4(c)] [112]. This splitting between the two spin channels in the conduction band make the investigated cobalt and nickel ferrites highly suitable for spin-filter applications.

3.2.6 Magnetism of ferrites

The ferrimagnetic behavior of Fe_3O_4, $CoFe_2O_4$, and $NiFe_2O_4$ originates from the competition of a couple of O^{2-} mediated exchange interactions of the TM cations within the inverse spinel ferrite unit cell (cf. Fig. 3.5). For magnetite, a theoretical approximation of the exchange constants J for the superexchange interactions between nearest cationic neighbors has been described by Uhl and Siberchicot [122]. Here, the strongest coupling was calculated to arise from the superexchange interactions between Fe^{3+} cations on tetra- (A) and octahedral (B) sites [cf. Fig. 3.5(a)]. The exchange is mediated by an overlap of the Fe 3d orbitals with the intermediate O 2p orbitals in an angle of $\sim$125°. According to the Goodenough-Kanamori-Anderson rules (cf. Sec. 2.8.2) this results in a strongly antiferromagnetic (AFM) exchange interaction between Fe^{3+} cations on tetra- and octahedral sites, giving the highest absolute superexchange constant of $J_{AB} = -2.88$ meV for magnetite. Note that negative signs of exchange constants are related to AFM coupling, whereas

positive values accord to ferromagnetic (FM) coupling. In addition to the intersublattice A-B exchange interactions, FM Fe^{3+}-Fe^{3+} and FM Fe^{2+}-Fe^{2+} coupling both located solely on octahedral lattice sites is stabilized via 90° intrasublattice superexchange interaction with an exchange constant $J_{\mathrm{BB}} = 0.83$ meV [cf. Fig. 3.5(b)]. According to the calculations applied by Uhl and Siberchicot, the weakest superexchange interaction in Fe_3O_4 is the AFM intrasublattice superexchange interaction among tetrahedral sites with an exchange constant $J_{\mathrm{AA}} = -0.18$ meV. Due to the small absolute value of J_{AA}, this interaction is masked by the other A-B and B-B superexchange interactions and antiferromagnetic alignment of A sites is therefore usually suppressed. Moreover, FM double-exchange (exchange constant J_{de}) occurs between octahedrally coordinated Fe^{3+} and Fe^{2+} cations [cf. Fig. 3.5(c)], which, however, is usually weaker than the dominant superexchange interactions: $|J_{\mathrm{de}}| < |J_{\mathrm{AB}}|, |J_{\mathrm{BB}}|$.
Due to the same crystal structure of $CoFe_2O_4$ and $NiFe_2O_4$ compared to Fe_3O_4, also the same exchange interactions occur and similar exchange constants J are assumed. Though, an exact determination of the exchange constants in the inverse spinel ferrites Fe_3O_4, CFO, and NFO as proposed in literature is still controversial [122–132]. Based on the assumptions made for theoretical predictions [122–127] or dependent on experimental preparation conditions as well as measurement and analysis methods [128–132], significant discrepancies in the exchange constants are established. However, independent of the used theoretical or experimental method, the AFM intersublattice superexchange interaction between Fe^{3+} cations located on A and B sites is always dominant for the investigated ferrites Fe_3O_4, $CoFe_2O_4$, and $NiFe_2O_4$.
Overall, the mentioned exchange interactions result in ferrimagnetic ordering of all investigated transition metal ferrites. The Fe^{3+} cations consist of five unpaired electrons in the $3d$ shell and therefore each Fe^{3+} cation exhibits an atomic magnetic moment of 5 μ_B/atom (considering solely spin magnetic moments and neglecting the comparably small contributions from angular magnetic moments), with $\mu_B = e\hbar/(2m_e)$ as the Bohr magneton. Due to the dominating antiferromagnetic A-B superexchange interactions the atomic magnetic moments of Fe^{3+} cations, which are equally distributed among O_h and T_d sites, cancel out due to antiparallel alignment and do not contribute to the overall net magnetic moment. Thus, solely the TM^{2+} cations are responsible for the net magnetization of each inverse spinel ferrite. In Fe_3O_4, the Fe^{2+} cations exhibit four unpaired $3d$ electrons, resulting in a total net magnetization of 4 μ_B/f.u. In contrast, Co^{2+} and Ni^{2+} cations each exhibit one and two unpaired electrons less than Fe^{2+} in the $3d$ shell, resulting in predicted net magnetizations of 3 μ_B/f.u. and 2 μ_B/f.u. for ideal bulk CFO and NFO, respectively.

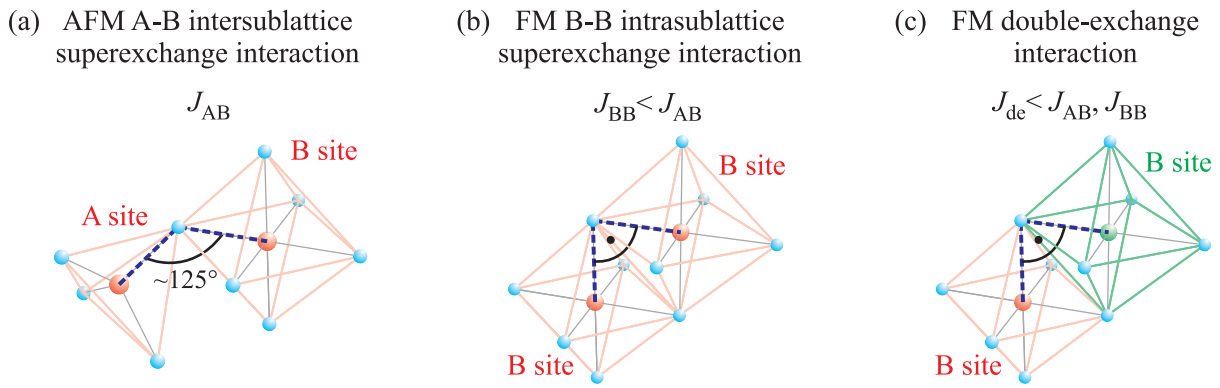

Fig. 3.5: Principal sketch of the dominant exchange interactions in transition metal ferrites: (a) AFM intersublattice superexchange interaction between Fe^{3+} cations located on tetrahedral (A) and octahedral (B) sites. (b) FM intrasublattice superexchange either between Fe^{3+} or between TM^{2+} cations located solely on B sites. (c) FM double-exchange interaction between Fe^{3+} and TM^{2+} cations each occupying B sites. Adapted from [63].

3.2.7 Antiphase boundaries in ferrites

Antiphase domains within a crystal denote structurally and chemically equal domains, which are shifted by a non-integer fraction of the respective lattice constant with respect to another. Thus, upon coalescence of antiphase domains so-called antiphase boundaries (APBs) emerge, which are characterized by a translational break in the periodicity of the lattice. On the one hand, APBs can occur when ordering of a disordered lattice starts at different lattice sites, so that APBs can evolve upon merging of the different ordered domains. On the other hand, APBs are commonly formed during film growth when the initial nucleation centers are located by non-integer multiples of the film lattice constant apart from each other. Then, APBs are formed upon merging of the respective initial film islands/layers, as the domains are shifted by only a fraction of the film lattice constant with respect to each other (cf. Fig. 3.6). The latter process commonly occurs for inverse spinel ferrites such as Fe_3O_4, CFO, or NFO deposited on MgO or $SrTiO_3$ substrates [15, 133–140], as the film lattice constants are approximately twice as large as the substrate lattice constants. In several detailed studies, it could be shown that the density of APBs crucially influences, e.g., the magnetic behavior [15, 133–135, 140–142], the magnetoresistance [143–145], and the electrical conductivity of ferrites [137, 146]. For instance, the magnetic properties are influenced due to altered exchange interactions across the APBs [133, 136], which can result, e.g., in decreased saturation magnetizations compared to ideal bulk structures [147] or in extremely high magnetic fields required for magnetic saturation due to antiferromagnetic alignment of adjacent antiphase domains [15, 133, 142]. Further, APBs are ascribed to additional strain components in heteroepitaxial film growth and, thus, are assumed to have significant impact on the relaxation behavior of, i.e., thin ferrite films [139, 148]. A reduction of the APB density of ferrite films deposited on MgO or $SrTiO_3$ substrates can be achieved by, e.g., postdeposition annealing [138]. Moreover, it is found that the density of APBs decreases with increasing ferrite film thickness [138, 149].

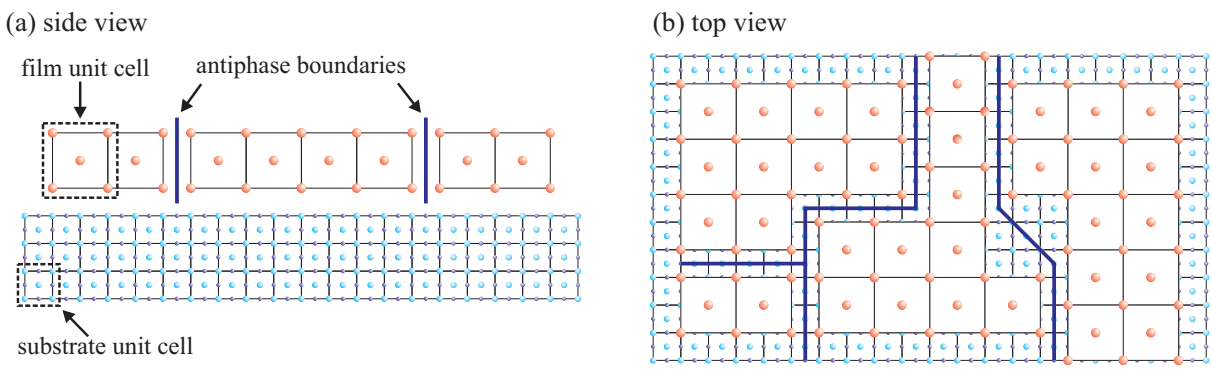

Fig. 3.6: (a) Side view and (b) top view of antiphase boundaries (APBs) emerging during thin film growth when the film lattice constant is twice as large as the lattice constant of the substrate.

4 Experimental setups

Within this chapter, the experimental methods and their respective setups used for the preparation and characterization of thin ferrite films are presented. First, the method of thin film preparation is introduced followed by the description of the laboratory based LEED and XPS setups. Further, the experimental setups of synchrotron radiation based characterization techniques, namely (GI)XRD, XRR, HAXPES, and XAS are presented. Finally, the magnetic characterization by means of superconducting quantum interference device (SQUID) magnetometry is described.

4.1 Sample preparation

Most of the thin films investigated in this work were prepared in a multi-chamber UHV system at Osnabrück University, Germany. This system consists of several interconnected single UHV chambers, allowing for sample transfer between each other without breaking the UHV. A small load lock chamber is used to introduce or extract samples into/from the UHV system. From the load lock, the samples can be transferred to the preparation chamber, which exhibits a base pressure of around 1×10^{-9} mbar. This chamber is used for substrate preparation after loading the samples from ambient conditions into UHV and for thin film deposition onto the prepared substrates. It comprises a rotary manipulator with a heating element attached closely to the sample stage. Here, heating is realized by setting a current through a filament, which is located directly behind the sample holder to anneal the samples up to 450°C. By additionally applying a high voltage between filament and sample holder, thus, accelerating the emitted electrons to the back of the sample holder, even higher temperatures of over 600°C could be achieved. The sample temperature is monitored by a thermocouple located at the sample stage directly next to the sample holder. Further, the preparation chamber is equipped with several thermal evaporation sources (effusion cells) and an O_2 valve, enabling substrate preparation and thin film deposition in a diluted molecular oxygen atmosphere. Moreover, the multi-chamber UHV system consists of an analysis chamber, which is equipped with a LEED and an XPS system. The setups of both measurement techniques are described in more detail in Secs. 4.2.1 and 4.2.2, respectively. The base pressure in the analysis chamber is 1×10^{-10} mbar.
The thin ferrite films investigated in this work were deposited via molecular beam epitaxy (MBE), which is a physical vapor deposition (PVD) technique. For this purpose, the respective transition metals (Fe, Co, Ni) were evaporated in effusion cells, enabling thermal evaporation from pure metal rods. Fig. 4.1 schematically depicts the design of the used effusion cells. Within these evaporators, electrons emitted by a filament are accelerated towards the pure metal rod by applying high voltage between filament and metal rod. If the sublimation temperature of the respective transition metal is reached, the emitted atoms or molecules are travelling through the aperture of the evaporator, forming a molecular beam directed towards the sample surface. The effusion cell body, in particular the copper cell surrounding the sublimating material, is cooled via a water supply during the evaporation process to avoid overheating and to minimize degassing. Further, a shutter at the end of the evaporator is used to start and end the deposition process at a certain point in time, while the amount of evaporated material is recorded by a flux monitor. Here, the deposition rates of each evaporating material are determined via *ex situ* film thickness measurements by means of XRR. For deposition of oxide films, as conducted in this work, the evaporation process is performed in

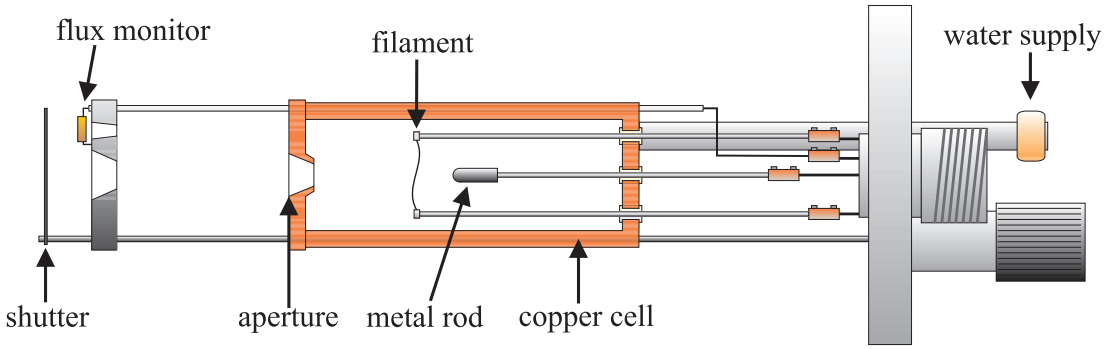

Fig. 4.1: Schematical side view of the used evaporators. The pure metal rod (Fe, Co, or Ni) is heated by electrons emitted from a filament and accelerated towards the metal by high voltage. The sublimated atoms/molecules escape from the effusion cell through an aperture and form a molecular beam directed towards the sample surface. A shutter starts and ends the deposition process, whereas the flux monitor is used to determine the amount of evaporated material. Water cooling prevents the effusion cell body (copper cell) to overheat and degas. Adapted from [150].

a diluted O_2 atmosphere to obtain oxidized films condensing on the substrate surface. Thus, the deposition process is called reactive molecular beam epitaxy (RMBE). Moreover, NFO films are prepared by simultaneously co-evaporating each pure metal (Fe and Ni) and by tuning the respective material flux to obtain the desired cationic stoichiometry. In order to prepare homogeneous high-quality thin films with specific stoichiometry and a well-defined crystallographic orientation with respect to the substrate, the deposition conditions, as, e.g., substrate temperature, oxygen pressure, deposition rates, etc., have to be controlled precisely.
Both types of substrates, namely MgO(001) and 0.05wt% Nb-doped $SrTiO_3$(001), were purchased from CrysTec GmbH. The surface orientation tolerance is mostly less than 0.1°, which was controlled via atomic force microscopy (AFM) measurements by the manufacturer. After introducing into UHV, the substrates have been annealed at 400°C for one hour in a molecular oxygen atmosphere of 1×10^{-4} mbar to remove surface contaminations and get a well-ordered surface structure. Both, the chemical cleanness and the crystal surface structure were both controlled *in situ* after substrate preparation by means of XPS and LEED, respectively. A successful substrate preparation was characterized by XPS spectra showing a stoichiometric composition of the substrate elements and an absence of other elemental quantities such as, i.e., carbon compounds. In addition, a well-ordered surface structure of the prepared substrates were determined by sharp diffraction spots with low background intensity in the LEED pattern. Then, thin films were grown on top of the prepared substrate surface. For the deposition of thin Fe_3O_4 and NFO films on MgO(001) and $SrTiO_3$(001), a sample temperature of 250°C and a molecular oxygen pressure of 5×10^{-6} mbar was used. These growth conditions have been reported to be best suited for well-ordered epitaxial growth of Fe_3O_4 thin films on MgO(001) by means of RMBE [151], while Mg diffusion into the ferrite film, as reported for higher substrate temperatures [152,153], is still suppressed. In contrast, for the deposition of Fe_3O_4/CoO bilayers on $SrTiO_3$(001), which are grown for the preparation of CFO films by interdiffusing both layers, different growth conditions for each of both films have been established [154]. Here, optimal growth conditions were found at 435°C substrate temperature in an O_2 atmosphere of 1×10^{-5} mbar for the thin CoO films on $SrTiO_3$, whereas the Fe_3O_4 film was deposited on top of the CoO film at a sample temperature of 350°C and in a molecular oxygen pressure of 5×10^{-6} mbar [154]. After film deposition, *in situ* XPS and LEED measurements were again performed to analyze the surface stoichiometry and structure, respectively.

4.2 Surface characterization

4.2.1 LEED - Experimental setup

LEED measurements were conducted in the analysis chamber with a 4-grid LEED optics (ErLEED 150, SPECS, Berlin). This LEED system is schematically depicted in Fig. 4.2. It consists of an electron gun, the sample holder with the sample under investigation, and a hemispherical fluorescent screen with four grids, allowing for detection of elastically scattered electrons.
The electron gun consists of a cathode filament, followed by a Wehnelt cylinder, an anode, an electrostatic lens, and a drift tube. The electrons emitted by the filament are accelerated towards the anode, passing the Wehnelt cylinder, which regulates the penetration of the anode potential towards the cathode and can therefore be used to narrow/optimize the beam size. After passing the anode, the electrons go through the electrostatic lens (and the drift tube), which is used to collimate and focus the electron beam onto the fluorescent screen (while the sample acts as a mirror). The electrons scattered at the sample surface pass a 4-grid system before they are detected on a fluorescent screen. All grids and the screen are hemispherically shaped around their center position, where the sample is located. As the first grid as well as the sample itself and the drift tube of the electron gun are set to ground potential, the electrons propagate in a field-free space after leaving the electron gun and being scattered at the sample surface until they pass the first hemispherical grid. The second and third grid are set to a suppressor potential -(V-ΔV), which is slightly lower in magnitude than the cathode potential -V. Therefore, the electrons are retarded and inelastically scattered electrons, which lost more energy than the potential difference ΔV, are filtered. Thus, by optimizing the suppressor voltage, only elastically scattered electrons pass the second and third grids to obtain an ideal spot-to-background ratio in the LEED pattern. The fourth grid is set to ground potential to screen the other grids from the field of the fluorescent screen, which is biased to a high voltage of typically 6 kV to reaccelerate the elastically scattered electrons and cause fluorescence on the screen. The resulting diffraction pattern is recorded by a camera located on the rear side of the screen system behind the electron gun.

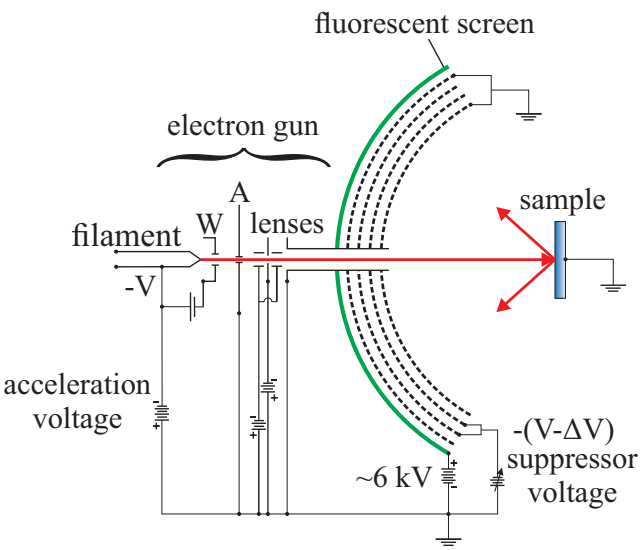

Fig. 4.2: Principle sketch of a 4-grid LEED system with an electron gun consisting of an electron emitting filament, followed by a Wehnelt cylinder (W), an anode (A), and an electrostatic lens system collimating the electron beam. The electrons scattered at the sample surface pass a system of four grids, which suppresses inelastically scattered electrons and accelerates elastically scattered electrons onto the fluorescent screen. Adapted from [38].

4.2.2 XPS - Experimental setup

The basic experimental setup of the used XPS system, as depicted in Fig. 4.3, consists of an x-ray source, electron optics, an energy discriminative hemispherical analyzer (Phoibos HSA 150, SPECS,

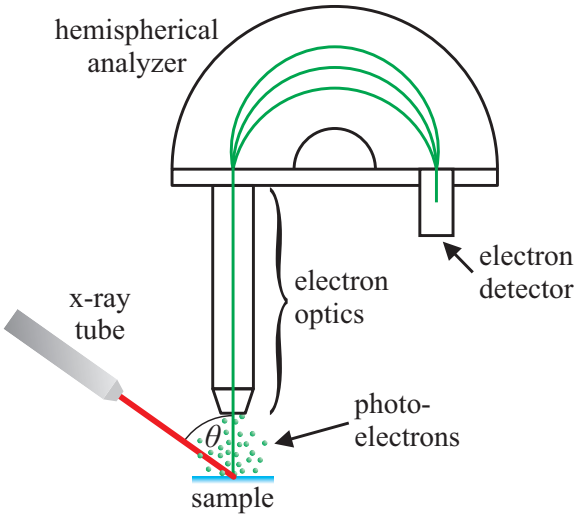

Fig. 4.3: Principle sketch of the used XPS system consisting of an x-ray source directed to the sample, electron optics, a hemispherical analyzer, and an electron detector. X-ray source and entrance to the electron optics enclose a fixed angle θ. The photoelectrons ejected from the sample due to irradiation by x-rays enter the electron optics, which involves electrostatic and magnetic lenses and apertures to focus and retard the electrons. Within the hemispherical analyzer the entering electrons are forced on a spherical trajectory by an electrostatic field and only electrons of a certain pass energy can reach the detector. Adapted from [50].

Berlin), and an electron detector. The x-ray tube is equipped with two anodes, one Al and one Mg anode, providing photon energies of $E_{\mathrm{ph}}(\mathrm{Al\ K}\alpha_{1,2}) = 1486.6$ eV and $E_{\mathrm{ph}}(\mathrm{Mg\ K}\alpha_{1,2}) = 1253.6$ eV, respectively. The photoelectrons emitted from the sample due to irradiation by the x-ray beam exhibit a large range of kinetic energies and directions. As the entrance of the electron optics encloses a fixed angle θ with the x-ray beam, only photoelectrons ejected in this direction can be collected. For the used setup, this angle equals the magic angle of $\theta = 54.7°$ (cf. Sec. 2.5.4). The electron optics section consists of several magnetic and electrostatic lenses and apertures, which mainly focus the collected photoelectrons onto the entrance of the hemispherical analyzer but also reduce their kinetic energy to an energy window characterized by the pass energy within the operation mode of fixed analyzer transmission (see below). Within the analyzer, an electrostatic field is applied between the inner and outer hemispherical analyzer plates to force the electron beam on predefined trajectories. Thus, only electrons with a certain energy can pass the analyzer and reach the electron detector at its exit. The detector itself consists of several channel electron multipliers (CEMs), which are arranged next to each other as a single block.
In general, the XPS system can be operated in two different modes. In this work, solely the so-called fixed analyzer transmission (FAT) mode is used. Here, the kinetic energy of the photoelectrons are all reduced to a pass energy window E_{p} before entering the hemispherical analyzer by tuning the retarding potential within the electron optics. In addition, the pass energy of the analyzer itself is fixed to a certain value, hence, ensuring a constant energy resolution independent of the kinetic energy of the photoelectrons. Further, setting the pass energy to a lower value increases the absolute energy resolution of the spectra but reduces the intensity of the XPS signal. In contrast, a higher pass energy decreases the energetic resolution but enhances the intensity-to-background ratio. The second mode of operation is the fixed retarding ratio (FRR) mode of the XPS system. In contrast to the FAT mode, the retarding ratio of the lens system is kept constant, while the pass energy of the analyzer is varied. Thus, electrons with different kinetic energies reach the detector. As a consequence, the resolution also varies with kinetic energy. This mode, however, is typically used to record Auger electron spectra (AES).

4.3 Experimental setups at synchrotron radiation facilities

Compared to laboratory based x-ray sources, synchrotron light exhibits several advantages, such as higher intensities, smaller divergence and beam sizes, as well as tunable photon energies. Thus, the use of synchrotron radiation enables high resolution measurements and even opens up a wider

range of experimental techniques, in particular, for the investigation of (ultra)thin films. Thus, several measurement techniques within this work were applied by using synchrotron radiation at different facilities. For instance, (GI)XRD (GI: grazing incidence) and XRR measurements were conducted at the diffraction beamline P08 of PETRA III at the Deutsches Elektronensynchrotron (DESY) in Hamburg, Germany, and at I07 of the Diamond Light Source (DLS) in Didcot, UK. Additional high-energy surface x-ray diffraction (HESXRD) measurements were conducted at P07-EH2 of PETRA III. Further, HAXPES measurements were performed at beamlines P09 and P22 of PETRA III at DESY and, in addition to HAXPES, beamline I09 of the DLS also served for the performed XAS measurements.

4.3.1 Generation of synchrotron radiation

The basic consideration for the generation of synchrotron radiation is the emission of electromagnetic radiation from charged particles (usually electrons or positrons in the case of a synchrotron) when they are accelerated. At non-relativistic energies, the charged particle exhibits a toroidal shaped dipole radiation pattern with its central axis pointing into the direction of acceleration [cf. Fig. 4.4(a)]. However, if the particle travels with a velocity, which is comparable to the speed of light, relativistic effects as well as the Doppler shift have to be taken into account. These considerations result in a cone shaped radiation pattern, which exhibits its center in tangential direction with respect to the propagation direction of the charged particle [cf. Fig. 4.4(b)].

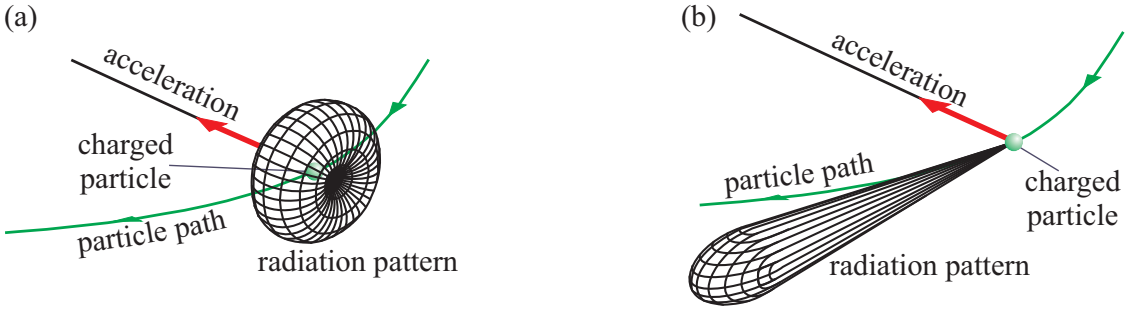

Fig. 4.4: Radiation pattern of an accelerated particle (a) in the non-relativistic case exhibiting a toroidal shape with the main axis pointing in the direction of acceleration and (b) in the relativistic case forming a cone shaped radiation pattern with its center pointing in tangential direction with respect to the propagation direction of the charged particle. Adapted from [50].

Nowadays, synchrotrons of the third generation are the main type in use. Here, either electrons or positrons are travelling with constant velocity close to the speed of light in a so-called storage ring. Though, to be more precise, this ring has a more polygonial shape with alternating straight and circularly shaped parts. The curved sections are equipped with bending magnets, which force the charged particles onto a circularly shaped trajectory. Thus, the accelerating Lorentz force points to the center of the ring and emission of electromagnetic radiation in tangential direction with respect to the propagation direction of the charged particles is obtained, as depicted in Fig. 4.4(b). The synchrotron radiation from such bending magnets covers a wide and continuous energy range from microwaves up to hard x-rays. However, the respective spectra crucially depend on the energy of the particles and on the curvature of the bending magnets and, thus, are determined by the geometry of the storage ring.
To further narrow the beam size and increase the intensity of radiation emitted by a synchrotron, so-called insertion devices are integrated in the straight parts of the storage ring. These assemblies consist of a row of magnetic dipoles with alternating polarity, forcing the charged particles on an undulating trajectory when passing through (cf. Fig. 4.5). Thus, an insertion device can be consid-

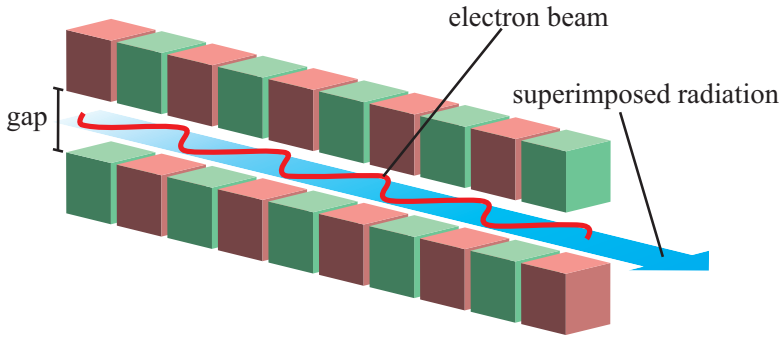

Fig. 4.5: Principle sketch of an insertion device (wiggler or undulator) consisting of several adjacent magnetic dipoles with alternating polarity, forcing the electrons on oscillating trajectories during the passthrough. Superposition of radiation caused by deflection at each magnetic dipole enhances the total radiation emitted from the insertion device. Adapted from [50].

ered as several smaller adjacent bending magnets. However, in contrast to a bending magnet, the superposition of radiation due to deflection at each magnetic dipole in an insertion device enhances the intensity of the emitted radiation and generates the characteristic emission spectra.
There are mainly two types of insertion devices, a wiggler and an undulator, which mainly differ in the magnitude of deflection of the charged particles. In a wiggler, for instance, the deflection of electrons/positrons is comparably large, which results in an incoherent superposition of the radiation emitted at each magnetic dipole. As a conseuqence, one obtains a wide and continuous spectrum, similar to that of a bending magnet but with considerably higher intensity. In contrast to a bending magnet, a wiggler does not significantly depend on the size or geometry of the ring, as it is integrated in the straight parts of the storage ring. Further, the assembly of a wiggler can be chosen to obtain emission spectra optimized for requirements of specific experimental techniques.
In contrast to wigglers, undulators are characterized by only small displacements of the charged particles from their straight trajectories. This results in a coherent superposition of radiation cones emitted at each magnetic dipole. Consequently, one obtains an emission spectrum consisting of sharp peaks with very high intensity at a certain energy and with repititions at respective higher harmonics. However, the characteristic energy can be varied by changing the strength of the deflecting magnetic field. This is usually done by varying the gap between the opposed magnetic dipole arrangements (cf. Fig. 4.5). All beamlines used for experiments within this work are equipped with undulators, providing high x-ray intensities with narrow beam sizes to enable high resolution measurements even for small amounts of the investigated material as present in ultrathin films.
After emission from the radiation sources (bending magnet, wiggler, or undulator) the beam passes through several beamline optics, which optimize the beam characteristics before using the radiation for experiments. These optics mainly consist of monochromators, focusing lenses and mirrors, as well as windows and slits to optimize the beam for the actual experiments, which are conducted in the endstation of the respective beamline.

4.3.2 HAXPES and XAS - Experimental setup

HAXPES measurements were performed at beamlines P09 and P22 of PETRA III at DESY in Hamburg, Germany, as well as at beamline I09 at DLS in Didcot, UK. Further, the setup at I09 also serves for the conducted XAS measurements. The principle experimental setup for HAXPES measurements is very similar for the different spectroscopy beamlines. Only minor deviations like the type of detector or the beam characteristics are present but without influencing the general principle of the measurement technique.
The geometry of the experimental layout is schematically depicted in Fig. 4.6 for the example of the endstation at beamline I09. The spectroscopy endstations are all equipped with a UHV chamber consisting of a sample holder attached to a 5-axes manipulator and a high-resolution photoelec-

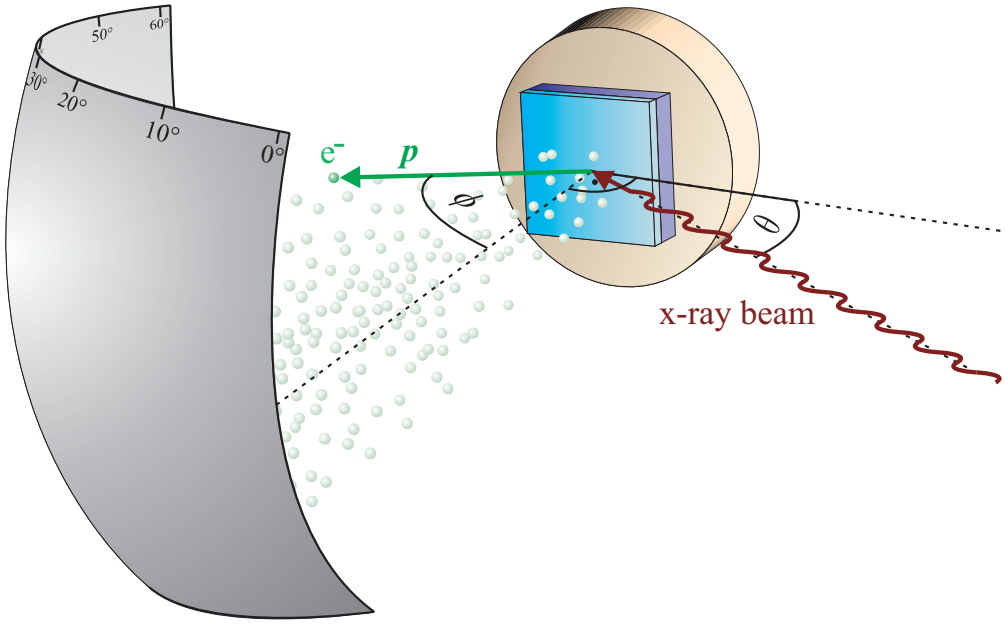

Fig. 4.6: Principle geometry of the experimental layout for depth-dependent HAXPES measurements. The incident angle θ between beam and surface plane is kept constant during the measurement. Photoelectrons are emitted in different directions from the sample surface denoted by momentum $\boldsymbol{p}$. A two-dimensional wide-area detector with a total acceptance angle of ∼60° enables simultaneous detection of photoelectrons emitted from the sample with different emission angles ϕ with respect to the surface normal. The center of the detector is arranged perpendicular to the beam direction.

tron detector, which is arranged perpendicular to the direction of the x-ray beam. To obtain higher probing depths and, thus, a more bulk-like sensitivity compared to laboratory-based soft XPS measurements, similar photon energies of 5948 eV, 6000 eV, and 5930 eV were used at beamlines P09, P22, and I09, respectively. Beamline I09 additionally comprises an x-ray branch providing photons with an energy of 1100 eV to perform complementary soft x-ray photoemission experiments.
A probing-depth variation in the hard x-ray regime was realized by using angle-dependent photoelectron detectors. For measurements at I09 a two-dimensional wide-area detector (VG Scienta EW4000 HAXPES) with an acceptance angle of ±30° was used. The same principle is realized at P09/P22 by using a high-resolution hemispherical analyzer (SPECS Phoibos 225 HV) with a delayline detector and a wide-angle lens with ±30° angular acceptance. Both setups therefore allow for simultaneous angle-resolved photoelectron detection with a total acceptance angle of ∼60° and, thus, can be used for depth-dependent HAXPES measurements. For better statistics, data within acceptance angle sections of 8° were summed up, thus dividing the detector into seven equally sized sections. Further, the regions close to the edges of the detector (±2°) were neglected.
For all angle-resolved HAXPES (AR-HAXPES) measurements (conducted at I09 and P09), the incident angle θ between x-ray beam and surface plane is kept constant ($\theta = 30°$ at I09 and $\theta = 40°$ at P09). Hence, the detection of photoelectrons in dependence of the emission angle ϕ with respect to the surface normal enables to record depth-dependent photoemission spectra. The angular-dependent information depth D_I^{95}, from which 95% of photoelectrons detected at the off-normal emission angle ϕ originate, is given by [155]

$$D_I^{95}(\phi) = -\lambda \cos\phi \ln(1 - 95/100) \tag{4.1}$$

with λ as the electrons' IMFP. For photoelectrons originating from, e.g., Fe $2p$, Co $2p$, or Ni $2p$ orbitals, maximum information depths (obtained for normal emission, $\phi = 0°$) of around ∼22 nm are

achieved for the used photon energies. Compared to that, for emission at $\phi = 60°$, the information depth is halved, which results in a higher surface-sensitivity.
At P22, however, the analyzer is operated in high-transmission mode and the photoelectrons are therefore not discriminated by their angular contribution within one measurement. Here, depth sensitivity can be realized by performing single measurements at different incident angles θ, thus, varying the detection of photoelectrons at different emission angles between the measurements. Though, within this work, the measurements conducted at P22 (cf. Chap. 7) are only used to gain a more bulk-like sensitivity, complementary to lab-based surface-sensitive XPS measurements. Therefore, a fixed incident angle of $\theta = 5°$ is used for the measurements at P22.
In addition to HAXPES, the experimental setup at I09 is also suited for XAS measurements. For this purpose, the incident photon energy is tuned across the absorption edge of interest (e.g., Fe, Co, and Ni L edges) and the absorbed intensity is recorded via the surface-sensitive TEY method (cf. Sec. 2.6.1). Here, the sample surface is contacted by conductive silver paste and connected to ground potential. As a result of the decay process in XAS, the emitted secondary electrons cause a positive charge of the sample (cf. Sec. 2.6.1). This charge is neutralized by a drain current between sample and ground potential, which therefore corresponds to the amount of absorbed intensity. The total electron yield is then obtained by normalizing the signal to the current from an Au-coated mesh located in the incident x-ray beam prior to sample irradiation. The TEY detection is a surface-sensitive method to record x-ray absorption spectra and provides probing depths of around 2-5 nm in the case of transition metal oxides [156–158].

4.3.3 (GI)XRD - Experimental setup

For (GI)XRD and XRR experiments performed in this work, beamlines I07 and P08 were used. The respective endstations both consist of a diffractometer, which enables sample and detector positioning with respect to the incident x-ray beam. Both setups are schematically depicted in Fig. 4.7.
At beamline I07, the endstation EH2 (EH: experimental hutch) consists of a UHV chamber mounted on a $(2S+3D)_v$-type diffractometer, allowing for *in situ* diffraction experiments under UHV conditions. Here, the sample has two rotational degrees of freedom (denoted as '2S'), whereas the detector exhibits three rotational degrees of freedom (denoted as '3D'). The sample surface is mounted vertically (indicated by index 'v') on a hexapod and aligned in the diffractometer center (DC), where it is irradiated by the incident x-rays [cf. Fig. 4.7(a)]. The polar and azimuthal sample rotations are given by angles α and φ, respectively, whereas δ denotes the vertical and γ the horizontal detector rotations. In addition, the detector with the attached four-slit system can be rotated by its azimuthal angle ν.
In contrast, the endstation of P08 is equipped with a six-circle diffractometer, which was designed to enable high-resolution x-ray diffraction (HR-XRD) experiments at PETRA III [cf. Fig. 4.7(b)]. Here, the sample has four and the detector exhibits two rotational degrees of freedom, resulting in the denotation of a (4S+2D)-type diffractometer. A closed Eulerian cradle which can be rotated by an angle χ enables to vary between, i.e., vertical (index 'v') or horizontal (index 'h') surface alignment (or in between). However, all measurements conducted within this work were applied in horizontal geometry (i.e. $\chi = 90°$). Thus, the polar and azimuthal sample rotations are denoted by angles ω and φ, respectively. Similar to the $(2S+3D)_v$ diffractometer, vertical and horizontal detector alignment is denoted by rotation angles δ and γ, respectively.
For diffraction experiments conducted in this work, two different scattering geometries were used. One geometry is applied for specular x-ray diffraction (XRD) and x-ray reflectivity (XRR) and the other one for grazing incidence x-ray diffraction (GIXRD). In the case of specular diffraction as well as reflectivity, the lateral components of the scattering vector are zero and incident and final wave

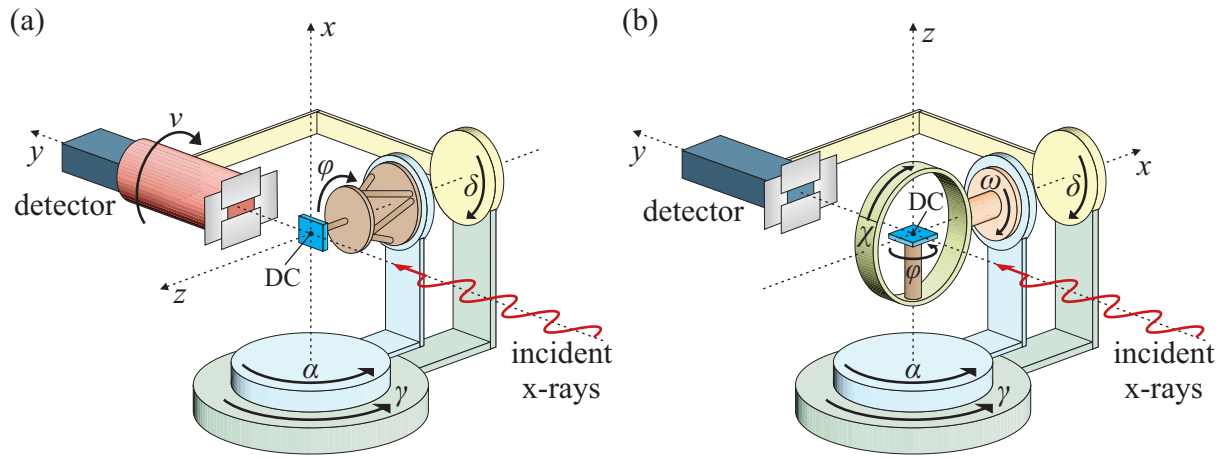

Fig. 4.7: Schematics of diffractometer types used for (GI)XRD and XRR measurements at different beamlines. (a) $(2S+3D)_v$-type diffractometer with a hexapod sample stage and vertical sample alignment (indicated by index v) as used at EH2 of beamline I07. (b) (4S+2D)-type diffractometer as used with horizontal sample alignment ($\chi = 90°$) at beamline P08. In both setups, the sample surface is aligned and irradiated by the incident x-ray beam in the diffractometer center (DC), where all rotation axes intersect.

vectors lie in a plane perpendicular to the sample surface. Thus, for XRD and XRR measurements at I07 (vertical geometry), δ and φ are fixed to zero and not varied during a measurement. Here the incident angle is varied by an angle $\alpha = \theta$ and the detector is rotated horizontally by the doubled incident angle $\gamma = 2\theta$ to obtain scattering vectors $\boldsymbol{q}$ oriented solely perpendicular to the sample surface. This setup is therefore also known as $\theta - 2\theta$ geometry. In the case of P08 with the diffractometer solely in horizontal geometry ($\chi = 90°$), the scattering condition for XRR and XRD measurements is varied by the incident and exiting angles $\omega = \theta$ and $\delta = 2\theta$, respectively, whereas α, γ, and φ are fixed to zero.

In contrast to the $\theta - 2\theta$ geometry used for XRD and XRR measurements, the incident angle (α for I07 and ω for P08) is fixed in the GIXRD setup. Here, typically small incident angles close to the critical angle of the investigated material (cf. Sec. 2.3.1) are used to enhance the near-surface and thin film contribution to the diffraction pattern. For instance, for GIXRD measurements at P08 (cf. Chap. 7), where a photon energy of 18 keV was applied (resulting in critical angles of, e.g., $\alpha_c^{MgO} = 0.12°$ and $\alpha_c^{STO} = 0.14°$ for MgO and $SrTiO_3$, respectively), a grazing incidence angle of $\omega = 0.3°$ was used. In contrast to XRR and XRD, also lateral scattering directions can be probed in GIXRD. Here, the azimuthal sample angle φ as well as the detector angles δ and γ can be rotated to fulfill the diffraction condition. Hence, other CTRs than the specular (00L) rod can be achieved and also lateral scans in the reciprocal space, e.g., so-called 'in-plane' measurements at $L \approx 0$, can be performed.

In addition to XRR and (GI)XRD measurements performed at I07 and P08 using hard x-rays, HESXRD experiments were conducted at beamline P07-EH2 of PETRA III (cf. Chap. 5). Here, the sample surface is irradiated by an x-ray beam of high energy (up to ~200 keV) at a grazing incident angle close to the critical angle of the investigated material. For the HESXRD studies performed in this work (cf. Chap. 5), a photon energy of 102 keV and a grazing incident angle of 0.03° was applied. Compared to common XRD experiments with photon energies typically below 30 keV, the use of high-energy x-rays decreases the exiting angles between different diffraction conditions and therefore shifts the Bragg peaks and CTRs closer together in real space. Thus, by using a fixed two-dimensional wide-area detector (PerkinElmer XRD 1621 flat panel detector) a large volume of the reciprocal space can be measured by rotating solely the sample around its azimuthal angle φ.

Then, for each angle φ a single two-dimensional slice of the reciprocal space as an intersection with the detector is recorded. The sample rotation therefore also turns the reciprocal space through the detector. Within this work, a diffraction pattern is then obtained by processing the detector images, that each pixel of the final image only consists of the maximum intensity of the respective pixel throughout the azimuthal rotation. With this, a reciprocal space map as a projection of CTRs and Bragg peaks to the detector plane is obtained. The final computed image can therefore serve for structural analysis in vertical and lateral scattering directions. A more detailed description of data acquisition and possible analysis methods for HESXRD data recorded at P07-EH2 is given in Ref. [159].

4.3.4 Correction and analysis of x-ray diffraction data

For all (GI)XRD and XRR measurements at I07 and P08 a two-dimensional detector (PILATUS 100k at I07 and P08, DECTRIS EIGER 1M at P08) was used. Thus, at each measurement point the detector plane covers a section of the reciprocal space. A single data point within one measurement, e.g., along L-direction of a CTR, is then obtained by integrating all intensities of pixels, which contribute to the diffraction condition of interest (e.g. Bragg peak or CTR). For this purpose, a rectangular region of interest (ROI) is defined on the two-dimensional detector images during data processing. The ROI dimensions are chosen to incorporate the complete intersection of a CTR or Bragg peak with the detector and are kept constant within single measurements. Further, a background is determined by integrating over a detector area, which does not contribute to the respective diffraction condition. Both integrated background and peak intensities are normalized to the number of respective summed up pixels. Consequently, a background corrected intensity is obtained at each data point by subtracting the background from the measured peak intensity.
However, prior to analysis of the recorded Bragg peaks and CTRs, the measured diffracted intensities have to be corrected by so-called angular (or geometric) correction factors. These corrections crucially depend on the geometry of the measurement and the used diffractometer. The factors applied in this thesis for the correction of XRD and GIXRD data recorded at the $(2S+3D)_v$- and the (4S+2D)-type diffractometer at I07 and P08, respectively, are given in Tab. 4.1. Note that, in comparison to the fixed vertical sample alignment at I07, the correction factors for P08 are solely considered for the applied horizontal geometry. Moreover, only contributions which exhibit angular dependencies and therefore vary during a measurement are presented, based on derivations made in Refs. [160–163]. More details and explanations about (additional) intensity corrections in (GI)XRD experiments also for other diffractometer types and geometries can be found in Refs. [161–166].
One intensity correction results from the polarization of the incident x-ray beam. The corresponding polarization factor can be generally expressed as $P = \sin^2(\alpha_{\mathrm{pol}})$ with α_{pol} as the angle between the polarization direction and the direction of the scattered photons [165]. For linearly polarized light the total polarization factor P can be expressed by

$$P = p_{\mathrm{h}} P_{\mathrm{hor}} + (1 - p_{\mathrm{h}}) P_{\mathrm{ver}} \tag{4.2}$$

as a superposition of vertical (P_{ver}) and horizontal (P_{hor}) polarization factors with p_{h} denoting the fraction of horizontal polarization. In the case of synchrotron radiation, typically linearly polarized light is emitted with a polarization vector almost completely lying in the horizontal deflection plane. In particular, radiation generated by undulators, as it is the case at beamlines I07 and P08, exhibits extremely high horizontal polarizations of 98% or even better ($p_{\mathrm{h}} \geq 0.98$). Thus, the fraction of vertical polarization can be neglected and solely horizontal polarization factors P_{hor}, as listed in Table 4.1, have to be considered.
Further, the detected intensity depends on the area of the sample, which is illuminated by the incident beam and simultaneously visible to the detector. Thus, this 'active area' varies with the

	$(2S+3D)_v$ at I07		(4S+2D) at P08	
	XRD	GIXRD	XRD	GIXRD
P_{hor}	$\cos^2(\gamma)$	$1-\sin^2(\gamma)\cos^2(\delta)$	1	$1-\sin^2(\gamma)\cos^2(\delta)$
C_{area}	$\frac{1}{\sin\alpha}$	$\frac{\sqrt{1-\cos^2(\delta)\sin^2(\gamma-\alpha)}}{\sin\delta}$	$\frac{1}{\sin\omega}$	$\frac{\sqrt{1-\cos^2(\gamma)\sin^2(\delta-\omega)}}{\sin\gamma}$
C_{rod}	$\cos(\gamma-\alpha)$	$\sqrt{1-\cos^2(\delta)\sin^2(\gamma-\alpha)}$	$\cos(\delta-\omega)$	$\sqrt{1-\cos^2(\gamma)\sin^2(\delta-\omega)}$

Tab. 4.1: Correction factors applied for XRD and GIXRD measurements performed at I07 with a $(2S+3D)_v$-type diffractometer with vertical sample alignment and at P08 in horizontal geometry with a (4S+2D)-type diffractometer. P_{hor} denotes the polarization factor for horizontal polarization, C_{area} the active area correction, and C_{rod} the rod interception correction factor.

incident angle as well as with the detector position with respect to the sample. Additionally, the area is determined by the slit settings and by the ROI defined during data processing (see above). Though, as both ROI and slits are not varied during the measurements, the area correction factor C_{area} solely depends on the respective diffractometer angles. For the case of specular diffraction (XRD), the area correction is affected by the incident angle, whereas for GIXRD the incident angle is kept constant and C_{area} is determined by the detection angles.
A further intensity correction applies, when considering the interception of, i.e., a CTR with the Ewald sphere, which in turn exhibits a finite width. Thus, the interception volume of the Ewald sphere with the crystal truncation rod most crucially decreases with increasing L values (meaning increasing out-of-plane angles γ and δ for the setups at I07 and P08, respectively). This intensity variation is taken into account by the correction factor C_{rod} for interception of the CTRs with the Ewald sphere.
Usually, an additional correction factor, the Lorentz factor C_{Lor}, which accounts for variations in the integration volume when converting from real to reciprocal space should be considered. Depending on the source in literature, this factor often includes the already mentioned interception factor C_{rod} (see above). However, within this work, both factors are treated separately. The Lorentz factor was traditionally introduced for CTR data acquisition using a point detector, where the intensity of the CTR for any given L value is obtained by rotating the sample around its normal (azimuthal angle) that the CTR will rotate through the detector and the signal will be scanned (mostly) laterally in reciprocal space to produce a so-called 'rocking curve' [167]. The performed linear angular rotation does not correspond to a linear scan in reciprocal space, which therefore has to be corrected by the Lorentz factor. However, when using a two-dimensional detector, the whole lateral (and vertical) extent of the CTR is captured within one single detector image and the sample does not need to be rotated around its azimuthal angle (also known as 'stationary mode'). Hence, no Lorentz factor has to be considered to correct an integrated rocking curve [163, 166]. Solely the rod interception factor C_{rod} (cf. above) has to be taken into account.
The total corrected intensity I_{cor} is consequently given by

$$I_{cor} = \frac{1}{P_{hor}\, C_{area}\, C_{rod}}\, I_{meas} \ , \tag{4.3}$$

where I_{meas} is the measured and background corrected intensity.
To further analyze the corrected x-ray diffraction data, an in-house built fitting program, namely RodsNPlots, is used, which was initially developed by A. Greuling [168] and further extended by S. Hahne and F. Bertram [169, 170]. This tool allows to calculate x-ray diffracted intensities, i.e., along different CTRs measured in specular or in GIXRD geometry. It is based on full kinematic

diffraction theory and, consequently, the calculated diffracted intensity is referred to Eq. (2.45). For the calculations, a user-defined model has to be implemented, which consists of a defined number of crystalline layers on a chosen substrate. Each film within the system (including the substrate) is defined by several structural parameters, which can either be fixed to certain values or be varied by the program within the fitting procedure of the calculation to the experimental data. For each film, e.g., the type of material has to be chosen, which contains the information about locations of different atoms within the unit cell and therefore comprises the respective structure factor. Further parameters are the number of unit cells in vertical direction (∼number of layers), scaling factors for layer and interface distances (only in vertical direction), the occupation factor, the adsorption site, top and bottom RMS roughnesses as well as the Debye-Waller factor for each film. Further, laterally coexisting columns each consisting of an independent number of layers can be considered, which is usually used to implement different laterally coexistent structural phases within the thin film system. However, for the calculations performed in this work, this option is not used, since single columns are sufficient to describe the experimental data of the investigated thin films properly. For fitting the calculations to the experimental data, different numerical optimization algorithms can be applied. Within this work, the (comparably fast) Nelder-Mead simplex algorithm followed by the (more accurate) differential evolution algorithm are used consecutively to obtain a model, which serves as the best description of the experimental data. More detailed descriptions and explanations concerning RodsNPlots, the used fitting parameters and optimization algorithms can be found in Ref. [50].

4.4 SQUID magnetometry

For the characterization of bulk magnetic properties of the prepared thin films, superconducting quantum interference device (SQUID) magnetometry is applied. This technique represents a highly-sensitive detection method of magnetic flux measurements. In the following, some fundamental mechanisms, which underlie the functionality of a SQUID, are briefly described. Further, the experimental setup of the used SQUID magnetometer and the processing scheme of measured magnetometry data is presented.

4.4.1 Fundamental mechanisms

The functionality of a SQUID is based on the combination of two physical phenomena, namely flux quantization [171] and the Josephson effect [172]. Thus, both effects are briefly described here. More details about the operation principle of a SQUID and the underlying effects but also about further developments and different applications can be found in Refs. [173–175].

Flux quantization

The current in a superconductor is carried by pairwise weakly coupled electrons, known as so-called Cooper pairs, which can be described collectively by a single (macroscopic) quantum wave function $\Psi = \Psi_0\, e^{i\theta}$, where Ψ_0 is the amplitude and θ the phase of the condensate. If one now considers a closed superconducting ring (present in the superconducting state), the phase of the wave function has to be continuous, meaning that when you trace the wave around the ring in one complete turn, the phase needs to go back to the same value as at the starting point (cf. Fig. 4.8). Thus, only certain discrete states are allowed within the superconducting ring.
Yet, when magnetic flux Φ is applied to the ring, this flux modifies the phase along the ring, corresponding to the Aharonov-Bohm effect [176]. However, due to only discretely allowed states

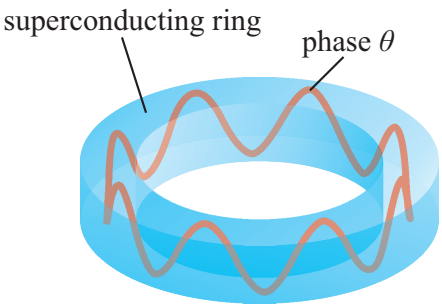

Fig. 4.8: Principle sketch of a superconducting ring. The phase variation of the condensate in the ring is represented as an oscillating line. The phase has to be continuous, which means that it needs to attain the same value when tracing the quantum wave around the ring in one complete turn. Intermediate states, where the phase within the loop is non-continuous, cannot exist.

within the ring, also solely certain amounts of flux are allowed within the ring. This behavior is known as flux quantization, initially predicted by F. London [171] and experimentally observed by B. S. Deaver and W. M. Fairbank [177] and, independently, by R. Doll and M. Näbauer [178]. Magnetic flux can therefore only exist in integer multiples of the flux quantum $\Phi_0 = h/2e = 2.068 \times 10^{-15}$ Wb (h: Planck constant, e: electron charge) within the ring.

Josephson effect

In 1962, B. D. Josephson predicted the possibility of Cooper pairs tunneling through a thin resistive (insulating) barrier between two superconducting regions [172]. This tunneling process is known as the Josephson effect (or Josephson tunneling), whereas the barrier with the two adjacent superconducting regions is known as the Josephson junction (often the barrier is denoted as a 'weak link'). It was found that the current I flowing through a junction is given by

$$I = I_c \sin(\delta) \ , \tag{4.4}$$

where $\delta = \theta_1 - \theta_2$ denotes the difference of phases θ_1 and θ_2 of the ground states in the two respective superconductors. I_c is the critical current of the junction, which is the maximum supercurrent that can flow across the junction without dissipation and, thus, without a voltage drop. When the current through the junction is increased from zero the flow of Cooper pairs constitutes a supercurrent and initially the voltage across the junction remains zero until the current reaches the critical current. Though, for $I > I_c$ a voltage U appears, and the phase shift δ evolves with time according to

$$\frac{d\delta}{dt} = \frac{2e}{\hbar} U = 2\pi \frac{U}{\Phi_0} \ . \tag{4.5}$$

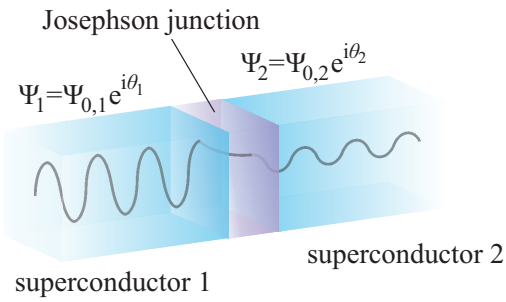

Fig. 4.9: Principle sketch of the Josephson effect. Two superconductors are separated by a resistive/insulating barrier, known as the Josephson junction. The Josephson effect describes the tunneling process of Cooper pairs through the junction.

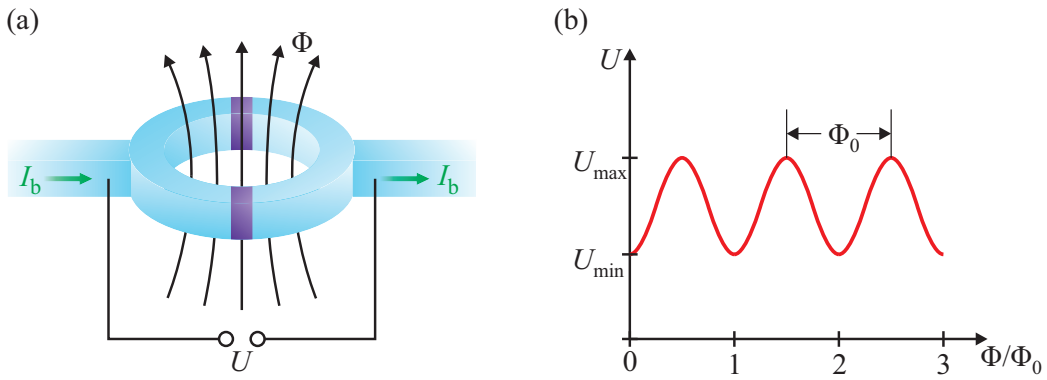

Fig. 4.10: (a) Principle design of a dc SQUID with a superconducting loop, which is interrupted by two similar Josephson junctions (purple), one in each branch of the loop. For operation, a biasing current I_b, which is slightly bigger than the sum of both critical currents of the Josephson junctions, is applied across the loop. Externally applied magnetic flux Φ results in a phase variation across both junctions. As the SQUID operates in the resistive mode, these phase variations cause a voltage drop across the SQUID. (b) The measured voltage U oscillates periodically as the applied flux is varied and exhibits a period of the flux quantum Φ_0.

SQUID sensor

A SQUID sensor simultaneously makes use of the flux quantization within a superconducting loop and the characteristics of a Josephson junction. In general, it consists of a superconducting ring, which is interrupted by one or more Josephson junctions, depending on the type of SQUID. Within this work, solely a dc SQUID (dc: direct current) is used for measurements of magnetic moments. This type of SQUID consists of two similar Josephson junctions connected in parallel on the superconducting ring, one in each branch of the loop [Fig. 4.10(a)]. In contrast, an rf SQUID (rf: radio frequency) only comprises a single junction within the superconducting loop, which makes its production and electronic control less complex but its performance also less sensitive [175].
For operation of a dc SQUID, a constant biasing current I_b close to (usually slightly above) the double value of the critical current I_c of each junction is applied across the SQUID. Due to the parallel arrangement, this current equally splits in the two branches of the superconducting loop. When an external magnetic flux is now coupled into the loop, a screening current I_s circulates in the ring to generate a magnetic field, which cancels out the external magnetic flux. This in turn results in a change of the phase differences across the Josephson junctions. As the current flowing through the junctions exceeds their critical current I_c, the SQUID operates in the resistive mode and the changing phase shift appears as a voltage drop across the junctions. This voltage oscillates periodically with the phase changes and therefore corresponds to the change of the externally applied magnetic flux. As the external flux increases (or decreases), the voltage will change in a periodic manner with the period being that of the flux quantum Φ_0 [cf. Fig. 4.10(b)]. Voltage minima are obtained at integer multiples of Φ_0, whereas the maxima are located in between at additional half integer multiples of Φ_0. Monitoring the change in voltage therefore allows to determine the magnetic flux that has been coupled to the SQUID. Note that unlike the flux contained within a closed superconducting loop, which can only achieve integer multiples of a flux quantum (cf. above), the flux applied to a SQUID can attain any value.
In fact, conventional electronics can detect voltages corresponding to magnetic flux changes of much less than one flux quantum Φ_0, which manifests the high sensitivity of a SQUID for magnetic flux measurements. In particular, by using external feedback electronics, the working point of a SQUID can be adjusted to a unique regime on the $U - \Phi$ curve [175]. Usually, a SQUID is operated at the steep part of the $U - \Phi$ curve where $|(\partial U/\partial \Phi)_I|$ is a maximum. In this regime the resulting

voltage change is approximately linear in magnetic flux changes. Hence, in essence the SQUID is a highly-sensitive flux-to-voltage transducer, converting a tiny change of magnetic flux into a voltage.

4.4.2 Experimental setup

Within this work, a SQUID magnetometer of type S700X from Cryogenic Ltd. is used, which allows to detect magnetic moments down to 10^{-8} emu = 10^{-11} Am^2 (emu: electromagnetic units). The main parts of this magnetometer are schematically depicted in Fig. 4.11.

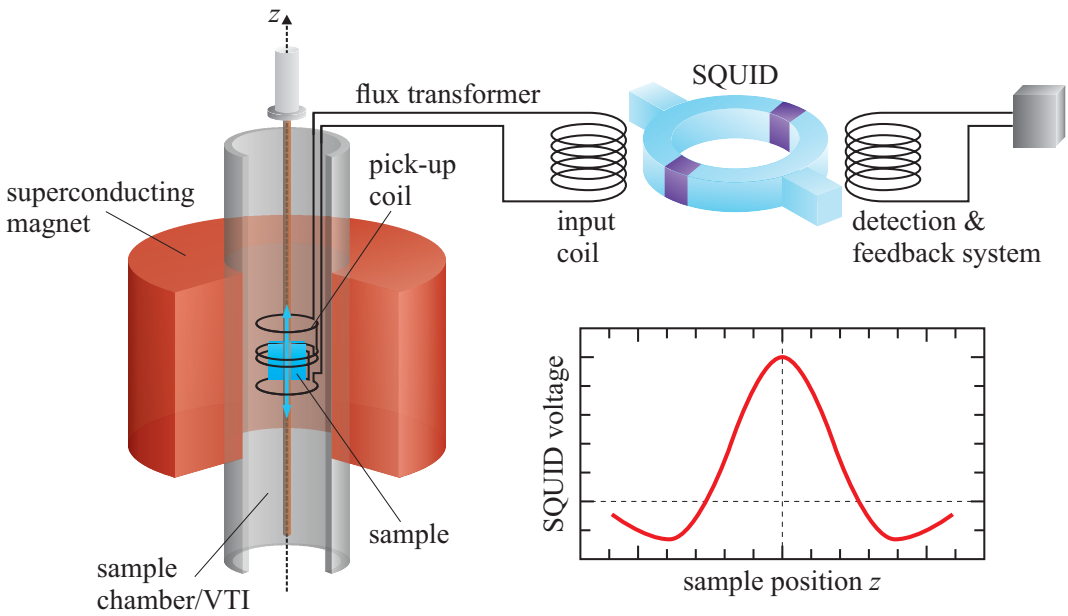

Fig. 4.11: Schematical drawing of the main parts of the used SQUID magnetometer. The superconducting magnet provides homogeneous magnetic fields up to 7 T along z-direction. The sample is attached to a Kapton straw in the center of the magnet and can be moved vertically within the sample chamber/variable temperature insert (VTI). The sample temperature can be controlled from 1.6 up to 400 K within the VTI. Moving the sample along the vertical axis induces a current in the superconducting flux transformer, which consists of the pick-up coil surrounding the sample and the input coil for coupling the induced current/magnetic flux to the dc SQUID. The detection and feedback system sets the working point of the dc SQUID and records the SQUID output voltage as a function of the sample position. Adapted from [63].

The magnetometer consists of a superconducting magnet, which supplies homogeneous magnetic fields up to 7 T along the vertical axis (z-axis). To maintain the magnet in the superconducting state, it is cooled via the surrounding liquid Helium dewar. The sample is positioned in a small sample chamber in the center of the magnet. It is attached to a Kapton straw and can be moved within the homogeneous magnetic field along the vertical axis. The sample chamber, also denoted as variable temperature insert (VTI), can be cooled down to 1.6 K via liquid He from the dewar and can be annealed up to 400°C by two seperate heating elements.
Within the used magnetometer, the SQUID itself is not directly exposed to the magnetic flux of the sample. Here, the flux is coupled to the SQUID by a flux transformer, which is a superconducting circuit consisting of a pick-up coil system surrounding the sample connected to an input coil for the coupling to the SQUID. The pick-up coils surround the sample and are therefore exposed to the magnetic flux to be measured. Thus, moving the sample through the detection coil along the vertical axis results in local magnetic flux variations, which in turn induce a current in the superconducting wire that is proportional to the change in magnetic flux. Note that due to the use

of a superconducting pick-up coil this current is not dependent on the rate of flux change (as in the case of conventional induction) but rather on the absolute change of magnetic flux while moving the sample. The induced current is in turn coupled to the SQUID via the input coil.
One advantage of the use of such a flux transformer is that the area within the pick-up coil can be arranged to the size necessary for the experiments and therefore be larger than the area within the SQUID loop, which increases sensitivity. However, to maximize efficiency of flux transfer also both inductances of detection and input coil have to be the same [173]. Another advantage of the use of flux transformers is that it allows placement of the SQUID sensor in a noise reduced environment, while the detection coil could be placed in field or temperature regimes well beyond the operational limits of the SQUID sensor itself [175]. Further, the pick-up coil system used in this magnetometer is designed as a second derivative gradiometer with two central clockwise loops and one counter-clockwise loop above and one below the central loop pair. With this arrangement magnetic field gradients as arising from external magnetic fields or due to drift of the applied magnetic field during sample motion are cancelled out.
The supercurrent induced in the flux transformer due to change in magnetic flux when moving the sample is coupled to the dc SQUID and is converted to a voltage output, which is proportional to the applied change in magnetic flux (cf. above). This voltage is therefore recorded as a function of the sample position along the z-axis within the detection coil. The resulting signal is fitted by a theoretical curve of an ideal dipole, which in turn provides the magnetic moment μ of the measured sample.

4.4.3 Processing of SQUID data

One disadvantage of SQUID magnetometry is that the magnetic response of the entire sample, i.e., of the substrate and the deposited thin film(s), is detected. However, to obtain the magnetic signal of only one film, all other contributions have to be subtracted from the overall detected signal.
Within this work, most of the investigated ferrite films were deposited directly on the substrates. Thus, to obtain the magnetic response in M vs H measurements solely of the thin films, one could measure the magnetic contribution from the substrate prior to film deposition (cf. purple curve in Fig. 4.12) and subtract it from the magnetic measurement after film deposition (cf. green curve in Fig. 4.12).

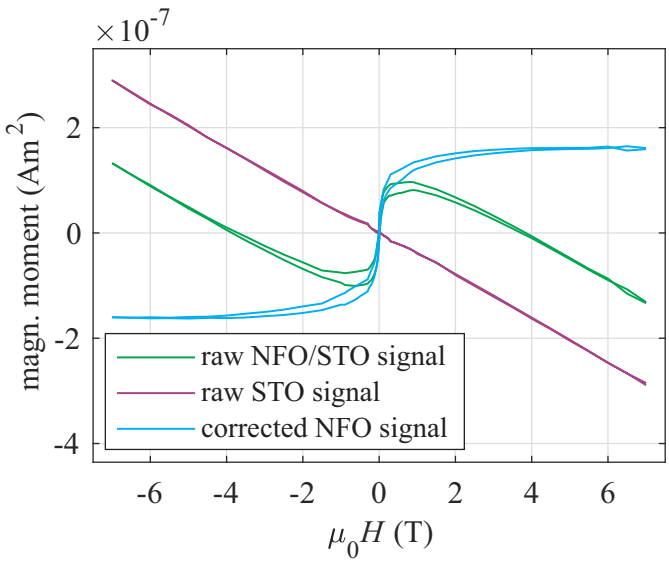

Fig. 4.12: Exemplary presentation of substrate and film contributions in M vs H measurements obtained for a $NiFe_2O_4$ film on SrTiO(001). The recorded signal of the complete sample (green curve) shows contributions of both STO substrate and NFO film. The magnetic response solely stemming from the ferrimagnetic NFO film (blue curve) can be obtained by subtracting the raw signal of a clean $SrTiO_3$ substrate (scaled to the volume of the substrate with the deposited film) from the total signal of the NFO/STO sample. The linear slope of the diamagnetic STO substrate coincides with the slope in the high-field regime ($|\mu_0 H| > 5$ T) of the total NFO/STO signal, where the ferrimagnetic NFO film is saturated.

Though, this procedure would be quite cumbersome and, alternatively, the single film contribution (cf. blue curve in Fig. 4.12) can also be extracted only from the overall signal of film and substrate. Since both substrate materials are diamagnetic at sample temperatures applied for M vs H measurements of the films on each substrate (300 K for MgO, 5 K for $SrTiO_3$), only diamagnetic/linear contributions have to be subtracted in the magnetization curves. The linear slope of these contributions can be determined by fitting the ferrimagnetically saturated high-field regions (usually for magnetic fields above 5 T) of the overall M vs H data of film and substrate. By subtracting a line with the resulting slope of the high-field regime from the overall data, the single (ferrimagnetic) film contribution to the magnetic response is obtained.
By comparing the overall data of a deposited film on a substrate with the data obtained for the single substrate (scaled to the same volume of the substrate with the deposited film, cf. Fig. 4.12) it becomes evident that the high-field slopes of both measurements coincide. Hence, for linear substrate contributions, the described background subtraction is a valid procedure to obtain solely the magnetic response of the deposited film. This method is also applied for the thin CFO films prepared by interdiffusion of CoO/Fe_3O_4 bilayers (cf. Chap. 8), since the additional signal from CoO also only contributes with a diamagnetic/linear response to the overall magnetic signal in the magnetization curve.
Moreover, the magnetic moment m obtained for a single film in SQUID measurements is further given in absolute values in units of Am^2. To achieve better comparability between different sample sizes and between films of different thickness, the magnetic moments were scaled to magnetizations M in units of μ_B/f.u. (f.u.: formula unit). The corresponding conversion is therefore given by

$$M\left(\frac{\mu_B}{\mathrm{f.u.}}\right) = \frac{a_0^3}{n_{\mathrm{f.u.}} \cdot \mu_B \cdot \mathrm{D} \cdot \mathrm{A}}\, m\left(\mathrm{Am}^2\right) \tag{4.6}$$

with $m\left(\mathrm{Am}^2\right)$ as the film magnetic moment in units of Am^2, a_0 as the lattice constant of the respective unit cell, $n_{\mathrm{f.u.}}$ as the number of formula units per unit cell ($n_{\mathrm{f.u.}} = 8$ for the case of spinel type ferrites), D as the film thickness (as determined by XRR), and A as the deposited area of the sample.

Original publication: Applied Physics Letters **117**, 011601 (2020)
available at http://dx.doi.org/10.1063/5.0013925

Real-time monitoring the growth of strained off-stoichiometric $Ni_xFe_{3-x}O_4$ ultrathin films on MgO(001)

J. Rodewald[1], J. Thien[1], T. Pohlmann[1,2], M. Hoppe[1,2], F. Bertram[2], K. Kuepper[1], and J. Wollschläger[1]

[1] *Department of Physics, Osnabrück University, Barbarastrasse 7, D-49076 Osnabrück, Germany*
[2] *DESY, Photon Science, Notkestraße 85, D-22607 Hamburg, Germany*

Abstract

$Ni_xFe_{3-x}O_4$ thin films with varying Ni amount ($0 \leq x \leq 1.5$) were deposited on MgO(001) via reactive molecular beam epitaxy. The growth process was monitored during film deposition by means of x-ray diffraction. All prepared films exhibit a well-ordered structure with complete vertical crystallinity throughout the whole film growth and flat surfaces of the final films independent of the Ni amount. An enhancement of vertical compression in the initial growth continuously decreases up to a film thickness of 8 nm. During further growth, all films exhibit residual and constant vertical compression with lateral adaption of the final films to the substrate lattice, as observed by high energy surface x-ray diffraction experiments. Hard x-ray photoelectron spectroscopy measurements of the final films reveal increasing Fe^{3+}:Fe^{2+} ratios for higher Ni content and point to additional NiO agglomerations within the films exceeding the stoichiometric Ni amount of $x = 1$.

Structural, electronic, and magnetic properties of thin off-stoichiometric $Ni_xFe_{3-x}O_4$ films on MgO(001)

Abstract

Off-stoichiometric $Ni_xFe_{3-x}O_4$ thin films ($x < 2.1$) with varying Ni content x and comparable thicknesses between 14.0 and 18.6 nm were grown on MgO(001) by reactive molecular beam epitaxy. Synchrotron-based high resolution x-ray diffraction measurements reveal vertical compressive strain for all films, resulting from a lateral adaption of the film to the substrate lattice without any strain relaxation. Complete vertical crystallinity with smooth interfaces and surfaces is obtained independent of the Ni content x. For $x < 1$ an expected successive conversion from Fe_3O_4 to $NiFe_2O_4$ is observed, whereas for $x > 1$ NiO agglomerations are formed within the films. However, angle resolved hard x-ray photoelectron spectroscopy measurements indicate homogeneous cationic distributions without strictly separated phases independent of the Ni content. The ferrimagnetic behavior, as observed by superconducting quantum interference device magnetometry, in addition to the high crystalline film quality independent of the Ni content x indicate high applicability of ferrite films with off-stoichiometric cationic ratios in the field of spintronics.

6.1 Introduction

Transition metal ferrites with (inverse) spinel structure represent a promising class of oxide-based materials for the application in, e.g., spnicaloritronics or spintronics [179–182], due to several intriguing properties like, i.e., significant magnetic saturation moments and high Curie temperatures [14]. In the field of spintronics, inverse spinel ferrites like $NiFe_2O_4$ and $CoFe_2O_4$ are suitable for the application as a spin filter [17, 18, 20, 21], where highly spin polarized tunneling currents are generated. The insulating and ferrimagnetic properties of nickel and cobalt ferrite with an exchange splitting of the energy levels in the conduction band result in different tunneling probabilities for the two spin orientations, which make these ferrites highly suited as spin filters [182]. However, the spin-filter efficiency is crucially determined by the structural quality of the tunneling barrier and its interfaces [21]. Thus, ferrites have to be prepared as thin films with low defect densities to obtain a high transmission of spin polarized tunneling currents.

Here, MgO(001) represents a suitable substrate material for the growth of thin ferrite films, since the lattice mismatch between, i.e., $NiFe_2O_4$ (lattice constant $a_{NiFe_2O_4} = 833.9$ pm) and MgO(001) ($a_{MgO} = 421.2$ pm) is only 1.0% and between Fe_3O_4 ($a_{Fe_3O_4} = 839.6$ pm) and MgO(001) is only 0.3% (comparing the halved lattice constant of $NiFe_2O_4$ and Fe_3O_4 with one lattice constant of MgO, respectively). Hence, only small strain and low defect densities are expected when depositing thin ferrite films on MgO(001).

In addition, the chemical composition of ferrites, i.e., the cationic ratio, can have significant impact on their structural, chemical, magnetic, and electronic properties [28, 29, 183, 184]. However, in contrast to investigations with focus on the cationic Co:Fe ratio within $Co_xFe_{3-x}O_4$ films [28, 29], a systematic study on the influence of the cationic stoichiometry in $Ni_xFe_{3-x}O_4$ (NFO) films is still lacking in literature. Thus, within this study, we prepare $Ni_xFe_{3-x}O_4$ thin films on MgO(001) via reactive molecular beam epitaxy and investigate the influence of the cationic stoichiometry on the

structural, chemical, and magnetic properties.
Chemical composition and structure of the $Ni_xFe_{3-x}O_4$ film surfaces were characterized by means of laboratory-based x-ray photoelectron spectroscopy (XPS) and low energy electron diffraction (LEED), respectively. Further, bulk structure was analyzed by synchrotron-based high resolution x-ray diffraction (HR-XRD), whereas film thicknesses were determined by analysis of x-ray reflectivity (XRR) measurements. The chemical composition and cationic valence states in deeper layers were investigated by hard x-ray photoelectron spectroscopy (HAXPES). In addition, angle resolved HAXPES (AR-HAXPES) measurements reveal information about the depth-dependent cationic stoichiometry. X-ray absorption (XAS) and x-ray magnetic circular dichroism (XMCD) measurements were complementary conducted to obtain information about the cationic valence states and site occupancies. Magnetic properties were characterized by means of superconducting quantum interference device (SQUID) magnetometry and additionally analyzed by applying the widely-used sum rules to the XMCD data.

6.2 Experimental details

In total, 14 $Ni_xFe_{3-x}O_4$ thin films with comparable thicknesses between 14.0 and 18.6 nm and varying Ni amounts x ($0 \leq x \leq 2.07$) were prepared on MgO(001) substrates via RMBE in an ultra high vacuum (UHV) chamber. However, due to the large number of samples, not every ferrite film could have been characterized by each conducted measurement technique. Nevertheless, each technique comprises data of a representative number of ferrite films and allows to follow the respective investigated characteristics in dependence of the Ni amount x.
Prior to film growth, the substrates were annealed at 400°C for 1 h in a molecular oxygen atmosphere of 1×10^{-4} mbar to obtain clean and well-ordered substrate surfaces. Chemical purity and surface structure were controlled after substrate annealing by means of laboratory-based *in situ* XPS and LEED, respectively. Thin NFO films were deposited on the cleaned substrates via thermal co-evaporation of Ni and Fe via electron bombardment of the respective pure metal rods in a molecular oxygen atmosphere of 5×10^{-6} mbar, while the substrate temperature was controlled to 250°C during film growth. The ratio of Ni and Fe in the prepared ferrite films was varied by tuning the flux of each evaporator to obtain NFO films with varying stoichiometry. Further, the overall deposition rate of 1-1.5 nm/min was approximately kept constant and the deposition time was accordingly adjusted to achieve comparable film thicknesses. The chemical composition, i.e., the Ni:Fe ratio in the ferrite films as well as the surface structure were again controlled *in situ* by means of surface sensitive XPS and LEED, respectively. For XPS measurements, Mg Kα radiation with a photon energy of $E_{ph}(Mg_{K\alpha}) = 1253.6$ eV was used.
After film preparation and *in situ* surface characterization (XPS, LEED), film thicknesses were determined *ex situ* by means of x-ray reflectivity (XRR) in a Philips X'Pert Pro diffractometer at Bielefeld University. Here, Cu Kα radiation with a photon energy of $E_{ph}(Cu_{K\alpha}) = 8048.0$ eV was used. XRR data was analyzed using an in-house-developed fitting tool, which is based on the Parratt algorithm [52] and the Névot-Croce roughness model [54].
Additionally, the ferrite thin film structure was characterized by high resolution x-ray diffraction (HR-XRD) measurements at beamline P08 of PETRA III at the Deutsches Elektronen-Synchrotron (DESY), Germany. Here, a photon energy of $E_{ph} = 18$ keV was used. Sample and detector were positioned with respect to the incident beam by using a six-circle (4S+2D-type) diffractometer (KOHZU NZD-3), while data acquisition was conducted by using a two-dimensional detector (PILATUS 100k or DECTRIS EIGER 1M). The HR-XRD measurements were conducted in θ-2θ geometry to perform scans along the (00L) crystal truncation rod (CTR) across the MgO(002) and NFO(004) Bragg reflections. Analysis of HR-XRD data was performed by using an in-house-developed fitting tool, which employs calculations based on full kinematic diffraction theory.

Complementary to laboratory-based surface sensitive XPS, HAXPES measurements were conducted at beamline P09 of PETRA III at DESY. In contrast to XPS, the higher used photon energy of $E_{ph} = 6$ keV for HAXPES measurements excites photoelectrons with higher kinetic energy and, thus, higher IMFPs and consequently higher probing depths. Thus, HAXPES is used to determine the chemical composition and cationic valencies not only in the near-surface region (as probed by XPS) but also in deeper subsurface layers. To record HAXPES spectra at beamline P09, the endstation is equipped with a SPECS Phoibos 225 HV hemispherical analyzer with a delayline detector.
Additionally, a wide-angle lens with ±30° angular acceptance was used to record angle-resolved HAXPES (AR-HAXPES) spectra of photoelectrons with different off-normal emission angles ϕ (cf. Fig. 4.6). The angular-dependent information depth D_I^{95}, from which 95% of photoelectrons (detected at the off-normal emission angle ϕ) originate, is given by

$$D_I^{95}(\phi) = -\lambda \cos\phi \ln(1 - 95/100) \tag{6.1}$$

with λ as the IMFP of the respective photoelectrons. Calculated values for λ and $D_I^{95}(\phi = 0)$ for electrons originating from Fe 2p and Ni 2p orbitals are given in Chap. 7. As a consequence, varying the detection angle ϕ in AR-HAXPES measurements allows for depth-dependent photoelectron detection. For this purpose, the incident angle $\theta = 40°$ between incident beam and surface plane was kept constant and data detected within acceptance angle sections of 8° were summed up for better statistics.
Magnetic properties of the prepared NFO films were characterized by using a SQUID of type S700X from CRYOGENIC. Here, the magnetization M was recorded at room temperature in dependence of the applied magnetic field H, which was tuned from +7 T down to -7 T and back again to obtain M vs H curves, which show hysteretic behavior for ferri-/ferromagnetic material.
Complementary, XAS and XMCD measurements were performed additionally to probe the cationic valence states and their occupancies within the film lattice. These measurements were performed at the Superconducting Vector Magnet Endstation at beamline 4.0.2 of the Advanced Light Source (ALS). All samples were measured at room temperature with an incident angle of 30° towards the [100] direction of the ferrite films. XMCD measurements were conducted in a magnetic field of 0.4 T along the x-ray beam. The degree of circular polarization was 90%. The XAS and XMCD spectra were measured across the Fe $L_{2,3}$ (690 - 750 eV) and Ni $L_{2,3}$ (835 - 890 eV) absorption edges in total electron yield (TEY) mode, which is very surface sensitive with probing depths of 2 - 5 nm in transition metal oxides [156–158]. XMCD data is further used to obtain information about the separate orbital and spin magnetic moments of the Ni and Fe cations within the ferrite films. Therefore, the sum rules derived by Thole *et al.* and Carra *et al.* [87, 88] and first successfully confirmed by Chen *et al.* [89] were applied. Here, the number of 3d holes as well as the correction factors derived by Teramura *et al.* [185] are adjusted according to the cationic stoichiometry within the respective film.

6.3 Results

6.3.1 Surface characterization: XPS and LEED

The chemical composition, i.e., the ratio between Ni and Fe of the prepared $Ni_xFe_{3-x}O_4$ films was determined by analyzing the Ni 3p and Fe 3p spectra measured *in situ* by surface sensitive XPS. The corresponding spectra are depicted in Fig. 6.1(a). For increasing Ni content x within the ferrite films, the intensity of the Ni 3p spectrum increases compared to the decreasing Fe 3p intensity. To determine the Ni:Fe ratio, the areas below the Ni 3p and Fe 3p spectra were

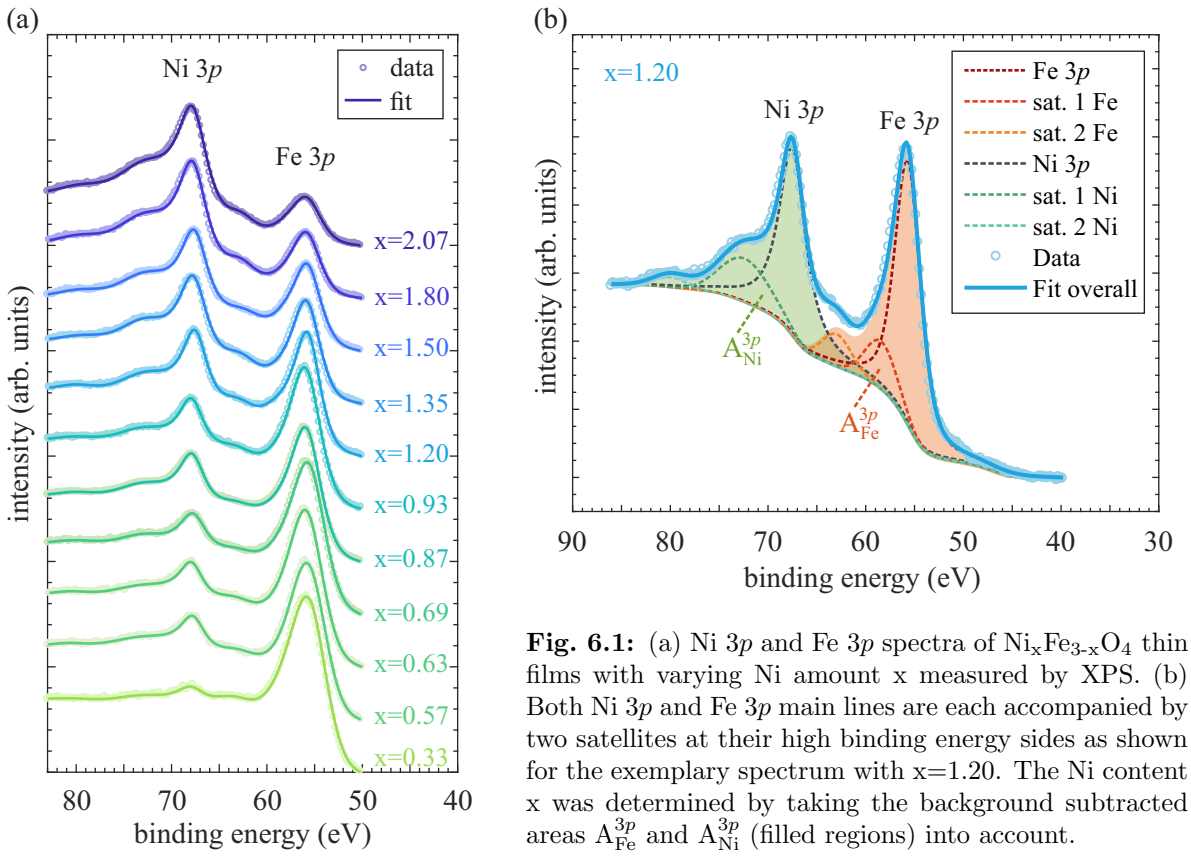

Fig. 6.1: (a) Ni 3*p* and Fe 3*p* spectra of $Ni_xFe_{3-x}O_4$ thin films with varying Ni amount x measured by XPS. (b) Both Ni 3*p* and Fe 3*p* main lines are each accompanied by two satellites at their high binding energy sides as shown for the exemplary spectrum with x=1.20. The Ni content x was determined by taking the background subtracted areas A^{3p}_{Fe} and A^{3p}_{Ni} (filled regions) into account.

determined after subtracting a Shirley background and deconvoluting each 3*p* spectrum into one main 3*p* photoemission line and two satellites located at the higher binding energy sides of each 3*p* spectrum [cf. Fig. 6.1(b)]. Main photoemission lines and satellites were each fitted by a convolution of a Lorentzian and a Gaussian, while the proportion of the Lorentzian and Gaussian contribution was kept variable during the fitting process. The sum of all fitted peaks results in the overall fits, which completely match with the measured data of each ferrite film, as seen in Fig. 6.1(a). As the binding energies of Ni 3*p* and Fe 3*p* spectra only differ by a few eV (∼12 eV) from each other, the energy dependent IMFPs $\lambda^{3p}_{Ni} \approx \lambda^{3p}_{Fe} = 2.3\,\text{nm}$ ($D^{95}_{I} = 6.9\,\text{nm}$) and the transmission function of the spectrometer are also very similar for these photoelectrons. As a consequence, the Ni amount x of the prepared ferrite films is determined via

$$x = 3\,\frac{I_{Ni}}{I_{Ni} + I_{Fe}} = 3\,\frac{A^{3p}_{Ni}/\sigma^{3p}_{Ni}}{A^{3p}_{Ni}/\sigma^{3p}_{Ni} + A^{3p}_{Fe}/\sigma^{3p}_{Fe}}\,, \tag{6.2}$$

with $A^{3p}_{Ni,Fe}$ as the area below the background subtracted Ni and Fe 3*p* spectra [including satellites, cf. Fig. 6.1(b)] and $\sigma^{3p}_{Ni,Fe}$ as the respective photoelectric cross sections [72]. The resulting Ni amounts x for the presented XPS spectra are given next to the respective measurements in Fig. 6.1(a). However, due to the variable contributions of the satellites in the 3*p* spectra, an experimental error of $\Delta x = \pm 0.08$ has to be considered.

In addition to the determination of the chemical composition by means of surface sensitive XPS, the surface structure of the prepared ferrite films is determined via *in situ* LEED measurements. Fig. 6.2 shows an exemplary selection of representative LEED pattern for varying Ni amounts in the ferrite films. For better comparison, the electron energy of 162 eV is the same for all depicted diffraction pattern.

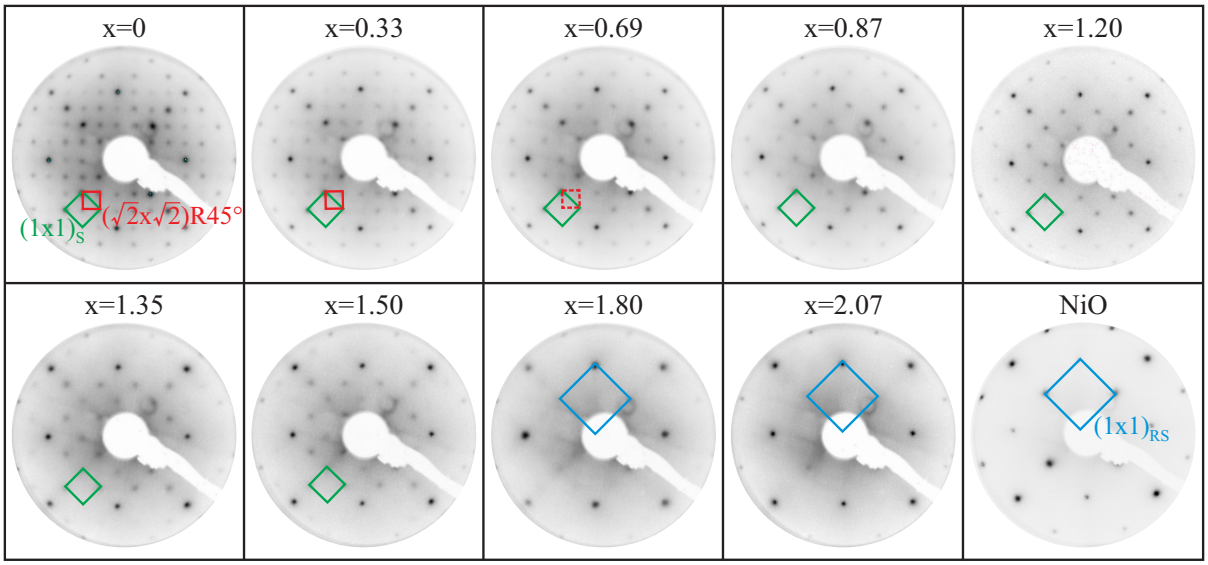

Fig. 6.2: LEED pattern at an electron energy of 162 eV for several exemplary $Ni_xFe_{3-x}O_4$ thin films on MgO(001) with varying Ni content x. The $(\sqrt{2} \times \sqrt{2})$R45° superstructure (red square), characteristic for an Fe_3O_4(001) surface (x = 0), vanishes for Ni contents of x ≥ 0.69, whereas the spinel type $(1 \times 1)_S$ surface structure (green square) stays visible up to x = 1.50. For x ≥ 1.80 solely a square $(1 \times 1)_{RS}$ structure (blue square) is obtained, which is four times larger than the reciprocal unit cell of the spinel type $(1 \times 1)_S$ structure and corresponds to the rock salt type surface unit cell, as seen by comparison to NiO.

For the Fe_3O_4 film (x = 0) a clear $(\sqrt{2} \times \sqrt{2})$R45° superstructure in addition to the spinel type (index S) square $(1 \times 1)_S$ surface structure is visible. This superstructure is characteristic for Fe_3O_4(001) surfaces and vanishes for Ni contents x ≥ 0.69, whereas the spinel type $(1 \times 1)_S$ surface structure stays visible up to x = 1.50. For even larger Ni contents x ≥ 1.80 solely a $(1 \times 1)_{RS}$ surface structure is visible, which exhibits a square reciprocal surface unit cell that is four times larger than the spinel type reciprocal $(1 \times 1)_S$ unit cell. This larger reciprocal unit cell corresponds to the surface unit cell of a rock salt type surface (index RS), as it is obtained for LEED at, e.g., NiO surfaces. These observations indicate the formation of merely spinel type structures up to a Ni content of x = 1.50 with parts of the surface formed by stoichiometric Fe_3O_4 up to a Ni amount of x = 0.69. However, the sole presence of a $(1 \times 1)_{RS}$ surface structure as obtained for x ≥ 1.80 with a four times larger reciprocal surface unit cell (meaning a four times smaller surface unit cell in real space) compared to the unit cell of the spinel type $(1 \times 1)_S$ structure points to a major formation of rock salt type structures at the surface.

6.3.2 XRR

In addition to the *in situ* surface characterization by means of XPS and LEED, XRR measurements were conducted *ex situ* after transport under ambient conditions. The resulting measurements of some representative NFO films with varying Ni content x and the corresponding calculated XRR curves are shown in Fig. 6.3. For all films clear Kiessig fringes, which result from interference of x-rays reflected at the film surface and at the interface between film and substrate, are visible and therefore point to low interface and surface roughnesses independent of the Ni amount x. For the calculations of XRR curves, the refractive index of the MgO substrate at the used x-ray energy of $E_{ph}(Cu_{K\alpha}) = 8048.0$ eV was kept fixed [186]. In contrast, thickness, interface/surface roughness, and refractive index of the film were used as free fit parameters. As seen in Fig. 6.3, the calculated

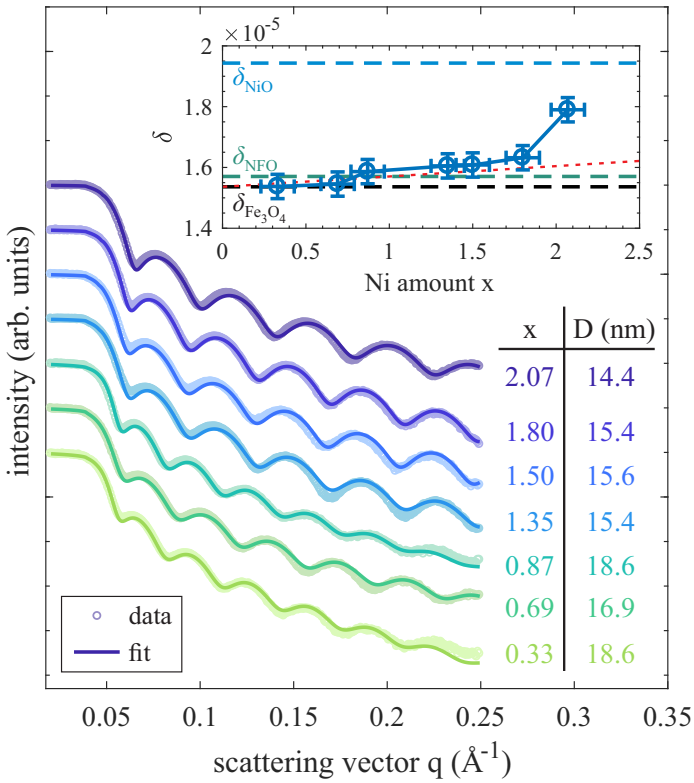

Fig. 6.3: XRR measurements for $Ni_xFe_{3-x}O_4$ thin films of film thickness D with varying Ni content x. The calculated XRR curves are in excellent agreement with the measured data. Clear Kiessig fringes point to low surface and interface roughnesses for all films. The dispersion δ is increasing for increasing Ni amount x (shown in the inset). The dispersion values for stoichiometric Fe_3O_4, $NiFe_2O_4$ (NFO), and NiO at the used x-ray energy of 8048.0 eV (Cu Kα) are depicted for comparison (dashed lines). The red dotted line represents the (linear) evolution of δ, if Ni cations were solely incorporated on spinel type lattice sites with increasing x.

XRR curves are in excellent agreement with the measured data, pointing to single homogeneous films for all Ni contents. The resulting film thicknesses range from 14.0 to 18.6 nm (not all curves are shown here). More remarkably, the obtained dispersions δ ($\delta \propto \rho_{el}$ with ρ_{el} as the electron density) are increasing for an increasing Ni amount x in the ferrite film (cf. inset of Fig. 6.3), as it is expected considering the literature values of stoichiometric Fe_3O_4 ($\delta_{Fe_3O_4} = 1.54 \cdot 10^{-5}$), $NiFe_2O_4$ ($\delta_{NFO} = 1.57 \cdot 10^{-5}$), and NiO ($\delta_{NiO} = 1.94 \cdot 10^{-5}$) [186]. For Ni amounts $x \leq 1.50$ only a slight increase of δ is observed with increasing x, matching the linear evolution obtained theoretically if Ni and Fe cations solely occupy spinel type lattice sites (red dotted line) according to the slight increase of the literature values of Fe_3O_4 and $NiFe_2O_4$. In contrast, for $x \geq 1.80$ (in particular for $x = 2.07$) the dispersions are clearly exceeding these values and are approaching the dispersion expected for NiO, which enforces the assumption of NiO-type phase formations.

6.3.3 HR-XRD

To characterize the structure of the prepared NFO films HR-XRD measurements were performed after transport to beamline P08 of PETRA III at DESY. The recorded data along the (00L) CTR close to the MgO(002) Bragg condition for several representative NFO films with varying Ni amount are depicted in Fig. 6.4(a). For all measurements, a clear NFO(004) Bragg peak is visible, which is located at slightly higher L values than the MgO(002) reflection due to the slightly lower layer distance of the ferrite film compared to the layer distance of the MgO substrate. Moreover, the measured (00L) CTRs exhibit clear Laue fringes, pointing to smooth interfaces and high crystalline film quality, which is in accordance with the XRR results (cf. Fig. 6.3).
Further, the recorded HR-XRD data was analyzed using calculations based on full kinematic diffraction theory. The resulting models show very good agreement with the measured diffraction data, as seen in Fig. 6.4(a). From these calculations, parameters like the vertical layer distance d_{vert}, the interface distance d_{IF}, the number of film monolayers (ML) N_{ML}, as well as the ferrite film surface

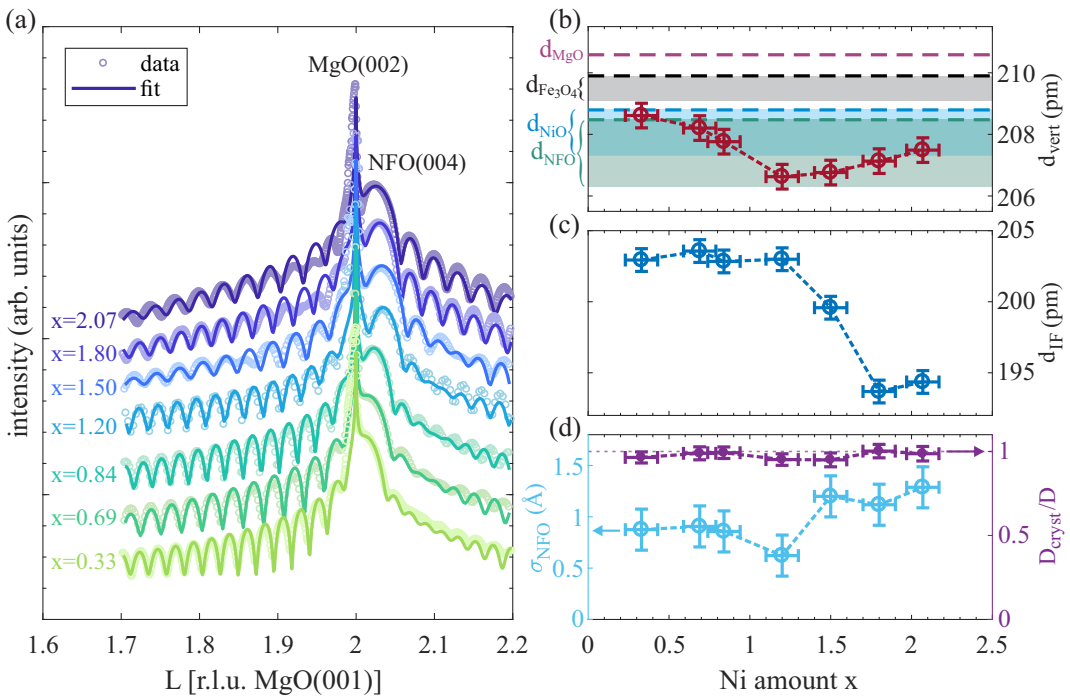

Fig. 6.4: (a) HR-XRD measurements along the (00L) CTR across the MgO(002) and NFO(004) Bragg conditions with corresponding calculations based on full kinematic diffraction theory for NFO films with different Ni amounts x. The calculated models show very good agreement with the measured data. Clear Laue fringes point to smooth interfaces and high crystalline quality. (b) Vertical layer distance d_{vert} compared to (relaxed) bulk layer distances of MgO, Fe_3O_4, $NiFe_2O_4$, and NiO (dashed horizontal lines). The filled regions cover the range between completely relaxed (upper boundary) and fully compressed layer distances (lower boundary), assuming an adaption of the film to the substrate lattice. (c) Interface distance d_{IF}, and (d) film surface roughness σ_{NFO} and (vertical) crystalline amount D_{cryst}/D as resulting from the calculated models for varying Ni amount x.

roughness σ_{NFO} are extracted. From the number of monolayers N_{ML} and the vertical layer distance d_{vert}, the crystalline film thickness $D_{cryst} = N_{ML} d_{vert}$ can be determined and compared to the total film thickness D (as determined by XRR, see above). The results d_{vert}, d_{IF}, as well as σ_{NFO} and the vertical crystalline amount D_{cryst}/D in dependence of the Ni amount x within the ferrite films are depicted in Fig. 6.4(b), (c), and (d), respectively.

The vertical layer distance d_{vert} within the NFO films decreases up to a Ni amount of $x = 1.20$ and increases for higher Ni content up to $x = 2.07$ [see Fig. 6.4(b)], which can be followed by regarding the position of the NFO(004) Bragg peak, which is increasing in L up to $x = 1.20$ and decreasing again for higher x [see Fig. 6.4(a)], meaning decreasing/increasing layer distances, respectively. This behavior can be understood qualitatively by comparing this trend with the bulk layer distances of stoichiometric Fe_3O_4, $NiFe_2O_4$, and NiO [cf. dashed lines within Fig. 6.4(b)]. Here, Fe_3O_4 ($x = 0$) exhibits the largest layer distance of $d_{Fe_3O_4} = 209.9$ pm, whereas for stoichiometric $NiFe_2O_4$ ($x = 1$) the smallest bulk layer distance of $d_{NiFe_2O_4} = 208.5$ pm is obtained, which can explain the decrease of d_{vert} for increasing x between $0 \leq x \leq 1.2$. In contrast, bulk NiO exhibits again a slightly larger layer distance of $d_{NiO} = 208.8$ pm compared to $NiFe_2O_4$. Thus a further increase of the Ni amount above the stoichiometric value of $x = 1$ should also result in an increase of the layer distance d_{vert}, if further Ni cations result in NiO-type formations. In fact, this behavior is observed here for $x > 1.20$ and therefore consistent with the obtained results, if saturation of the spinel type lattice sites is assumed for $x \geq 1.20$. In accordance with LEED and XRR results, such a saturation of the spinel-type lattice sites can be assumed for the range $1.20 \leq x \leq 1.50$.

However, as seen in Fig. 6.4(b), all films are compressively strained in vertical direction, since the absolute values of d_{vert} are clearly below the bulk values of Fe_3O_4, $NiFe_2O_4$, and NiO for stoichiometries of $x < 1$, $x \approx 1$, and $x > 1$, respectively. This observation can be understood by assuming a lateral adaption of the ferrite film to the substrate lattice and, consequently, the presence of lateral tensile strain, which results in vertical compression within the ferrite films. A more detailed (quantitative) analysis of this assumption is given in Sec. 6.4.
Furthermore, the interface distance d_{IF} is smaller than the determined layer distances and almost constant for Ni amounts $x \leq 1.20$, whereas it is significantly decreasing for further increasing Ni content [see Fig. 6.4(c)]. Complementary to the LEED results (cf. Fig. 6.2), which indicate the emergence of an almost single rock salt like structure at the surface for $x > 1.50$, the observed trend of the interface distance also points to the formation of another structural phase (at the interface) for a Ni content $1.20 \leq x \leq 1.50$.
The film surface roughness σ_{NFO}, as determined from HR-XRD analysis [cf. Fig. 6.4(d)], is very low ($\sigma_{NFO} < 1.0$ Å) and constant for $x \leq 1.20$, whereas it is only slightly increased but constant for $x \geq 1.50$ ($\sigma_{NFO} \approx 1.3$ Å). In fact, these very low values for all films indicate smooth surfaces, which is in accordance with the sharp reflexes obtained in the LEED pattern (see Fig. 6.2), and comes along with complete vertical crystallinity $D_{cryst} = D$ independent of the Ni content x [cf. Fig. 6.4(d)].

6.3.4 HAXPES

Complementary to surface sensitive XPS, HAXPES measurements were conducted at P09 of PETRA III at DESY to determine the chemical composition and the cationic valencies also in deeper subsurface layers. While for laboratory based (soft) XPS the maximum information depth $D_I^{95}(\phi = 0)$ [cf. Eq. (6.1)] of the analyzed Ni $2p$ and Fe $2p$ photoelectrons passing through $NiFe_2O_4$ is about 3-4 nm, it is crucially enhanced to about 22 nm for HAXPES with an x-ray energy of 6 keV. Hence, the performed HAXPES measurements completely probe the prepared NFO films in vertical direction, as the film thicknesses of up to 18.6 nm are still well below the maximum information depths. This determination is supported by the fact that the Mg $1s$ photoemission signal originating from the substrate is still visible in all HAXPES measurements.
The recorded Ni $2p$ spectra for $Ni_xFe_{3-x}O_4$ films with varying x are depicted in Fig. 6.5(a). All spectra exhibit the main spin-orbit split $2p_{1/2}$ and $2p_{3/2}$ photoemission peaks with satellites ~7 eV above the main lines, which are characteristic for Ni^{2+} present in several oxides as, e.g., NiO or $NiFe_2O_4$ [187–189]. For a more detailed analysis, the Ni $2p_{3/2}$ spectra were fitted by several peaks [cf. inset of Fig. 6.5(b)], each one described by a convolution of a Lorentzian and a Gaussian, whereas the ratio between both contributions was kept variable during fitting. The number and positions of individual peaks were based on the theoretical description of Ni $2p$ spectra by Veenendaal and Sawatzky [189], resulting in one peak for the main photoemission line in addition to one peak describing the high binding energy shoulder, as well as four contributions to the satellite structure located ~7 eV above the main Ni $2p_{3/2}$ line [cf. Fig. 6.5(b)].
As seen in Figs. 6.5(a) and (b), the Ni $2p$ spectra undergo several changes when varying the Ni content within the ferrite films. First, the binding energy position of the Ni $2p_{3/2}$ main photoemission line (determined as the position of the maximum overall intensity) for Ni amounts $x < 1.0$ remains constant at ~855.2(1) eV, while it is significantly decreasing for further increasing Ni content $x > 1.0$ [cf. Figs. 6.5(b) and (c)]. For Ni amounts close to the stoichiometric $NiFe_2O_4$ value of $x = 1$ the Ni $2p_{3/2}$ position is comparable to the value of 855.0(2) eV for Ni in $NiFe_2O_4$ as reported by Kuschel *et al.* [36]. Since the Ni $2p_{3/2}$ position of ~854.5 eV as reported for NiO [190] is significantly lower than the Ni $2p_{3/2}$ position in $NiFe_2O_4$, the observed subsequent decrease of the binding energy down to ~854.7 eV for $x = 2.07$ is a behavior to be expected when further increasing the Ni content.

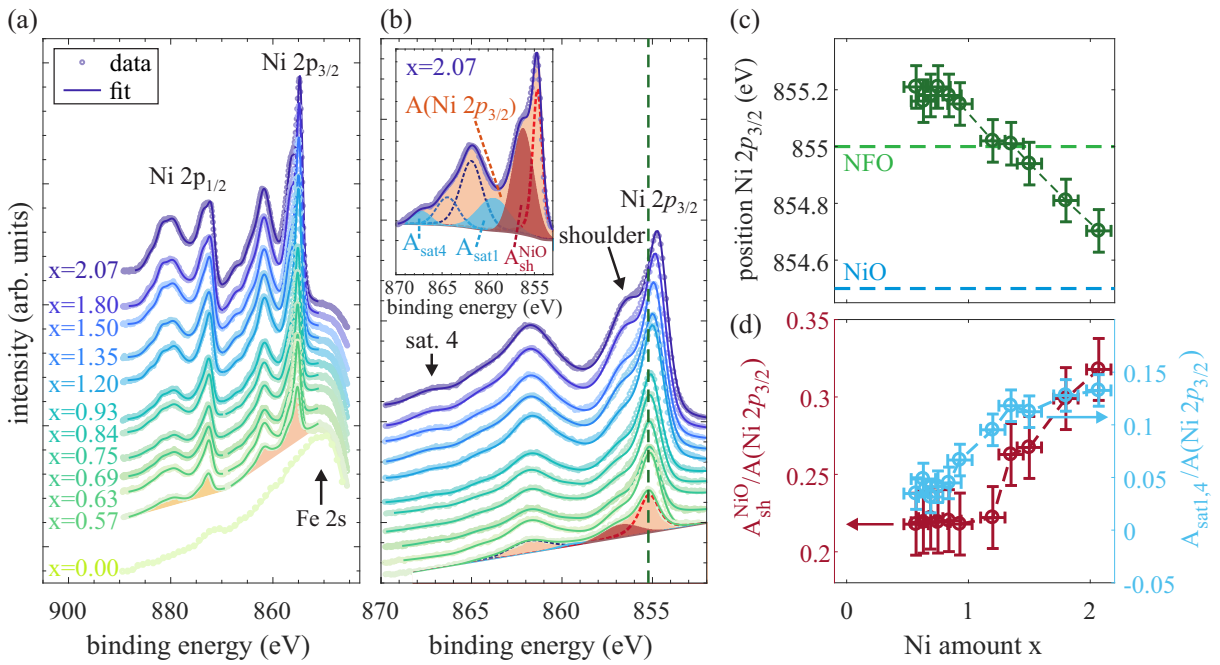

Fig. 6.5: (a) Ni $2p$ spectra of several prepared $Ni_xFe_{3-x}O_4$ films with varying Ni content x measured by HAXPES along with overall fits (solid lines). (b) Enlarged section of the Ni $2p_{3/2}$ region with an emerging high binding energy shoulder of the Ni $2p_{3/2}$ main line for increasing Ni amount. The deconvoluted peaks for the overall fit are depicted in the inset exemplarily for $x = 2.07$. (c) Position of the maximum intensity of the Ni $2p_{3/2}$ main line. (d) Background subtracted areas of the high binding energy shoulder A_{sh}^{NiO} and of the emerging satellites $A_{sat1,4} = A_{sat1} + A_{sat4}$ compared to the area below the whole Ni $2p_{3/2}$ spectrum A(Ni $2p_{3/2}$).

In addition to the decreasing Ni $2p_{3/2}$ position, the high binding energy shoulder ~1.5 eV apart from the main line is significantly enhanced [and visibly distinguishable from the main line, cf. Fig. 6.5(b)] for $x > 1.35$ compared to lower Ni contents. In particular, the background subtracted area A_{sh}^{NiO} of this shoulder in relation to the total area A(Ni $2p_{3/2}$) of the Ni $2p_{3/2}$ spectrum is steadily increasing for increasing Ni content $x \geq 1.35$ [cf. Fig. 6.5(d)]. This shoulder can be theoretically described as a result of a screening process by electrons not originating from the oxygen orbitals around the respective Ni atom, but from neighboring NiO_6 clusters (with Ni^{2+} cations occupying octahedral sites) [189]. Hence, the appearance and enhancement of this shoulder can be ascribed to the presence and increasing content of NiO agglomerations within the ferrite films with increasing x.

Furthermore, the satellite structure ~7 eV above the main Ni $2p_{3/2}$ line slightly changes during variation of the Ni content. In particular, the intensities of the two satellites at ~859.2 (sat. 1) and ~866.9 eV (sat. 4) change for varying x. Fig. 6.5(d) shows the summed up intensities/background subtracted areas $A_{sat1,4} = A_{sat1} + A_{sat4}$ in relation to the overall intensity A(Ni $2p_{3/2}$) of the Ni $2p_{3/2}$ spectrum. While the intensity of both satellites almost vanishes for low Ni content $x < 1.0$, it increases with further increasing x above the stoichiometric value ($x > 1.0$). According to Veenendaal and Sawatzky, these satellites also result from the presence of neighboring NiO_6 clusters. Hence, the observed increasing intensities of both high binding energy shoulder and the mentioned satellites correspond to the enhanced formation of NiO agglomerations within the ferrite films with increasing Ni amount x.

In addition, Fe $2p$ HAXPES spectra were recorded to determine the existent valence states of Fe cations within the ferrite films with varying Ni:Fe ratios, as depicted in Fig. 6.6(a). For analysis, both spin-orbit split Fe $2p_{3/2}$ and Fe $2p_{1/2}$ background subtracted spectra were fitted by several

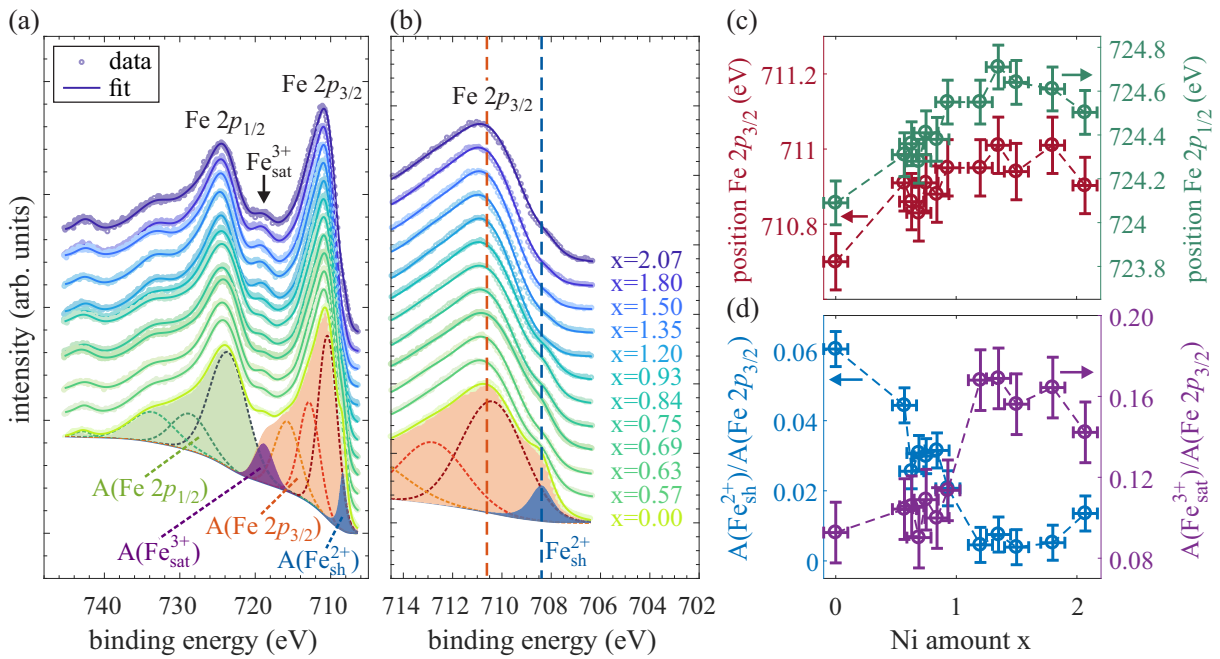

Fig. 6.6: (a) Fe $2p$ spectra of several prepared $Ni_xFe_{3-x}O_4$ films with varying Ni content x measured by HAXPES along with overall fits (solid lines). The deconvoluted peaks for the overall fit are depicted exemplarily for the Fe_3O_4 film (x = 0) with filled background subtracted areas of the Fe $2p_{3/2}$ (red) and the Fe $2p_{1/2}$ spectrum (green). (b) Enlarged section of the Fe $2p_{3/2}$ region with a low binding energy shoulder Fe^{2+}_{sh} of the Fe $2p_{3/2}$ main line at ~708.4 eV. Additionally, the position of the Fe $2p_{3/2}$ maximum as reported in literature for the case of Fe_3O_4 is marked by a (red) dashed line. (c) Positions of the maximum intensity of the Fe $2p_{3/2}$ and Fe $2p_{1/2}$ main lines. (d) Background subtracted areas of the low binding energy shoulder $A(Fe^{2+}_{sh})$ and of the Fe^{3+} satellite $A(Fe^{3+}_{sat})$ compared to the area below the whole Fe $2p_{3/2}$ spectrum A(Fe $2p_{3/2}$).

functions, which are each described by a convolution of a Lorentzian and a Gaussian. The ratio between both contributions in each peak was again kept variable during the fitting procedure. Here, the Fe $2p_{3/2}$ region is analyzed in more detail. It generally consists of two peaks forming the main photoemission line as well as of two charge-transfer satellites at ~715.6 and ~718.8 eV, which can be assigned to the presence of Fe^{2+} and Fe^{3+}, respectively [191]. Moreover, a shoulder Fe^{2+}_{sh} at the low binding energy side of the main line at ~708.4 eV [cf. enlarged region of the Fe $2p_{3/2}$ region in Fig. 6.6(b)] results from the presence of Fe^{2+} cations [188].

First, the binding energies of the main Fe $2p_{3/2}$ and Fe $2p_{1/2}$ lines can serve as an indication for the major Fe valency. Both values were determined as the positions of the maximum intensity of the overall fit in each region and are depicted in Fig. 6.6(c) in dependence of the Ni amount x. For the Fe_3O_4 film (x = 0), binding energies of 710.7(1) and 724.1(1) eV are obtained for the Fe $2p_{3/2}$ and Fe $2p_{1/2}$ line, respectively, which both are in accordance with the values of stoichiometric Fe_3O_4 reported in literature [191]. Both positions shift to higher values for increasing Ni content in the regime x < 1. If x is further increased (x > 0), both Fe $2p_{3/2}$ and Fe $2p_{1/2}$ positions approximately remain constant at 711.0(1) and 724.6(1) eV, respectively, which agree with reported values obtained for Fe_2O_3, where only Fe^{3+} cations are present [191].

Second, the intensities/background subtracted areas $A(Fe^{3+}_{sat})$ and $A(Fe^{2+}_{sh})$ of the respective Fe^{3+}_{sat} charge-transfer satellite at ~718.8 eV and the low binding energy shoulder Fe^{2+}_{sh} at ~708.4 eV are determined in dependence of x in relation to the total area of the Fe $2p_{3/2}$ spectrum A(Fe $2p_{3/2}$) [cf. Fig. 6.6(d)]. The Fe^{3+} satellite is almost constant for low Ni amounts, whereas its intensity is significantly increased when surpassing the stoichiometric Ni amount of x = 1 and almost constant

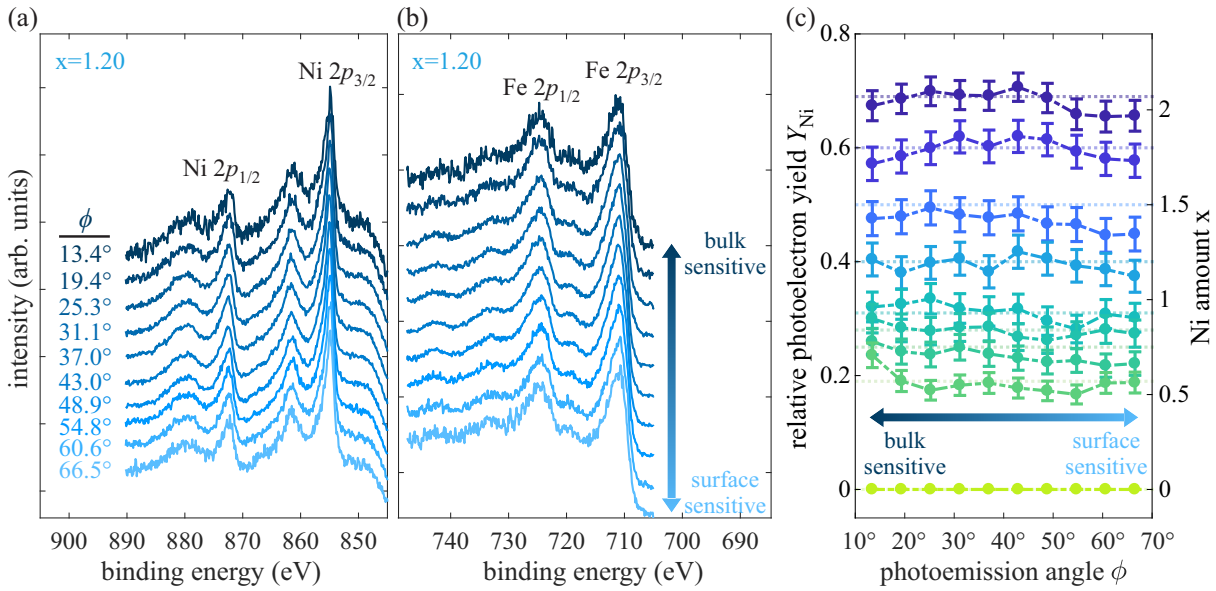

Fig. 6.7: (a) Ni $2p$ spectra and (b) Fe $2p$ spectra recorded at different off-normal photoemission angles ϕ for the sample with $x = 1.20$. Low photoemission angles correspond to more bulk-like sensitivity, whereas higher photoemission angles mean higher surface sensitivity. (c) Relative photoelectron yields Y_{Ni} and Ni amounts $x = 3 \cdot Y_{\mathrm{Ni}}$ in dependence of the photoemission angle for films with varying Ni content. The respective Ni amounts x as determined by surface sensitive XPS are indicated by dotted lines.

for further increased x. In contrast, the intensity of the low binding energy Fe^{2+} shoulder is continuously decreasing for an increasing Ni amount up to $x \approx 1$, while it almost vanishes for even higher Ni content. Both observations therefore constitute a decreasing relative amount of Fe^{2+} cations when increasing the Ni content up to $x = 1$ in the ferrite films, whereas the relative Fe^{3+} amount is increased and constant for $x > 1$. Further, this behavior is in accordance with the shift to higher binding energies of the Fe $2p_{3/2}$ and Fe $2p_{1/2}$ spectra, as demonstrated above.
Note that only for the ferrite film with the highest Ni content of $x = 2.07$ a slight decrease of the Fe^{3+} satellite and a small increase of the Fe^{2+} shoulder is noticed, which is in accordance with the small shift of the Fe $2p_{3/2}$ and Fe $2p_{1/2}$ main lines back to lower binding energies for this sample. These observation indicate a regain of Fe^{2+} cations in exchange of Fe^{3+} valencies for Ni amounts of $x > 2$. However, to determine a clear trend this behavior should be investigated in more detail by examining ferrite films with even higher Ni content $x > 2.07$.
In addition to the investigation of the cationic valencies within the prepared $Ni_xFe_{3-x}O_4$ films, a depth-dependent determination of the cationic stoichiometry is conducted by means of angle resolved detection of Ni $2p$ and Fe $2p$ spectra. Figs. 6.7(a) and (b) show the respective AR-HAXPES Ni $2p$ and Fe $2p$ spectra detected at different photoemission angles ϕ exemplarily for the ferrite film with $x = 1.20$. Lower angles of photoemission correspond to a more bulk-like sensitivity, whereas higher photoemission angles mean higher surface sensitivity. All Ni and Fe $2p$ spectra exhibit no significant deviations in shape and position among each other in dependence of the detection angle. Thus, the cationic valencies (as determined above) do not change with depth, which points to a uniform distribution of the determined cationic oxidation states in vertical direction.
Further, a depth-dependent determination of the Ni amount x is performed by calculating the relative photoelectron yield

$$Y_{\mathrm{Ni}} = \frac{I^{2p}_{\mathrm{Ni}}}{I^{2p}_{\mathrm{Ni}} + I^{2p}_{\mathrm{Fe}}} = \frac{A^{2p}_{\mathrm{Ni}}/\sigma^{2p}_{\mathrm{Ni}}}{A^{2p}_{\mathrm{Ni}}/\sigma^{2p}_{\mathrm{Ni}} + A^{2p}_{\mathrm{Fe}}/\sigma^{2p}_{\mathrm{Fe}}} \tag{6.3}$$

from the numerically integrated areas $A^{2p}_{Ni,Fe}$ after subtracting a Shirley background from the AR-HAXPES Ni and Fe $2p$ spectra and using the differential photoelectric cross sections $\sigma^{2p}_{Ni,Fe}$ from Trzhaskovskaya *et al.* under consideration of non-dipole parameters of the photoelectron angular distribution [74, 75]. With this, the Ni amount $x = 3 \cdot Y_{Ni}$ for each sample is determined in dependence of the detection angle ϕ. The results are depicted in Fig. 6.7(c) along with the calculated values obtained from surface sensitive XPS (dotted lines). The Ni amount as determined by AR-HAXPES analysis shows no significant variations in dependence of the photoemission angle ϕ, indicating uniform vertical distributions of Ni and Fe cations within the films independent of the Ni content. Further, within the experimental errors the Ni amount x as determined by AR-HAXPES is similar to the values obtained by surface sensitive XPS for all films. Hence, all films can be considered as exhibiting homogeneous cationic distributions in vertical direction without indicating the existence of layers with separated phases within the films or at the interface/surface.

6.3.5 SQUID

Magnetic characterization of the prepared $Ni_xFe_{3-x}O_4$ films with varying x was performed by applying SQUID magnetometry. Therefore, M vs H measurements with a maximum applied magnetic field of 7 T oriented parallel to the sample surface in [100] direction (according to the magnetic easy axis of Fe_3O_4 and $NiFe_2O_4$) of substrate and film (in-plane geometry) were conducted at 300 K sample temperature. To determine the magnetic response solely of the $Ni_xFe_{3-x}O_4$ film, a linear background stemming from the diamagnetic response of the MgO substrate was subtracted from the data. The resulting M vs H curves are depicted in Fig. 6.8.

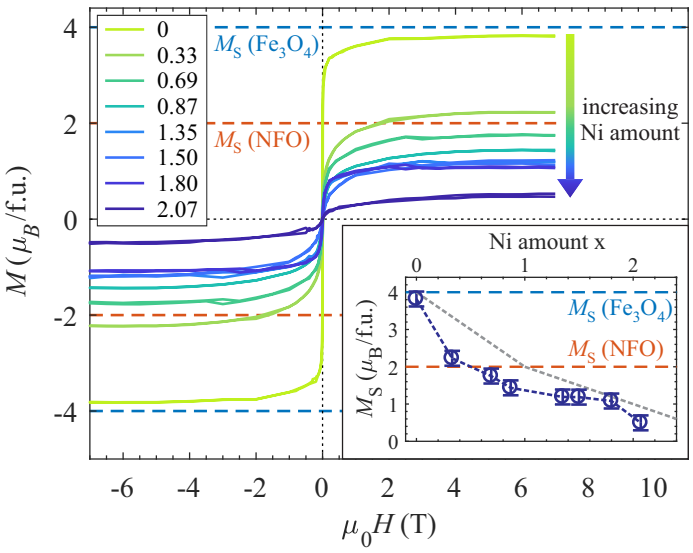

Fig. 6.8: M vs H measurements for $Ni_xFe_{3-x}O_4$ thin films with varying Ni content x measured by SQUID magnetometry. The saturation magnetization M_S is decreasing for increasing Ni content (see inset). The M_S values for stoichiometric Fe_3O_4 and $NiFe_2O_4$ (NFO) are depicted for comparison (dashed horizontal lines). If Ni^{2+} cations ideally substitute Fe^{2+} for $x \leq 1$ on octahedral sites and further Ni^{2+} cations in the overstoichiometric regime $x > 1$ solely occupy octahedral sites, a linear decrease is expected with a vanishing saturation magnetization for $x = 3$. Both linear decreases are indicated by the grey dashed line in the inset.

All magnetization curves exhibit hysteretic behavior, which is characteristic for ferro-/ferrimagnetic material, with magnetic saturation reached at an applied magnetic field above ~5 T. However, the coercive fields H_C (where the magnetization vanishes) is very small with values between 5 and 20 mT without showing any trend in dependence of the Ni content x. In contrast, the saturation magnetization M_S of the ferrite films exhibits a continuous decrease with increasing x (cf. inset of Fig. 6.8). For the Fe_3O_4 film ($x = 0$) the saturation magnetization almost matches the bulk magnetization of stoichiometric Fe_3O_4 of $4\,\mu_B$/f.u. (if only spin magnetic moments are considered and the comparably small orbital magnetic moments are neglected due to orbital quenching). However, already for $x \geq 0.87$ the saturation magnetization drops below the expected value of $2\,\mu_B$/f.u. for

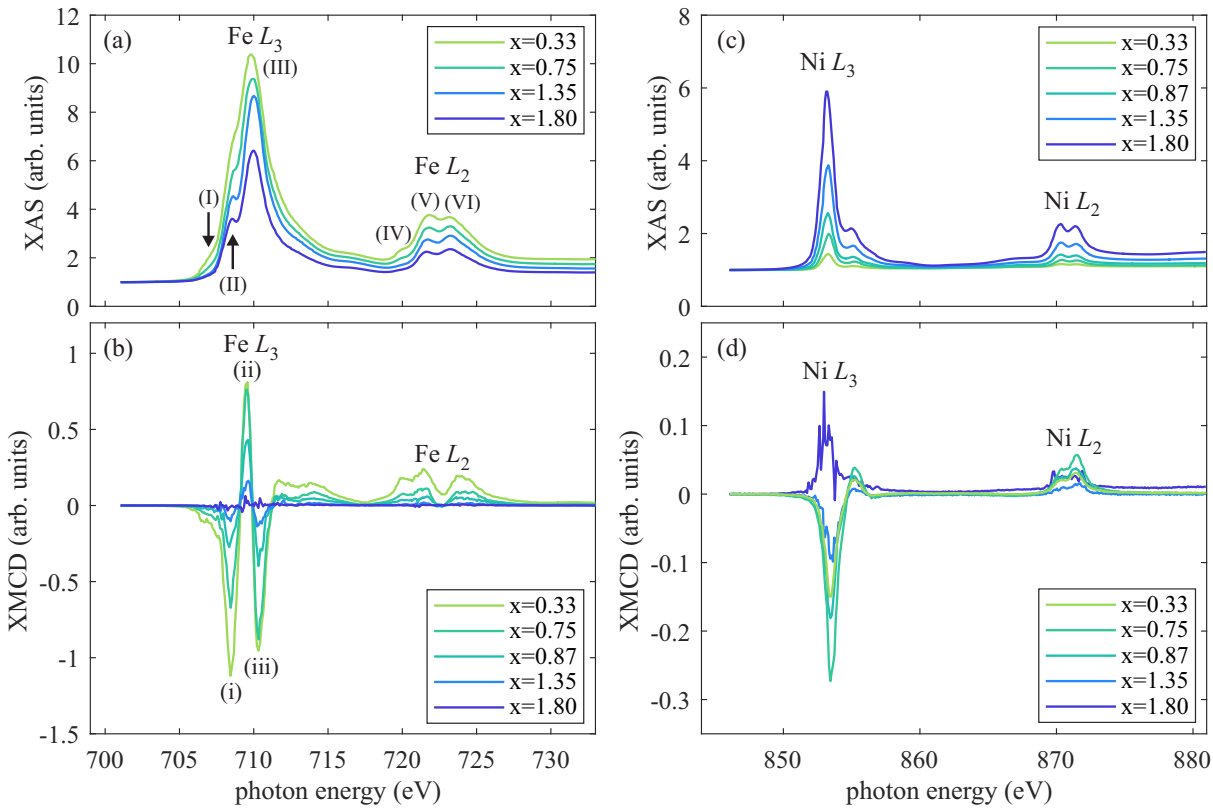

Fig. 6.9: (a) XAS and (b) XMCD spectra of the ferrite films with varying Ni content x at the Fe $L_{2,3}$ edges. (c) Respective XAS and (d) XMCD spectra at the Ni $L_{2,3}$ edges. Not all recorded spectra are depicted due to reasons of clarity.

stoichiometric bulk $NiFe_2O_4$. A further increase of x also results in a further decrease of M_S down to a value of $0.5\,\mu_B$/f.u. for the film with $x = 2.07$. If ideal substitution of Fe^{2+} by Ni^{2+} cations on octahedral sites is considered within the understoichiometric regime ($x \leq 1$) a linear decrease from $4\,\mu_B$/f.u. for $x = 0$ to $2\,\mu_B$/f.u. for $x = 1$ would be expected (grey dashed line in the inset of Fig. 6.8). If further incorporation of Ni^{2+} cations in the overstoichiometric regime ($x > 1$) solely takes place on octahedral sites, which would give rise to the formation of NiO-type agglomerations, a further linear decrease with a vanishing saturation magnetization for $x = 3$ should be expected (grey dashed line in the inset of Fig. 6.8). Though, the determined values within both regimes remain below this theoretical predictions. This discrepancy could be mainly explained by the presence of antiphase boundaries or by different Ni^{2+} occupancies than in the ideal case as described above.

6.3.6 XMCD

Complementary to the conducted HAXPES and SQUID investigations, XMCD measurements were performed additionally to probe the cationic valence states as well as their occupancies and to obtain information about the orbital and spin magnetic moments of the Ni and Fe cations within the ferrite films. The recorded XMCD spectra at the Fe $L_{2,3}$ and Ni $L_{2,3}$ absorption edges for varying Ni content x are depicted in Figs. 6.9(b) and (d), respectively, in addition to the corresponding XAS spectra in Figs. 6.9(a) and (c).

Due to the decreasing relative Fe content within the films the overall intensity of the total Fe $L_{2,3}$ XAS signal also decreases with increasing x. In addition to this decrease, some further variations

in the shape of the spectra are observed. First, the pre-edge feature (I) [cf. Fig. 6.9(a)] at the low energy side of the Fe L_3 edge, which is still present for $x < 1$, decreases and vanishes for $x > 1$. Second, with increasing Ni content x a more distinct feature (II) becomes distinguishable from the main Fe L_3 absorption line (III). As feature (I) can be attributed to the presence of octahedrally coordinated Fe^{2+}_{oct}, its decrease in intensity can be assigned to the decreasing and vanishing Fe^{2+}_{oct} content, which is in excellent agreement with the HAXPES results (cf. Sec. 6.3.4). In addition, the fact that feature (II) is clearly visible for $x > 1$ and not smeared out with the main Fe L_3 line also indicates the loss of Fe^{2+}_{oct}, as the Fe^{2+}_{oct} absorption spectrum would add significant intensity between lines (II) and (III) and result in a broader smeared out main Fe L_3 absorption line as it is observed for $x < 1$ [192]. A similar behavior can be observed at the Fe L_2 absorption edge, where features (IV) and (V) are decreasing compared to feature (VI) with increasing x, also verifying the decreasing Fe^{2+}:Fe^{3+} ratio.

In addition, the respective XMCD spectra of the Fe $L_{2,3}$ absorption edges in Fig. 6.9(b) also reasonably decrease in intensity with decreasing Fe content. For the film with a Ni content of $x = 1.80$, the dichroic signal completely vanishes. The distinct features (i) at 708.4 eV, (ii) at 709.5 eV, and (iii) at 710.3 eV can be mainly attributed to Fe^{2+}_{oct}, Fe^{3+}_{tet}, and Fe^{3+}_{oct} cations, respectively [193]. Here, the ferromagnetic coupling between Fe^{2+}_{oct} and Fe^{3+}_{oct} results in negative dichroic signals (i) and (iii), while the antiferromagnetic coupling of these cations to Fe^{3+}_{tet} causes a positive feature (ii), mainly resulting from absorption of tetrahedral Fe^{3+}_{tet}. The absolute magnitudes of features (ii) and (iii) are approximately similar as compared within the single measurements, indicating a constant Fe^{3+}_{tet}:Fe^{3+}_{oct} ratio with similar tetra- and octahedral site occupancies of Fe^{3+} cations independent of the Ni content. For $x = 0.33$, signal (i) exhibits a higher magnitude than feature (iii), whereas for higher Ni content the intensity of (i) decreases below the intensity of (iii). As the spectrum of Fe^{2+}_{oct} mainly contributes to the minimum (i), this observation can be once more assigned to the decrease of the Fe^{2+}_{oct} amount with increasing x.

In contrast to the intensity decrease of the Fe $L_{2,3}$ absorption spectra, the overall intensity of the Ni $L_{2,3}$ XAS spectra increases with increasing x. However, the shapes of the spectra remain constant independent of the Ni content x and closely resemble reported NiO and $NiFe_2O_4$ x-ray absorption spectra [21, 187, 194–196]. This indicates a major presence of only Ni^{2+}_{oct} cations within the films without any significant variation in the valence state or site occupancy with varying x. Moreover, the shape of the Ni $L_{2,3}$ XMCD spectra up to $x = 1.35$ are also in accordance with XMCD spectra reported for $NiFe_2O_4$ [21, 195, 196], confirming the presence of mainly Ni^{2+}_{oct} cations. The dichroic signal rises up to $x = 0.75$ and decreases again for higher Ni content. More remarkably, the sign of the Ni L_3 dichroic signal changes from negative to positive for the film with $x = 1.80$, while the sign of the Ni L_2 edge remains positive. This indicates a decreasing contribution of the spin magnetic moment and a major orbital contribution to the total magnetic moment [197] of Ni^{2+} cations for $x \geq 1.80$. Further, this observation could be correlated to a change of the major site occupancy. However, quantitative analysis by means of charge transfer multiplet calculations should be applied to shed light on this assumption.

Both Fe and Ni $L_{2,3}$ XMCD spectra were analyzed by applying the sum rules [87–89]. Here, the number of $3d$ holes and the correction factors of the respective cations derived by Teramura *et al.* [185] were adjusted according to the determined cationic stoichiometry. The resulting orbital and spin magnetic moments $m^{Fe,Ni}_{orb}$ and $m^{Fe,Ni}_{spin}$ in units of μ_B/f.u. as well as the total magnetization $M^{tot}_{XMCD} = m^{Fe}_{orb} + m^{Fe}_{spin} + m^{Ni}_{orb} + m^{Ni}_{spin}$ are depicted in Fig. 6.10. In addition, the magnetizations M_{SQUID} determined by SQUID magnetometry at the magnetic field of 0.4 T as applied for the XMCD measurements are given for comparison. As the descending and ascending branches of the corresponding hysteresis loops already coincide at 0.4 T (cf. Fig. 6.8), the magnetization value $M(0.4\,T)$ should be independent of whether the film was magnetically saturated before measurement (in the respective direction) or not.

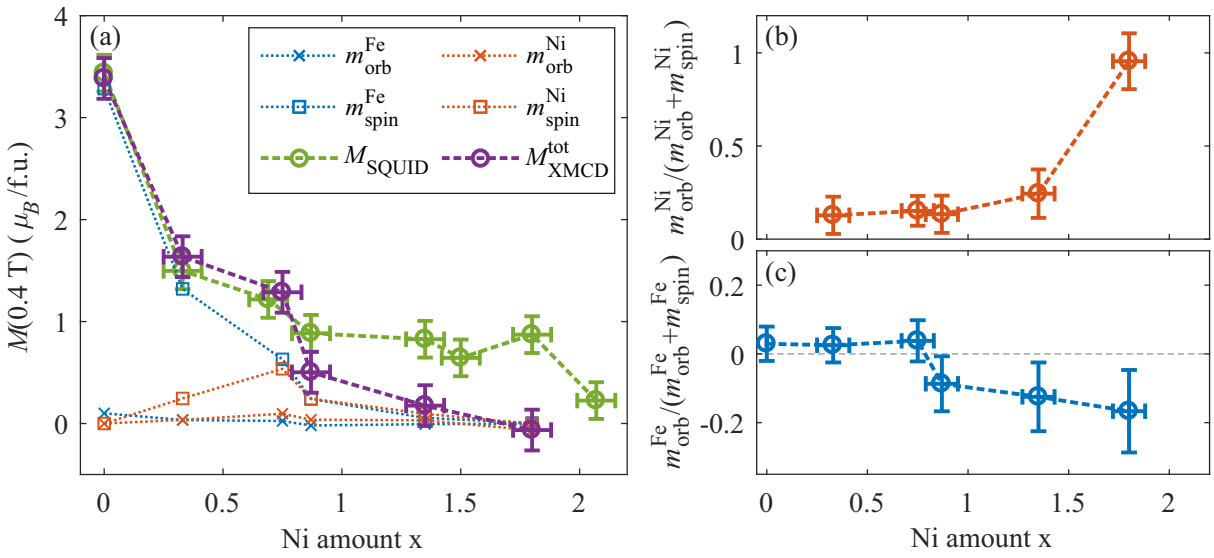

Fig. 6.10: (a) Orbital and spin magnetic moments $m^{\mathrm{Fe,Ni}}_{\mathrm{orb}}$ and $m^{\mathrm{Fe,Ni}}_{\mathrm{spin}}$ of Fe and Ni cations with varying x as determined by sum rule analysis of XMCD data. The total magnetization is given by $M^{\mathrm{tot}}_{\mathrm{XMCD}} = m^{\mathrm{Fe}}_{\mathrm{orb}} + m^{\mathrm{Fe}}_{\mathrm{spin}} + m^{\mathrm{Ni}}_{\mathrm{orb}} + m^{\mathrm{Ni}}_{\mathrm{spin}}$. The magnetizations M_{SQUID} determined by SQUID magnetometry at the magnetic field of 0.4 T as applied for the XMCD measurements are given for comparison. (b) Relative orbital magnetic moment of Ni and (c) relative orbital magnetic moment of Fe with varying x.

As seen in Fig. 6.10, the magnetizations of the different films (for x<1.80) are mainly determined by the spin magnetic moments, as the orbital magnetic contributions are very small with values of $m^{\mathrm{Fe}}_{\mathrm{orb}} \leq 0.11\,\mu_B$/f.u. and $m^{\mathrm{Ni}}_{\mathrm{orb}} \leq 0.09\,\mu_B$/f.u. for Fe and Ni, respectively. The spin magnetic moment of Fe exhibits its maximum $m^{\mathrm{Fe}}_{\mathrm{spin}} = 3.28\,\mu_B$/f.u. as expected for the Fe_3O_4 film and consecutively decreases with increasing Ni content. In contrast, the spin magnetic moment of Ni increases up to x = 0.75 with a maximum value of $m^{\mathrm{Ni}}_{\mathrm{spin}} = 0.54\,\mu_B$/f.u. followed by a subsequent decrease. Consequently, the resulting total magnetizations $M^{\mathrm{tot}}_{\mathrm{XMCD}}$, as determined by sum rule analysis of the XMCD data, steadily decrease and agree well with the overall magnetizations $M_{\mathrm{SQUID}}(0.4\,\mathrm{T})$ determined by SQUID magnetometry for understoichiometric films with x < 1. Though, for overstoichiometric films with x > 1, the magnetizations obtained by the sum rule analysis deviate to smaller values compared to the magnetizations obtained from SQUID measurements. However, it has to be noted that the sum rule analysis only provides magnetization values with uncertainties of up to 30% for the involved transition metal cations [90], which could be one explanation for the observed deviation. Further, as XMCD spectra measured in TEY mode only provide information of the near-surface region, while SQUID magnetometry probes the magnetization of the complete film, the observed deviation could be due to smaller magnetic moments at the surface compared to those moments present in the bulk of the film. Nevertheless, the general decreasing behavior of the magnetization with increasing Ni content x is reproduced by both analysis methods.
Moreover, the relative orbital magnetic contributions $m^{\mathrm{Ni,Fe}}_{\mathrm{orb}}/(m^{\mathrm{Ni,Fe}}_{\mathrm{orb}} + m^{\mathrm{Ni,Fe}}_{\mathrm{spin}})$ of both cationic species Ni and Fe with varying x are depicted in Figs. 6.10(b) and (c), respectively. It is found that the magnitude of the relative orbital magnetic moments increases with increasing x for both Ni and Fe cations. For Ni, this increase is most significant for x = 1.80, where the spin magnetic moment vanishes but still a finite orbital magnetic moment is obtained [see Fig. 6.10(b)]. This result is a consequence of the inverted intensity of the Ni L_3 XMCD signal [cf. Fig. 6.9(d)]. However, note that the total Ni magnetic moment is still very low. In contrast, the orbital magnetic moments of Fe slightly increase in magnitude but more remarkably change sign for x ≥ 0.87 [see Fig. 6.10(c)]. For x ≤ 0.75, the Fe orbital magnetic moments are still aligned parallel to the spin magnetic mo-

ments (positive sign). For higher Ni content the orbital moments switch sign and can therefore be regarded as aligned antiparallel to the spin magnetic moments. This inversion of orbital magnetic moments is not understood so far and is in need of further studies. However, one should note that the total Fe magnetic moments within the regime with reversed orbital alignment are still very low and almost vanishing for $x = 1.80$.

6.4 Discussion

The *in-situ* LEED measurements of $Ni_xFe_{3-x}O_4$ thin films with varying Ni content x reveal a structural change at the surface as expected for conversion from Fe_3O_4 to $NiFe_2O_4$ for understoichiometric (concerning the Ni content: $x < 1$) ferrite films: the $(\sqrt{2} \times \sqrt{2})R45°$ superstructure characteristic for Fe_3O_4 surfaces is vanishing for $x \geq 0.69$, while the square $(1 \times 1)_S$ surface structure corresponding to the spinel type ferrite surface unit cell remains unchanged even for higher Ni content. This behavior comes along with a decreasing vertical layer distance as determined by HR-XRD analysis, which is also expected considering the decrease of bulk layer distances from Fe_3O_4 to $NiFe_2O_4$. These observations made in LEED and XRD therefore indicate a subsequent conversion from Fe_3O_4 to NFO when increasing the Ni content x. Further, within this conversion for $x < 1$, HAXPES measurements reveal a decrease of the relative Fe^{2+} content accompanied by an increase of the relative Fe^{3+} amount within the Fe cations. However, the Ni^{2+} valency remains unchanged, which indicates that the increase of the Ni content can be associated with the expected exchange of Fe^{2+} by Ni^{2+} cations.
In contrast, for overstoichiometric NFO films ($x > 1$) the intensity of the single spinel type $(1 \times 1)_S$ surface structure decreases in LEED and vanishes at the surface for $x \geq 1.80$. Only a square $(1 \times 1)_{RS}$ structure corresponding to a surface unit cell that is four times smaller in real space than the ferrite unit cell remains visible, which points to the formation of a rock salt like structure as it is expected for the presence of merely NiO. This formation is in accordance with the subsequent increase of the vertical layer distance when increasing x in the overstoichiometric regime as determined by HR-XRD, which is also according to the slight increase when comparing the bulk layer distances of $NiFe_2O_4$ and NiO. In addition, due to the larger (relaxed) NiO layer distance compared to the one of $NiFe_2O_4$, NiO exhibits a smaller lattice mismatch to the MgO substrate. This should also result in smaller vertical compressive strain, which could further explain the increased layer distances for increasing x in the overstoichiometric regime. Moreover, a significant decrease of the interface distance for $x > 1.20$ as determined by HR-XRD analysis also points to the formation of a different phase at the interface. However, the ferrite film surface is still extremely smooth and its roughness is only slightly increased for the overstoichiometric films compared to the understoichiometric regime.
As revealed by HAXPES, the overstoichiometric films exhibit nearly constant Fe^{3+} content, which is clearly enhanced in comparison to $x < 1$ and which comes along with almost vanishing Fe^{2+} amounts. Only for $x = 2.07$ this behavior is again slightly reversed, i.e., a small increase (decrease) is noticed in the Fe^{2+} (Fe^{3+}) content accompanied by a slight decrease of the Fe $2p$ main line binding energy positions. However, this implied behavior is in need of further investigations with more data for $x > 2$. In addition, the rising high binding energy shoulder as well as the altered satellite structure and the shift to lower binding energies of the Ni $2p_{3/2}$ photoemission spectrum for $x > 1$ can be ascribed to the increased formation of NiO agglomerations within the ferrite films with increasing x. This observation therefore is completely in accordance with the assumed partial and increasing structural conversion from the ferrite spinel to a rock salt like structure with increasing NiO content.
Nevertheless, XRR and AR-HAXPES give no indications of layers of additional/separated phases neither in the conversion from Fe_3O_4 to $NiFe_2O_4$ for $x < 1$ nor from $NiFe_2O_4$ to an NiO-like phase

for $x > 1$. In fact, both measurement techniques point to single homogeneous films with homogeneous cation and valence state distributions in vertical direction. Thus, in particular the rising NiO agglomerations in the overstoichiometric regime are assumed to be statistically distributed within the ferrite film without forming distinctly separated layers. The latter has been reported by Kuschel *et al.*, where $NiFe_2O_4$ films have been prepared by interdiffusion of Fe_3O_4/NiO bilayers on $SrTiO_3$(001) induced by post-deposition annealing (PDA) [36]. The final film stack of the PDA treatment exhibits a segregated NiO layer on top of the $NiFe_2O_4$ film, when the initial Ni:Fe ratio exceeds the stoichiometric ratio of 1:2. Note that the same behavior is noticed for similar PDA treatement of Fe_3O_4/CoO bilayers, where a thin CoO layer segregates to the top of the formed $CoFe_2O_4$ film, as presented in Chap. 8. As a consequence, the co-evaporation method as performed in this study suppresses the NiO segregation to the surface due to the significantly lower sample temperature of 250°C during film growth compared to at least 600°C for the alternate PDA preparation method.

The assumption of single crystalline films with homogeneous cationic distributions throughout the whole range in x is confirmed by the observation of only single diffraction peaks in HR-XRD measurements. Two strictly separated phases with different lattice constants in the relaxed case would also result in different (vertical) layer distances in the observed strained case and therefore in the observation of separated diffraction peaks. Thus, the assumed NiO agglomerations in the overstoichiometric regime are completely homogeneously distributed within the films without clearly separating between NiO and ferrite like NFO phases giving rise to a single diffraction peak and a mean overall vertical lattice constant.

The obtained lattice constants are all compressively strained in vertical direction, which can be explained by an at least partial adaption of the film to the substrate lattice resulting in lateral expansion and vertical compression. Consequently, the expected vertical layer distance can be estimated by Eq. (2.8), which is based on elastic theory for continuum and implies homogeneous tetragonal in-plane distortion. Following Eq. (2.8) and taking the poisson ratios for the stoichiometric cases of Fe_3O_4 ($\nu_{Fe_3O_4} = 0.356$ [198]), $NiFe_2O_4$ ($\nu_{NFO} = 0.338$ [198]), and NiO ($\nu_{NiO} = 0.297$ [198]) into account, compressed vertical layer distances of $d_{vert}^{Fe_3O_4} = 209.1$ pm, $d_{vert}^{NFO} = 206.3$ pm, and $d_{vert}^{NiO} = 207.3$ pm are obtained for the three respective stoichiometric oxides, assuming complete adaption of the lateral lattice constants to the lattice constant of the MgO substrate. These estimated values [according to the lower limits of the filled regions in Fig. 6.4(b)] match very well with the evolution of the measured strained vertical layer distances, which in turn confirms complete adaption of the film to the substrate lattice without any hint of strain relaxation. As a consequence thereof, all prepared ferrite films are assumed to exhibit less defects like misfit dislocations, which would release the applied strain. This assumption is confirmed by the complete vertical crystallinity and high crystalline quality of the ferrite films with very smooth interfaces/surfaces independent of the Ni content as determined by HR-XRD analysis.

Further, the assumed absence of strain releasing defects can be followed by estimating the theoretical critical thickness D_c above which misfit dislocations are incorporated into the film to release strain by using the model of Matthews and Blakeslee as formulated in Eq. (2.10) [41]. Here, for Fe_3O_4 and $NiFe_2O_4$ the burgers vectors $b_{Fe_3O_4} = a_0/4\,\langle 110\rangle = 296.8$ pm and $b_{NFO} = 294.8$ pm (a_0: bulk lattice constants) is considered, allowing for dislocation dissociation to achieve the smallest D_c possible [199]. For NiO the burgers vector is given by $b_{NiO} = a_0/2\,\langle 110\rangle = 295.3$ pm. Taking the respective poisson ratios into account (see above), critical thicknesses of 103.9 nm, 27.4 nm, and 34.8 nm are obtained for Fe_3O_4, $NiFe_2O_4$, and NiO, respectively. All values are significantly larger than the prepared film thicknesses within this study (up to 18.6 nm) and are therefore consistent with the observed strain. Moreover, this observation completely agrees with the results obtained for the off-stoichiometric NFO films in Chap. 5.

Apart from the structural and electronic characterization, magnetic M vs H measurements reveal a

decrease of saturation magnetizations M_S as it is expected for increasing x. For $x = 0$, the measured saturation magnetization matches the expected value of $4\,\mu_B$/f.u. with only a slight deviation to a lower value. The subsequent decrease of M_S for increasing x is stronger than expected, since already for $x \geq 0.87$ the saturation magnetization drops below the value of $2\,\mu_B$/f.u. as expected for stoichiometric bulk $NiFe_2O_4$ ($x = 1$). However, this deviation could be ascribed to the presence of antiphase boundaries (APBs) in the ferrite films, which are typically formed during film growth of the ferrite with a double-sized lattice constant compared to the one of the MgO substrate (cf. Sec. 3.2.7): islands or layers during film growth with nucleation centers that are non-integer multiples of the ferrite lattice constant apart from each other are out-of-phase upon merging and form APBs. Strong antiferromagnetic coupling across the APBs as it is known for, e.g., Fe_3O_4 on MgO(001) [133], could consequently result in a lower saturation magnetization as it is observed here for all prepared ferrite films. Further, the observed discrepancy to lower M_S values than expected for the ideal case of solely octahedral occupancy of Ni^{2+} could also be due to different lattice site occupancies of the incorporated Ni^{2+} cations. Further, NiO agglomerations within the films would also lower the total film magnetization due to the antiferromagnetic coupling in NiO and could therefore give rise to an increased discrepancy between ideal expectation and measurement.
Sum rule analysis of XMCD spectra reveal an expected main contribution of the spin magnetic moments and almost negligible orbital contributions of Fe and Ni cations to the overall magnetization for $x \leq 1$, as it is expected due to orbital quenching. However, for higher Ni content, as the total magnetization decreases, the relative orbital contribution increases, most crucially for Ni cations for $x = 1.80$, whereas the respective spin magnetic contributions almost vanish. The magnitude of the orbital magnetic contribution of Fe cations only slightly increases with increasing x, but more remarkably, it changes sign for $x \geq 0.87$, which indicates a change from parallel to antiparallel alignment of orbital and spin magnetic moments. Contrary to the expected sole contribution of Ni^{2+}_{oct} cations to the overall magnetization for stoichiometric $NiFe_2O_4$, also comparably large spin magnetic moments of Fe and Ni cations are observed within the overstoichiometric regime $x \geq 1$. This behavior could be the result of different site occupancies than assumed in the simplest case of equally distributed Fe^{3+} cations among octa- and tetrahedral sites and Ni^{2+} cations occupying solely octahedral sites. The dominating orbital magnetic contribution of the Ni cations in the case of $x = 1.80$ (although very low in magnitude) could also be due to such different cationic site occupancies. However, analysis of XAS and XMCD spectra by charge transfer multiplet calculations could be performed to shed light on this assumption.

6.5 Summary

Within this study, a structural, chemical, and magnetic characterization of $Ni_xFe_{3-x}O_4$ thin films with varying Ni content x and comparable thicknesses between 14 and 18.6 nm prepared by RMBE on MgO(001) was conducted. As determined by synchrotron-based high resolution XRD measurements, all films are compressively strained in vertical direction due to an expected lateral tensile strain, resulting from an adaption of the film to the substrate lattice. As a consequence, the prepared films are assumed to exhibit very low defect densities as the results and theoretical predictions show no evidence of released strain by defects like, e.g., misfit dislocations. Complete vertical crystallinity with extremely low interface and surface roughnesses independent of the cationic stoichiometry confirm this assumption.
Further, for understoichiometric Ni contents $x < 1$ a successive conversion from Fe_3O_4 to stoichiometric $NiFe_2O_4$ with increasing x is observed. Within this regime, Fe^{2+} cations are most likely replaced by Ni^{2+} cations, according to the decreasing Fe^{2+}:Fe^{3+} ratio with constant Ni^{2+} valency as observed in HAXPES, XAS, and XMCD. Instead, for the overstoichiometric regime $x > 1$ solely Fe^{3+} and Ni^{2+} cations are present within the films as it is also expected for stoichiometric NFO,

whereas for further increasing x additional rock salt type NiO agglomerations are formed due to the high Ni content. However, these agglomerations are homogeneously distributed within the films and not strictly separated from the ferrite-like NFO phase, as deduced from complementary angle resolved HAXPES, XRR, and HR-XRD measurements. SQUID magnetometry measurements reveal decreasing saturation magnetizations as expected for the conversion from Fe_3O_4 to $NiFe_2O_4$ up to NiO. This behavior is confirmed by sum rule analysis of XMCD data. However, the slightly stronger decrease than expected for the conversion from Fe_3O_4 to $NiFe_2O_4$ within the understoichimetric regime can be related to the presence of antiphase boundaries and different cationic occupancies than expected for a perfect inverse spinel structure.
Apart from the presence of APBs, which is intrinsic for growth of spinel type ferrites on substrates like MgO(001) with a half-sized lattice constant, all films exhibit high crystalline quality with low defect densities and sharp interfaces and surfaces, which is crucial for the implementation in spin filter applications. Hence, from the results in the presented study, high applicability in spintronics not only for stoichiometric $NiFe_2O_4$, but also for NFO films with off-stoichiometric cationic ratios is expected. For these cases, one should expect slightly inferior magnetic properties. However, electric investigations of these off-stoichiometric ferrite films should be conducted additionally to check this assumption.

6.6 Acknowledgments

Financial support from the Deutsche Forschungsgemeinschaft (Nos. DFG under KU2321/6-1 and WO533/20-1) is gratefully acknowledged. We acknowledge DESY (Hamburg, Germany), a member of the Helmholtz Association HGF, for the provision of experimental facilities. Parts of this research were carried out at PETRA III and we would like to thank Florian Bertram and Andrei Gloskovskii for assistance in using beamlines P08 and P09, respectively. Additionally, we gratefully acknowledge A. Becker, T. Peters, T. Kuschel and G. Reiss from Bielefeld University for providing measurement time at the x-ray diffractometer to perform XRR measurements.

Original publication: Physical Review Materials **4**, 064404 (2020)
available at http://dx.doi.org/10.1103/PhysRevMaterials.4.064404

Enhanced magnetization of ultrathin $NiFe_2O_4$ films on $SrTiO_3(001)$ related to cation disorder and anomalous strain

J. Rodewald[1], J. Thien[1], K. Ruwisch[1], F. Bertram[2], K. Kuepper[1], and J. Wollschläger[1]

[1] *Department of Physics, Osnabrück University, Barbarastrasse 7, D-49076 Osnabrück, Germany*
[2] *DESY, Photon Science, Notkestraße 85, D-22607 Hamburg, Germany*

Abstract

$NiFe_2O_4$ thin films with varying thickness were grown on $SrTiO_3(001)$ by reactive molecular beam epitaxy. Soft and hard x-ray photoelectron spectroscopy measurements reveal a homogeneous cation distribution throughout the whole film with stoichiometric Ni:Fe ratios of 1:2 independent of the film thickness. Low energy electron diffraction and high resolution (grazing incidence) x-ray diffraction in addition to x-ray reflectivity experiments were conducted to obtain information of the film surface and bulk structure, respectively. For ultrathin films up to 7.3 nm, lateral tensile and vertical compressive strain is observed, contradicting an adaption at the interface of $NiFe_2O_4$ film and substrate lattice. The applied strain is accompanied by an increased lateral defect density, which is decaying for relaxed thicker films and attributed to the growth of lateral grains. Determination of cationic site occupancies in the inverse spinel structure by analysis of site sensitive diffraction peaks reveals low tetrahedral occupancies for thin, strained $NiFe_2O_4$ films, resulting in the partial presence of deficient rock salt like structures. These structures are assumed to be responsible for the enhanced magnetization of up to ∼250% of the $NiFe_2O_4$ bulk magnetization as observed by superconducting quantum interference device magnetometry for ultrathin films below 7.3 nm thickness.

Original publication: Physical Review B **100**, 155418 (2019)
available at http://dx.doi.org/10.1103/PhysRevB.100.155418

Formation of ultrathin cobalt ferrite films by interdiffusion of Fe_3O_4/CoO bilayers

J. Rodewald[1], J. Thien[1], T. Pohlmann[1,2], M. Hoppe[1,2], F. Timmer[1], F. Bertram[2], K. Kuepper[1], and J. Wollschläger[1]

[1] *Department of Physics, Osnabrück University, Barbarastrasse 7, D-49076 Osnabrück, Germany*
[2] *DESY, Photon Science, Notkestraße 85, D-22607 Hamburg, Germany*

Abstract

In this work an alternate pathway is demonstrated to form ultrathin cobalt ferrite ($Co_xFe_{3-x}O_4$) films by interdiffusion of Fe_3O_4/CoO bilayers. Bilayer samples with different Fe_3O_4/CoO thickness ratios have been prepared by reactive molecular beam epitaxy on Nb-doped $SrTiO_3$(001) substrates to obtain cobalt ferrite films of varied stoichiometry. Subsequently, oxygen-assisted post deposition annealing experiments for consecutive temperature steps between 300°C and 600°C have been conducted monitoring the interdiffusion process by means of high-resolution x-ray reflectivity, soft and angle-resolved hard x-ray photoelectron, and x-ray absorption spectroscopy. Magnetic properties were characterized using superconducting quantum interference device magnetometry. The interdiffusion process starts from 300°C annealing temperature and is completed for temperatures above 500°C. For completely interdiffused films with Co:Fe ratios larger than 0.84:2 a thin segregated CoO layer on top of the ferrite is formed. This CoO segregation is attributed to surface and interface effects. In addition, multiplet calculations of x-ray absorption spectra are performed to determine the occupancy of different sublattices. These results are correlated with the magnetic properties of the ferrite films. A stoichiometric $CoFe_2O_4$ film with partial inversion has been formed exhibiting homogeneously distributed Co^{2+} and mainly Fe^{3+} valence states if the initial Co:Fe content is 1.09:2. Thus, for the formation of stoichiometric cobalt ferrite by the proposed postdeposition annealing technique an initial Co excess has to be provided as the formation of a top CoO layer is inevitable.

9 Summary and outlook

Within this thesis, (ultra)thin ferrite films, i.e., $NiFe_2O_4$ and $CoFe_2O_4$, grown on MgO(001) and $SrTiO_3$(001) substrates have been investigated in terms of their structural, electronic, and magnetic properties. Overall, the presented results can be divided into four major steps of investigation.
In a first step, the structural properties of four off-stoichiometric $Ni_xFe_{3-x}O_4$ films ($0 \leq x \leq 1.5$) with final thicknesses of (16.7 ± 1.9) nm deposited via RMBE on MgO(001) were investigated *in situ* during film growth by means of synchrotron radiation-based XRD. With this, the structure of the prepared ferrite films could be characterized in dependence of the film thickness. Independent of the cationic stoichiometry, all films exhibit high crystalline quality with sharp interfaces/surfaces and complete vertical crystallinity during the whole growth process. For ferrite films within the ultrathin regime up to ~8 nm, enhanced vertical compression compared to the expected strain induced by the substrate is observed, which can be attributed to an increased presence of antiphase boundaries. The density of these APBs is reduced with increasing film thickness, which results in vertical compression and lateral expansion, as obtained from HESXRD measurements of the final films, that is expected for an adaption of the film to the substrate lattice. This in turn reinforces the high crystalline quality of the strained films, as less defects, which could release strain, are assumed to be incorporated. Additional HAXPES measurements are in accordance with a gradual substitution of Fe^{2+} by Ni^{2+} cations in the ferrite inverse spinel structure for increasing x and additionally indicate the formation of NiO agglomerations within the films that exceed the stoichiometric value of $x = 1$. However, due to the rather small data set with only four investigated samples, the structural and electronic properties should be analyzed in more detail in a systematic study of even more ferrite films with similar thicknesses but different cationic stoichiometries.
Thus, in a second step, the principal dependencies of the structural, electronic, and also the magnetic properties of off-stoichiometric $Ni_xFe_{3-x}O_4$ thin films were further systematically investigated. Therefore, 14 ferrite films with similar thicknesses between 14.0 and 18.6 nm and varying Ni content x ($0 \leq x \leq 2.07$) were grown on MgO(001) via RMBE. Here, all films exhibit smooth surfaces, sharp interfaces between substrate and film, as well as a high crystalline quality with complete vertical crystallinity within the whole film, as observed by LEED, XRR, and HR-XRD measurements. However, these structural investigations indicate an expected successive transformation from the ferrite inverse spinel structures Fe_3O_4 to $NiFe_2O_4$ for $x < 1$, but also point to the emergence of a rock salt type structure for films clearly exceeding the stoichiometric Ni content of $x = 1$. HAXPES measurements are, first, in accordance with the gradual substitution of Fe^{2+} by Ni^{2+} cations when increasing x from Fe_3O_4 to $NiFe_2O_4$ in the understoichiometric regime (concerning the Ni content, $x < 1$). Second, HAXPES also reveals the emergence of NiO agglomerations within the overstoichiometric films ($x > 1$), which can be attributed to the major presence rock salt type structures, as observed in the structural characterization. However, as seen in angle resolved (AR-)HAXPES, which provides a depth-dependent chemical analysis of the thin ferrite films, these agglomerations are homogeneously distributed within the films without forming separate layers (as confirmed by the XRR measurements). In addition, the decreasing saturation magnetizations of the ferrite films with increasing x, as determined by SQUID magnetometry, are in accordance with the decrease expected for the transition from Fe_3O_4 over $NiFe_2O_4$ to NiO. Complementary XMCD data confirm this behavior. As a consequence, also off-stoichiometric NFO thin films indicate high applicability in spintronics due to high structural quality within the film and at the interfaces. However, one

should pay attention to the strong variations in the magnetic properties dependent on the cationic Ni:Fe ratio.
The origin of these variations could be clarified in future investigations by comparing charge transfer multiplet calculations to the obtained XAS and XMCD data, as such analysis could shed light on the different site occupancies of Ni and Fe cations, which determine the magnetic properties. Moreover, the preparation conditions, i.e., the sample temperature and the oxygen partial pressure during film deposition could be varied in future studies to investigate their dependence on the physical properties. In particular, instead of evaporating the transition metals in molecular oxygen, one could grow the ferrite films in assistance with oxygen plasma to enhance the reactivity with the transition metal atoms and to reduce possible oxygen vacancies in the films. This could in turn likely improve the magnetic properties of the thin off-stoichiometric ferrite films.
In a third step, the influence of larger strain in the ferrite film induced by the use of another substrate is investigated. For this purpose, stoichiometric $NiFe_2O_4$ films of different thicknesses between 3.7 and 55.5 nm were grown on $SrTiO_3$(001) via RMBE. Soft XPS and HAXPES measurements reveal a homogeneous cationic distribution in vertical direction without any hint of other chemical phases and with merely Fe^{3+} and Ni^{2+} cations as expected for ideal $NiFe_2O_4$. As seen by analysis of LEED, XRR, and high resolution (GI)XRD measurements, the lateral grain size at the surface and in bulk is increasing for increasing film thickness. In contrast, in vertical direction these grains are incoherently separated from each other, most likely due to the incorporation of (strain releasing) defects, resulting in a smaller vertical crystallite size than the film thickness, most apparent for NFO films thicker than 15 nm. For (ultra)thin films up to a thickness of 7.3 nm, an unexpected type of strain, i.e., vertical compressive and lateral tensile strain, is observed, which is in contradiction to a lateral adaption of the NFO film lattice to the substrate lattice. Though, thicker films are completely relaxed. The unusual strain for thin films is accompanied by a remarkably lower tetrahedral site occupancy than expected for a perfect inverse spinel structure. The comparably high relative octahedral site occupancy is ascribed to a major presence of deficient rock salt type $Ni_{0.25}Fe_{0.5}O$ structures with all cations on octahedral sites in addition to octahedral cation vacancies compared to spinel type NFO. These deficient rock salt type structures and the anomalous strain are assumed to be responsible for the enhanced saturation magnetizations of the ultrathin films of up to ∼250% compared to the NFO bulk magnetization.
Future investigations by means of XMCD could shed light on the enhanced magnetization by probing element specific site occupancies of Ni and Fe cations via charge transfer multiplet analysis. This could be particularly interesting for the ultrathin NFO films and could investigate a direct correlation between enhanced magnetization and rock salt type structures in the ultrathin film limit. In addition, this behavior could also be investigated in other types of ferrites (e.g., Fe_3O_4, $CoFe_2O_4$) to clarify whether the magnetic enhancement is a systematic property for ultrathin ferrite films or whether it is only limited to a specific type of ferrite. Further, it would be interesting to know if this magnetic enhancement is also apparent for ultrathin ferrite films deposited on more lattice matched substrates as, e.g., MgO(001) or if it is particularly depending on/originating from the larger induced strain as indicated by the results obtained here.
Apart from the growth and characterization of NFO films, the fourth step within this thesis describes an alternative pathway to prepare thin $CoFe_2O_4$ films on $SrTiO_3$(001). Here, in contrast to the co-evaporation method used for NFO film growth in the first three steps, CFO films were prepared by first growing Fe_3O_4/CoO bilayers on $SrTiO_3$ via RMBE and, second, inducing interdiffusion of this bilayer system due to thermal annealing, resulting in the formation of thin CFO films. This post deposition annealing technique was applied for three samples with different initial Fe_3O_4/CoO thickness ratios, whereas the annealing temperature was successively enhanced from 300°C up to 600°C. The interdiffusion process starts at 300°C and is completed for temperatures above 500°C. However, as observed by analysis of XRR data and confirmed by XPS and AR-

HAXPES measurements, an ultrathin (∼0.8 nm) CoO layer is formed on top of the final film stack due to segregation through the ferrite film during interdiffusion, even if the provided Co amount is not sufficient to form stoichiometric $CoFe_2O_4$. Thus, in order to form a stoichiometric $CoFe_2O_4$ film by the proposed PDA technique, more Co than theoretically needed has to be provided in the initial bilayer stack, allowing a certain amount of CoO to form a segregated CoO layer on top. This has been successfully achieved for one sample with a stoichiometric $CoFe_2O_4$ film underneath an ultrathin CoO layer on top. However, analysis of XAS data reveals only partial inversion in the spinel structure of the final $CoFe_2O_4$ film. This determination is further confirmed by SQUID magnetometry data. The determined degree of inversion is in accordance with conventional preparation methods of $CoFe_2O_4$, stating the proposed PDA treatment of Fe_3O_4/CoO bilayers on $SrTiO_3$(001) as a promising pathway to prepare cobalt ferrite thin films.
However, this type of film preparation is still in need of further investigations to completely understand the mechanisms during interdiffusion. Therefore, more PDA experiments have to be performed, e.g., with an inversed CoO/Fe_3O_4 stacking order of the initial bilayer system instead of the Fe_3O_4/CoO bilayer system used here. Due to the observation of an ultrathin CoO film segregated to the surface in the PDA experiments made here, it should be investigated if the inversed bilayer stack would interdiffuse at all at similar annealing temperatures or if the interdiffusion behavior is generally different in that case. Moreover, as the proposed PDA treatment is a promising pathway for the preparation of thin ferrite films, this method should also be applied and investigated for other types of ferrites ($ZnFe_2O_4$, $MnFe_2O_4$, etc.) or, e.g., cobaltites ($NiCo_2O_4$).
Overall, within this thesis, it was demonstrated that NFO and CFO thin films can be prepared in high structural quality with sharp interfaces and surfaces, which is crucial for the applicability in the fields of spintronics and spincaloritronics. However, parameters like film thickness and cationic stoichiometry as well as the choice of the substrate and the preparation method should be carefully considered as they may have significant impact on the performance of certain devices in these fields. In fact, a variation of these parameters enables to tailor the physical characteristics of such devices to match specific purposes for certain applications. Though, before implementation, e.g., as a spin filter, electric properties by means of, i.e., (temperature-dependent) conductivity measurements should be characterized in future studies to ensure the insulating character of the prepared high-quality ferrite films and to prove their applicability in spintronic devices.

10 List of publications

1. L. Schneider, J. Wehmeier, U. Wiedwald, **J. Rodewald**, V. R. Galakhov, M. S. Udintseva, V. Mesilov, F. Radu, C. Luo, J. P. Klare, H.-J. Steinhoff, M. Haase, and K. Kuepper
"Magnetic and electronic properties of highly Mn-doped β-$NaGdF_4$ and β-$NaEuF_4$ nanoparticles with a narrow size distribution"
The Journal of Physical Chemistry C **124**, 18194 (2020);
doi:10.1021/acs.jpcc.0c04639

2. **J. Rodewald**, J. Thien, T. Pohlmann, M. Hoppe, F. Bertram, K. Kuepper, and J. Wollschläger
"Real-time monitoring the growth of strained off-stoichiometric $Ni_xFe_{3-x}O_4$ ultrathin films on MgO(001)"
Applied Physics Letters **117**, 011601 (2020);
doi:10.1063/5.0013925

3. **J. Rodewald**, J. Thien, K. Ruwisch, F. Bertram, K. Kuepper, and J. Wollschläger
"Enhanced magnetization of ultrathin $NiFe_2O_4$ films on $SrTiO_3$(001) related to cation disorder and anomalous strain"
Physical Review Materials **4**, 064404 (2020);
doi:10.1103/PhysRevMaterials.4.064404

4. **J. Rodewald**, J. Thien, T. Pohlmann, M. Hoppe, F. Timmer, F. Bertram, K. Kuepper, and J. Wollschläger
"Formation of ultrathin cobalt ferrite films by interdiffusion of Fe_3O_4/CoO bilayers"
Physical Review B **100**, 155418 (2019);
doi:10.1103/PhysRevB.100.155418

5. R. Silber, M. Tomíčková, **J. Rodewald**, J. Wollschläger, J. Pištora, M. Veis, T. Kuschel, and J. Hamrle
"Quadratic magnetooptic spectroscopy setup based on photoelastic light modulation"
Photonics and Nanostructures - Fundamentals and Applications **31**, 60 (2018);
doi:10.1016/j.photonics.2018.05.007

6. O. Kuschel, N. Pathé, T. Schemme, K. Ruwisch, **J. Rodewald**, R. Buß, F. Bertram, T. Kuschel, K. Kuepper, and J. Wollschläger
"Impact of strain and morphology on magnetic properties of Fe_3O_4/NiO bilayers grown on Nb:$SrTiO_3$(001) and MgO(001)"
Materials **11**, 1122 (2018); doi:10.3390/ma11071122

7. O. Kuschel, F. Dieck, H. Wilkens, S. Gevers, **J. Rodewald**, C. Otte, M. H. Zoellner, G. Niu, T. Schroeder, and J. Wollschläger
"Plasma enhanced complete oxidation of ultrathin epitaxial praseodymia films on Si(111)"
Materials **8**, 6379 (2015); doi:10.3390/ma8095312

8. H. Wilkens, **J. Rodewald**, S. Gevers, M. H. Zoellner, T. Schroeder, and J. Wollschläger
"Surface morphology of ultrathin hex-Pr_2O_3 films on Si(111)"
Journal of Physics D: Applied Physics **46**, 285306 (2013);
doi:10.1088/0022-3727/46/28/285306

Literature

[1] J. Malmodin, Å. Moberg, D. Lundén, G. Finnveden and N. Lövehagen. "Greenhouse Gas Emissions and Operational Electricity Use in the ICT and Entertainment & Media Sectors". *J. Ind. Ecol.*, 14(5), 770–790, 2010. doi:10.1111/j.1530-9290.2010.00278.x.

[2] J. Malmodin and D. Lundén. "The Energy and Carbon Footprint of the Global ICT and E&M Sectors 2010-2015". *Sustainability*, 10(9), 3027, 2018. doi:10.3390/su10093027.

[3] S. A. Wolf, D. D. Awschalom, R. A. Buhrman, J. M. Daughton, S. von Molnár, M. L. Roukes, A. Y. Chtchelkanova and D. M. Treger. "Spintronics: A Spin-Based Electronics Vision for the Future". *Science*, 294(5546), 1488–1495, 2001. doi:10.1126/science.1065389.

[4] M. N. Baibich, J. M. Broto, A. Fert, F. N. Van Dau, F. Petroff, P. Etienne, G. Creuzet, A. Friederich and J. Chazelas. "Giant Magnetoresistance of (001)Fe/(001)Cr Magnetic Superlattices". *Phys. Rev. Lett.*, 61, 2472–2475, 1988. doi:10.1103/PhysRevLett.61.2472.

[5] G. Binasch, P. Grünberg, F. Saurenbach and W. Zinn. "Enhanced magnetoresistance in layered magnetic structures with antiferromagnetic interlayer exchange". *Phys. Rev. B*, 39, 4828–4830, 1989. doi:10.1103/PhysRevB.39.4828.

[6] T. Miyazaki and N. Tezuka. "Spin polarized tunneling in ferromagnet/insulator/ferromagnet junctions". *J. Magn. Magn. Mater.*, 151(3), 403–410, 1995. doi:10.1016/0304-8853(95)00563-3. Spin Polarized Electron Transport.

[7] J. S. Moodera, L. R. Kinder, T. M. Wong and R. Meservey. "Large Magnetoresistance at Room Temperature in Ferromagnetic Thin Film Tunnel Junctions". *Phys. Rev. Lett.*, 74, 3273–3276, 1995. doi:10.1103/PhysRevLett.74.3273.

[8] M. Julliere. "Tunneling between ferromagnetic films". *Phys. Lett. A*, 54(3), 225–226, 1975. doi:10.1016/0375-9601(75)90174-7.

[9] Z. Zhang and S. Satpathy. "Electron states, magnetism, and the Verwey transition in magnetite". *Phys. Rev. B*, 44(24), 13319–13331, 1991. doi:10.1103/PhysRevB.44.13319.

[10] R. Arras, L. Calmels and B. Warot-Fonrose. "Interface States in the Full-Oxide Fe_3O_4-MgO-Fe_3O_4 Magnetic Tunnel Junction". *IEEE Trans. Magn.*, 46(6), 1730–1732, 2010. doi:10.1109/TMAG.2010.2042577.

[11] X. W. Li, A. Gupta, G. Xiao, W. Qian and V. P. Dravid. "Fabrication and properties of heteroepitaxial magnetite (Fe_3O_4) tunnel junctions". *Appl. Phys. Lett.*, 73(22), 3282–3284, 1998. doi:10.1063/1.122745.

[12] P. J. van der Zaag, P. J. H. Bloemen, J. M. Gaines, R. M. Wolf, P. A. A. van der Heijden, R. J. M. van de Veerdonk and W. J. M. de Jonge. "On the construction of an Fe_3O_4-based all-oxide spin valve". *J. Magn. Magn. Mater.*, 211(1), 301–308, 2000. doi:https://doi.org/10.1016/S0304-8853(99)00751-9.

[13] F. Greullet, E. Snoeck, C. Tiusan, M. Hehn, D. Lacour, O. Lenoble, C. Magen and L. Calmels. "Large inverse magnetoresistance in fully epitaxial Fe/Fe_3O_4/MgO/Co magnetic tunnel junctions". *Appl. Phys. Lett.*, 92(5), 053508, 2008. doi:10.1063/1.2841812.

[14] V. A. M. Brabers. "Chap. 3: Progress in spinel ferrite research". In K. H. J. Buschow (Editor), "Handbook of Magnetic Materials", volume 8, pages 189–324. Elsevier, 1995. doi:10.1016/S1567-2719(05)80032-0.

[15] S. Venzke, R. B. van Dover, J. M. Phillips, E. M. Gyorgy, T. Siegrist, C.-H. Chen, D. Werder, R. M. Fleming, R. J. Felder, E. Coleman and R. Opila. "Epitaxial growth and magnetic behavior of $NiFe_2O_4$ thin films". *J. Mater. Res.*, 11, 1187, 1996. doi:10.1557/JMR.1996.0153.

[16] F. Rigato, S. Estradé, J. Arbiol, F. Peiró, U. Lüders, X. Martí, F. Sánchez and J. Fontcuberta. "Strain-induced stabilization of new magnetic spinel structures in epitaxial oxide heterostructures". *Mat. Sci. Eng: B*, 144(1), 43–48, 2007. doi:10.1016/j.mseb.2007.07.102.

[17] S. Matzen, J.-B. Moussy, R. Mattana, K. Bouzehouane, C. Deranlot and F. Petroff. "Nanomagnetism of cobalt ferrite-based spin filters probed by spin-polarized tunneling". *Appl. Phys. Lett.*, 101(4), 042409, 2012. doi:10.1063/1.4738790.

[18] A. V. Ramos, M.-J. Guittet, J.-B. Moussy, R. Mattana, C. Deranlot, F. Petroff and C. Gatel. "Room temperature spin filtering in epitaxial cobalt-ferrite tunnel barriers". *Appl. Phys. Lett.*, 91(12), 122107, 2007. doi:10.1063/1.2787880.

[19] A. V. Ramos, T. S. Santos, G. X. Miao, M.-J. Guittet, J.-B. Moussy and J. S. Moodera. "Influence of oxidation on the spin-filtering properties of $CoFe_2O_4$ and the resultant spin polarization". *Phys. Rev. B.*, 78(18), 180402, 2008. doi:10.1103/PhysRevB.78.180402.

[20] U. Lüders, A. Barthélémy, M. Bibes, K. Bouzehouane, S. Fusil, E. Jacquet, J.-P. Contour, J.-F. Bobo, J. Fontcuberta and A. Fert. "$NiFe_2O_4$: A versatile spinel material brings new opportunities for spintronics". *Adv. Mater.*, 18(13), 1733–1736, 2006. doi:10.1002/adma.200500972.

[21] S. Matzen, J.-B. Moussy, P. Wei, C. Gatel, J. C. Cezar and M. A. Arrio. "Structure, magnetic ordering, and spin filtering efficiency of $NiFe_2O_4(111)$ ultrathin films". *Appl. Phys. Lett.*, 104(18), 182404, 2014. doi:10.1063/1.4871733.

[22] J. Rodewald, J. Thien, T. Pohlmann, M. Hoppe, F. Bertram, K. Kuepper and J. Wollschläger. "Real-time monitoring the growth of strained off-stoichiometric $Ni_xFe_{3-x}O_4$ ultrathin films on MgO(001)". *Appl. Phys. Lett.*, 117(1), 011601, 2020. doi:10.1063/5.0013925.

[23] M. Sorescu, A. Grabias, R. A. Brand, J. Voss, D. Tarabasanu-Mihaila and L. Diamandescu. "A Mössbauer study of the Verwey transition in cobalt-doped magnetite". *J. Magn. Magn. Mater.*, 246(3), 399–403, 2002. doi:10.1016/S0304-8853(02)00112-9.

[24] M.-S. Lee, T.-Y. Kim, C.-S. Lee, J.-C. Park, Y. I. Kim and D. Kim. "Magnetic and structural anisotropy of the Co-Fe_3O_4 films deposited by the thin-liquid film method". *J. Magn. Magn. Mater.*, 268(1), 62–69, 2004. doi:10.1016/S0304-8853(03)00473-6.

[25] D. Tripathy, A. O. Adeyeye, S. N. Piramanayagam, C. S. Mah, X. Gao and A. T. S. Wee. "Effect of cobalt doping concentration on the structural and magnetic properties of Fe_3O_4". *Thin Solid Films*, 505(1), 45–49, 2006. doi:10.1016/j.tsf.2005.10.036.

[26] D. Tripathy, A. O. Adeyeye, C. B. Boothroyd and S. N. Piramanayagam. "Magnetic and transport properties of Co-doped Fe_3O_4 films". *J. Appl. Phys.*, 101(1), 013904, 2007. doi:10.1063/1.2404469.

[27] F. Y. Ran, Y. Tsunemaru, T. Hasegawa, Y. Takeichi, A. Harasawa, K. Yaji, S. Kim and A. Kakizaki. "Valence band structure and magnetic properties of Co-doped $Fe_3O_4(100)$ films". *J. Appl. Phys.*, 109(12), 123919, 2011. doi:10.1063/1.3597825.

[28] J. A. Moyer, C. A. F. Vaz, E. Negusse, D. A. Arena and V. E. Henrich. "Controlling the electronic structure of $Co_{1-x}Fe_{2+x}O_4$ thin films through iron doping". *Phys. Rev. B*, 83(3), 035121, 2011. doi:10.1103/PhysRevB.83.035121.

[29] J. A. Moyer, D. P. Kumah, C. A. F. Vaz, D. A. Arena and V. E. Henrich. "Epitaxial strain-induced changes in the cation distribution and resistivity of Fe-doped $CoFe_2O_4$". *Appl. Phys. Lett.*, 101(2), 021907, 2012. doi:10.1063/1.4735233.

[30] M. Saidani, W. Belkacem and N. Mliki. "Chemical charge neutrality coupled to low temperature magnetic measurements method to estimate the cationic distribution for spinel ferrites". *J. Alloys Compd.*, 729, 1177–1182, 2017. doi:10.1016/j.jallcom.2017.09.235.

[31] V. Q. Nguyen, Y. Shin, A. T. Duong, S. Cho and C. Meny. "Tuning transport and magnetic properties of $Co_xFe_{3-x}O_4$ thin films by Co content". *J. Alloys Compd.*, 772, 1095–1099, 2019. doi:10.1016/j.jallcom.2018.09.007.

[32] C. Y. Chou, P. C. Kuo, Y. D. Yao, A. C. Sun, S. C. Chen, I. J. Chang and J. W. Chen. "Magnetoresistance and microstructure of the sintered Ni doped Fe_3O_4 ferrites". *IEEE Trans. Magn.*, 41(2), 906–908, 2005. doi:10.1109/TMAG.2004.842088.

[33] M. Hoppe, S. Döring, M. Gorgoi, S. Cramm and M. Müller. "Enhanced ferrimagnetism in auxetic $NiFe_2O_4$ in the crossover to the ultrathin film limit". *Phys. Rev. B*, 91(5), 054418, 2015. doi:10.1103/PhysRevB.91.054418.

[34] U. Lüders, M. Bibes, J.-F. Bobo, M. Cantoni, R. Bertacco and J. Fontcuberta. "Enhanced magnetic moment and conductive behavior in $NiFe_2O_4$ spinel ultrathin films". *Phys. Rev. B*, 71, 134419, 2005. doi:10.1103/PhysRevB.71.134419.

[35] J. Rodewald, J. Thien, K. Ruwisch, F. Bertram, K. Kuepper and J. Wollschläger. "Enhanced magnetization of ultrathin $NiFe_2O_4$ films on $SrTiO_3$(001) related to cation disorder and anomalous strain". *Phys. Rev. Materials*, 4, 064404, 2020. doi:10.1103/PhysRevMaterials.4.064404.

[36] O. Kuschel, R. Buß, W. Spiess, T. Schemme, J. Wöllermann, K. Balinski, A. T. N'Diaye, T. Kuschel, J. Wollschläger and K. Kuepper. "From Fe_3O_4/NiO bilayers to $NiFe_2O_4$-like thin films through Ni interdiffusion". *Phys. Rev. B*, 94, 094423, 2016. doi:10.1103/PhysRevB.94.094423.

[37] J. Rodewald, J. Thien, T. Pohlmann, M. Hoppe, F. Timmer, F. Bertram, K. Kuepper and J. Wollschläger. "Formation of ultrathin cobalt ferrite films by interdiffusion of Fe_3O_4/CoO bilayers". *Phys. Rev. B*, 100, 155418, 2019. doi:10.1103/PhysRevB.100.155418.

[38] K. Oura, V. G. Lifshits, A. Saranin, A. V. Zotov and M. Katayama. *Surface science - an introduction.* Springer-Verlag, Berlin, Heidelberg, 2003. doi:10.1007/978-3-662-05179-5.

[39] S. Hashimoto, J.-L. Peng, W. M. Gibson, L. J. Schowalter and R. W. Fathauer. "Strain measurement of epitaxial CaF_2 on Si(111) by MeV ion channeling". *Appl. Phys. Lett.*, 47, 1071, 1985. doi:10.1063/1.96383.

[40] R. Gross and A. Marx. *Festkörperphysik.* De Gruyter Oldenbourg, Berlin, Boston, 2014. doi:10.1524/9783110358704.

[41] J. W. Matthews and A. E. Blakeslee. "Defects in epitaxial multilayers: I. Misfit dislocations". *J. Cryst. Growth*, 27, 118, 1974. doi:10.1016/S0022-0248(74)80055-2.

[42] W. H. Bragg and W. L. Bragg. "The reflection of x-rays by crystals". *Proc. Royal Soc. Lond. A*, 88, 428, 1913. doi:10.1098/rspa.1913.0040.

[43] W. Friedrich, P. Knipping and M. Laue. "Interferenzerscheinungen bei Röntgenstrahlen". *Ann. Phys.*, 346, 971, 1913. doi:10.1002/andp.19133461004.

[44] R. Feidenhans'l. "Surface structure determination by X-ray diffraction". *Surf. Sci. Rep.*, 10(3), 105–188, 1989. doi:10.1016/0167-5729(89)90002-2.

[45] I. K. Robinson and D. J. Tweet. "Surface x-ray diffraction". *Rep. Prog. Phys.*, 55, 599, 1992. doi:10.1088/0034-4885/55/5/002.

[46] *International tables for x-ray crystallography.* Kynoch Press for the International Union of Crystallography, Birmingham, 1952 - 1974.

[47] B. E. Warren. *X-ray diffraction.* Addison-Wesley Pub. Co, Boston, 1969.

[48] J. Als-Nielsen and D. McMorrow. *Elements of modern x-ray physics.* John-Wiley & Sons, Ltd, 2001.

[49] P. Scherrer. "Bestimmung der Größe und der inneren Struktur von Kolloidteilchen mittels Röntgenstrahlen". *Nachrichten von der Gesellschaft der Wissenschaften zu Göttingen, Mathematisch-Physikalische Klasse*, 1918, 98–100, 1918.

[50] F. Bertram. *The structure of ultrathin iron oxide films studied by x-ray diffraction.* Ph.D. thesis, Osnabrück University, 2012.

[51] M. Tolan. *X-Ray Scattering from Soft-Matter Thin Films - Materials Science and Basic Research.* Springer-Verlag Berlin Heidelberg, 1999. doi:10.1007/BFb0112834.

[52] L. G. Parratt. "Surface studies of solids by total reflection of x-rays". *Phys. Rev.*, 95(2), 359–369, 1954. doi:10.1103/PhysRev.95.359.

[53] F. Bertram. *Röntgenreflektometrie an ultradünnen Schichten.* Bachelor's thesis, Osnabrück University, 2007.

[54] L. Névot and P. Croce. "Caractérisation des surfaces par réflexion rasante de rayons X. Application à l'étude du polissage de quelques verres silicates". *Revue de Physique Appliquée*, 15(3), 761–779, 1980. doi:10.1051/rphysap:01980001503076100.

[55] M. P. Seah and W. A. Dench. "Quantitative electron spectroscopy of surfaces: A standard data base for electron inelastic mean free paths in solids". *Surf. Interface Anal.*, 1(1), 2–11, 1979. doi:10.1002/sia.740010103.

[56] M. Henzler. "Measurement of surface defects by low-energy electron diffraction". *Appl. Phys. A*, 34, 205, 1984. doi:10.1007/BF00616574.

[57] F. De Groot and A. Kotani. *Core Level Spectroscopy of Solids.* Advances in Condensed Matter Science. Taylor & Francis Group, 2008.

[58] S. Hüfner. *Photoelectron Spectroscopy.* Springer-Verlag Berlin Heidelberg, 2003. doi:10.1007/978-3-662-09280-4.

[59] H. Hertz. "Über einen Einfluss des ultravioletten Lichtes auf die electrische Entladung". *Ann. Phys.*, 267(8), 983–1000, 1887. doi:10.1002/andp.18872670827.

[60] W. Hallwachs. "Über den Einfluss des Lichtes auf electrostatisch geladene Körper". *Ann. Phys.*, 269(2), 301–312, 1888. doi:10.1002/andp.18882690206.

[61] A. Einstein. "Über einen die Erzeugung und Verwandlung des Lichtes betreffenden heuristischen Gesichtspunkt". *Ann. Phys.*, 322(6), 132–148, 1905. doi:10.1002/andp.19053220607.

[62] V. I. Nefedov. *X-ray photoelectron spectroscopy of solid surfaces.* VSP, 1988.

[63] M. Hoppe. *Magnetic, structural, and electronic properties of $NiFe_2O_4$ ultrathin films.* Ph.D. thesis, Forschungszentrum Jülich, 2016.

[64] A. E. Bocquet, T. Mizokawa, T. Saitoh, H. Namatame and A. Fujimori. "Electronic structure of 3d-transition-metal compounds by analysis of the 2p core-level photoemission spectra". *Phys. Rev. B*, 46(7), 3771, 1992. doi:10.1103/PhysRevB.46.3771.

[65] D. A. Shirley. "High-resolution x-ray photoemission spectrum of the valence bands of gold". *Phys. Rev. B*, 5(12), 4709, 1972. doi:10.1103/PhysRevB.5.4709.

[66] D. Briggs and M. P. Seah (Editors). *Practical surface anlysis.* John Wiley & Sons, Hoboken, 1990.

[67] P. J. Cumpson and M. P. Seah. "Elastic scattering corrections in AES and XPS. II. Estimating attenuation lengths and conditions required for their valid use in over-

layer/substrate experiments". *Surf. Interf. Anal.*, 25, 430, 1997. doi:10.1002/(SICI)1096-9918(199706)25:6<430::AID-SIA254>3.0.CO;2-7.

[68] S. Tanuma, C. J. Powell and D. R. Penn. "Calculations of Electron Inelastic Mean Free Paths. V. Data for 14 Organic Compounds over the 50-2000 eV Range". *Surf. Interface Anal.*, 21(3), 165–176, 1994. doi:10.1002/sia.740210302.

[69] J. H. Scofield. "Angular distribution of photoelectrons from polarized X-rays". *Phys. Scr.*, 41(1), 59–62, 1990. doi:10.1088/0031-8949/41/1/015.

[70] J. W. Cooper and S. T. Manson. "Photo-Ionization in the Soft X-Ray Range: Angular Distributions of Photoelectrons and Interpretation in Terms of Subshell Structure". *Phys. Rev.*, 177, 157–163, 1969. doi:10.1103/PhysRev.177.157.

[71] J. Cooper and R. N. Zare. "Angular Distribution of Photoelectrons". *J. Chem. Phys.*, 48(2), 942–943, 1968. doi:10.1063/1.1668742.

[72] J. H. Scofield. "Hartree-Slater subshell photoionization cross-sections at 1254 and 1487 eV". *J. Electron Spectrosc. Relat. Phenom.*, 8(2), 129–137, 1976. doi:10.1016/0368-2048(76)80015-1.

[73] J. W. Cooper. "Photoelectron-angular-distribution parameters for rare-gas subshells". *Phys. Rev. A*, 47, 1841, 1993. doi:10.1103/PhysRevA.47.1841.

[74] M. B. Trzhaskovskaya, V. I. Nefedov and V. G. Yarzhemsky. "Photoelectron angular distribution parameters for elements Z=1 to Z=54 in the photoelectron energy range 100-5000 eV". *At. Data Nucl. Data Tables*, 77(1), 97–159, 2001. doi:10.1006/adnd.2000.0849.

[75] M. B. Trzhaskovskaya, V. K. Nikulin, V. I. Nefedov and V. G. Yarzhemsky. "Non-dipole second order parameters of the photoelectron angular distribution for elements Z=1-100 in the photoelectron energy range 1-10 keV". *At. Data Nucl. Data Tables*, 92(2), 245–304, 2006. doi:10.1016/j.adt.2005.12.002.

[76] Z. Tan, J. I. Budnick and S. M. Heald. "Structural parameter determination in fluorescence EXAFS of concentrated samples". *Rev. Sci. Instrum.*, 60(6), 1021–1025, 1989. doi:10.1063/1.1140311.

[77] D. M. Pease, D. L. Brewe, Z. Tan, J. I. Budnick and C. C. Law. "Accurate X-ray absorption spectra obtained from concentrated bulk samples by fluorescence detection". *Phys. Lett. A*, 138(4), 230–234, 1989. doi:10.1016/0375-9601(89)90035-2.

[78] E. Zschech, L. Tröger, D. Arvanitis, H. Michaelis, U. Grimm and K. Baberschke. "A study of the self-absorption effect in the fluorescence yield of NiO at the oxygen K-edge". *Solid State Commun.*, 82(1), 1–5, 1992. doi:10.1016/0038-1098(92)90395-P.

[79] S. Eisebitt, T. Böske, J.-E. Rubensson and W. Eberhardt. "Determination of absorption coefficients for concentrated samples by fluorescence detection". *Phys. Rev. B*, 47, 14103–14109, 1993. doi:10.1103/PhysRevB.47.14103.

[80] J. L. Erskine and E. A. Stern. "Calculation of the M_{23} magneto-optical absorption spectrum of ferromagnetic nickel". *Phys. Rev. B*, 12, 5016–5024, 1975. doi:10.1103/PhysRevB.12.5016.

[81] G. Schütz, W. Wagner, W. Wilhelm, P. Kienle, R. Zeller, R. Frahm and G. Materlik. "Absorption of circularly polarized x rays in iron". *Phys. Rev. Lett.*, 58, 737–740, 1987. doi:10.1103/PhysRevLett.58.737.

[82] J. Stöhr. "X-ray magnetic circular dichroism spectroscopy of transition metal thin films". *J. Electron Spectrosc. Relat. Phenom.*, 75, 253–272, 1995. doi:10.1016/0368-2048(95)02537-5. Future Perspectives for Electron Spectroscopy with Synchrotron Radiation.

[83] U. Fano. "Spin Orientation of Photoelectrons Ejected by Circularly Polarized Light". *Phys. Rev.*, 178, 131–136, 1969. doi:10.1103/PhysRev.178.131.

[84] H. A. Bethe and E. E. Salpeter. *Quantum Mechanics of One- and Two-Electron Atoms*. Springer-Verlag Berlin Heidelberg, 1957. doi:10.1007/978-3-662-12869-5.

[85] J. Stöhr and Y. Wu. "X-Ray Magnetic Circular Dichroism: Basic Concepts and Theory for 3D Transition Metal Atoms". In A. S. Schlachter, F. J. Wuilleumier (Editor), "New Directions in Research with Third-Generation Soft X-Ray Synchrotron Radiation Sources", volume 254, pages 221–250. Springer, Dordrecht, 1994. doi:10.1007/978-94-011-0868-3_9.

[86] H. Ebert. "Magneto-optical effects in transition metal systems". *Rep. Prog. Phys.*, 59(12), 1665–1735, 1996. doi:10.1088/0034-4885/59/12/003.

[87] B. T. Thole, P. Carra, F. Sette and G. van der Laan. "X-ray circular dichroism as a probe of orbital magnetization". *Phys. Rev. Lett.*, 68, 1943–1946, 1992. doi:10.1103/PhysRevLett.68.1943.

[88] P. Carra, B. T. Thole, M. Altarelli and X. Wang. "X-ray circular dichroism and local magnetic fields". *Phys. Rev. Lett.*, 70, 694–697, 1993. doi:10.1103/PhysRevLett.70.694.

[89] C. T. Chen, Y. U. Idzerda, H.-J. Lin, N. V. Smith, G. Meigs, E. Chaban, G. H. Ho, E. Pellegrin and F. Sette. "Experimental Confirmation of the X-Ray Magnetic Circular Dichroism Sum Rules for Iron and Cobalt". *Phys. Rev. Lett.*, 75, 152–155, 1995. doi:10.1103/PhysRevLett.75.152.

[90] C. Piamonteze, P. Miedema and F. M. F. de Groot. "Accuracy of the spin sum rule in XMCD for the transition-metal L edges from manganese to copper". *Phys. Rev. B*, 80, 184410, 2009. doi:10.1103/PhysRevB.80.184410.

[91] J. M. D. Coey. *Magnetism and Magnetic Materials*. Cambridge University Press, 2010. doi:10.1017/CBO9780511845000.

[92] B. D. Cullity and C. D. Graham. *Introduction to Magnetic Materials*. John Wiley & Sons, Ltd, 2008. doi:10.1002/9780470386323.

[93] N. A. Spaldin. *Magnetic Materials: Fundamentals and Applications*. Cambridge University Press, 2010. doi:10.1017/CBO9780511781599.

[94] K. Kopitzki and P. Herzog. *Einführung in die Festkörperphysik*. Vieweg+Teubner, 2007.

[95] W. Heisenberg. "Zur Theorie des Ferromagnetismus". *Zeitschrift für Physik*, 49, 619–636, 1928. doi:10.1007/BF01328601.

[96] N. F. Mott. "The Basis of the Electron Theory of Metals, with Special Reference to the Transition Metals". *Proc. Phys. Soc. Lond., Sect. A*, 62(7), 416–422, 1949. doi:10.1088/0370-1298/62/7/303.

[97] J. Hubbard. "Electron correlations in narrow energy bands". *Proc. R. Soc. Lond. A*, 1963. doi:10.1098/rspa.1963.0204.

[98] J. B. Goodenough. *Magnetism and the chemical bond*. Interscience Publishers, 1963.

[99] J. Kanamori. "Superexchange interaction and symmetry properties of electron orbitals". *J. Phys. Chem. Solids*, 10(2), 87–98, 1959. doi:10.1016/0022-3697(59)90061-7.

[100] P. W. Anderson. "Chapter 2 - Exchange in Insulators: Superexchange, Direct Exchange, and Double Exchange". In G. T. Rado and H. Suhl (Editors), "Magnetism", pages 25–83. Academic Press, 1963. doi:10.1016/B978-0-12-575301-2.50009-2.

[101] Alex Hubert and Rudolf Schäfer. *Magnetic Domains: The Analysis of Magnetic Microstructures*. Springer-Verlag Berlin Heidelberg, 1998. doi:10.1007/978-3-540-85054-0.

[102] M. Bass (Editor). *Handbook of Optics: Devices, measurements, and properties*, volume 2. McGraw-Hill, Inc., 1995.

[103] D. M. Roessler and W. C. Walker. "Electronic spectrum and ultraviolet optical properties of crystalline MgO". *Phys. Rev.*, 159, 733, 1967. doi:10.1103/PhysRev.159.733.

[104] C. Y. Fong, W. Saslow and M. L. Cohen. "Pseudopotential Calculation of the Optical Constants of MgO from 7-28 eV". *Phys. Rev.*, 168, 992–999, 1968. doi:10.1103/PhysRev.168.992.

[105] I. Nedkov and M. Ausloos (Editors). *Nano-crystalline and thin film magnetic oxides*. Kluwer Academic Publishers (The Netherlands), 1998.

[106] M. Cardona. "Optical Properties and Band Structure of $SrTiO_3$ and $BaTiO_3$". *Phys. Rev.*, 140, A651–A655, 1965. doi:10.1103/PhysRev.140.A651.

[107] R. Kannan and M. S. Seehra. "Percolation effects and magnetic properties of the randomly diluted fcc system $Co_pMg_{1-p}O$". *Phys. Rev. B*, 35, 6847–6853, 1987. doi:10.1103/PhysRevB.35.6847.

[108] V. I. Anisimov, M. A. Korotin and E. Z. Kurmaev. "Band-structure description of Mott insulators (NiO, MnO, FeO, CoO)". *J. Phys.: Condens. Matter*, 2(17), 3973–3987, 1990. doi:10.1088/0953-8984/2/17/008.

[109] F. B. Lewis and N. H. Saunders. "The thermal conductivity of NiO and CoO at the Néel temperature". *J. Phys. C: Solid State Phys.*, 6(15), 2525–2532, 1973. doi:10.1088/0022-3719/6/15/012.

[110] G. W. Pratt and R. Coelho. "Optical Absorption of CoO and MnO above and below the Néel Temperature". *Phys. Rev.*, 116, 281–286, 1959. doi:10.1103/PhysRev.116.281.

[111] R. M. Cornell and U. Schwertmann. *The iron oxides: Structure, properties, reactions, occurences and uses*. John Wiley & Sons, Ltd, Weinheim, 2004. doi:10.1002/3527602097.

[112] Z. Szotek, W. M. Temmerman, D. Ködderitzsch, A. Svane, L. Petit and H. Winter. "Electronic structures of normal and inverse spinel ferrites from first principles". *Phys. Rev. B*, 74(17), 174431, 2006. doi:10.1103/PhysRevB.74.174431.

[113] Z. Li, E. S. Fisher, J. Z. Liu and M. V. Nevitt. "Single-crystal elastic constants of Co-Al and Co-Fe spinels". *J. Mater. Sci.*, 26, 2621, 1991. doi:10.1007/BF00545546.

[114] R. C. Liebermann. "Pressure and temperature dependence of the elastic properties of polycrystalline trevorite ($NiFe_2O_4$)". *Phys. Earth Planet. Inter.*, 6(5), 360–365, 1972. doi:10.1016/0031-9201(72)90059-3.

[115] V. N. Antonov, B. N. Harmon and A. N. Yaresko. "Electronic structure and x-ray magnetic circular dichroism in Fe_3O_4 and Mn-, Co-, or Ni-substituted Fe_3O_4". *Phys. Rev. B*, 67(2), 024417, 2003. doi:10.1103/PhysRevB.67.024417.

[116] M. Pénicaud, B. Siberchicot, C. B. Sommers and J. Kübler. "Calculated electronic band structure and magnetic moments of ferrites". *J. Magn. Magn. Mater.*, 103(1), 212–220, 1992. doi:10.1016/0304-8853(92)90255-M.

[117] D. J. Singh, M. Gupta and R. Gupta. "First-principles investigation of $MnFe_2O_4$". *Phys. Rev. B*, 65, 064432, 2002. doi:10.1103/PhysRevB.65.064432.

[118] Z. Szotek, W. M. Temmerman, A. Svane, L. Petit, P. Strange, G. M. Stocks, D. Ködderitzsch, W. Hergert and H. Winter. "Electronic structure of half-metallic ferromagnets and spinel ferromagnetic insulators". *J. Phys.: Condens. Matter*, 16(48), 5587–5600, 2004. doi:10.1088/0953-8984/16/48/015.

[119] H.-T. Jeng and G. Y. Guo. "First-principles investigations of the electronic structure and magnetocrystalline anisotropy in strained magnetite Fe_3O_4". *Phys. Rev. B*, 65(9), 094429, 2002. doi:10.1103/PhysRevB.65.094429.

[120] H.-T. Jeng and G. Y. Guo. "First-principles investigations of the magnetocrystalline anisotropy in strained Ni-substituted magnetite ($NiFe_2O_4$)". *J. Magn. Magn. Mater.*, 240(1), 436–438, 2002. doi:10.1016/S0304-8853(01)00886-1. 4th International Symposium on Metallic Multilayers.

[121] H.-T. Jeng and G. Y. Guo. "First-principles investigations of the magnetocrystalline anisotropy in strained Co-substituted magnetite ($CoFe_2O_4$)". *J. Magn. Magn. Mater.*, 239(1), 88–90, 2002. doi:10.1016/S0304-8853(01)00559-5.

[122] M. Uhl and B. Siberchicot. "A first-principles study of exchange integrals in magnetite". *J. Phys.: Condens. Matter*, 7(22), 4227–4237, 1995. doi:10.1088/0953-8984/7/22/006.

[123] Néel, M. Louis. "Propriétés magnétiques des ferrites; ferrimagnétisme et antiferromagnétisme". *Ann. Phys.*, 12(3), 137–198, 1948. doi:10.1051/anphys/194812030137.

[124] M. L. Glasser and F. J. Milford. "Spin Wave Spectra of Magnetite". *Phys. Rev.*, 130, 1783–1789, 1963. doi:10.1103/PhysRev.130.1783.

[125] K. T. Möglestue. "Exchange integrals in magnetite". In "Neutron Inelastic Scattering - Proceedings of a Symposium", volume 2, pages 117–121. IAEA, 1968.

[126] P. G. Bercoff and H. R. Bertorello. "Exchange constants and transfer integrals of spinel ferrites". *J. Magn. Magn. Mater.*, 169(3), 314–322, 1997. doi:10.1016/S0304-8853(96)00748-2.

[127] C. M. Srivastava, G. Srinivasan and N. G. Nanadikar. "Exchange constants in spinel ferrites". *Phys. Rev. B*, 19, 499–508, 1979. doi:10.1103/PhysRevB.19.499.

[128] G. A. Sawatzky, F. van der Woude and A. H. Morrish. "Mössbauer Study of Several Ferrimagnetic Spinels". *Phys. Rev.*, 187, 747–757, 1969. doi:10.1103/PhysRev.187.747.

[129] J. G. Na, T. D. Lee, S. J. Park, Y. J. Tang and H. L. Luo. "Effects of cation distribution on superexchange interaction in cobalt ferrites". *IEEE Trans. Magn.*, 31(6), 3970–3972, 1995. doi:10.1109/20.489833.

[130] S. J. Kim, W. C. Kim, C. S. Kim and S. W. Lee. "Mössbauer Studies of Superexchange Interactions in $NiFe_2O_4$". *J. Kor. Phys. Soc.*, 36(6), 430–434, 2000.

[131] S. J. Kim, S. W. Lee and C. S. Kim. "Mössbauer Studies on Exchange Interactions in $CoFe_2O_4$". *Jpn. J. Appl. Phys.*, 40(8), 4897–4902, 2001. doi:10.1143/jjap.40.4897.

[132] S. J. Kim, C. S. Kim and E. J. Hahn. "Mössbauer Studies on Superexchange Interactions in Fe_3O_4". *J. Kor. Phys. Soc.*, 64(6), 852–856, 2014.

[133] D. T. Margulies, F. T. Parker, M. L. Rudee, F. E. Spada, J. N. Chapman, P. R. Aitchison and A. E. Berkowitz. "Origin of the Anomalous Magnetic Behavior in Single Crystal Fe_3O_4 Films". *Phys. Rev. Lett.*, 79(25), 5162–5165, 1997. doi:10.1103/PhysRevLett.79.5162.

[134] F. C. Voogt, T. T. M. Palstra, L. Niesen, O. C. Rogojanu, M. A. James and T. Hibma. "Superparamagnetic behavior of structural domains in epitaxial ultrathin magnetite films". *Phys. Rev. B*, 57, R8107–R8110, 1998. doi:10.1103/PhysRevB.57.R8107.

[135] T. Hibma, F. C. Voogt, L. Niesen, P. A. A. van der Heijden, W. J. M. de Jonge, J. J. T. M. Donkers and P. J. van der Zaag. "Anti-phase domains and magnetism in epitaxial magnetite layers". *J. Appl. Phys.*, 85, 5291, 1999. doi:10.1063/1.369857.

[136] S. Celotto, W. Eerenstein and T. Hibma. "Characterization of anti-phase boundaries in epitaxial magnetite films". *Eur. Phys. J. B*, 36, 271, 2003. doi:10.1140/epjb/e2003-00344-7.

[137] W. Eerenstein, T. T. M. Palstra, T. Hibma and S. Celotto. "Origin of the increased resistivity in epitaxial Fe_3O_4 films". *Phys. Rev. B*, 66, 201101, 2002. doi:10.1103/PhysRevB.66.201101.

[138] W. Eerenstein, T. T. M. Palstra, T. Hibma and S. Celotto. "Diffusive motion of antiphase domain boundaries in Fe_3O_4 films". *Phys. Rev. B*, 68, 014428, 2003. doi:10.1103/PhysRevB.68.014428.

[139] S. K. Arora, R. G. S. Sofin, I. V. Shvets and M. Luysberg. "Anomalous strain relaxation behavior of Fe_3O_4/MgO(100) heteroepitaxial system grown using molecular beam epitaxy". *J. Appl. Phys.*, 100(7), 073908, 2006. doi:10.1063/1.2349468.

[140] J. D. Wei, I. Knittel, U. Hartmann, Y. Zhou, S. Murphy, I. V. Shvets and F. T. Parker. "Influence of the antiphase domain distribution on the magnetic structure of magnetite thin films". *Appl. Phys. Lett.*, 89(12), 122517, 2006. doi:10.1063/1.2356308.

[141] G. J. Strijkers, J. T. Kohlhepp, P. A. A. van der Heijden, H. J. M. Swagten, W. J. M. de Jonge and J. M. Gaines. "Magnetization of Fe_3O_4/MgO multilayers studied with Mössbauer spectroscopy". *J. Appl. Phys.*, 85(8), 5294–5296, 1999. doi:10.1063/1.369858.

[142] J.-B. Moussy, S. Gota, A. Bataille, M.-J. Guittet, M. Gautier-Soyer, F. Delille, B. Dieny, F. Ott, T. D. Doan, P. Warin, P. Bayle-Guillemaud, C. Gatel and E. Snoeck. "Thickness dependence of anomalous magnetic behavior in epitaxial Fe_3O_4(111) thin films: Effect of density of antiphase boundaries". *Phys. Rev. B*, 70, 174448, 2004. doi:10.1103/PhysRevB.70.174448.

[143] J. M. D. Coey, A. E. Berkowitz, L. Balcells, F. F. Putris and F. T. Parker. "Magnetoresistance of magnetite". *Appl. Phys. Lett.*, 72(6), 734–736, 1998. doi:10.1063/1.120859.

[144] M. Ziese and H. J. Blythe. "Magnetoresistance of magnetite". *J. Phys.: Condens. Matter*, 12(1), 13–28, 1999. doi:10.1088/0953-8984/12/1/302.

[145] W. Eerenstein, T. T. M. Palstra, S. S. Saxena and T. Hibma. "Spin-Polarized Transport across Sharp Antiferromagnetic Boundaries". *Phys. Rev. Lett.*, 88, 247204, 2002. doi:10.1103/PhysRevLett.88.247204.

[146] R. J. M. van de Veerdonk, M. A. M. Gijs, P. A. A. van der Heijden, R. M. Wolf and W. J. M. de Jonge. "Study of the Verwey Transition of Fe_3O_4 Films and Fe_3O_4/MgO Multilayers Grown by MBE". *Mat. Res. Soc. Symp. Proc.*, 401, 455, 1996.

[147] P. A. A. van der Heijden, P. J. H. Bloemen, J. M. Gaines, J. T. W. M. van Eemeren, R. M. Wolf, P. J. van der Zaag and W. J. M. de Jonge. "Magnetic interface anisotropy of MBE-grown ultra-thin (001) Fe_3O_4 layers". *J. Magn. Magn. Mater.*, 159(3), L293–L298, 1996. doi:10.1016/0304-8853(96)00376-9.

[148] K. Balakrishnan, S. K. Arora and I. V. Shvets. "Strain relaxation studies of the Fe_3O_4/MgO(100) heteroepitaxial system grown by magnetron sputtering". *J. Phys.: Condens. Matter*, 16(30), 5387–5393, 2004. doi:10.1088/0953-8984/16/30/001.

[149] A. V. Ramos, J.-B. Moussy, M.-J. Guittet, A. M. Bataille, M. Gautier-Soyer, M. Viret, C. Gatel, P. Bayle-Guillemaud and E. Snoeck. "Magnetotransport properties of Fe_3O_4 epitaxial thin films: Thickness effects driven by antiphase boundaries". *J. Appl. Phys.*, 100(10), 103902, 2006. doi:10.1063/1.2386927.

[150] C. Otte. *Rastertunnelmikroskopie an epitaktischen Eisenschichten auf MgO(001)*. Diploma thesis, Osnabrück University, 2010.

[151] F. Bertram, C. Deiter, T. Schemme, S. Jentsch and J. Wollschläger. "Reordering between tetrahedral and octahedral sites in ultrathin magnetite films grown on MgO(001)". *J. Appl. Phys.*, 113(18), 184103, 2013. doi:10.1063/1.4803894.

[152] N.-T. H. Kim-Ngan, A. G. Balogh, J. D. Meyer, J. Brötz, M. Zając, T. Ślęzak and J. Korecki. "Thermal and irradiation induced interdiffusion in magnetite thin films grown on magnesium oxide (001) substrates". *Surf. Sci.*, 603(9), 1175–1181, 2009. doi:10.1016/j.susc.2009.02.028.

[153] J. F. Anderson, M. Kuhn, U. Diebold, K. Shaw, P. Stoyanov and D. Lind. "Surface structure and morphology of Mg-segregated epitaxial Fe_3O_4(001) thin films on MgO(001)". *Phys. Rev. B*, 56, 9902–9909, 1997. doi:10.1103/PhysRevB.56.9902.

[154] J. Thien. *Bildung und Charakterisierung von Cobaltferritschichten durch Interdiffusion von Cobaltoxid- und Magnetitschichten.* Master's thesis, Osnabrück University, 2017.

[155] C. J. Powell and A. Jablonski. "Surface sensitivity of X-ray photoelectron spectroscopy". *Nucl. Instrum. Methods Phys. Res., Sect. A*, 601(1), 54–65, 2009. doi:10.1016/j.nima.2008.12.103. Special issue in honour of Prof. Kai Siegbahn.

[156] R. Nakajima, J. Stöhr and Y. U. Idzerda. "Electron-yield saturation effects in L-edge x-ray magnetic circular dichroism spectra of Fe, Co, and Ni". *Phys. Rev. B*, 59(9), 6421–6429, 1999. doi:10.1103/PhysRevB.59.6421.

[157] S. Gota, M. Gautier-Soyer and M. Sacchi. "Fe 2p absorption in magnetic oxides: Quantifying angular-dependent saturation effects". *Phys. Rev. B*, 62(7), 4187–4190, 2000. doi:10.1103/PhysRevB.62.4187.

[158] A. Ruosi, C. Raisch, A. Verna, R. Werner, B. A. Davidson, J. Fujii, R. Kleiner and D. Koelle. "Electron sampling depth and saturation effects in perovskite films investigated by soft x-ray absorption spectroscopy". *Phys. Rev. B*, 90(12), 125120, 2014. doi:10.1103/PhysRevB.90.125120.

[159] M. Shipilin, U. Hejral, E. Lundgren, L. R. Merte, C. Zhang, A. Stierle, U. Ruett, O. Gutowski, M. Skoglundh, P.-A. Carlsson and J. Gustafson. "Quantitative surface structure determination using in situ high-energy SXRD: Surface oxide formation on Pd(100) during catalytic CO oxidation". *Surf. Sci.*, 630, 229–235, 2014. doi:10.1016/j.susc.2014.08.021.

[160] H. You. "Angle calculations for a '4S+2D' six-circle diffractometer". *J. Appl. Cryst.*, 32(4), 614–623, 1999. doi:10.1107/S0021889899001223.

[161] E. Vlieg. "Integrated Intensities Using a Six-Circle Surface X-ray Diffractometer". *J. Appl. Cryst.*, 30(5), 532–543, 1997. doi:10.1107/S0021889897002537.

[162] E. Vlieg. "A (2+3)-Type Surface Diffractometer: Mergence of the z-Axis and (2+2)-Type Geometries". *J. Appl. Cryst.*, 31(2), 198–203, 1998. doi:10.1107/S0021889897009990.

[163] C. M. Schlepütz, R. Herger, P. R. Willmott, B. D. Patterson, O. Bunk, C. Brönnimann, B. Henrich, G. Hülsen and E. F. Eikenberry. "Improved data acquisition in grazing-incidence X-ray scattering experiments using a pixel detector". *Acta Cryst. Sec. A*, 61(4), 418–425, 2005. doi:10.1107/S0108767305014790.

[164] K. W. Evans-Lutterodt and M. T. Tang. "Angle Calculations for a '2+2' Surface X-ray Diffractometer". *J. Appl. Cryst.*, 28(3), 318–326, 1995. doi:10.1107/S0021889894011131.

[165] D.-M. Smilgies. "Geometry-independent intensity correction factors for grazing-incidence diffraction". *Rev. Sci. Instrum.*, 73(4), 1706–1710, 2002. doi:10.1063/1.1461876.

[166] J. Treacy. *Synchrotron studies of TiO_2 single crystal surfaces.* Ph.D. thesis, Manchester University, 2014.

[167] E. D. Specht and F. J. Walker. "A method for the accurate determination of crystal truncation rod intensities by X-ray diffraction". *J. Appl. Cryst.*, 26(2), 166–171, 1993. doi:10.1107/S0021889892011592.

[168] A. Greuling. *Röntgenstrukturanalyse von Isolatorschichten.* Masters's thesis, Osnabrück University, 2007.

[169] S. Hahne. *Strukturanalyse von Praseodymoxidschichten mit Röntgenbeugung.* Bachelor's thesis, Osnabrück University, 2008.

[170] F. Bertram. *Röntgenstrukturanalyse von Oxidschichten*. Masters's thesis, Osnabrück University, 2009.

[171] F. London. *Superfluids*, volume 1. Wiley, New York, 1950.

[172] B. D. Josephson. "Possible new effects in superconductive tunnelling". *Phys. Lett.*, 1(7), 251–253, 1962. doi:10.1016/0031-9163(62)91369-0.

[173] H. Weinstock (Editor). *SQUID Sensors - Fundamentals, Fabrication and Applications*, volume 329 of *NATO ASI Series (Series E: Applied Sciences)*. Springer Netherlands, 1996. doi:10.1007/978-94-011-5674-5.

[174] J. Clarke and A. I. Braginski (Editors). *The SQUID Handbook: Fundamentals and Technology of SQUIDs and SQUID systems*, volume 1. John Wiley & Sons, Ltd, 2004. doi:10.1002/3527603646.

[175] R. L. Fagaly. "Superconducting quantum interference device instruments and applications". *Rev. Sci. Instrum.*, 77(10), 101101, 2006. doi:10.1063/1.2354545.

[176] Y. Aharonov and D. Bohm. "Significance of Electromagnetic Potentials in the Quantum Theory". *Phys. Rev.*, 115, 485–491, 1959. doi:10.1103/PhysRev.115.485.

[177] B. S. Deaver and W. M. Fairbank. "Experimental Evidence for Quantized Flux in Superconducting Cylinders". *Phys. Rev. Lett.*, 7, 43–46, 1961. doi:10.1103/PhysRevLett.7.43.

[178] R. Doll and M. Näbauer. "Experimental Proof of Magnetic Flux Quantization in a Superconducting Ring". *Phys. Rev. Lett.*, 7, 51–52, 1961. doi:10.1103/PhysRevLett.7.51.

[179] G. E. W. Bauer, E. Saitoh and B. J. van Wees. "Spin caloritronics". *Nat. Mater.*, 11, 391–399, 2012. doi:10.1038/nmat3301.

[180] A. Hoffmann and S. D. Bader. "Opportunities at the frontiers of spintronics". *Phys. Rev. Appl*, 4(4), 047001, 2015. doi:10.1103/PhysRevApplied.4.047001.

[181] J. Cibert, J.-F. Bobo and U. Lüders. "Development of new materials for spintronics". *C. R. Physique*, 6(9), 977–996, 2005. doi:10.1016/j.crhy.2005.10.008.

[182] J.-B. Moussy. "From epitaxial growth of ferrite thin films to spin-polarized tunnelling". *J. Phys. D: Appl. Phys.*, 46(14), 143001, 2013. doi:10.1088/0022-3727/46/14/143001.

[183] M. Lenglet and A. D'Huysser and C. K. Jørgensen. "Optical spectra, x-ray photoelectron spectra and XANES of divalent nickel in mixed spinels $NiFe_{2-x}Cr_xO_4$". *Inorg. Chim. Acta*, 133(1), 61–65, 1987. doi:10.1016/S0020-1693(00)84373-X.

[184] R. S. de Biasi and H. dos Santos. "Cation distribution, saturation magnetization and magnetocrystalline anisotropy of mixed ferrite $NiAl_xFe_{2-x}O_4$ nanoparticles". *Ceram. Int.*, 43(5), 4557–4561, 2017. doi:10.1016/j.ceramint.2016.12.111.

[185] Y. Teramura, A. Tanaka and T. Jo. "Effect of Coulomb Interaction on the X-Ray Magnetic Circular Dichroism Spin Sum Rule in 3 *d* Transition Elements". *J. Phys. Soc. Jpn.*, 65(4), 1053–1055, 1996. doi:10.1143/JPSJ.65.1053.

[186] B. L. Henke, E. M. Gullikson and J. C. Davis. "X-ray interactions: photoabsorption, scattering, transmission, and reflection at E=50-30000 eV, Z=1-92". *At. Data. Nucl. Data Tables*, 54, 181–342, 1993. doi:10.1006/adnd.1993.1013.

[187] D. Alders, F. C. Voogt, T. Hibma and G. A. Sawatzky. "Nonlocal screening effects in 2p x-ray photoemission spectroscopy of NiO(100)". *Phys. Rev. B*, 54, 7716–7719, 1996. doi:10.1103/PhysRevB.54.7716.

[188] M. C. Biesinger and B. P. Payne and A. P. Grosvenor and L. W. M. Lau and A. R. Gerson and R. St. C. Smart. "Resolving surface chemical states in XPS analysis of first row transition

metals, oxides and hydroxides: Cr, Mn, Fe, Co and Ni". *Appl. Surf. Sci.*, 257(7), 2717–2730, 2011. doi:10.1016/j.apsusc.2010.10.051.

[189] M. A. van Veenendaal and G. A. Sawatzky. "Nonlocal screening effects in 2p x-ray photoemission spectroscopy core-level line shapes of transition metal compounds". *Phys. Rev. Lett.*, 70, 2459–2462, 1993. doi:10.1103/PhysRevLett.70.2459.

[190] A. F. Carley, S. D. Jackson, J. N. O'Shea and M. W. Roberts. "The formation and characterisation of Ni^{3+} - an X-ray photoelectron spectroscopic investigation of potassium-doped Ni(110)-O". *Surf. Sci.*, 440(3), L868–L874, 1999. doi:10.1016/S0039-6028(99)00872-9.

[191] T. Yamashita and P. Hayes. "Analysis of XPS spectra of Fe^{2+} and Fe^{3+} ions in oxide materials". *Appl. Surf. Sci.*, 254(8), 2441–2449, 2008. doi:10.1016/j.apsusc.2007.09.063.

[192] J. P. Crocombette, M. Pollak, F. Jollet, N. Thromat and M. Gautier-Soyer. "X-ray absorption spectroscopy at the Fe $L_{2,3}$ threshold in iron oxides". *Phys. Rev. B*, 52(5), 3143–3150, 1995. doi:10.1103/PhysRevB.52.3143.

[193] P. Kuiper, B. G. Searle, L.-C. Duda, R. M. Wolf and P. J. van der Zaag. "Fe $L_{2,3}$ linear and circular magnetic dichroism of Fe_3O_4". *J. Electron Spectrosc. Relat. Phenom.*, 86(1), 107–113, 1997. doi:10.1016/S0368-2048(97)00053-4.

[194] T. J. Regan, H. Ohldag, C. Stamm, F. Nolting, J. Lüning, J. Stöhr and R. L. White. "Chemical effects at metal/oxide interfaces studied by x-ray-absorption spectroscopy". *Phys. Rev. B*, 64(21), 214422, 2001. doi:10.1103/PhysRevB.64.214422.

[195] G. van der Laan, C. M. B. Henderson, R. A. D. Pattrick, S. S. Dhesi, P. F. Schofield, E. Dudzik and D. J. Vaughan. "Orbital polarization in $NiFe_2O_4$ measured by $Ni - 2p$ x-ray magnetic circular dichroism". *Phys. Rev. B*, 59, 4314–4321, 1999. doi:10.1103/PhysRevB.59.4314.

[196] Y. K. Wakabayashi, Y. Nonaka, Y. Takeda, S. Sakamoto, K. Ikeda, Z. Chi, G. Shibata, A. Tanaka, Y. Saitoh, H. Yamagami, M. Tanaka, A. Fujimori and R. Nakane. "Cation distribution and magnetic properties in ultrathin $(Ni_{1-x}Co_x)Fe_2O_4$ $(x = 0 - 1)$ layers on Si(111) studied by soft x-ray magnetic circular dichroism". *Phys. Rev. Materials*, 2, 104416, 2018. doi:10.1103/PhysRevMaterials.2.104416.

[197] G. Schütz, P. Fischer, E. Goering, K. Attenkofer, D. Ahlers and W. Rößl. "X-ray magnetic circular dichroism". *Synchrotron Radiation News*, 10(4), 13–26, 1997. doi:10.1080/08940889708260897.

[198] A. G. Every and A. K. McCurdy. *Second and higher order elastic constants*. Springer Materials - The Landolt-Börnstein Database, Springer-Verlag Berlin Heidelberg, 1992. doi:10.1007/b44185.

[199] T. E. Mitchell, L. Hwang and A. H. Heuer. "Deformation in spinel". *J. Mater. Sci.*, 11, 264–272, 1976. doi:10.1007/BF00551437.

Danksagung

An dieser Stelle möchte ich mich bei allen Personen bedanken, die zur Erstellung dieser Doktorarbeit beigetragen haben. Allen voran sei dabei meinem Mentor Herrn Prof. Dr. Joachim Wollschläger gedankt, der während der gesamten Zeit der Dissertation immer Ansprechpartner für Probleme und Fragestellungen jeglicher Art war und sich viel Zeit genommen hat, diese zu diskutieren. Vielen Dank für die Geduld und das entgegengebrachte Vertrauen. Weiterhin danke ich Herrn Prof. Dr. Thomas Schröder, der sich noch sehr kurzfristig bereit erklärt hat, die Rolle des Zweitgutachters zu übernehmen. Außerdem sei noch Herrn Prof. Dr. Robin Steinigeweg und Dr. Karsten Küpper gedankt, die die Promotionskommission komplettieren.
Des Weiteren möchte ich mich bei allen ehemaligen und aktuellen Mitgliedern der Arbeitsgruppe "Dünne Schichten und Grenzflächen" im Fachbereich Physik der Universität Osnabrück bedanken, die einerseits inhaltlich zu dieser Arbeit beigetragen haben, andererseits aber vor allem die Arbeitsatmosphäre im Labor und im Büro so angenehm wie nur möglich gemacht haben. Dabei sind vor allem Jannis Thien, Tabea Nordmann, Kevin Ruwisch, Kristina Sprenger, Michaela Tomíčková, Tobias Pollenske und Simon Spiller zu nennen, die mit ihren eigenen Abschlussarbeiten unter anderem auch zu dieser Arbeit beigetragen haben. Auch Tobias Pohlmann, Martin Hoppe und Frederic Timmer, die mich sowohl bei der Arbeit im Labor, als auch bei etlichen Synchrotronmesszeiten und der Datenauswertung unterstützt haben, sei hierbei ausdrücklich gedankt. Ein weiterer Dank gilt Florian Bertram für die Unterstützung bei einigen Messzeiten und für die kompetente Hilfestellung bei der Datenauswertung. Ebenfalls möchte ich mich bei Timo Kuschel für seine Ideen und die hilfreichen Diskussionen bedanken. Außerdem sei der Feinmechanischen Werkstatt und der Werkstatt für Elektronik für die Betreuung bei Konstruktionen und den schnellen Einsatz bei Reparaturen gedankt. Ihr alle habt damit maßgeblich zum Gelingen dieser Arbeit beigetragen.
Explizit möchte ich mich an dieser Stelle bei unserem Techniker und meinem geschätzten Bürokollegen Gregor Steinhoff für die tatkräftige Unterstützung beim Aufbau einiger experimenteller Apparaturen und bei der Lösung etwaiger technischer Probleme bedanken. Auch meiner langjährigen Bürokollegin Olga Kuschel möchte ich danken, da sie sich immer die Zeit genommen hat, nicht nur inhaltliche Fragestellungen zu diskutieren und mir dadurch erheblich weiterhelfen konnte. Euch beiden habe ich eine sehr angenehme Büroatmosphäre zu verdanken. Außerdem sei auch allen an dieser Stelle nicht namentlich genannten AG-Mitgliedern für die entspannte aber auch produktive Arbeitsatmosphäre gedankt. Nicht zuletzt durch die vielen außeruniversitären Veranstaltungen habe ich mich sehr wohl bei euch gefühlt.
Ein besonderer Dank gilt an dieser Stelle meinen Freunden und meiner Familie, auf die ich mich zu jeder Zeit verlassen kann. Insbesondere bei meinen Eltern möchte ich mich hier für ihre unersetzliche Unterstützung in jeder Lebenslage bedanken, ohne die es gar nicht zu dieser Arbeit gekommen wäre. Vor allem aber danke ich meiner Freundin und Lebenspartnerin Tina, die mich immer unterstützt, sowohl bei dieser Arbeit als auch in allen anderen Lebensbereichen. Danke für das Verständnis, die Geduld und die Unterstützung vor allem auch in den letzten Monaten dieser Arbeit. Ohne dich wäre all das so nicht möglich gewesen. Vielen Dank!